NREL/TP-451-7056 • UC Category: 1263 • DE94011895

Processing and Modeling Issues for Thin-Film Solar Cell Devices

Annual Subcontract Report
16 January 1993 – 15 January 1994

R. W. Birkmire, J. E. Phillips,
W. A. Buchanan, S. S. Hegedus,
B. E. McCandless, W. N. Shafarman,
T. A. Yokimcus
Institute of Energy Conversion
Newark, Delaware

NREL technical monitor: B. von Roedern

National Renewable Energy Laboratory
1617 Cole Boulevard
Golden, Colorado 80401-3393
A national laboratory of the U.S. Department of Energy
Managed by Midwest Research Institute
for the U.S. Department of Energy
under contract No. DE-AC36-83CH10093

Prepared under Subcontract No. X-AV-13170-01

September 1994

Available to DOE and DOE contractors from:
Office of Scientific and Technical Information (OSTI)
P.O. Box 62
Oak Ridge, TN 37831
Prices available by calling (615) 576-8401

Available to the public from:
National Technical Information Service (NTIS)
U.S. Department of Commerce
5285 Port Royal Road
Springfield, VA 22161
(703) 487-4650


Printed on paper containing at least 50% wastepaper and 10% postconsumer waste

Preface

The efforts of the first year of an integrated program of research on thin film solar cells based on a-Si:H and its alloys, $CuInSe_2$ and its alloys, and CdTe are described. The objective of this ongoing research is to advance the development and acceptance of thin-film photovoltaic modules by: investigating scalable, cost-effective deposition processes, preparing thin-film materials and device layers and completed cell structures, performing detailed material and device analysis, and participating in collaborative research efforts that address the needs of PV manufacturers and other laboratories.

Results from these efforts presented in this report address the relationships among the deposition and processing, materials properties, and device performance of these thin film materials. The reaction chemistry of $CuInSe_2$ films formed by the selenization of Cu/In bi-layers in both flowing H_2Se and elemental selenium vapor are presented. Bandgap modified $CuInSe_2$ has been evaluated with $Cu(InGa)Se_2$ deposited by thermal evaporation. Detailed microstructural characterization of CdTe/CdS devices has been used to explain the critical deposition and processing parameters needed to fabricate high efficiency cells. Device measurements and modeling of a-Si p-i-n solar cells have been used to characterize plasma-CVD deposition of the a-Si and improve device performance and reproducibility. Current-voltage measurements of $CuInSe_2$ and $Cu(InGa)Se_2$ cells made by a variety of different processes and laboratories were analyzed showing that the basic operation of these cells is the same, regardless of differences in deposition or Ga content. Finally, a number of collaborations with other laboratories and industries dealing with all aspects of thin film solar cell research are reviewed.

Summary

Objectives

The overall objective of the research presented in this report is to advance the development and acceptance of thin-film photovoltaic modules by increasing the understanding of film growth and processing and its relationship to materials properties and solar cell performance. The specific means toward meeting this larger goal include: 1) investigating scalable, cost-effective deposition processes; 2) preparing thin-film materials and device layers and completed cell structures; 3) performing detailed material and device analysis; and 4) participating in collaborative research efforts that address the needs of PV-manufacturers. These objectives are being pursued with $CuInSe_2$, CdTe and a-Si based solar cells.

Results

This report covers the results of the first year of a four year integrated research program of Deposition and Process Research, Solar Cell Measurements and Analysis, and Research and Development Collaborations.

$CuInSe_2$ films have been formed by the selenization of Cu/In bi-layer precursors in both flowing hydrogen selenide (H_2Se) and elemental selenium vapor. A reactor analysis of the formation of $CuInSe_2$ by selenization in H_2Se has been completed based on sets of time progressive experiments in H_2Se alone and H_2Se/oxygen mixtures. A film growth model is proposed and the rate constants are determined for reactions both with and without oxygen. It is shown that oxygen plays a critical role in both the gas phase chemistry and the morphology and growth kinetics of the reacting film. This model for $CuInSe_2$ film growth has lead to a process for fabricating solar cells with over 11.5% efficiency. The sensitivity of this process to specific process variables such as the selenizing gas composition, the Cu/In layer deposition, and post-selenization processing is evaluated. Initial results are also presented for the reaction of CuGa/In precursors for the formation of $Cu(InGa)Se_2$ by selenization in H_2Se.

The reaction chemistry leading to the formation of $CuInSe_2$ by the selenization of Cu/In layers in an elemental Se vapor has been determined based on a set of experiments at reaction temperatures from 150°C to 650°C. Detailed x-ray diffraction (XRD) analysis was used to determine starting phases in the precursors and the intermediate phases at different selenization temperatures leading to a proposed reaction chemistry. This analysis revealed that the In reactions in particular, can be controlled by the time profile of substrate temperature to enhance the formation of In-Se phases with low volatility. This enables the high temperature selenization to proceed with no loss of In and the formation of single phase $CuInSe_2$.

$CuInSe_2$ with the bandgap increased by alloying with Ga is being investigated with the deposition of $Cu(InGa)Se_2$ by four source thermal evaporation. Films have been deposited with the ratio of Ga/(In+Ga) varying from 0 to 0.6 corresponding to a range of bandgaps from 1.0 to 1.3 eV. Detailed XRD characterization of these films shows that they have a composition variation through the film which increases as the Ga content increases. Splitting of the XRD peaks indicates the segregation of regions with different compositions. Solar cells fabricated with these films show that the device performance and quantum efficiency falls off as the Ga content increases suggesting a degradation of the electrical properties of the $Cu(InGa)Se_2$. The best cell results have been achieved with Ga/(In+Ga) less than 0.3 corresponding to a bandgap less than ~1.15 eV.

Microstructural characterization of CdTe/CdS devices before and after the $CdCl_2$ heat treatment is used to increase the understanding of this critical processing step. The CdTe layer grows heteroepitaxially on the CdS but significant recrystallization and grain coalescence occurs in the first 2-5 minutes at 415°C. The CdTe film becomes randomly oriented and the grain size increase to 2-5 μm. The CdTeS layer, which forms as a result of interdiffusion during the heat treatment, is compositionally non-uniform with sulfur-enhanced regions around grain boundaries and crystallographic defects. This non-uniformity can limit the device performance. However, it is shown that the interdiffusion can be controlled by pre-treatment of the CdS with $CdCl_2$, increasing its density. Understanding the relation between the CdS and the post-deposition processing of the CdTe/CdS enables the heat treatment procedures to be optimized with thin CdS layers, improving J_{sc} and device performance.

The CdTe devices are completed with diffusion doping of Cu from the back contact. Increasing the dopant concentration in the CdTe had lead to V_{oc} of 830 mV and, with the optimized use of CdS less than 2000Å thick, cell efficiencies over 12%. Finally, an alternative process to the $CdCl_2$ heat treatment, in which chlorine gas is used to restructure CdTe/CdS, is demonstrated.

The primary focus in amorphous silicon deposition and process research has been on improving the performance and reliability of the plasma-enhanced CVD deposition with the goal of reproducibly fabricating single junction a-Si cells with 9% initial efficiency. This device making capability will be used to support the NREL a-Si Team objectives. Device results and quantum efficiencies are used as the primary guide to improving the reactor performance. Both boron and phosphorus contamination in the i-layer were separately identified from device measurements. The design of the PECVD reactor was found to be flawed. Consequently, modifications to the reactor and the deposition procedures were made to reduce the contamination

leading directly to improved device efficiencies and reproducibility.

The current voltage characteristics of a number of $CuInSe_2/CdS$ and $Cu(InGa)Se_2/CdS$ solar cells made under various conditions and laboratories have been measured under a wide range of temperatures and illumination conditions and then analyzed and compared. The cells all have non-linear contributions to the current-voltage behavior which are attributed to non-ohmic contributions in series with the main diode. All of the $CuInSe_2/CdS$ and $Cu(InGa)Se_2/CdS$ devices have forward J-V current behavior which appears to be dominated by the same mechanism, which is, electron - hole or Shockley-Read-Hall recombination in the absorber layer. There are indications that this recombination is through a continuous exponential-like distribution of recombination centers within the bandgap of the light absorbing material. Preliminary current voltage measurements on CdTe/CdS solar cells are also analyzed and appear to be dominated by Shockley-Read-Hall recombination.

A method has been developed to determine the optical absorption losses due to the p-layer in amorphous silicon p-i-n devices which requires a measurement of the spectral response. This method has been used to determine the thickness and optical losses of devices made at IEC. Measurements of V_{oc} vs. $\ln(J_{sc})$ have been made on abruptly graded a-Si:a-SiGe devices in order to determine equivalent circuit diode parameters. The values of J_o and the diode A-factors determined from this technique suggest that the equivalent circuit diode is determined by the a-SiGe material.

IEC has done collaborative research with a number of industrial and national laboratories and other research organizations dealing with all aspects of thin-film solar cell research. This has included the sharing of information regarding process, material, and device characterization and the supplying and sharing of films, devices, measurements and analyses. Several collaborations have been established to specifically address the goals of the NREL a-Si Research Teams.

List of Contributors

Robert W. Birkmire	Principal Investigator
James E. Phillips	Principal Investigator
Wayne A. Buchanan	Principal Researcher
Steven S. Hegedus	Principal Researcher
Brian E. McCandless	Principal Researcher
William N. Shafarman	Principal Researcher
Tracey A. Yokimcus	Principal Researcher
Scott J. Jones	Post Doctoral Fellow
Saibal Mitra	Post Doctoral Fellow
Satoshi Yamanaka	Post Doctoral Fellow
Sarah K. Buchanan	Technical Support
Ronald D. Dozier	Technical Support
Shannon Fields	Technical Support
Sally I. Gordon	Technical Support
Kevin E. Hart	Technical Support
Herbert O. Wardell	Technical Support
Axel Hartmann	Graduate Student
Joseph Shan	Graduate Student
Sandeep Verma	Graduate Student
Mark Cress	Student
Mike Goetz	Student
Tony Gladwell	Student
Richard Thompson	Student
Elaine Koronik	Document Preparation

Table of Contents

List of Figures

page

page

page

page

page

page

page

List of Tables

page

1.0 INTRODUCTION

Photovoltaic modules based on thin film systems of a-Si:H and its alloys, $CuInSe_2$ and its alloys, and CdTe, are promising candidates to meet DOE long range efficiency, reliability and cost goals. Although the commercial development of these modules is at different stages, there are generic research issues that need to be addressed. These include:

1) quantitative analysis of processing steps to develop efficient commercial scale equipment and processes;

2) device characterization relating the device performance to materials properties and process conditions;

3) development of alloy materials with different bandgap to allow improved device structures for stability and compatibility with module design;

4) development of improved window/heterojunction layers and contacts to improve device performance and reliability; and,

5) evaluation of cell stability with respect to illumination, temperature and ambient and with respect to device structure and module encapsulation.

Key R&D issues that need to be addressed to develop a viable commercial process and to improve the device performance for a-Si, $CuInSe_2$ and CdTe-based solar cells as well as general thin film device issues have been identified and are listed below.

<u>a-Si:H and its Alloys</u>

Light induced degradation of modules is the primary issue limiting commercialization of a-Si:H. Two approaches to improving the stabilized efficiency of these devices have been:

1) to develop ways to deposit more stable a-Si:H i-layers that can be incorporated in p-i-n devices;

2) to improve the device design, in particular to consider multijunction devices which require development of both high and low bandgap a-Si:H alloys compatible with multijunction cell fabrication.

In using the second approach, the number of 'interfaces' increases, and reducing interface losses becomes an important issue.

Transparent semiconductors are used in a-Si devices, both as a front contact, to allow light into the device and increase its

optical path length through scattering, and as a back contact, in conjunction with a metal as a back surface reflector. Improvements in the TCO's can improve the device performance and module process yield.

$CuInSe_2$/CdS

Presently the most attractive process to grow $CuInSe_2$ films for module production is the selenization of Cu/In films in an H_2Se atmosphere. This process has not been characterized in terms of the chemical pathways to film growth; the key parameters leading to 'good' quality films have not been identified. Further, since H_2Se is a toxic gas, an alternative to H_2Se is highly desirable.

$CuInSe_2$ has a bandgap of 1 eV, about 0.4 eV less than the optimal bandgap for a single junction device for terrestrial applications, and the V_{oc} of the devices are typically less than 0.5 V. Further, such high-current devices can reduce module performance due to cell spacing and series resistance losses compared to lower current devices based on wider bandgap absorbers. Thus, it is desirable to increase the bandgap of the $CuInSe_2$ by alloying with materials such as Ga or S.

Poor adhesion and spatial uniformity of $CuInSe_2$ films and devices appear to have resulted in low process yield. Methods to characterize adhesion and uniformity need to be developed. The relationships between film uniformity and adhesion with respect to the glass/Mo substrate and process conditions need to be examined. Additionally, the $CuInSe_2$/Mo contact has been reported to be non-ohmic and thus, alternative contacts are desirable.

CdTe/CdS

The effects of high temperature processing, either during deposition or after film growth, and $CdCl_2$ treatments on the operation of the device are not well characterized, particularly with regard to process tolerance and uniformity required for large area module production. Questions concerning CdS-CdTe interdiffusion, O and Cl doping, and chemical reactions between $CdCl_2$ and CdTe have not been addressed quantitatively.

Most high efficiency CdTe devices use a graphite/copper contact to the CdTe which is not compatible with monolithic integration using laser scribing technologies. Unfortunately, alternative metal contacts appear to be unstable. Thus, there is a need to develop a stable ohmic contact for CdTe compatible with monolithic integration technologies.

Reports, by several groups, on encapsulation requirements for CdTe modules indicate that the performance of CdTe/CdS solar cells is sensitive to moisture and oxygen is required to maintain it. An understanding of the sensitivity of CdTe cells to

different ambient conditions and approaches to stabilizing the cell structure are needed to develop a low cost module packaging process.

Thin Film Device Issues

In addition to modifying the bandgap of thin film devices by alloying, it is also possible to change the amount of alloying during deposition by grading the bandgap of the material. Various grading schemes can then be used to enhance carrier collection or to improve junction properties. Promising results have emerged from experiments with the a-Si,Ge:H alloys and with Ga and S alloys of $CuInSe_2$.

CdTe and CdS compounds are classified as being both toxic and probable carcinogens. For CdTe modules, devices with thinner, <500 nm, CdTe layers could be developed which can improve the environmental acceptability. For $CuInSe_2$ modules, alternate non-toxic window layers could be developed which would improve the acceptability of $CuInSe_2$ modules and reduce safety issues associated with manufacturing.

The objective of the ongoing research presented in this report is to advance the development and acceptance of thin-film photovoltaic modules;

1) by investigating scalable, cost-effective deposition processes;

2) by preparing thin-film materials and device-layers and completed cell structures;

3) by performing detailed material and device analysis; and

4) by participating in collaborative research efforts that address the needs of PV-manufactures.

In this report we describe the significant results and conclusions reached in the first year of a four year integrated thin film research program. The report is divided into three sections. Section 2 will cover "Deposition and Process Research", Section 3 covers "Solar Cell Measurement and Analysis", and Section 4 is "Research and Development Collaboration." Each chapter includes research results on $CuInSe_2$, CdTe, and a-Si based materials and devices.

Section 2, "Deposition and Process Research", describes the thin film deposition and device fabrication steps that comprise the solar cells and the material and device characterization that further the understanding of these processes. These include the formation of $CuInSe_2$ by selenization of Cu/In in both flowing H_2Se and elemental Se in Section 2.1 and the fabrication and

characterization of films and devices made with $Cu(InGa)Se_2$ deposited by elemental evaporation in Section 2.2. Section 2.3 describes process analysis and microstructural characterization of CdTe films and devices. Finally, a-Si reactor analysis and characterization is covered in Section 2.4.

Section 3, "Solar Cell Measurement and Analysis", describes the device measurements and analysis necessary to understand the basic operation of these solar cells. This enables evaluation of critical processing parameters on device and module performance.

Section 4, "Research and Development Collaboration", describes the materials and device processing, measurements, and analysis performed in collaboration with, and in support of, other research organizations.

2.0 MATERIALS AND DEVICE PROCESSING

2.1 $CuInSe_2$ Formation by Selenization

$CuInSe_2$ has been formed by reaction of Cu/In layers in either H_2Se or elemental Se. The Cu/In layers were deposited by electron beam evaporation or sputtering. The selenization with H_2Se was performed in a flowing gas tubular reactor. We previously reported on the chemical pathways leading to the formation of $CuInSe_2$ films using H_2Se (1) and the pyrolysis of H_2Se and reaction kinetics (2). In this report, we present a reaction analysis leading to the formation of $CuInSe_2$. This process has lead to solar cells with efficiencies over 11%. We also discuss the sensitivity of the selenization reaction to process variables such as the source of the H_2Se, the Cu/In layer deposition, and post-selenization etching.

Selenization of Cu/In layers with elemental Se at temperatures ranging from 150°C to 650°C was performed to evaluate the reaction chemistry leading to the formation of $CuInSe_2$ films. The chemical reaction pathways for Cu/In precursors to form single phase $CuInSe_2$, deduced from the detailed analysis of intermediate phases by x-ray diffractometry, and a proposed reaction model are reported. Guided by this model, high temperature selenization, with no loss of In, was demonstrated, indicating the importance of thermal history during the selenization processes.

Section 2.1.1 Selenization in Flowing H_2Se

Reaction Analysis

Cu/In layers were reacted to form $CuInSe_2$ in a continuous flow tubular reactor at atmospheric pressure using a 14% H_2Se mixture in an Ar balance. The transport of the gas to the substrate surface in this type of research system is complicated and was not evaluated except to insure that the reaction of the H_2Se-Se species with the Cu/In was not supply limited. High efficiency solar cells could not be made from $CuInSe_2$ films formed using H_2Se as the only reacting gas. Better cells were achieved by selenizing with an O_2/H_2Se mixture.

A schematic of the flowing H_2Se tube reactor and gas handling system is shown in Figure 1. To form $CuInSe_2$ films suitable for solar cells, the selenization reactor was evacuated to less than 2×10^{-6} torr prior to each reaction to remove gas phase contaminants. (Residual gas analysis was used to ensure consistent starting conditions.) The system was then back-filled with an Ar/O_2 mixture at a gas flow rate of 66 cm/min. The substrate temperature was simultaneously increased at a rate of 40 °C/min., to a final reaction temperature of 400 °C. Once at temperature, H_2Se was introduced into the system at O_2/H_2Se

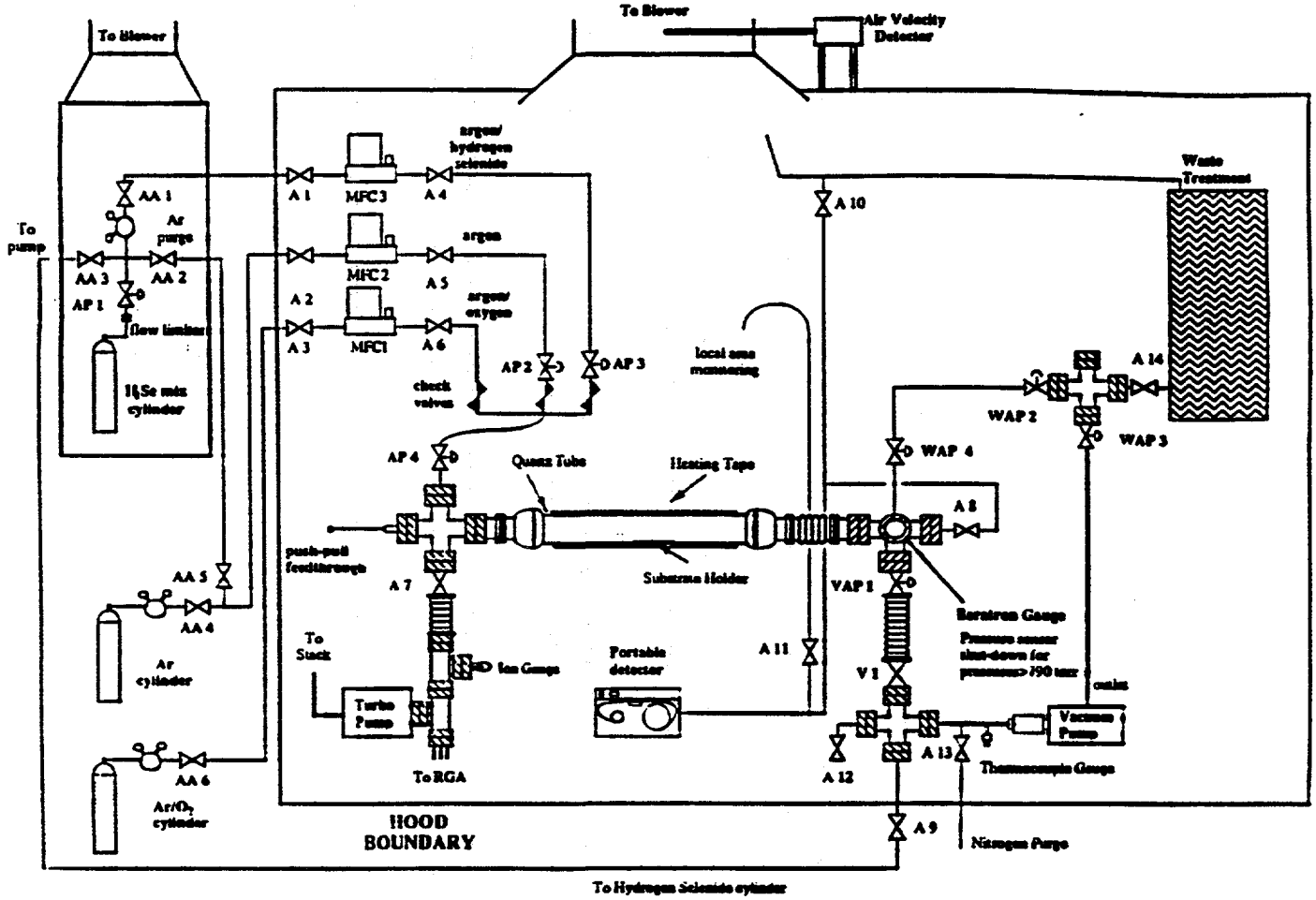

Figure 1. Schematic of the flowing H_2Se tubular reactor and gas handling system.

ratios from 0.004 to 0.01 and a total gas flow rate of 76 cm/min. The system was back-filled with O_2/Ar to prevent segregation of the Cu/In layers prior to the reaction. The presence of O_2 during heat-up appears to cause the formation of an oxide skin on the Cu/In film changing the surface tension. If the O_2 is not present during heat-up, the Cu/In film segregates into islands of Cu/In.

To evaluate the growth of $CuInSe_2$, a set of time progressive experiments (TPE) were carried out with reaction times varying from 1 to 45 minutes at a substrate temperature of 400°C with and without O_2 in the reacting gas. A quantitative XRD analysis was developed to estimate reacting species concentrations in the film as a function of time. Based on this, the following film growth mechanism is proposed:

$$2In + Se \Rightarrow In_2Se \qquad k_2$$
$$In_2Se + Se \Rightarrow 2InSe \qquad k_3$$
$$2Cu_{11}In_9 + 20\,Se \Rightarrow 11Cu_2Se + 9\,In_2Se \qquad k_5$$
$$Cu_2Se + In_2Se + 2Se \Rightarrow 2CuInSe_2 \qquad k_6$$
$$Cu_2Se + 2InSe + Se \Rightarrow 2CuInSe_2 \qquad k_7$$

From these chemical equations a set of differential mass balance relations were developed and integrated for the growing film by assuming a constant selenium species concentration. From this model the rate constants k_2-k_7 were determined and are given in Table 1 for reactions without and with O_2. In the latter case, it is assumed that the presence of O_2 affects only the rate of decomposition of H_2Se.

Table 1. Rate Constants for Time Progressive Experiments

Estimated rate constants		TPE1 (H_2Se alone)	TPE2 (H_2Se/O_2)
k_2	(min^{-1})	1.09	0.40
k_3	(min^{-1})	0.19	0.22
k_5	(min^{-1})	0.23	0.06
k_6	($cc.gmol^{-1}min^{-1}$)	0.029	0.20
k_7	($cc.gmol^{-1}min^{-1}$)	0.0074	0.0066

The model-generated species formation as a function of time compares well with experimental values as shown in Figure 2a for TPE1 (for H_2Se alone) and Figure 2b for TPE2 (for H_2Se/O_2). Thus, time progressive experiments have identified the species present at specific times and have enabled chemical equations to be written for $CuInSe_2$ film growth.

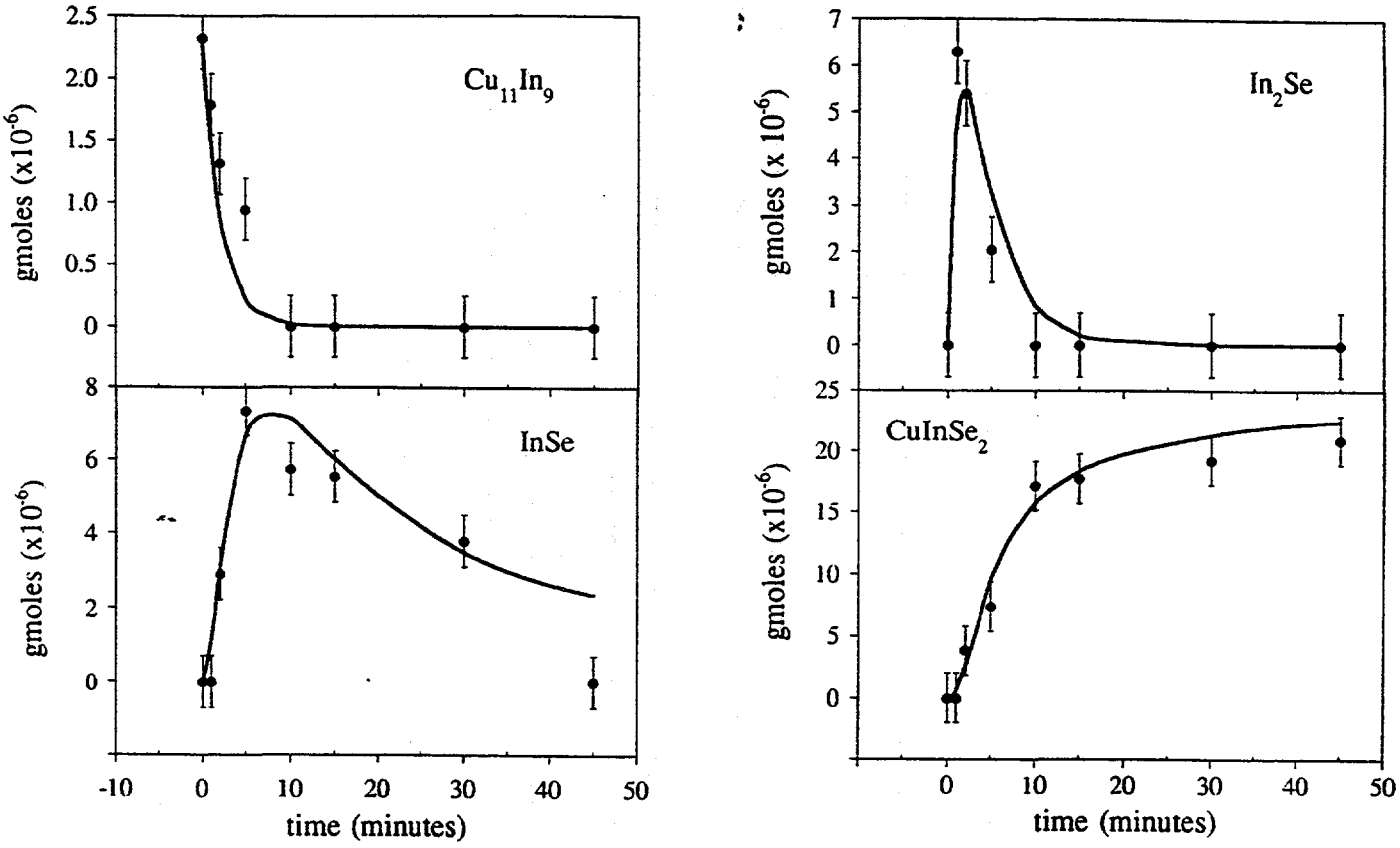

Figure 2a. Comparison of the model generated specie profiles with the estimated profiles for H_2Se alone.

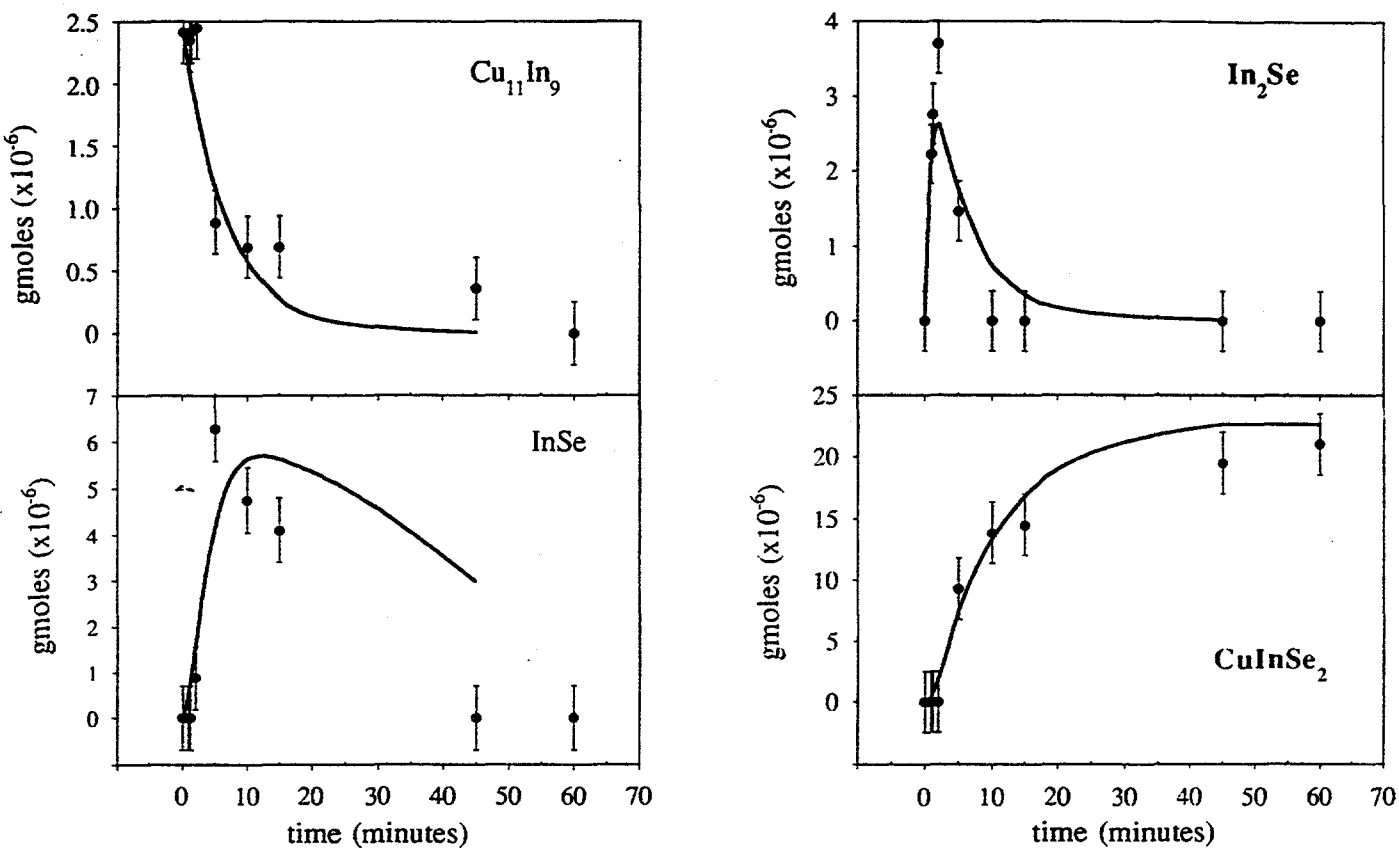

Figure 2b. Comparison of the model generated specie profiles with the estimated profiles for H_2Se/O_2.

The gas phase chemistry of the O_2-H_2Se was evaluated based on the reaction (16):

$$H_2Se + O_2 \text{ --> } H_2O + (1/x)Se_x$$

analogous to the reaction of O_2 with H_2S. Since there was no kinetic data on the H_2Se reaction, estimates of the conversion of H_2Se were made using the rate constant for H_2S with O_2 (17). The amount of Se available for reaction as a function of time was calculated from the solution of the energy and mass balance equations for O_2/H_2Se ratios from 0 (only thermal decomposition) to 0.02 and compared with the amount of Se in the growing film (determined from TPE).

The presence of O_2 increases the amount of Se available for reaction, but a ratio of 0.004 does not provide enough Se to account for the total amount of Se in the film. Thus, it is not possible to establish whether the reaction would proceed solely by reaction with Se_x. Oxygen, therefore, affects both the H_2Se pyrolysis and Cu/In layer morphology and could be a critical issue in a manufacturing environment.

Process Characterization - Gas Composition

The sensitivity of the selenization reaction to the H_2Se gas mixture was evaluated when a new H_2Se cylinder was installed in July 1993. Based on the supplier's Certificates of Analysis, the new cylinder composition was 13.3% H_2Se (mole basis) with the balance argon, as opposed to the replaced cylinder's composition of 14.9% H_2Se. This concentration difference was taken into consideration by adjusting the process gas flow rates so that the following established standard reaction conditions were maintained:

$[H_2Se]$ = 1.7%	T (reaction) = 410°C
$[O_2]/[H_2Se]$ = 0.01	t (heat up) = 10 min
gas velocity = 76 cm/min	t (reaction) = 60 min.

Repeated reaction of Cu/In bilayers at these standard process conditions resulted in films which did not adhere to the glass/Mo substrates. The H_2Se concentration was subsequently reduced in a series of experiments in order to determine if the films were being reacted too quickly. Reactions with reduced $[H_2Se]$ resulted in the formation of two-layer selenized films. The top selenized layers were poorly adhered to the bottom layers, but the bottom layers appeared well adhered to the SL/Mo substrates.

SEM, EDS, and XRD analyses were done on the films which identified morphological, compositional, and component differences between the two layers. Figure 3 presents SEM micrographs of the layers. EDS measurements indicated a Cu-rich bottom layer and a Cu-deficient top layer, as compared to stoichiometric $CuInSe_2$. XRD analysis indicated multi-phase films for both layers, as follows:

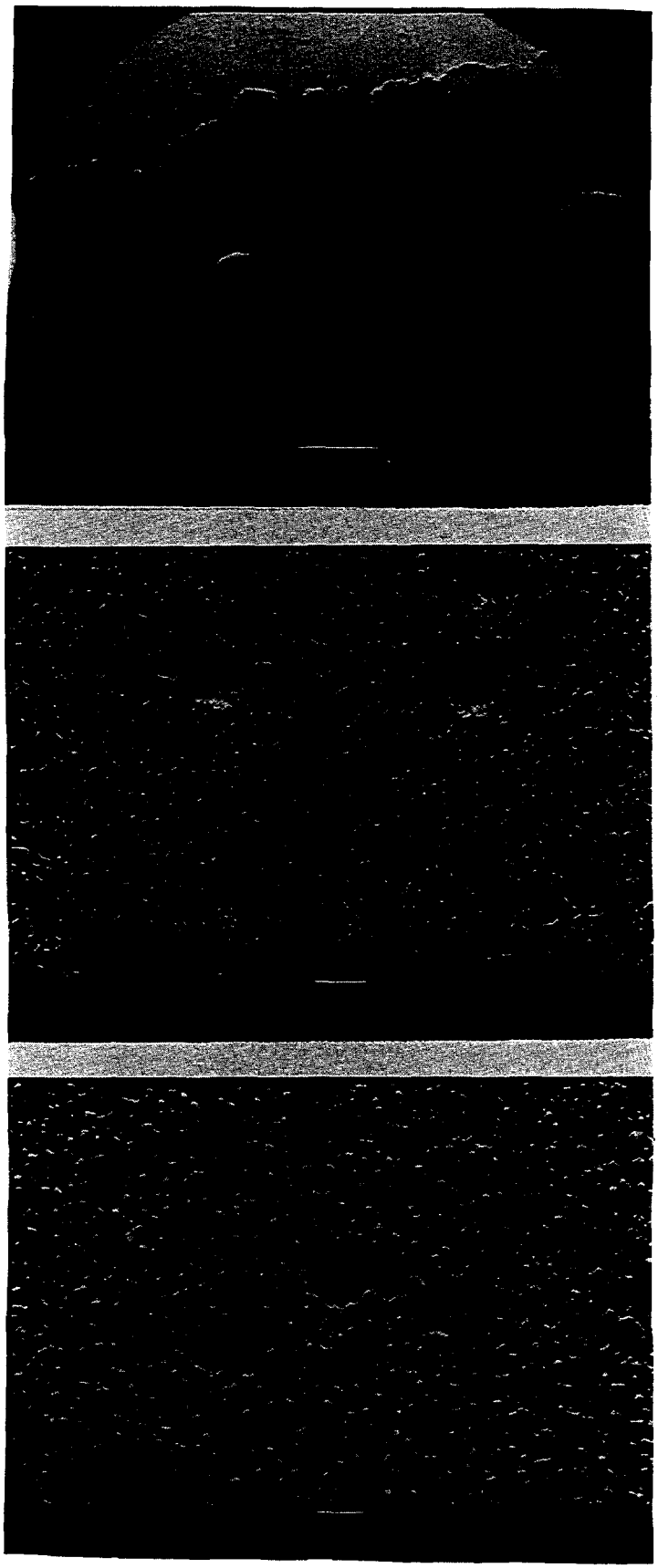

Figure 3. SEM micrographs of 2-layer selenized films.

top layer - $CuInSe_2$, $Cu_2In_4Se_7$
bottom layer - $CuInSe_2$, Cu_7Se_4.

The [H_2Se] was continually reduced until adherent, single-layer film formation was achieved, which occurred at [H_2Se] = 0.35%. This necessary reduction of [H_2Se] to approximately one-fifth of its original level illustrates the extreme sensitivity of the reaction process to [H_2Se]. It is apparent that the relative concentration differences between the two H_2Se cylinders, as indicated by the supplier, is not accurate and could be attributed to one of the following: the old cylinder [H_2Se] concentration was actually lower than the assayed value, the new cylinder [H_2Se] concentration is actually higher than the assayed value, or the rate of decomposition of the H_2Se in the old cylinder was enough to cause significant drop in concentration over time.

The process variables of reaction time and post-reaction heat treatment time were explored in a set of experiments to determine if any modifications were necessary due to the change in [H_2Se] during selenization. Cu/In bilayers from one e-beam evaporation run were selenized in a series of four runs. The first experiment reproduced original standard conditions, the second added a post-reaction heat treatment step without H_2Se, the third increased standard reaction time by 50% and the fourth included the introduction of H_2Se during heat up from room temperature rather than after a temperature of 410°C was reached. All other variables were held constant at their standard levels.

The selenized films received an etch in potassium cyanide (KCN) to remove any potential Cu_2Se (3) and devices were made and evaluated. Table 2 presents the experimental parameters and the device results achieved.

Table 2. Comparison of Device Results for Selenization Reaction Time Experiments

sample	conditions	rxn t (min)	postHT t(min)	V_{oc} (V)	J_{sc} (mA/cm^2)	FF (%)	EFF (%)
89161-1	original conditions	60	-	0.40	33.6	54.7	7.3
89162-1	post-rxn. HT	60	30	0.43	37.4	59.9	9.6
89163-1	longer rxn. time	90	-	0.46	37.5	64.1	11.0
89164-1	H_2Se during heatup	60	-	0.29	34.0	42.7	4.2

Based on this experiment the standard reaction time was increased to 90 minutes. The modified standard run conditions are as follows:

[H_2Se] = 0.35%
[O_2]/[H_2Se] = 0.01
gas velocity = 76 cm/min
T (reaction) = 410°C
t (heat up) = 10 min
t (reaction) = 90 min.

A few major changes in selenized films have been observed since the H_2Se cylinder change and the subsequent standard process modifications. The morphology of the $CuInSe_2$ is more uniform, smoother and typically has larger features. Figure 4 presents SEM micrographs of films selenized in standard runs before and after the procedural changes. Both films achieved conversion efficiencies of over 10% when processed into devices. An improvement in device results for selenized films with chemically deposited CdS has been seen, and could be due, in part, to smoother textured films resulting in more complete coverage with thin (<700Å) CdS.

Pre-Selenization Processing - Cu/In Bilayer Formation

A new Kurt Lesker DC sputtering system was purchased for deposition of Cu/In bilayers and the results compared to electron beam evaporated layers which were used previously. The sputtering system contains four trays which each have the capacity to hold nine substrates in a '3 x 3' configuration. In this system a total of 36 substrates can be coated in one deposition run, as opposed to nine in the e-beam evaporator.

Depositions of Cu/In bilayers revealed very different indium morphologies than those obtained by e-beam evaporation. Figure 5 presents SEM micrographs of Cu/In bilayers deposited by these two methods. E-beam evaporation yields the expected "peanut" or island morphology, whereas sputtering of the indium forms more disconnected oblong nuggets.

Initial selenizations of the sputtered layers resulted in poor device performance. The sputtering conditions were subsequently modified and it was determined that morphology and feature size could be controlled by sputter conditions, in particular, deposition pressure and current. A set of experiments for the deposition of Cu/In layers with various indium sputter conditions was done to establish optimal morphologies for device-quality $CuInSe_2$ formation by selenization. The resulting bilayers were reacted in H_2Se, devices were processed, and device parameters were used to evaluate the indium morphologies. Table 3 presents the indium deposition conditions and the device results for the samples. Sputter conditions of 10 mT sputter pressure and 0.1 A current resulted in the best devices. These conditions yield indium morphologies as seen in Figure 5. These indium sputter conditions also yielded the best device performance when selenized in elemental Se and have been used as standard conditions and for all subsequent depositions.

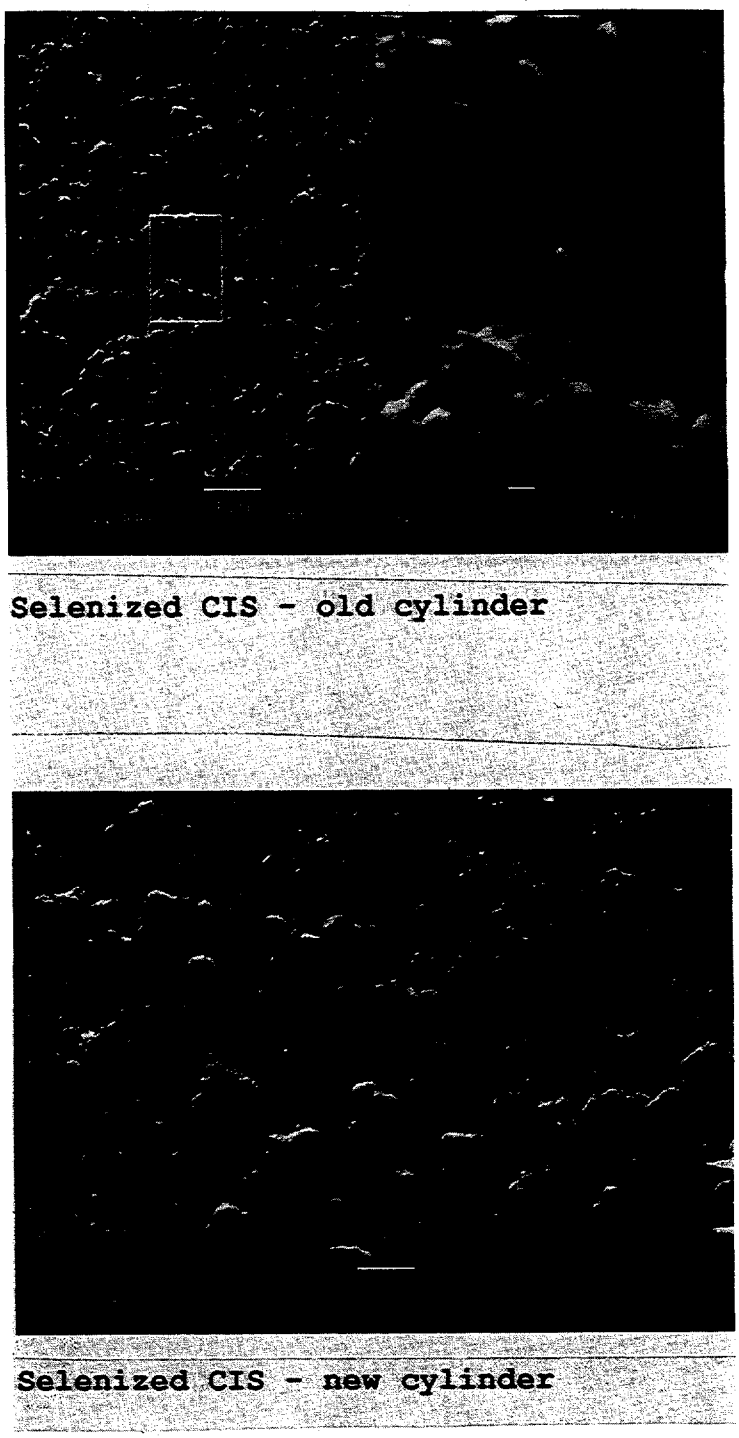

Figure 4. SEM micrographs of selenized $CuInSe_2$ before (a) and after (b) changing H_2Se cylinder and procedures.

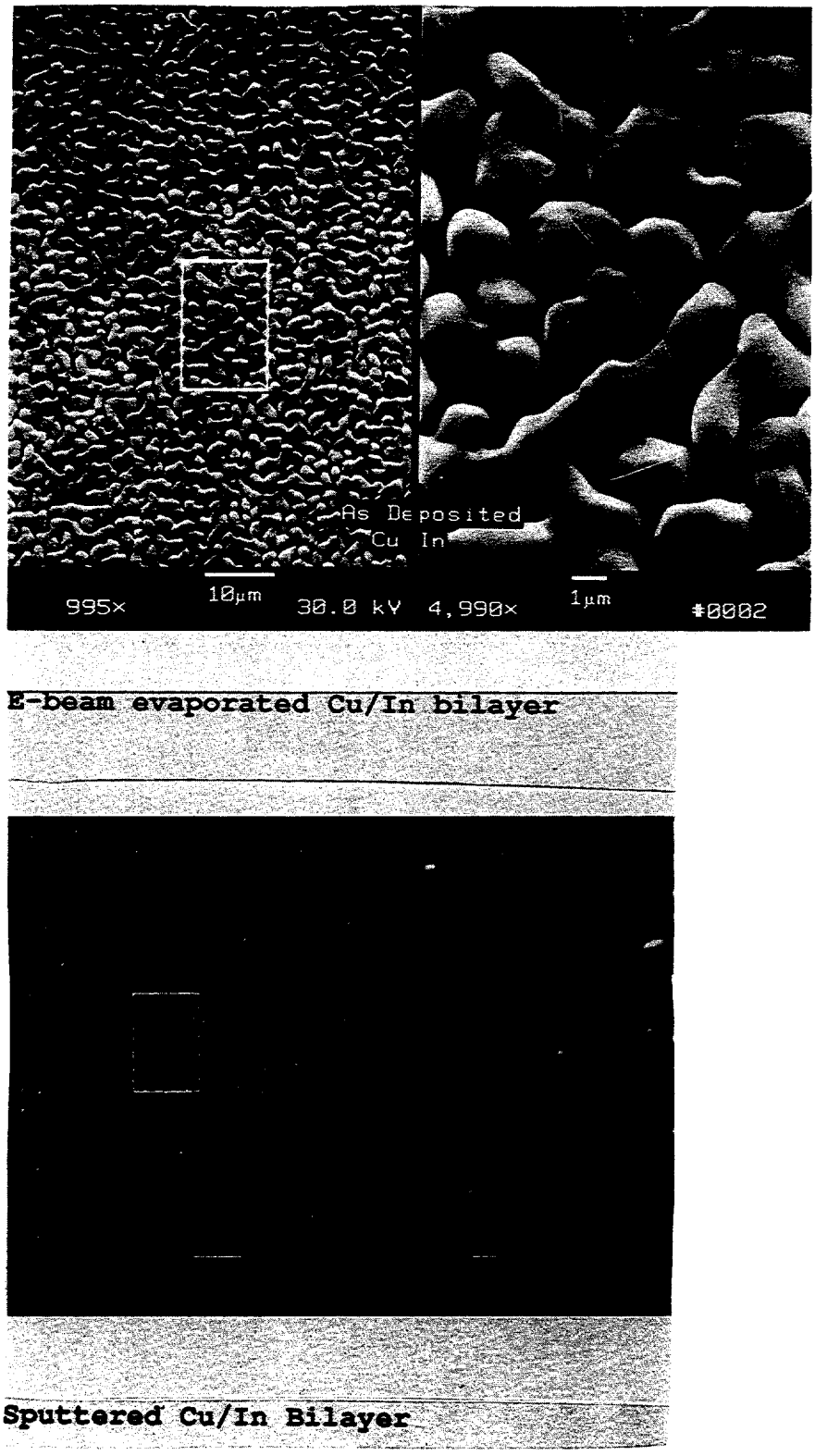

Figure 5. SEM micrographs of Cu/In bilayers

Table 3. Comparison of Device Results for H_2Se Selenization of $CuInSe_2$ with Various Indium Sputtering Conditions

SAMPLE	INDIUM DEPOSITION PRESSURE	CURRENT	V_{oc} (V)	J_{sc} (mA/cm^2)	FF (%)	EFF (%)
89179-1	10 mT	0.1 A	0.44	39.6	62.6	10.9
89179-2	5 mT	0.2 A	0.44	38.0	61.9	10.3
89178-3	10 mT	0.2 A	0.40	38.6	59.4	9.2
89179-4	30 mT	0.2 A	0.43	38.3	49.6	8.2

An analysis of the uniformity of the film thicknesses, and hence Cu/In ratios, over the 3" x 3" sputtering substrate holder was done. Atomic absorption spectrophotometric measurements of the dissolved films were used to calculate film thicknesses for all of the substrates from one single tray in a bilayer sputtering run. This analysis yielded Cu thickness, In thickness and Cu/In ratio for each position in the tray. Figure 6 presents the results of this analysis for the tray. Thicknesses and ratios are listed, along with their deviations from the sample in the number 6 position, which is used for standard characterization. A 'racetrack' pattern due to the circular geometry of the sputter target and magnet is somewhat evident with the 2, 4, 6, and 8 positions having similar thicknesses and compositions. A target Cu/In ratio of 0.90 resulted in a range of ratios over the tray from 0.92 to 1.0.

Cell efficiencies exceeding 11.5% have been attained with both evaporated and sputtered Cu/In layers. These results are listed in Table 4. The cells were completed with chemical bath deposited CdS and sputtered ZnO:Al.

Table 4. Best cell results with e-beam evaporated and sputtered Cu/In layers selenized in H_2Se

Cell #	Cu/In deposition	V_{oc} (Volts)	J_{sc} (mA/cm^2)	FF (%)
89168-1	evaporated	0.46	38.3	67.5
89203-1	sputtered	0.45	40.5	64.4

Bandgap Modified Materials - Selenization of CuGa/In Bilayers

Preliminary results have been obtained with sputtered CuGa layers as a precursor to formation of $Cu(InGa)Se_2$. A CuGa sputter target with ~20% Ga was used which would result in a Ga/Ga+In ratio of 25% in a homogeneous $Cu(InGa)Se_2$ film formed with a bilayer of Cu/In+Ga ratio of 1.0.

(1) Cu = 2575 Å (-9.6%) In = 5987 Å (-10.1%) R = 0.949 (+0.6%)	(2) Cu = 2851 Å (+0.1%) In = 6498 Å (-2.5%) R = 0.968 (+2.7%)	(3) Cu = 2657 Å (-6.7%) In = 6050 Å (-9.2%) R = 0.969 (+2.8)
(4) Cu = 2888 Å (+1.4%) In = 6684 Å (+0.3%) R = 0.953 (+1.1%)	(5) Cu = 3042 Å (+6.8%) In = 6919 Å (+3.8%) R = 0.970 (+2.9%)	(6) Cu = 2848 Å (0.0%) In = 6663 Å (0.0%) R = 0.943 (0.0%)
(7) Cu = 2731 Å (-4.1%) In = 6007 Å (-9.8%) R = 1.003 (+6.4%)	(8) Cu = 2812 Å (-1.3%) In = 6498 A (-2.5%) R = 0.955 (+1.3%)	(9) Cu = 2459 Å (-13.4%) In = 5900 Å (-11.5%) R = 0.920 (-2.4%)

	average	target
Cu	2763 Å	2500 Å
In	6356 Å	6139 Å
Ratio	0.959	0.900

Figure 6. Uniformity of sputtered Cu/In film thickness and Cu/In ratio

CuGa/In layers were selenized in a set of temperature progressive experiments (runs 89195-89201) at temperatures from 400-600°C. Reaction times as a function of temperature were roughly estimated from an approximate activation energy for $CuInSe_2$ of 15-20 kcal/mole and an Arrhenius relationship. EDS, XRD, and atomic absorption spectroscopy (AAS) were done on the samples. The EDS probes the top 0.5-1.0 μm of the film while the XRD and AAS samples the entire film thickness of 2.5-3.0 μm.

Only small amounts (0-4%) of Ga were detected in the films by EDS analysis. The relative level of Ga in the films increased with selenization temperature such that the detected levels of Ga for films selenized at 450 (89195-3), 500 (89197-3) and 550°C (89196-3) were 1.1, 3.1, and 5.1%, respectively.

Atomic absorption for Ga was measured in each of the films and for an unselenized bilayer in order to determine if there was any loss of Ga during heat-up or reaction of the films. Results indicated equivalent levels of Ga in all of the films and in the unselenized bilayer, establishing that there is no loss of Ga as a volatile specie in selenizations up to 550°C.

The X-ray diffraction patterns for the selenized films are presented in Figure 7. Some $MoSe_2$ was formed in the higher temperature selenizations. The primary $Cu(InGa)Se_2$ peaks are indicated and asymmetric broadening of these peaks, particularly evident at higher temperature selenizations, provides evidence of the presence of both $CuInSe_2$ and some compositions of $Cu(InGa)Se_2$.

Figure 8 shows a detailed scan of the <220> $CuInSe_2$ peak. The broadening and shifting of the peak with the increase in selenization temperature is apparent and indicative of the presence of various compositions of $Cu(InGa)Se_2$ in the films. At the highest temperatures the tails of the <220> peaks approach the position for $CuGaSe_2$.

Based on EDS and XRD analyses it is evident that the Ga is not homogeneously distributed throughout the films, but instead, is primarily located near the CIS/Mo interface. Reaction at higher temperatures appears to disperse the Ga somewhat more through the films, since %Ga by EDS measurements increases, and it also tends to result in the formation of $Cu(InGa)Se_2$ with higher Ga compositions, as seen by the shift in the XRD $Cu(InGa)Se_2$ peaks.

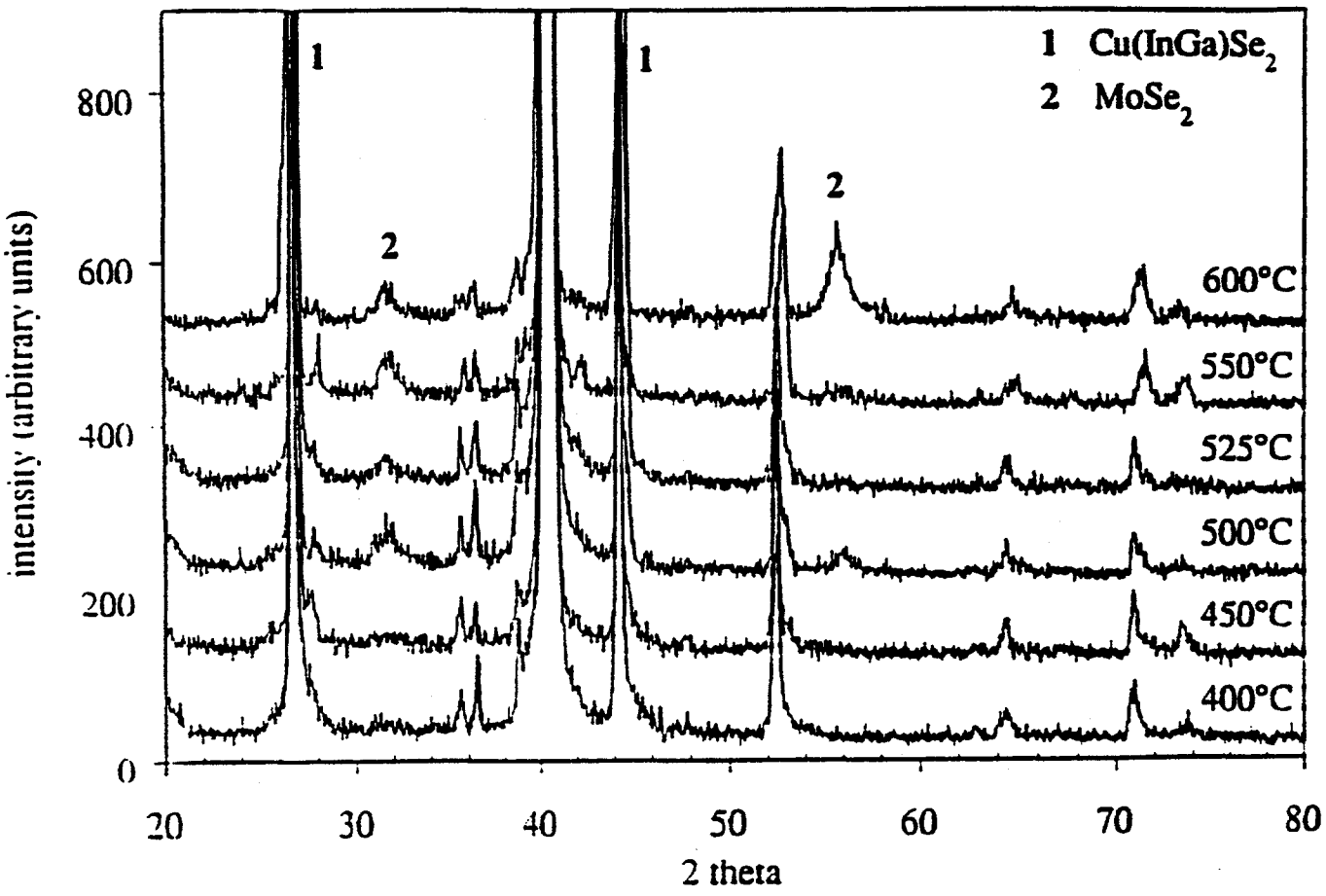

Figure 7. XRD scans of CuGa/In bilayers selenized at 400-600°C.

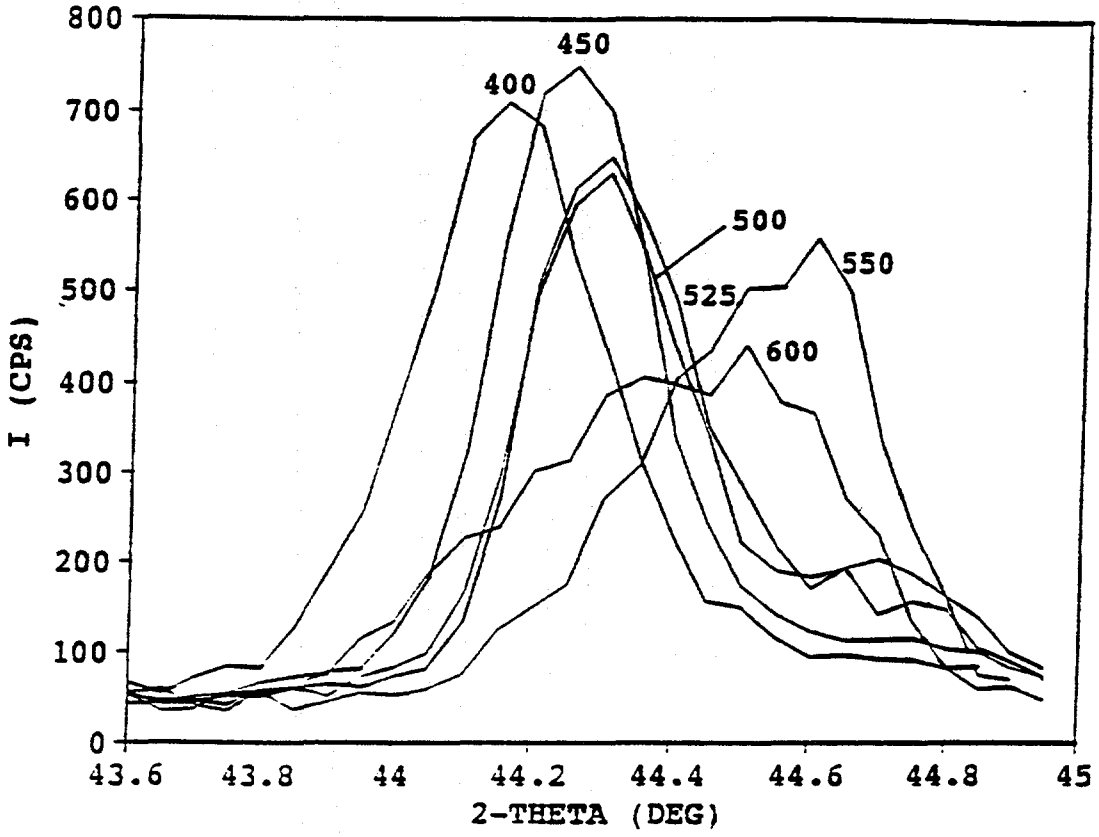

Figure 8. Detailed scan of <204 and 220> $Cu(InGa)Se_2$ XRD peaks of selenized films

Devices were processed from these CuGa/In bilayers selenized at 400, 450, 500, and 550°C. The preliminary cell results were dominated by poor fill factors which may have been due to poor adherence of the selenized films to the Mo. This seemed worse for films selenized at the higher temperatures (>450°C) which also have very rough-textured surfaces.

2.1.2. Reaction with elemental Se

Cu/In layers were reacted by physical vapor deposition of Se from an open crucible. The Cu and In were sequentially deposited at room temperature on to 2μm-thick Mo-coated soda lime glass substrates by electron beam evaporation to form the starting Cu/In layers. The Cu thickness was fixed at 250nm, while the In thickness was varied from 430nm to 690nm to give the initial Cu/In ratios ranging from 0.8 (In-rich) to 1.3 (Cu-rich) and yielded a final $CuInSe_2$ thickness of about 2μm. In this approach, Se transport is 'line of sight' to the substrate and was monitored by a quartz crystal rate monitor.

To form $CuInSe_2$ films suitable for solar cells, approximately 1.5μm of Se, enough to completely react with the Cu/In layer, was evaporated onto the Cu/In substrates at room temperature. Following the Se deposition, the substrate temperature was increased to the reaction temperature, 400 to 550 °C, at a rate of ~35 °C/min in the presence of Se vapor at an effective impingement rate of 10Å/sec and reacted for 60 min. In some cases, the Cu/In layers were reacted at an intermediate temperature of 300 °C for 30 min. prior to the final high temperature reaction.

This process sequence can be understood in terms of a semi-quantitative model of the chemical pathways to form $CuInSe_2$ films based on the evaluation of Cu, In, and Cu/In layers reacted in elemental Se at different temperatures and times. The starting Cu/In films form a two phase structure consisting of $Cu_{11}In_9$, and In(Cu) alloy at ~ 100 °C. By the addition of Se at near room temperature the structure of the Cu/In layer is maintained during reaction. Without the Se, the Cu/In segregates into islands when heated above 300 °C in vacuum.

To evaluate the reaction chemistry leading to the formation of $CuInSe_2$ films, selenization of Cu/In layers with elemental Se at temperatures of 150 °C to 650 °C was performed. The films were analyzed by scanning electron microscopy (SEM) and EDS to confirm film morphology and composition. XRD was used to identify phases and to provide relative peak intensities and orientations for each phase. Phases were identified by comparison of the sample d-spacings with JCPDS card files. For $Cu_{11}In_9$ and In_2Se phases, computer generated XRD patterns from the crystal structure of those compounds were used as reported elsewhere (1).

To prepare device quality $CuInSe_2$ films, reaction temperatures of ~400°C are required. Time progressive reaction studies cannot be carried out at this temperature in the evaporation system due to the relatively long time required to cool the substrate. Thus, we have made the assumption that the reactions which occur early in selenization at high temperature are similar to those at low temperatures for longer times. The reactions below 400°C were evaluated for Cu, In and Cu/In layers. In addition, reactions at temperatures above 400°C were evaluated using Cu/In layers.

LOW TEMPERATURE REACTION

Reaction of Cu and In with Se

Single layer Cu(~2500Å) and In(~6000Å) deposited on Mo-coated glass substrates were selenized to examine the reaction of each element independently with Se.

Cu and Se react at room temperature and above to form Cu-Se compounds. Reaction at 200°C resulted in poor film adhesion in most cases, so that it was difficult to identify the phases present at low temperature.

In and In_2Se were detected for In films selenized for 30 min at temperatures from 150°C to 250°C. The XRD peak intensities of In_2Se were almost constant with reaction temperature, while In peaks decreased with reaction temperature. In addition, a few weak, broad peaks, which are close to those reported for some In-Se compounds but remain unidentified, were observed with the intensity increasing slightly with temperature. It is suspected that a certain amount of amorphous or extremely-disordered In-Se phases were formed. In general, In reacts with Se slowly to form only In_2Se at temperatures up to 250°C.

At 300°C, strong peak intensities for InSe and β-In_2Se_3 phases were observed, while peaks associated with In_2Se and In phases completely disappeared. At 400°C, β-In_2Se_3 was the dominant phase observed.

Reaction of Cu/In with Se

Table 5 presents a summary of phases observed on Cu/In layers selenized for 30min at different temperatures and Cu/In ratios. The low, broad unidentified peak found with the selenized In films was not observed for the Cu/In layers.

At 150°C, $Cu_{11}In_9$, In and In_2Se were detected. The XRD intensity of In_2Se was quite small and independent of initial Cu/In ratio. The $Cu_{11}In_9$ peak intensity also seemed to be independent of initial Cu/In ratio consistent with the fixed amount of Cu used in the starting layers. The intensity of the In peak increased as the initial Cu/In ratio decreased.

Table 5. Phases Formed on Selenized Cu/In Layers at 150°C-400°C

Temperature	Phases Observed													
	Cu/In<1							Cu/In>1						
150°C	$Cu_{11}In_9$	In	In_2Se					$Cu_{11}In_9$	In*	In_2Se				
200°C	$Cu_{11}In_9$	In	In_2Se		CuSe	Cu_7Se_4	$CuInSe_2$	$Cu_{11}In_9$		In_2Se		CuSe	Cu_7Se_4*	$CuInSe_2$
225°C	$Cu_{11}In_9$	In	In_2Se	InSe	CuSe*	Cu_7Se_4	$CuInSe_2$	$Cu_{11}In_9$		In_2Se			Cu_7Se_4*	$CuInSe_2$
250°C	$Cu_{11}In_9$		In_2Se	InSe		Cu_7Se_4	$CuInSe_2$	$Cu_{11}In_9$		In_2Se			Cu_7Se_4	$CuInSe_2$
300°C	$Cu_{11}In_9$			InSe		Cu_7Se_4	$CuInSe_2$	$Cu_{11}In_9$			InSe*		Cu_7Se_4	$CuInSe_2$
400°C							$CuInSe_2$							$CuInSe_2$

* dependent on initial Cu/In ratio

At 200°C, $Cu_{11}In_9$, In, In_2Se, CuSe, Cu_7Se_4 and $CuInSe_2$ were detected on the In-rich films. For Cu-rich films, the same phases were observed except for In.

At 225°C, $Cu_{11}In_9$, In, In_2Se, InSe, CuSe, Cu_7Se_4 and $CuInSe_2$ were detected on the In-rich films. The peak intensities of InSe and CuSe were quite small and broad. On the Cu-rich films, no In nor InSe were detected.

At 250°C, $Cu_{11}In_9$, In_2Se, InSe, Cu_7Se_4 and $CuInSe_2$ were detected on In-rich films with all In completely reacted. On the Cu-rich films, no InSe was detected.

At 300°C, $Cu_{11}In_9$, InSe, Cu_7Se_4 and $CuInSe_2$ were detected on the In-rich films. In the Cu-rich films, no or very little InSe was detected. No In_2Se_3 was detected in any of the films, which is counter to that observed with elemental In films. At 400°C, $CuInSe_2$ was the only phase observed.

Evaluation of XRD Intensities

No dependence of $Cu_{11}In_9$ peak intensity on initial Cu/In ratio was observed. In addition, the peak intensities decreased very little with reaction temperature up to 250°C, maintaining their initial intensities as seen in the Cu/In layer thermally alloyed to $Cu_{11}In_9$ + In(Cu). $Cu_{11}In_9$ peak intensities dramatically decreased at 300°C, suggesting that the onset of $Cu_{11}In_9$ reaction with Se occurs between 250°C and 300°C.

Figure 9 shows the dependence of the XRD intensity of $CuInSe_2$ (112) peak on initial Cu/In ratio for different reaction temperatures. The intensity is independent of the initial Cu/In ratio and is relatively low for reaction temperatures below 250°C. The intensity increased rapidly at 300°C, which corresponds to the decrease in intensity of the $Cu_{11}In_9$ peaks.

Figure 10 shows the XRD intensity dependence of the In peak on initial Cu/In ratio for different reaction temperatures, where intensities of the three largest peaks, (101), (112), and (200) were summed. These orientations represent the three brightest In peaks for randomly oriented films and the sum of their intensities removes slight orientation differences from film to film. This result shows that elemental In is present in In-rich films and that the amount of In decreases with both reaction temperature and initial Cu/In ratio. On the other hand, the result for Cu-rich films reflects the initially low quantity of elemental In in the film. No In is detected at 250°C for either In-rich or Cu-rich films.

Figure 11 shows the XRD intensity dependence of the In_2Se (040) peak on initial Cu/In ratio for different reaction temperatures, where the (040) peak is the largest of all In_2Se peaks

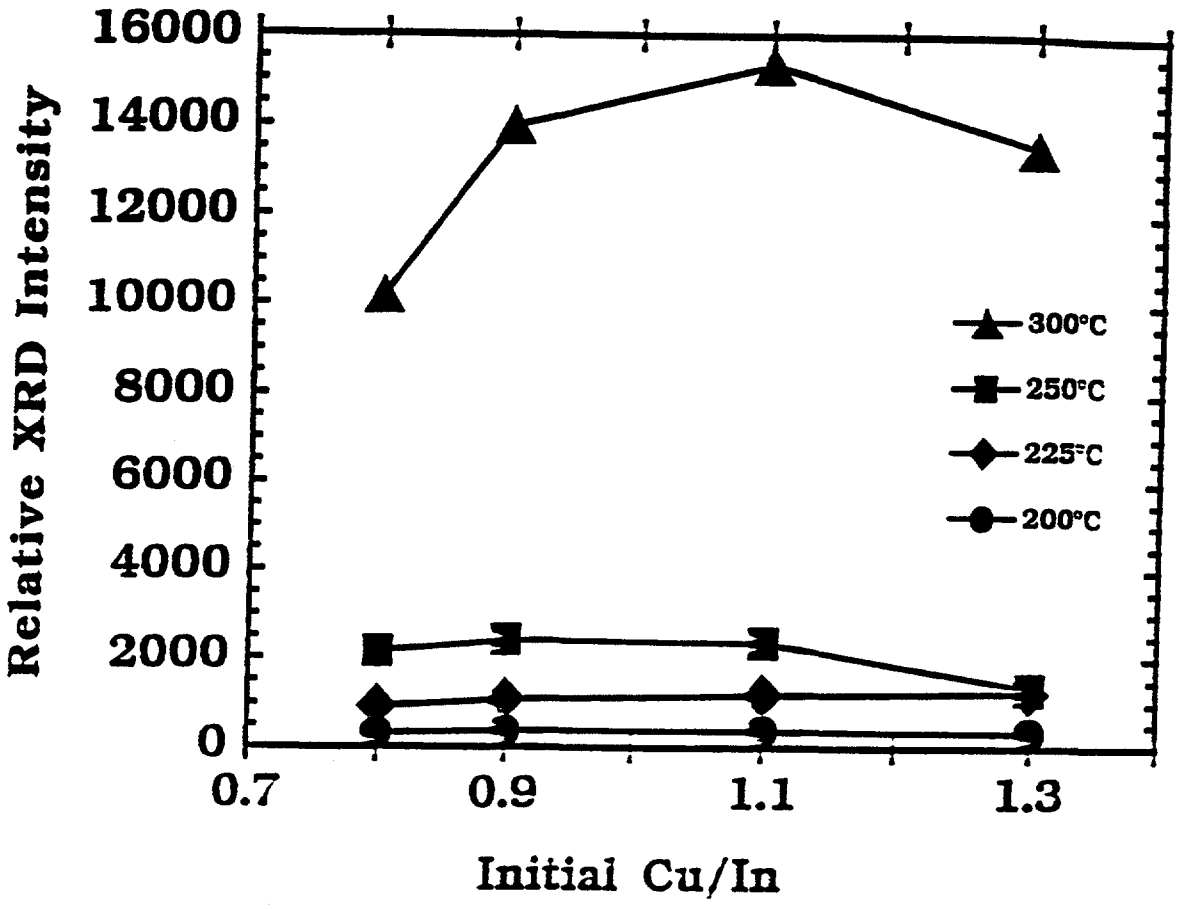

Figure 9. Variation of $CuInSe_2$ (112) XRD peak intensity on initial Cu/In ratio for different reaction temperatures.

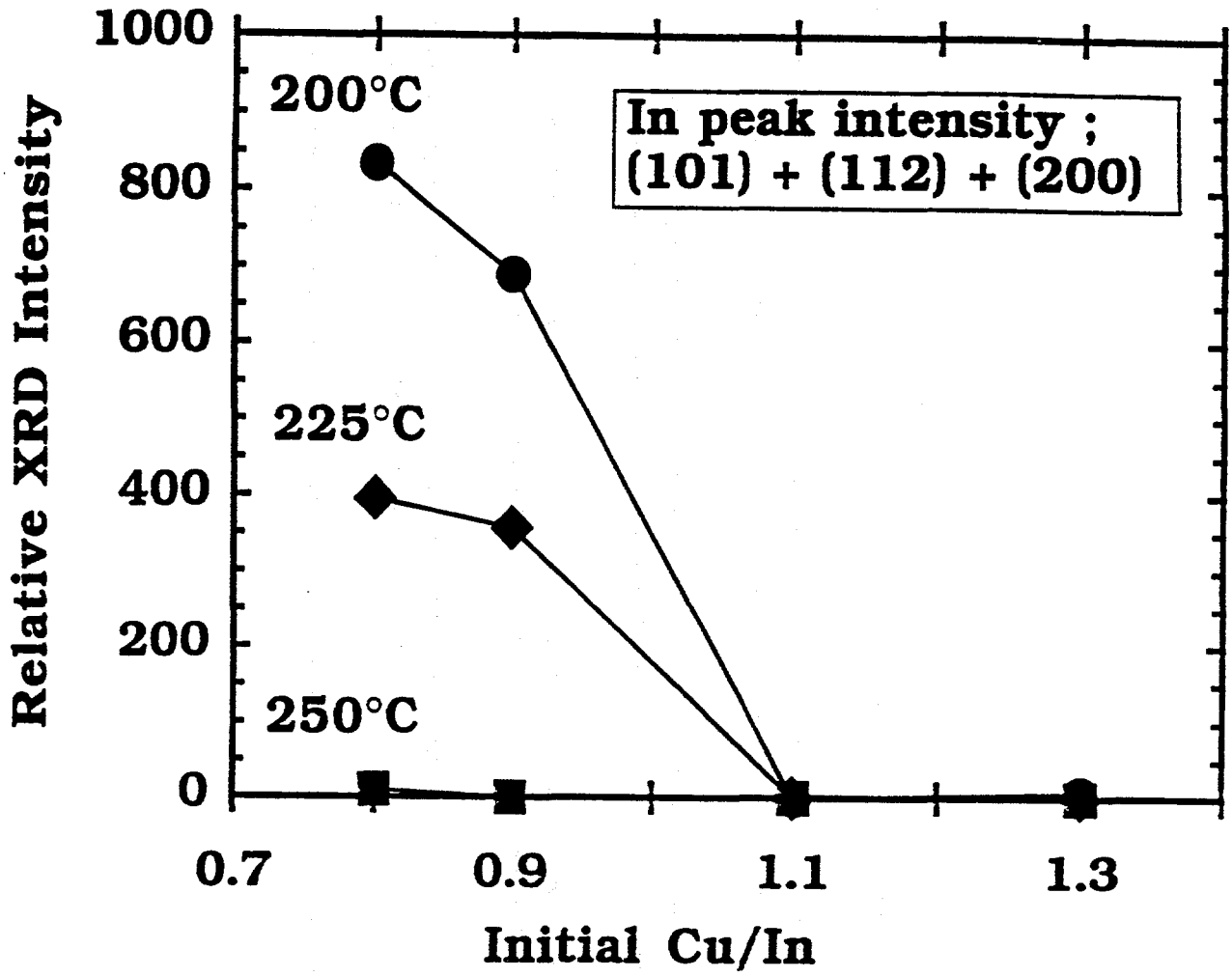

Figure 10. Variation of In XRD peak intensity on initial Cu/In ratio for different reaction temperatures.

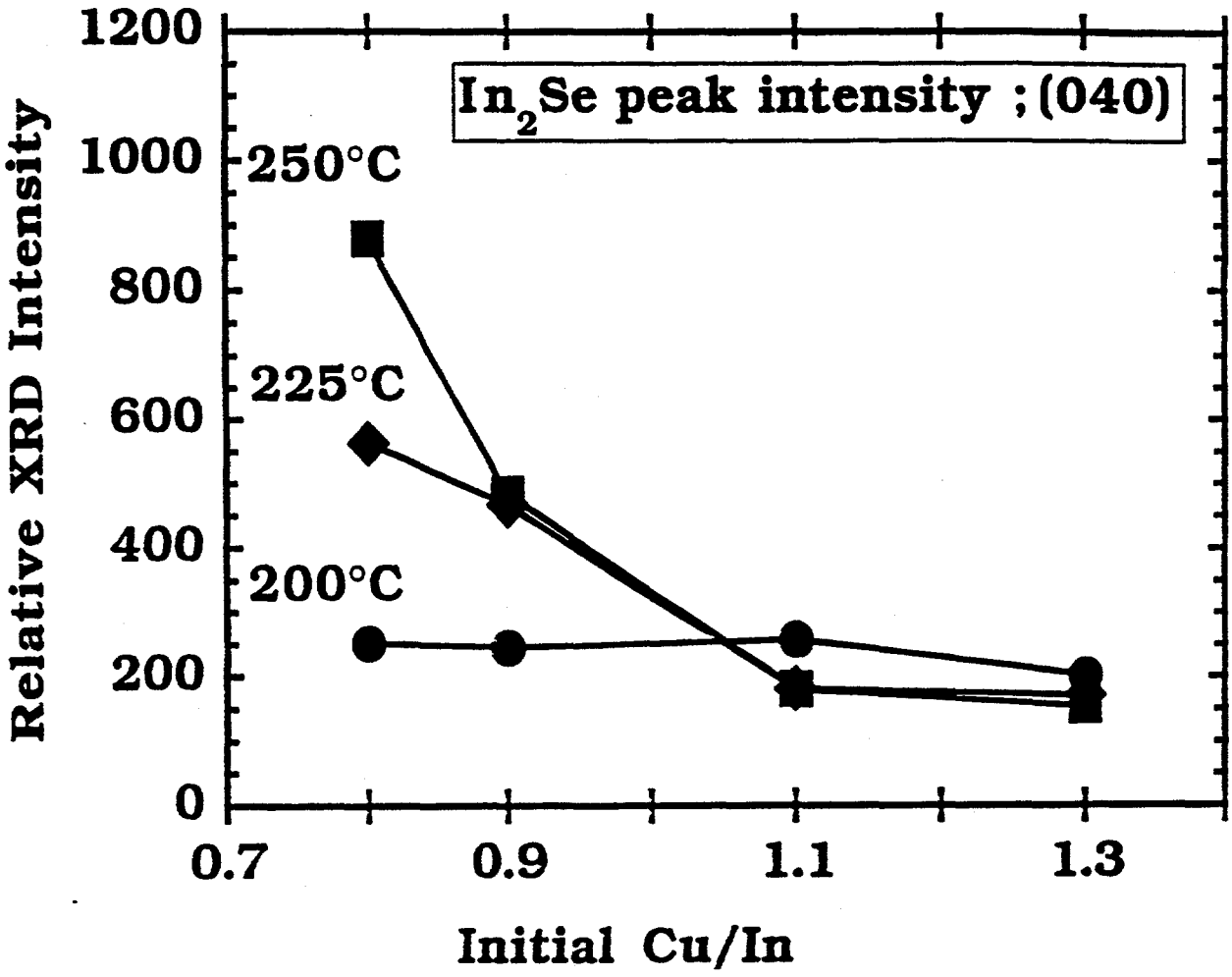

Figure 11. Variation of In_2Se (040) XRD peak intensity on initial Cu/In ratio for different reaction temperatures.

experimentally observed. The data shows that In_2Se increases with reaction temperature up to 250 °C on the In-rich films. For the Cu-rich films, the In_2Se peak intensity is small and does not change much with either reaction temperature or initial Cu/In ratio. This suggests that the formation of In_2Se via elemental In was completed faster on the Cu-rich films than on the In-rich films due to the limited amount of elemental In. The increasing In_2Se peak intensity correlates well with decreasing In peak intensity, suggesting that the In phase reacts with Se to form In_2Se with a relatively slow reaction rate.

A low intensity InSe peak was detected at 225°C and 250°C on the In-rich films. The InSe peak intensity significantly increased at 300°C on these films. It is believed that the liquid In phase was converted to InSe at this temperature similar to the selenization of In films. Since InSe is not detected for selenized In at temperatures below 300°C, InSe detected for Cu/In films at 225°C and 250°C is considered to be a reaction product of $Cu_{11}In_9$ with Se.

CuSe was detected primarily in films reacted at 200°C, with the intensity independent of initial Cu/In ratio. CuSe seems to be preferable at only lower temperature. Cu_7Se_4 was detected independent of both initial Cu/In ratio and reaction temperature below 400°C and should be considered as a precursor to form $CuInSe_2$ formation. At temperatures from 200°C to 250°C, the Cu_7Se_4 peak intensity tends to be slightly higher on the In-rich films.

REACTION CHEMISTRY

The Cu/In binary phase diagram (4) shows that a Cu/In layer at equilibrium consists of solid phase $Cu_{11}In_9$ and liquid phase In(Cu) at temperatures from 157°C to 310°C. The amount of Cu and In in both solid and liquid phases at temperatures around 200°C-300°C were estimated based on the phase diagram. In our experiments the total amount of Cu has been fixed which implies that after alloying, the amount of $Cu_{11}In_9$ is nearly constant with both initial Cu/In ratio and temperatures from ~200°C to ~300°C. Table 6 shows the estimated amount of elemental Cu and In in In(Cu) liquid phase relative to the total amount of each element in the film for In-rich and Cu-rich films. The In-rich films have more In(Cu) liquid and thus contain higher amounts of elemental In and Cu.

From the above results, some key features of the reactions found in this study and the postulated reaction pathways can be summarized as follows.

Table 6. Amount of elemental Cu and In in liquid phase relative to total amount of each element based on the Cu/In phase diagram and assuming the presence of $Cu_{11}In_9$.

Temperature	Cu/In=0.8		Cu/In-=1.1	
	Cu%	In%	Cu%	In%
200°C	1.1	35.3	0.2	10.2
225°C	1.4	35.5	0.3	10.3
400°C	4.3	37.3	0.9	10.8
500°C	8.9	40.4	1.9	11.7
600°C	46.9	65.2	9.9	18.9

At temperatures from 200°C to 250°C, the In(Cu) liquid phase reacts with Se to form In_2Se, similar to the reaction of elemental In films with Se. A small amount of Cu in the In(Cu) liquid phase reacts to form Cu_7Se_4. More elemental Cu on the In-rich films results in slightly more Cu_7Se_4.

$Cu_{11}In_9$ reacts with Se to form InSe and Cu_7Se_4 (or CuSe), then InSe and Cu_7Se_4 react, taking up more Se to form $CuInSe_2$. Alternatively, no more Se is necessary for the reaction: InSe + CuSe -> $CuInSe_2$. Since the $Cu_{11}In_9$ phase contains more Cu than In, an excess of Cu_7Se_4 is always formed for the reaction of $Cu_{11}In_9$ with Se. The rate of this reaction, however, must be extremely slow at temperatures up to 250°C. This is indicated by the experimental result that the $Cu_{11}In_9$ XRD peak intensity changes only slightly for reaction temperatures up to 250°C.

It seems that the reactions of $Cu_{11}In_9$ and In(Cu) with Se occur independently at temperatures up to 250°C. A phenomenological model for the low temperature reactions of Cu/In layers with Se is formulated as:

- $Cu_{11}In_9$ solid phase -

$$Cu_{11}In_9 + Se \rightarrow InSe + Cu_7Se_4 \quad [1]$$
$$InSe + Cu_7Se_4 + Se \rightarrow CuInSe_2 + Cu_7Se_4 \quad [2]$$

- In(Cu) liquid phase -

$$In + Se \rightarrow In_2Se \quad [3]$$
$$Cu + Se \rightarrow Cu_7Se_4 \quad [4]$$
$$In_2Se + Se \rightarrow InSe \quad (\text{at } \geq 300^{\circ}C) \quad [5]$$

At 300°C and above, the liquid phase In completely converts to InSe. This reacts with excess Cu_7Se_4 from the $Cu_{11}In_9$ phase to form $CuInSe_2$.

The detection of InSe at 225°C and 250°C for the In-rich films indicates that the effusion rate of Se is not sufficient to drive reaction [2] above to completion. A selenization with the Se effusion rate increased from 10Å/sec to 20Å/sec at 250°C was performed to verify this reaction and no InSe was detected for the resultant films. This result suggests that the Se impingement is another control parameter for the formation of $CuInSe_2$.

HIGH TEMPERATURE REACTION

Selenization reactions were also performed at temperatures ranging 400°C to 650°C. Figure 12 shows the Cu/In ratios of the resultant films measured by EDS as a function of the initial Cu/In ratio. At 400°C, final Cu/In ratios were consistent with initial Cu/In ratios. This suggests that at this temperature In loss is negligible. However, more significant deviation of the Cu/In ratio towards Cu-rich composition occurred at higher reaction temperatures. The relative amount of In in the In(Cu) liquid phase at higher temperatures, which was estimated from the phase diagram and included in Table 6, is much greater than at low temperatures. Therefore, the reaction of In to In_2Se is enhanced (see reaction (3) above). The deviation of compositions after reaction shown in Figure 12 is explained by the loss of In due to volatile In_2Se. This sublimation process competes with the formation of InSe at higher reaction temperatures.

It is also interesting to note that the dependence of the final Cu/In ratio on the initial ratio was reversed at high temperature (650°C). The Cu/In binary phase diagram indicates that for fixed temperature, the relative proportion of liquid phase increases with decreasing Cu/In ratio (see Table 6). Thus, more In can be lost through the formation of In_2Se.

As the phenomenological model proposes, volatile In_2Se is formed only from the liquid phase of In. Therefore, the In loss could be prevented by completing the conversion of In_2Se to InSe at a temperature at which In_2Se vapor pressure is low. To verify this, we performed a selenization at 550°C with an intermediate temperature hold at 300°C for 30 min prior to ramp up to 550°C. As seen in Figure 12, the high temperature selenization was successfully performed with no measurable In loss. This shows the importance of the substrate thermal history during the selenization process.

To summarize, chemical reaction pathways to the formation of $CuInSe_2$ by selenization using elemental Se were evaluated. A phenomenological model for reaction was established as follows:

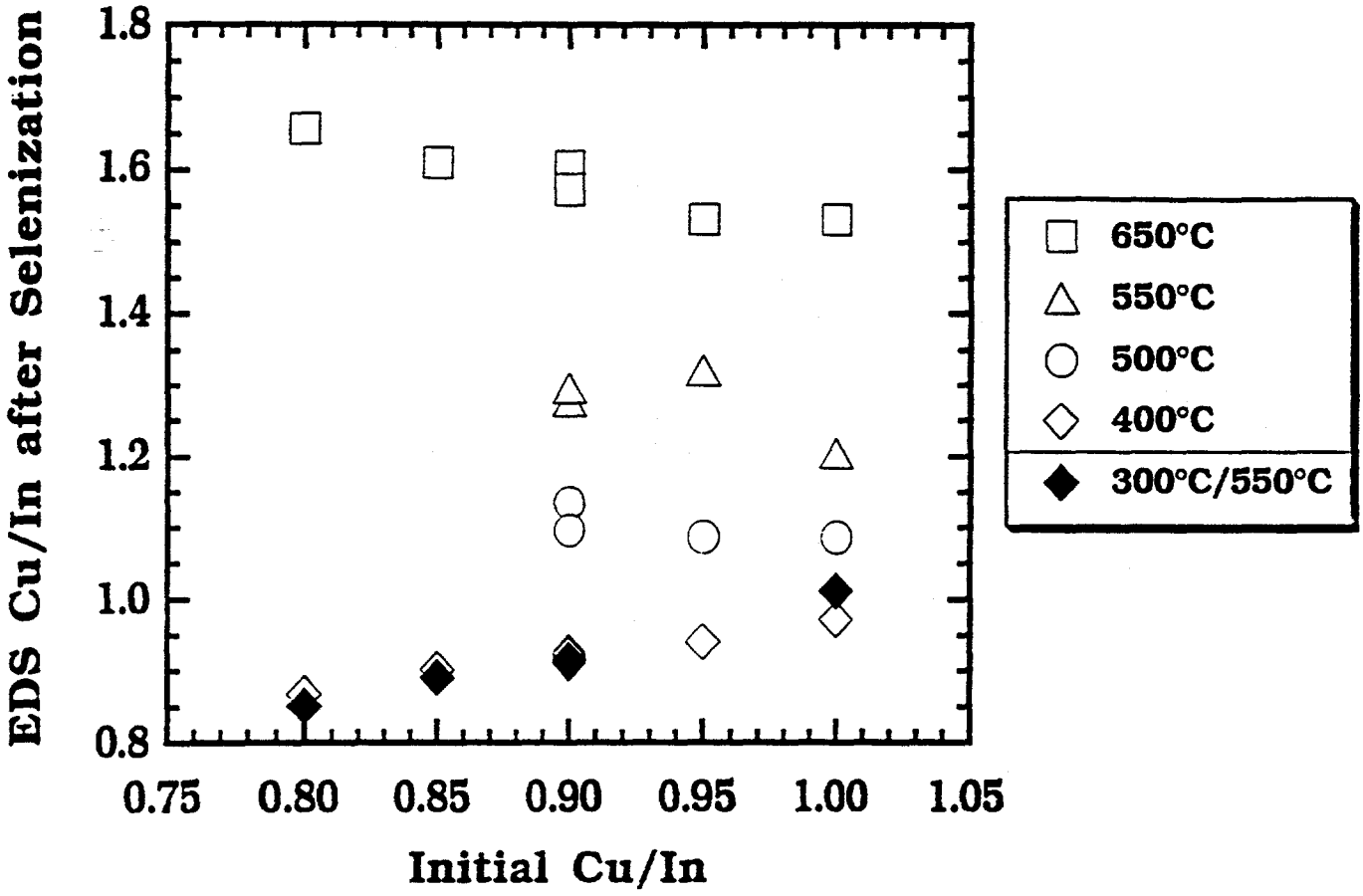

Figure 12. EDS Cu/In ratio of selenized Cu/In films compared with initial Cu/In ratio.

At temperatures up to 250°C,

- In(Cu) liquid phase reacts with Se to form In_2Se and Cu_7Se_4.

- $Cu_{11}In_9$ solid phase reacts with Se to form InSe and Cu_7Se_4, then InSe and Cu_7Se_4 react further with Se to form $CuInSe_2$. The rate of these reactions is very slow and may be diffusion limited.

At temperatures above 250°C,

- In in the liquid phase reacts with Se to form InSe, then reacts with Cu_7Se_4 to form $CuInSe_2$. At these temperatures, $CuInSe_2$ is the dominant phase in the film.

The phenomenological model at low temperatures is assumed to represent the reactions which occur very early in the selenization of films at higher temperatures.

High temperature selenization of In-rich films with no loss of In can be accomplished by an intermediate reaction temperature hold (300°C) in the presence of excess Se which converts volatile In_2Se to InSe.

2.2 BANDGAP MODIFIED $CuInSe_2$ BY EVAPORATION

Significant improvements have been reported recently for $CuInSe_2$ based solar cells by modifying the bandgap with the addition of Ga or S. Several issues related to the use of these multinary compounds need to be addressed before these materials can be successfully used in moving from laboratory to manufacturing scales. These include: 1) determining the effect of increasing the Ga concentration on the film growth and device performance; 2) determining the effect of compositional non-uniformities. This includes both lateral and through-film variations in the Ga and Cu concentrations; 3) examining the role of intentionally bandgap graded structures from both a film and device perspective; and finally 4) developing methods to characterize multinary films and devices.

$CuIn_{1-x}Ga_xSe_2$ films have been deposited by four source elemental evaporation with x ranging from 0 to 0.6. Detailed X-ray diffraction analysis of these films shows that they have a compositional distribution, i.e. a variation in x through the film or laterally, which increases as x increases. Splitting of the XRD peaks indicates the segregation of regions of different compositions. Device results show that as x increases beyond 0.3, the device performance falls off suggesting a degradation of the electrical properties of the $CuInGaSe_2$.

The window/heterojunction forming layers used to fabricate $CuInGaSe_2$/CdS/ZnO:Al devices have been improved enabling device efficiencies to be improved. The CdS is deposited by a chemical bath deposition which has been improved to increase utilization of the reactant materials. Electrical and optical properties of the RF sputtered ZnO have been characterized as a function of the sputter gas composition to improve control of the films.

2.2.1 $CuInGaSe_2$ Deposition

$CuIn_{1-x}Ga_xSe_2$ films with $0 \leq x \leq 0.6$ have been deposited by four source elemental evaporation. The elemental composition of the film is adjusted by controlling the relative atomic fluxes from the various sources which are adjusted by changing the temperatures of the sources. For example, the value of x in $CuIn_{1-x}Ga_xSe_2$ can be changed continuously by changing the relative fluxes of indium and gallium atoms.

The films were deposited with a modified two layer process developed for $CuInSe_2$ by the Boeing group (5). The entire deposition process can be broadly divided into three distinct parts. During the first stage of the deposition process, a "copper rich" layer (layer A) where [Cu] > ([In] + [Ga]) was grown. In the second stage, a "copper poor" layer (layer B), where [Cu] < ([In] + [Ga]), was grown on top of layer A. The substrate temperature, T_{ss}, and the time of the deposition of

these two layers could be varied. T_{ss} for layer A was either 350°C or 450°C with deposition times of 12 or 21 mins. T_{ss} for layer B was always held at 550°C. The combined deposition time of both layers was 38 mins. It has been reported that higher substrate temperatures (T_{ss} > 530°C) improve film morphology and cell performance (6). The transition from layer A to layer B was accomplished by simultaneously increasing both the substrate temperature and the source temperatures of the group III elements (i.e., In and Ga). Finally, after layer B had been deposited, all the sources were turned off and samples cooled in a Se rich atmosphere for about 10 min. The changes in the source and the substrate temperatures with time during the course of a typical deposition is shown in Figure 13. The deposited samples can be broadly classified into two groups, namely, "uniform" and "graded". The former contained samples where the value of x was held constant during the entire deposition process while the latter had different values of x in layers A and B.

The $CuIn_{1-x}Ga_xSe_2$ films were deposited on either soda lime (SL) glass with a Mo coating deposited by rf sputtering or bare SL glass. The former were used for XRD and EDS measurements and for device fabrication while the latter were used mainly for optical characterization. Samples were deposited on 8 SL substrates arranged in 3 x 3 grid. The remaining position was occupied by a thermocouple imbedded in a glass sample and used for controlling T_{ss}. Each piece of the substrate is referred as the .mn piece where m and n refer to the row and column numbers respectively.

In order to characterize the layers A and B separately, one half of the .12 piece was shuttered during the growth of layer A while the other half was shuttered when layer B was grown. However, it should be noted that while layer B grows on layer A on the composite films, its growth on the .12 piece takes place on the Mo substrate.

2.2.2 $CuInGaSe_2$ Material Characterization

The $Cu(In,Ga)Se_2$ films were characterized using scanning electron microscopy (SEM), energy dispersive spectroscopy (EDS), x-ray diffraction (XRD) and optical band gap measurements. The grain size of the polycrystalline films could be directly estimated from SEM while EDS provided information on the elemental composition in the films. The value of x (=Ga/(Ga + In)) could then be compared with those determined from both optics and XRD. XRD was used to check the compositional uniformity and the relative orientation of the crystallites within the film, identify the different phases present, etc.

The EDS measurements were performed with a 20 kV acceleration voltage and a sample tilt of 20^0. The compositions were calculated from the integrated intensities of the different

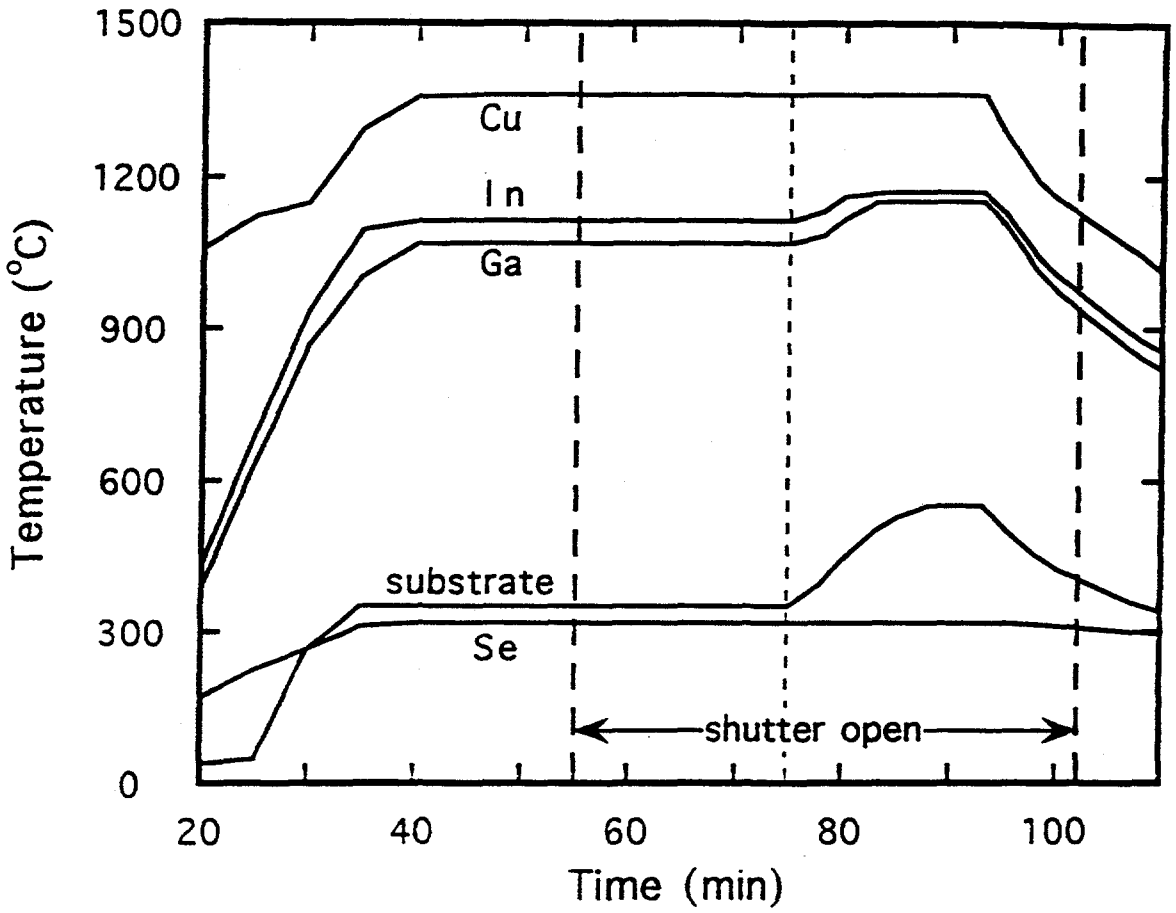

Figure 13. Changes in source and substrate temperatures during a typical run. Layers A and B were deposited for 21 and 17 mins., respectively. Note the cool down time of 10 mins.

peaks. There was some variation (~ 1 at. %) in the elemental composition of the films depending on the location of the substrates on the substrate holder. This is not surprising since the distance of the substrates from the sources varied. In addition there was some non uniformity in the substrate temperatures.

Scanning 2θ x-ray measurements were performed using standard CuK_α radiation. The orientation of the film was calculated from the relative intensities of the different diffraction peaks. Since the peak widths on some of the samples were broad, the intensities were calculated by measuring the area under the diffraction peaks. The precision lattice parameter a_0 (and hence x) was calculated from the extrapolation of the NRST plot on a series of h,k,l and 2θ values. As gallium replaces indium in $Cu(In,Ga)Se_2$, a_0 decreases, which in turn, shifts the diffraction peaks to higher angles. Thus, in some samples the value of x was also estimated from this shift. However, in these cases, the signal was stripped of its α_2 component.

The optical band gap (E_g) of the $CuIn_{1-x}Ga_xSe_2$ films was measured from their absorption coefficient, α. Since these have a direct band gap, E_g was determined from the intercept of the horizontal axis in the α^2 versus E plot, where E is the incident photon energy. Once E_g is known the value of x can be computed since its dependence on composition has been measured (7). The optical measurements were always performed on the .21 piece. Thus, the composition of the films can be measured using EDS, XRD and optics. The values of x thus calculated are referred to as x_{EDS}, x_{XRD}, x_{opt}, respectively.

Figure 14 is a plot of the absorption coefficient α^2 versus E for a series of $CuIn_{1-x}Ga_xSe_2$ samples used to determine E_g. The values of x_{opt} calculated from E_g are compared to x_{EDS} in Table 7. There is good agreement between the two techniques for value of $x_{EDS} \leq 0.40$.

Table 7. Optical and EDS results for a series of $CuIn_{1-x}Ga_xSe_2$ samples.

Sample #	E_g (eV)	x_{opt}	x_{EDS}
32359	0.98	0	0
32381	1.08	0.17	0.15
32380	1.11	0.22	0.20
32372	1.20	0.36	0.37
32373	1.20	0.36	0.40
32374	1.28	0.48	0.57

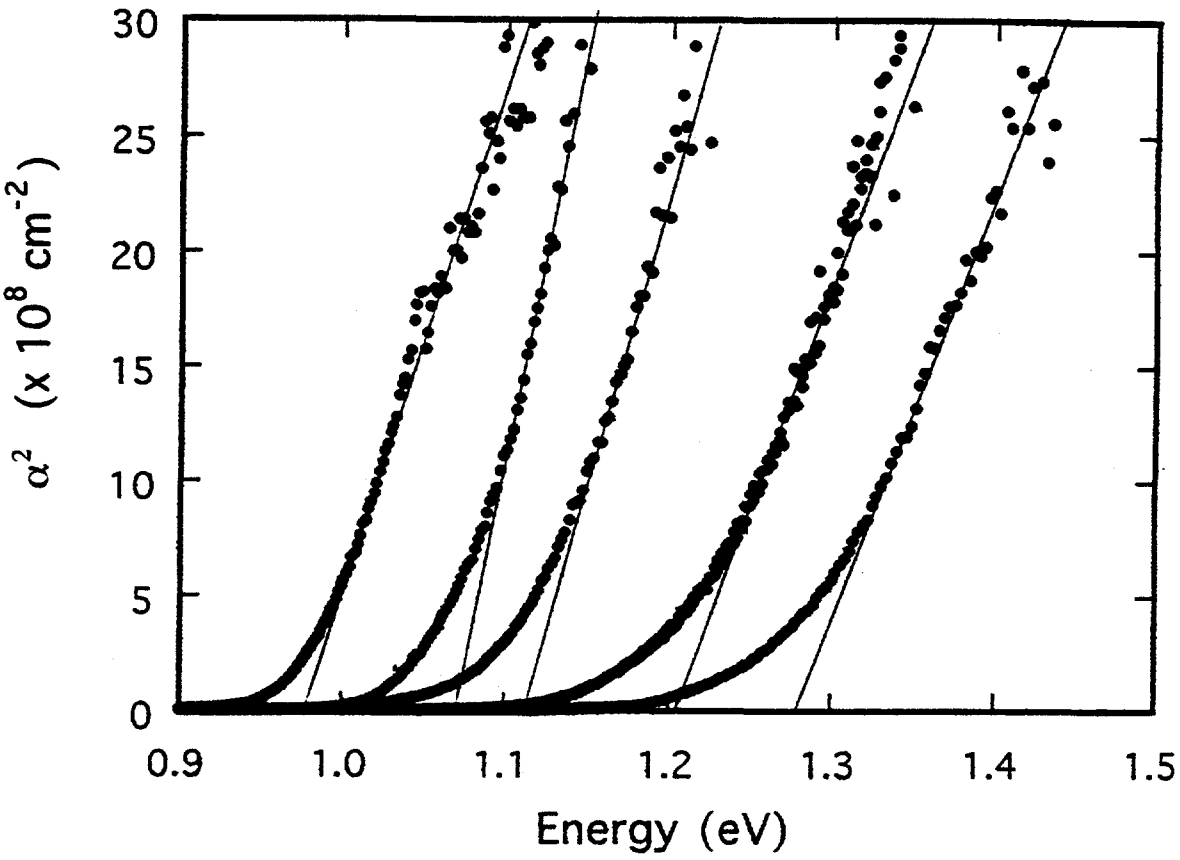

Figure 14. α^2 **vs. E for** $CuIn_{(1-x)}Ga_xSe_2$ **for** $0 \leq x_{EDS} \leq 0.6$.

A typical x-ray diffraction pattern for a uniformly grown $CuIn_{0.82}Ga_{0.18}Se_2$ sample (32382) is shown in Figure 15. A NRST fit to the peaks yield $x_{XRD} = 0.23$, which is in good agreement with both EDS and optical measurements. The full width at half maximum (FWHM) of the (112) peaks were $0.15^0, 0.21^0, 0.15^0$ for A, B, and the composite layers respectively. While the (112) peak for the A and the composite layer was narrow, it was much broader for the B layer. This is expected since the $CuIn_3Se_5$ phase is expected to be present in this copper poor layer. This result is fairly typical of uniformly grown samples.

Recent XRD work on $CuInSe_2$ had suggested a correlation between the relative orientation of the (112) peak with device performance in $CuInSe_2$ (2). The relative intensities of the (112) and the (220) peak of the $CuIn_{1-x}Ga_xSe_2$ films as a function of x_{EDS} is shown in Figure 16. The samples shown in this plot have both 12 and 24 A layer deposition times with $T_s = 350°C$ and $450°C$. The expected intensities of these peaks if the crystallites were randomly oriented (the powder diffraction pattern) were also calculated from the JCPDS cards and are plotted for comparison. Samples deposited with $T_s = 350°C$ for the initial layer are found to be generally randomly oriented. However, samples grown at $450°C$ were found to be preferentially oriented in the (220) direction. There is no clear correlation between the relative orientation and device performance of these samples.

Detailed analyses of peak shapes were undertaken on a set of uniform and graded samples. The details of the deposition parameters and characterization results are shown in Table 8. The diameter of the individual grains (d_G) on the surface of the film was estimated from SEM. For the initial layer the crystallites had rounded edges while those on layer B were more facetted with $d_G \leq 1\mu m$. These observations were independent of the growth conditions. On the other hand, the composite layer (.22 piece) had well facetted, larger grains.

Detailed scans of the XRD peaks for samples 32382, 32392, and 32386 are shown in Figures 17-19. The diffraction peaks are due to the $CuK_{\alpha 1}$ line only and the scan step is 0.01^0. The peaks have been fitted to a single gaussian, and when possible to double (and in one case, triple) gaussians.

(i) Uniform samples

The "uniform" samples listed in Table 8 were chosen in order to study the effects of changing x_{EDS} on the film properties. As x increases both a_0 and c/a decrease. For example, the c/a ratio varies between 2.010 ($CuInSe_2$) and 1.961 ($CuGaSe_2$) and for x ~ 0.2 it is equal to 2.0. Thus, for 32382 ($x_{EDS} = 0.21$) the (220)/(204), (312)/(116), and (332)/(316) peaks cannot be resolved. This is not the case for the other two samples since the c/a ratio deviates from 2.

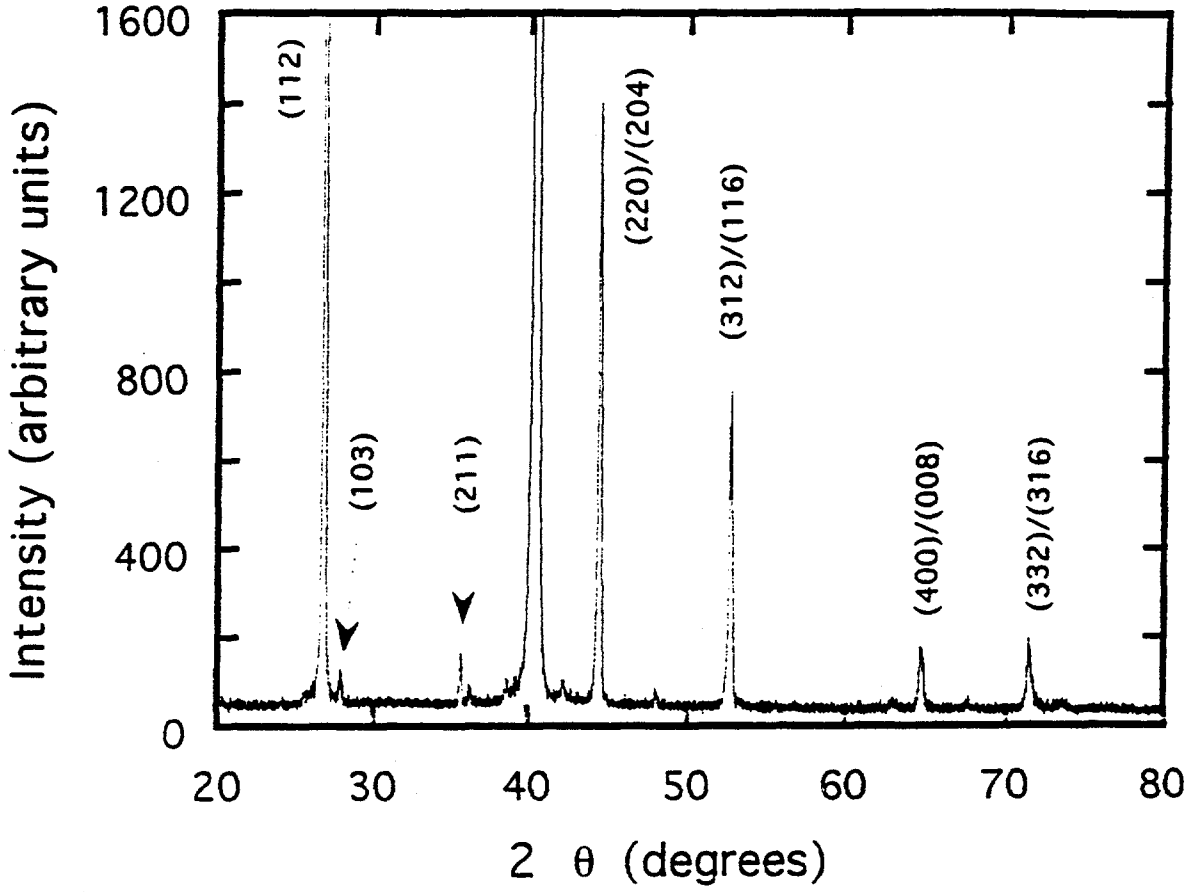

Figure 15. An X-ray diffraction pattern for a $CuIn_{0.79}Ga_{0.21}Se_2$ sample. Only the CIGS peaks are marked. The large peak at 40.44^0 is due to the Mo (110).

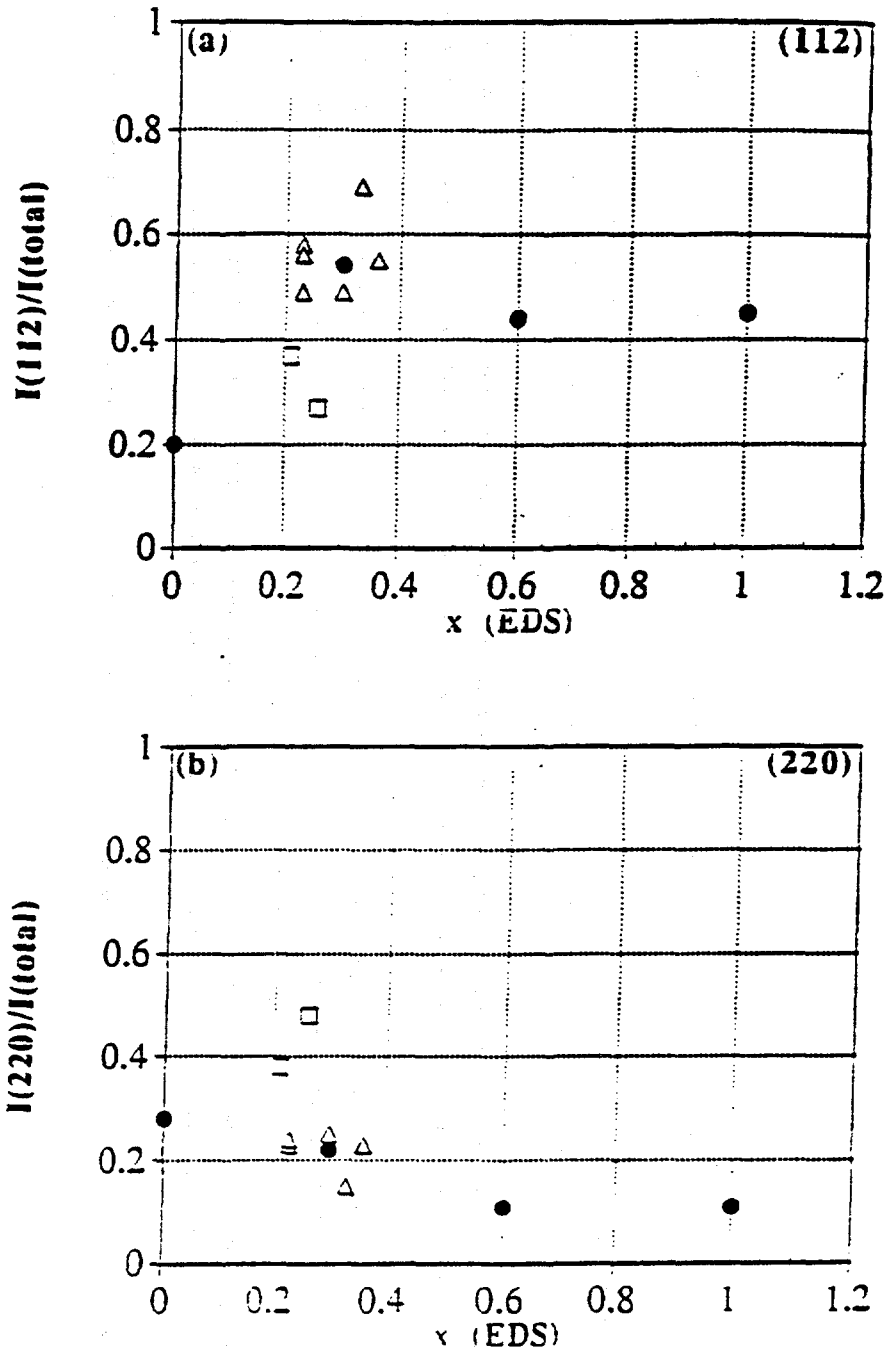

Figure 16. The relative intensities of the (a) (112) and (b) (220) peaks. The open circles and squares represent samples deposited with T_s=350°C and 450°C for layer A. The solid circles represent expected intensities if the crystallites in the film were randomly oriented.

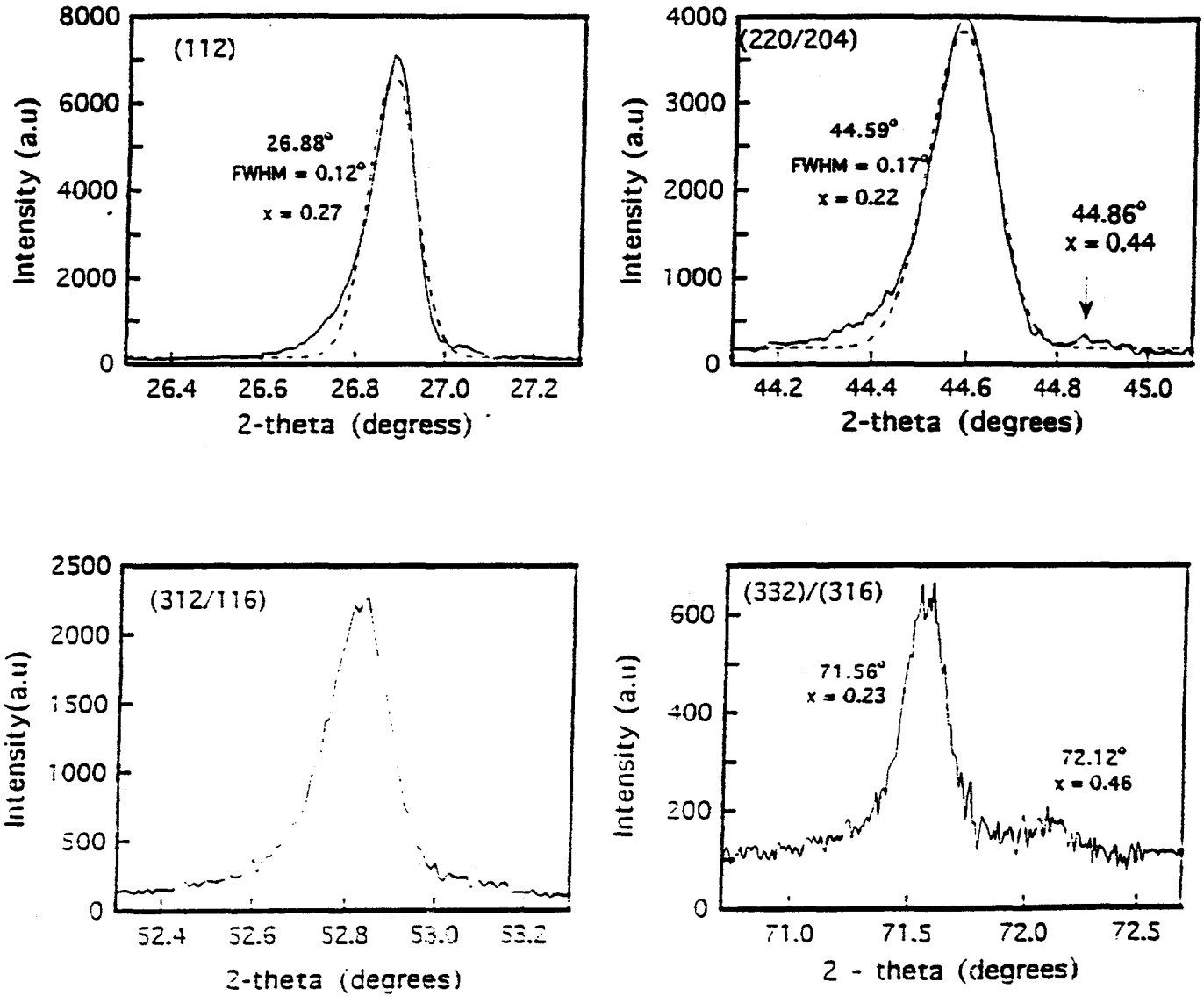

Figure 17. Intensity vs. 2θ plot for sample 32382.13 of (a) (112), (b) (220)/(204), (c) (312)/(116), and (d) (332)/(316) peaks. Note the small peaks at 44.86^0 and 72.12^0 corresponding to x=0.44 and 0.46 respectively.

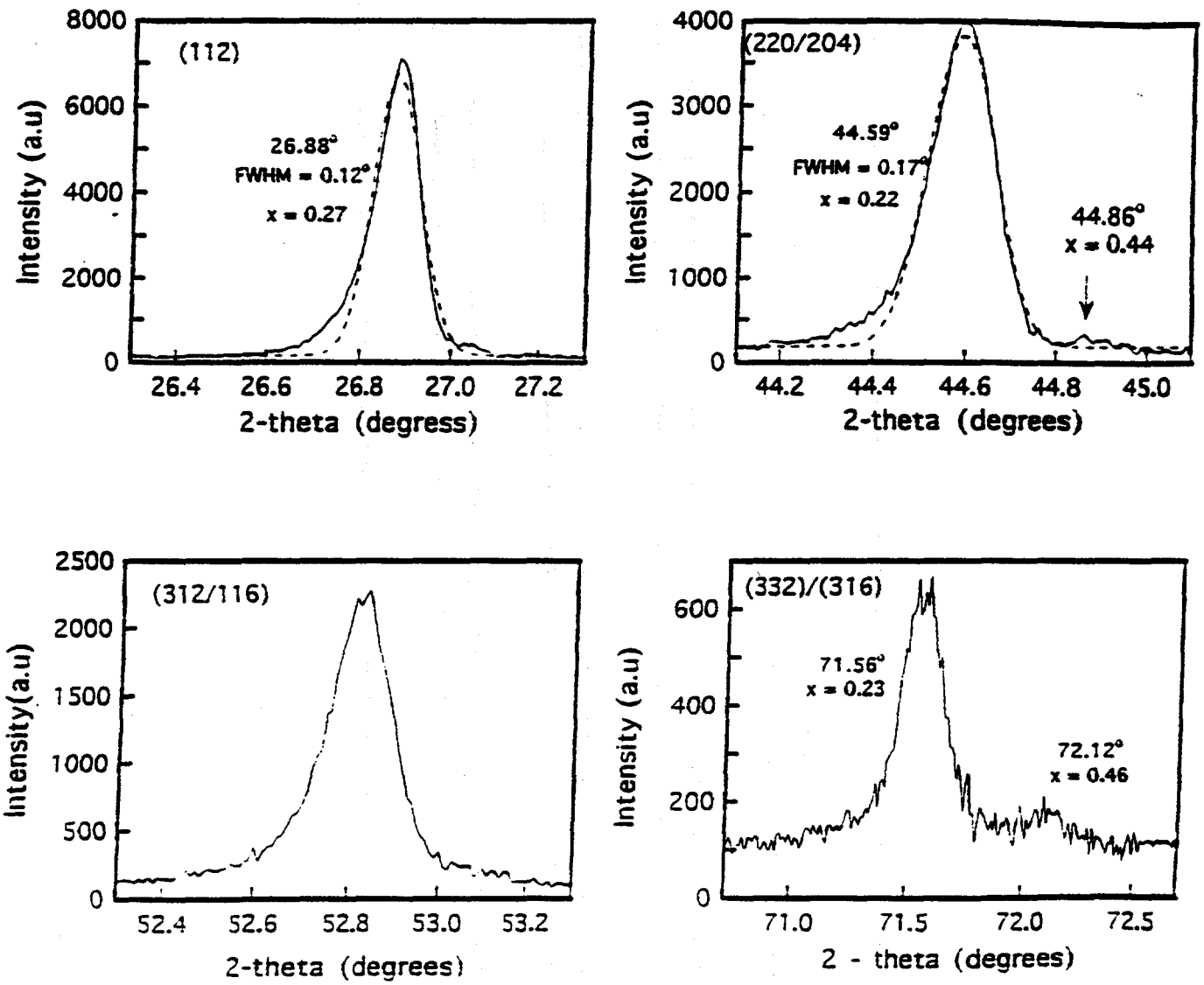

Figure 18. Intensity vs. 2θ plot for sample 32392.12 of (a) (112), (b) (220)/(204), (c) (312)/(116), and (d) (332)/(316) peaks. Note the FWHM of the peaks corresponding to higher gallium content is larger.

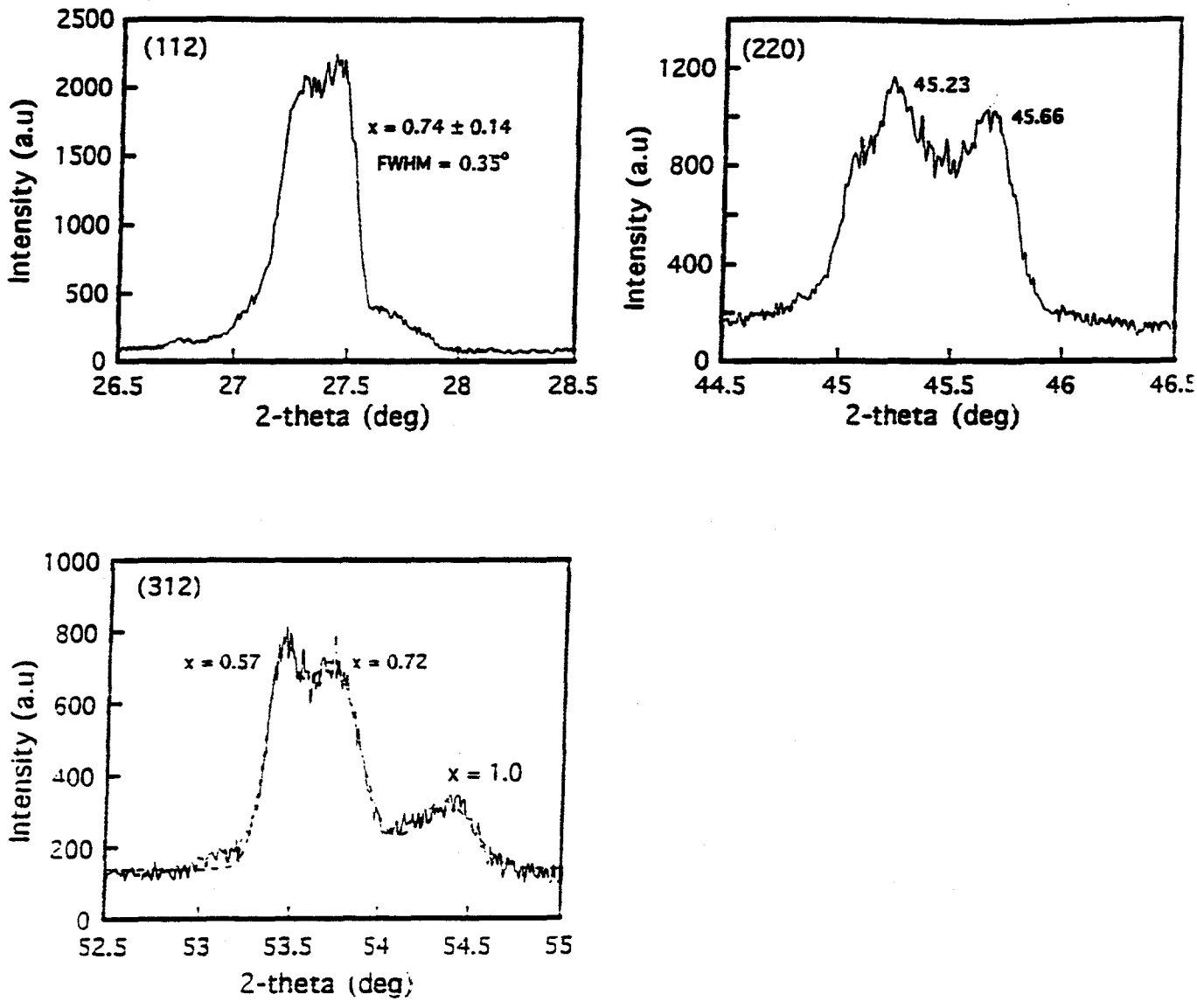

Figure 19. Intensity vs. 2θ for sample 32386.23 of (a) (112), (b) (220)/(204), and (c) (312)/(116). Note the FWHM of the peaks corresponding to higher gallium content is larger.

Table 8. The deposition parameters and elemental composition of $CuIn_{(1-x)}Ga_xSe_2$ prepared in EV-3. Note that the first three samples are uniform while the last sample is graded. The grain sizes were estimated by electron microscopy.

Sample#	Ts (^{0}C)	Time (mins)	Cu	In	Ga	Se	x_{EDS}	x_{opt}	d_G (mm)
			(atomic percent)						
32382.12A	350	21	35.1	15.0	4.1	45.8	0.21	~ 1	
	.12B	550 17		21.3	23.3	5.7	49.7 0.20		~ 1
	.22	10		25.2	22.0	5.2	48.4 0.18		1.5 - 2
	.13			25.9	21.7	6.0	46.4 0.22	0.22	
32386.12A	350	21	29.2	12.5	11.0	47.3	0.47	≤ 1	
	.12B	550 17		19.7	14.6	16.4	49.3 0.53		~ 1
	.22	10		22.0	14.2	15.3	48.5 0.52		1- 1.5
	.23			22.5	11.4	17.1	49.0 0.60	0.38	
32392.12A	450	12	34.9	11.6	4.0	49.5	0.26	≤ 1	
	.12B	550 26		21.2	20.7	8.6	49.5 0.29		~ 1
	.22	10		22.5	20.4	8.6	48.5 0.30	0.26	1.5 - 2

Once again the position of these peaks indicates a value of x of ~ 0.45.

It is evident that the FWHM of the (112) peaks increased with increasing x_{EDS}. Sample 32382 exhibited a narrow (instrumentally broadened) peak while sample 32386 exhibits a broad peak. Broadening of the peaks indicates either the presence of crystallites having a range of composition and/or small sized grains. The asymmetry of both the (112) and (220)/(204) peaks in 32382 suggests the presence of concentration gradients within the film. In addition to the large main peak another small peak is visible in Figures 17a and 17b indicating the presence of regions with a higher value of x.

The results described above become increasingly pronounced as the value of x_{EDS} increases. In both samples 32392 and 32386, two or more peaks were observed at the higher angles and were thus fitted to multiple gaussians. Assuming the composition is uniform within the films, d_{hkl}, the interplanar distance between the planes (h,k,l) may be calculated. Consider sample 32386.23, for example. Assuming x = 0.60 and is uniformly distributed through the film, the difference in the lattice spacings between the (312) and the (116) planes was calculated to be 0.011 Å while the observed value was 0.077 Å (Fig. 19).

A strong shoulder/peak to the right (Figs. 19a and c) approaches $CuGaSe_2$. This variation in composition is also reflected in the broad (112) peak (FWHM = 0.35^0). Since the resolution improves at higher angles, the gallium content was estimated from these higher angle peaks. The XRD results suggest that there were at least two different compositions corresponding to x_{XRD} ~ 0.30 and 0.42 and x_{XRD} ~ 0.58 and 0.75 in samples 32392 and 32386, respectively. Calculations indicate that these cannot be explained by assuming a split due to the (220)/(204), (312)/(116) and (332)/(116) peaks.

The peak broadening and the presence of additional peaks indicates that there exists a range of composition within the films. As the Ga content increases, the compositional variation increases with evidence of segregation of different compositions. There is good agreement between x_{EDS} and the value of x calculated from the left edge of the XRD peaks. The EDS only probes the top 0.5 to 1.0μm of the film while the XRD probes the entire film thickness. This suggests that the regions of the film with higher Ga are nearer to the $CuInGaSe_2$/Mo contact.

2.2.3. $CuInGaSe_2$ Device Characterization

For fabricating solar cells, the $CuIn_{1-x}Ga_xSe_2$ is deposited on SL glass coated with sputtered Mo, 1 or 2 μm thick. Cells are formed with chemical bath deposited (CBD) CdS, typically 50-70 nm thick. This is followed by a bi-layer ZnO:Al film deposited by

rf sputtering as discussed in Section 2.2.4. Finally, Ni contacts are deposited and the cell areas are defined by mechanical scribing.

The CBD CdS behaves differently on the $CuIn_{1-x}Ga_xSe_2$ than on $CuInSe_2$, in that the cells with $CuInGaSe_2$ can be heat treated, improving V_{oc} and the current collection, without the cell developing shunts. This allows the cell efficiency to be improved with heat treatment in air at 200°C. In addition, the cells are much closer to their maximum efficiency with no heat treatment than $CuInSe_2$ cells and require substantially shorter heat treatments.

$CuIn_{1-x}Ga_xSe_2$ based solar cells have been fabricated with x ranging from 0 to 0.57. The best cell results obtained at 6 values of x spanning this range are listed in Table 9. The poor performance of the cell with no Ga is typical with the CBD CdS. The quantum efficiency curves for these cells are shown in Figure 20. The shift in the long wavelength fall-off of the response corresponds to the change in Ga as listed in Table 9.

Table 9. J-V parameters for the best cells at 5 increasing Ga contents. The Ga content, x, and bandgap are determined by EDS on the -22 piece from the same deposition.

Cell #	Voc (V)	Jsc (mA/cm^2)	FF (%)	eff (%)	x	Eg (eV)
32359-23	0.374	35.0	61.3	8.0	0	1.00
32381-33	0.521	35.3	69.9	12.9	0.15	1.09
32384-23	0.537	34.0	70.0	12.8	0.23	1.14
32391-23	0.573	32.6	68.5	12.8	0.29	1.18
32373-23	0.596	27.7	70.1	11.6	0.40	1.25
32374-32	0.623	23.7	69.1	10.2	0.57	1.36

A semilog plot of the same QE data is shown in Figure 21. It can be seen that as the Ga content increases, the QE falloff becomes more gradual.

The variation of device parameters V_{oc}, J_{sc}, FF, and eff. with bandgap as the Ga content is varied is shown in Figures 22-25. There is considerable scatter in these plots since they show parameters for the best cell on all substrates processed. This includes experiments to evaluate different $CuIn_{1-x}Ga_xSe_2$ compositions and deposition conditions as well as variations in the Mo, CdS, and ZnO depositions. Results at x=0 are not shown because the CBD CdS does not behave the same in that case, giving much lower V_{oc} and FF than evaporated CdS.

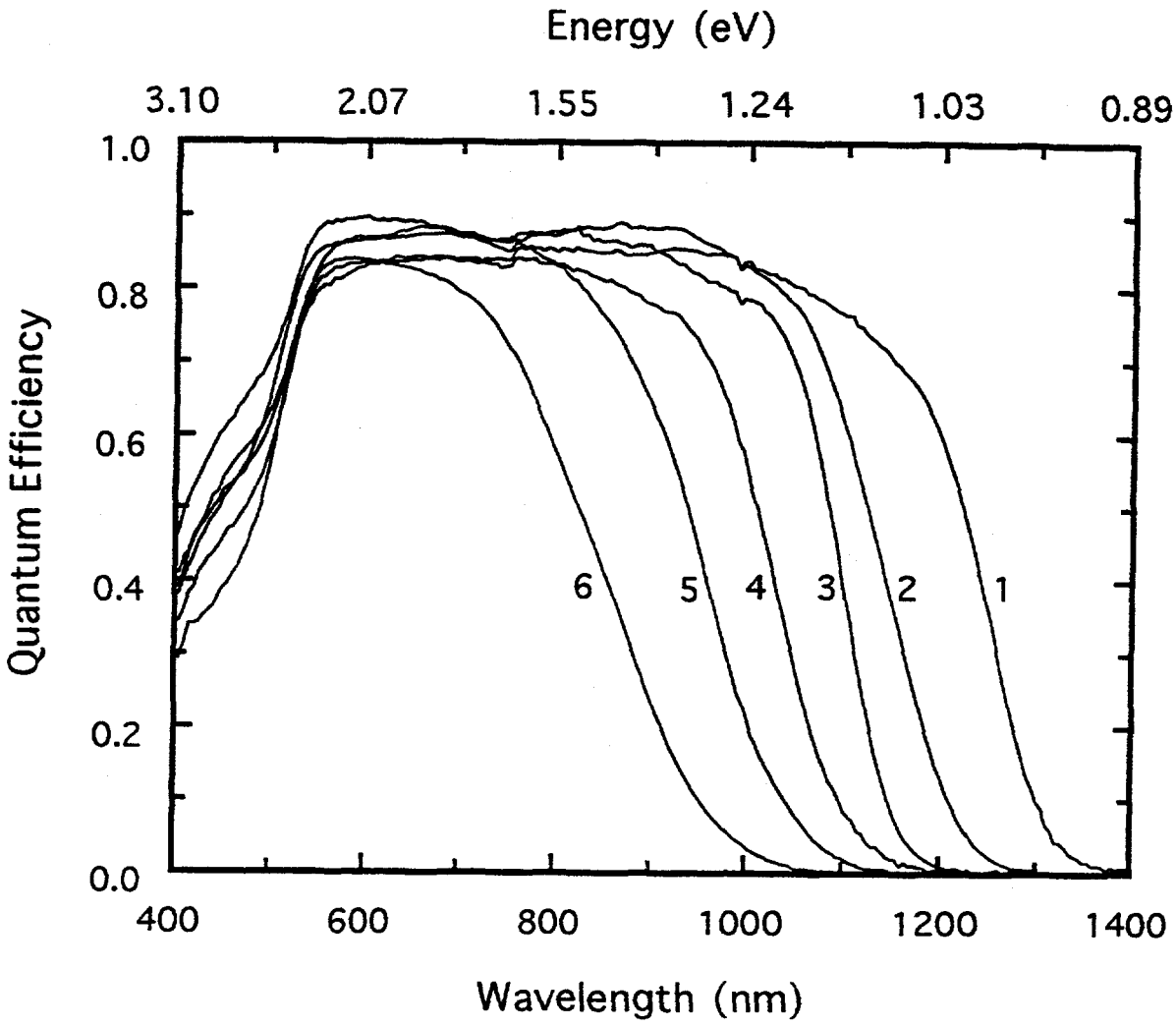

Figure 20. Quantum efficiency curves of 6 $CuIn_{1-x}Ga_xSe_2$ solar cells with x ranging from 0 to 0.57.

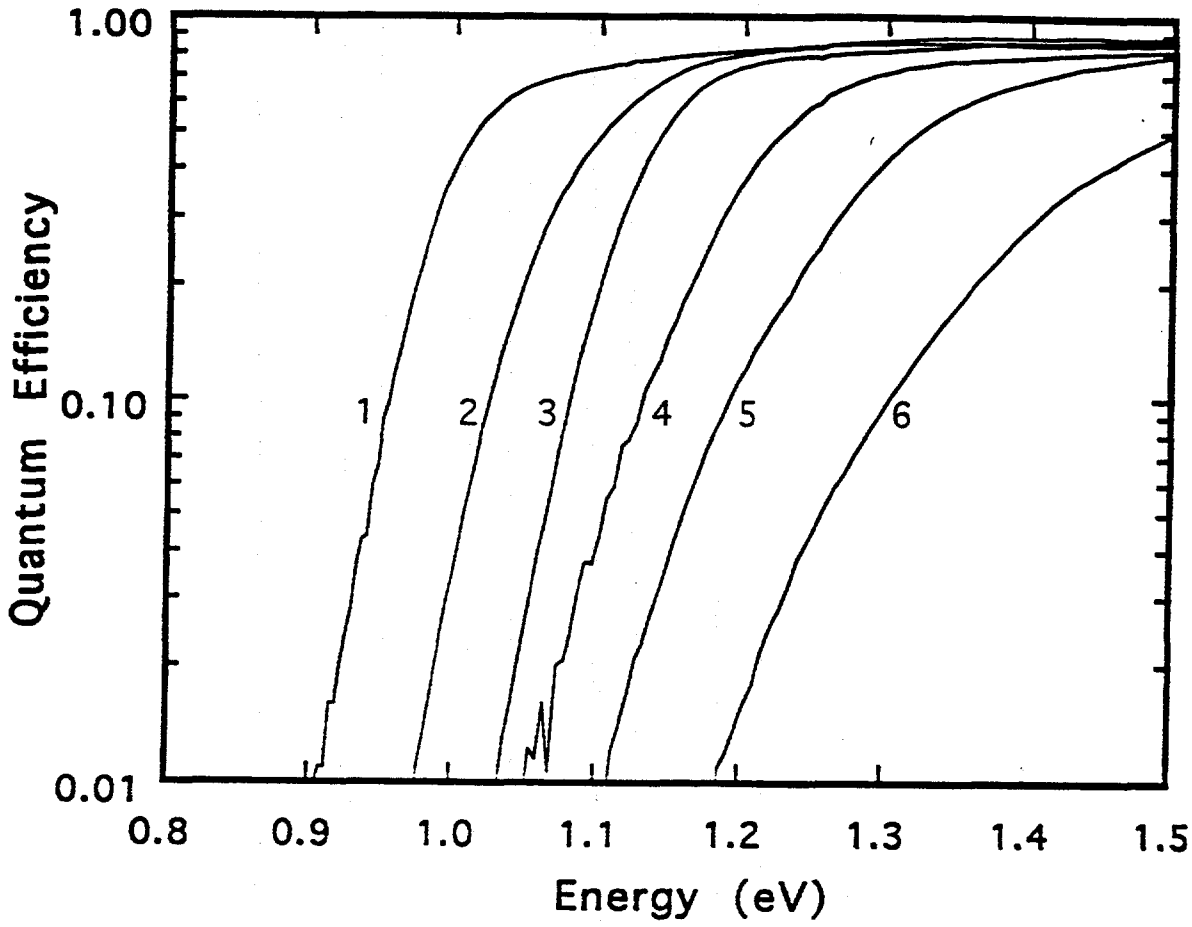

Figure 21. Long wavelength fall-off of the quantum efficiencies in Figure 20 re-plotted on a logarithmic scale showing the shift as x increases corresponding to the increase in E_g.

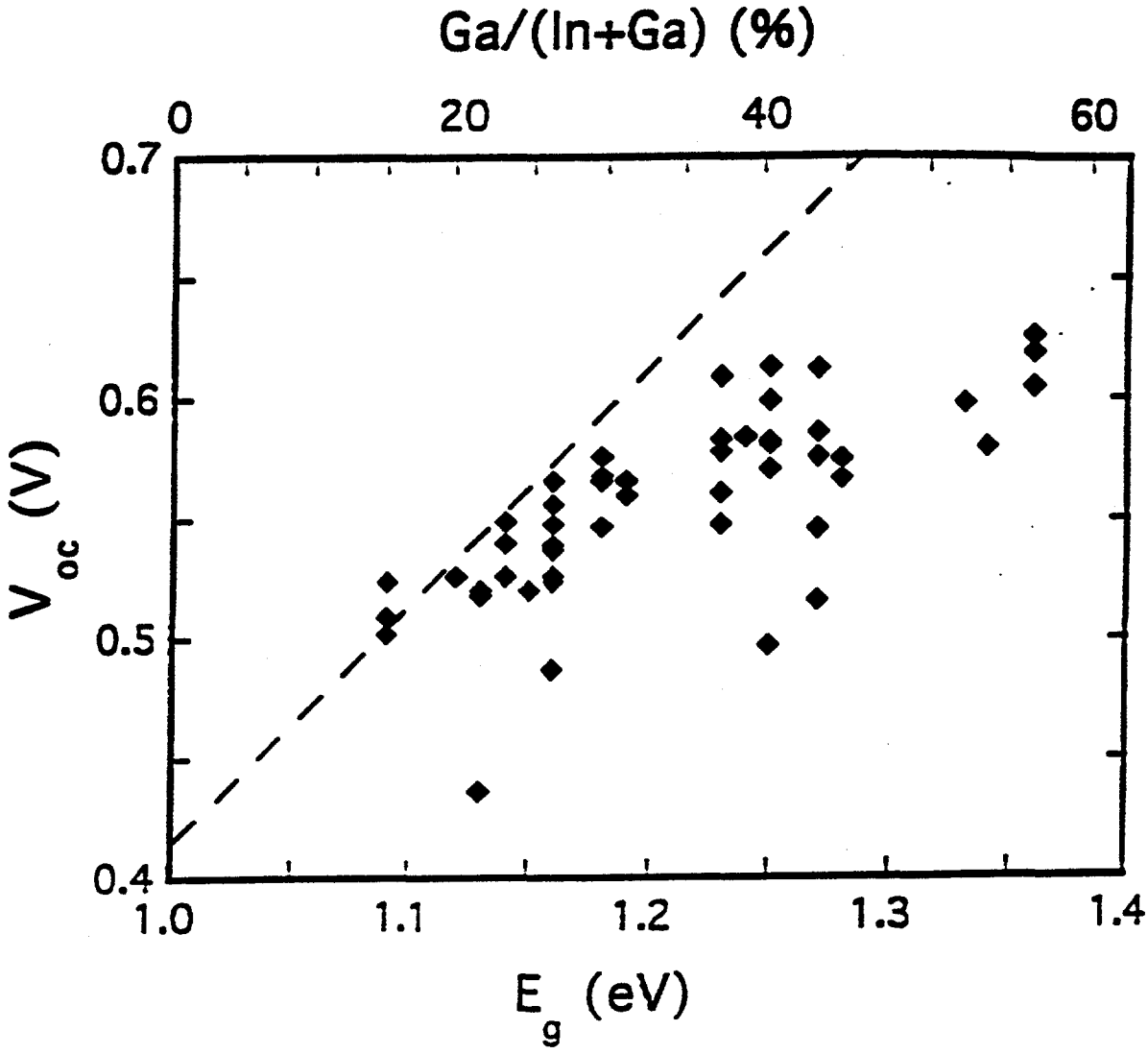

Figure 22. Increase in V_{oc} with E_g. The dashed line shows the slope expected if V_{oc} increases proportionately to E_g.

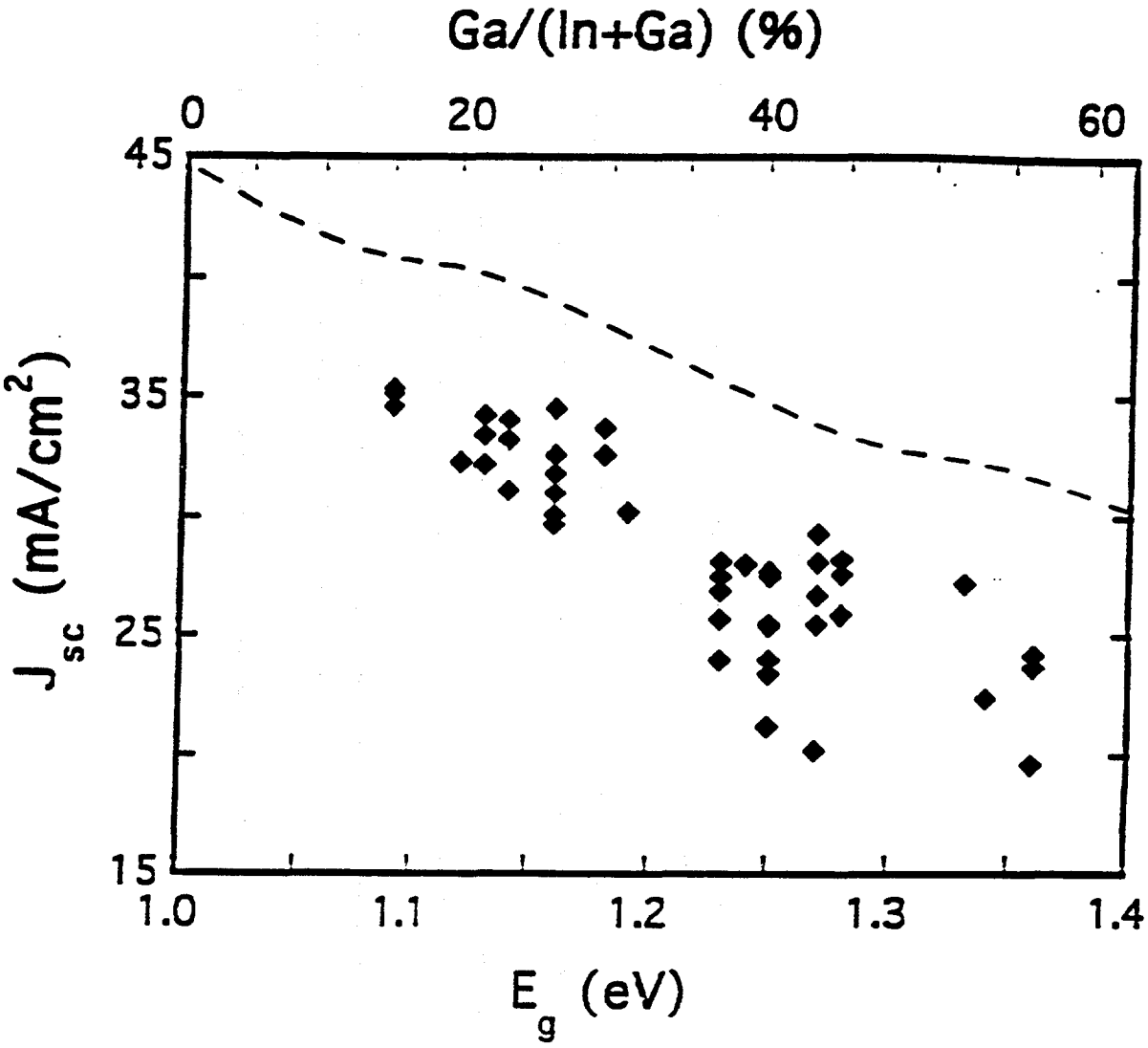

Figure 23. Decrease in J_{sc} with E_g. The dashed line shows the total current available, obtained by integrating the AM1.5 spectrum.

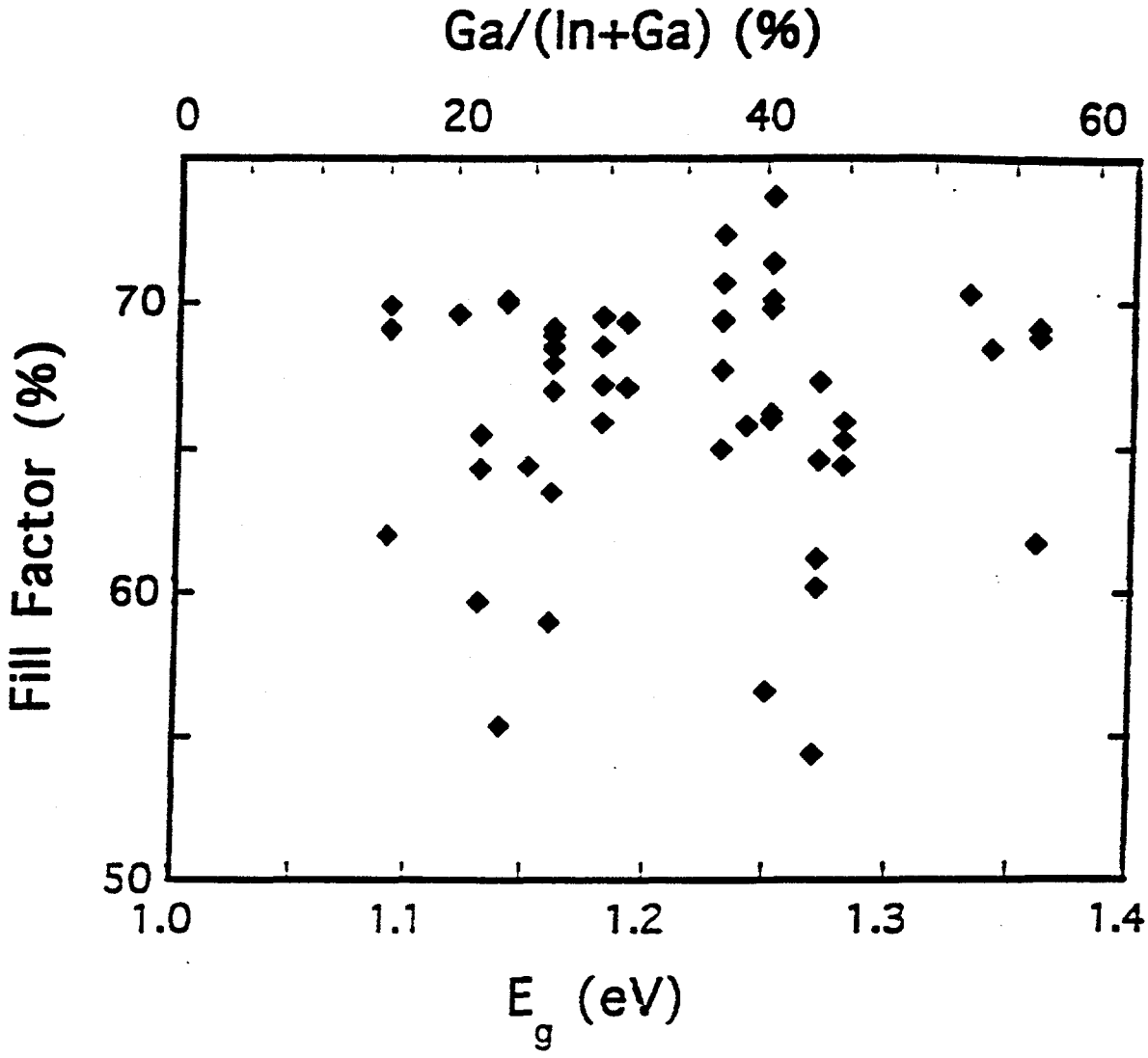

Figure 24. Fill factor for cells with varying E_g showing no clear dependence.

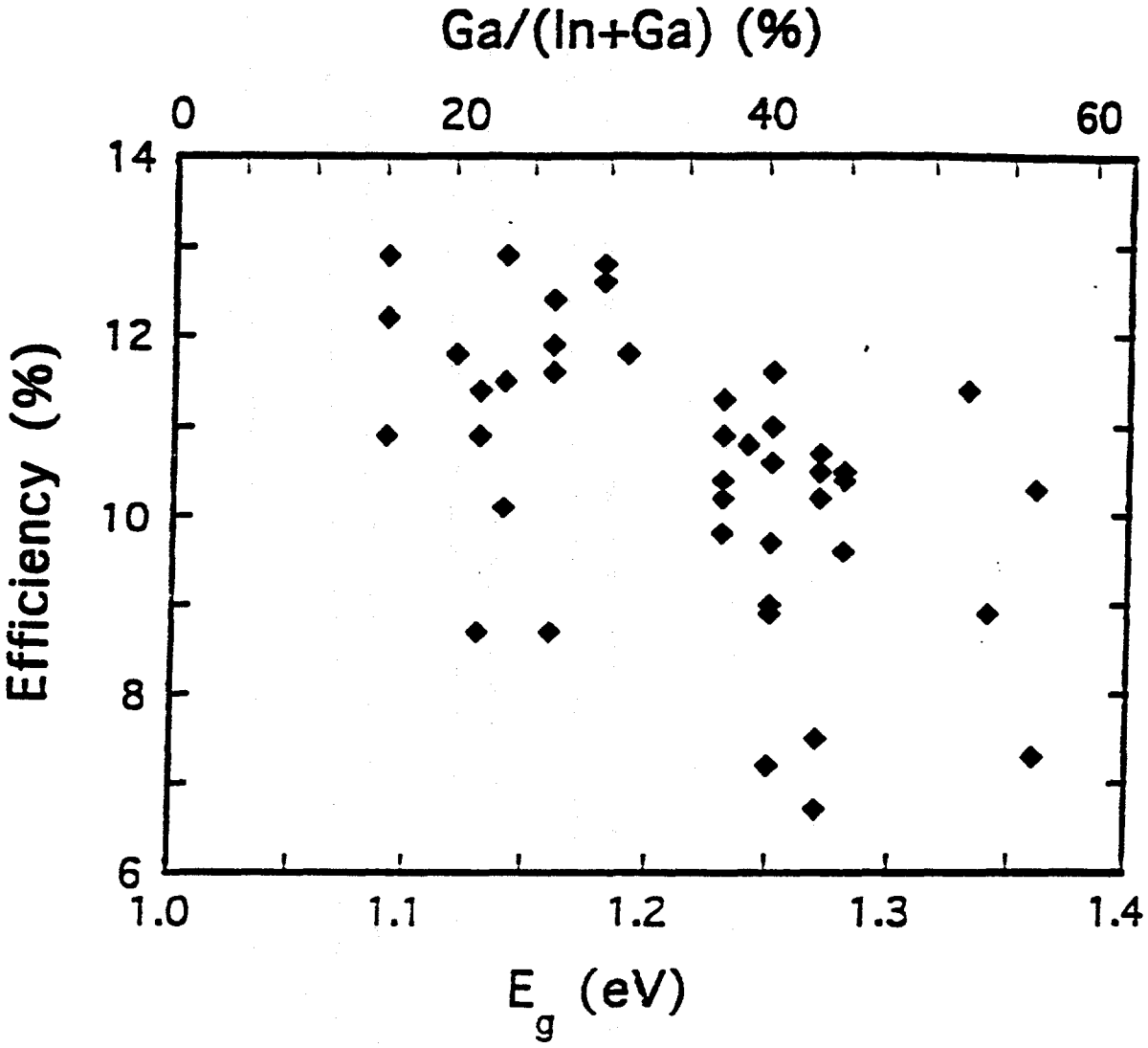

Figure 25. Efficiency for cells with varying E_g. The highest efficiency as a function of x is level for E_g < 1.2 eV but falls off as the Ga content increases further.

The increase in V_{oc} levels off for E_g greater than ~1.15 eV corresponding to $x \approx 0.3$. The dashed line on Figure 22 shows the slope expected if V_{oc} increases proportionately to E_g. For this set of cells the increase is less than expected.

The slow increase in V_{oc} for E_g > 1.15 eV and the fall-off in the QE suggest a degradation of the electrical properties of the $CuIn_{1-x}Ga_xSe_2$ as x increases. The specific cause of this leveling-off of V_{oc} will require further analysis of $CuIn_{1-x}Ga_xSe_2$ cells over a wide range of Ga compositions.

The dashed line in Figure 23 is the total current available in the AM1.5 spectrum. The fall-off of the measured J_{sc} values follows this drop in the available current. The difference in current between the best cells and the total available current is ~5-8mA/cm^2. Typically, these cells lose 2.5 mA/cm^2 due to reflection (with no AR coating), 1-1.5 mA/cm^2 due to absorption in the ZnO, and 2-3 mA/cm^2 in the CdS. Additional current loss occurs due to incomplete collection of carriers generated deep in the $CuIn_{1-x}Ga_xSe_2$.

The fill factor, in Figure 24, shows no dependence on the Ga content. The best efficiencies are ~13% for E_g less than ~1.2 eV. Above that the efficiency falls off corresponding to the leveling off of V_{oc}.

Experiments have been conducted to evaluate variations in the deposition parameters and the resulting effect on cell results. The Cu-rich A layer has been deposited with T_s=350 or 450°C. Two sets of times for deposition of the A and B layers have been used while keeping the total deposition time constant. With a total time of 38 minutes the A layer has been deposited for either 12 or 21 minutes. The device results in Table 10 compare two set of cells with the different times and values of T_{ss}. In general, there is no difference in the cell results.

Table 10. $CuIn_{1-x}Ga_xSe_2$/CdS cell results with different deposition times and substrate temperatures in the A and B layers.

Cell	T_{ss} (A/B) (°C)	time (A/B) (min)	V_{oc} (V)	J_{sc} (mA/cm^2)	FF (%)	eff (%)	$\frac{Ga}{In+Ga}$ (%)
32383.32	350/550	21/17	0.553	32.6	68.4	12.3	26
32384.23	450/550	21/17	0.537	34.0	70.0	12.8	23
32391.33	350/550	12/26	0.565	31.3	69.5	12.3	29
32394.22	450/550	12/26	0.563	30.2	69.3	11.8	31

2.2.4 Window/Heterojunction Layers for $CuInSe_2$

Cadmium sulfide thin films deposited by a chemical bath deposition have been used in the fabrication of $CuInGaSe_2$/CdS/ZnO:Al solar cells. Improvements have been made in the deposition process to increase the utilization of the reactant materials and reduce chemical waste. Alternative bath processing has also been investigated. The ZnO:Al is deposited in a bi-layer, comprising a high resistive layer followed by low resistive layer, by RF sputtering from a ZnO/Al_2O_3 target. The resistivity and transparency are controlled by varying the sputter gas mixture of Ar and O_2.

Cadmium Sulfide Chemical Bath Deposition

The processing conditions for the chemical bath deposition of CdS have been modified in order to reduce film deposition rates and increase utilization of reactant materials with subsequently less chemical waste. All reactant concentrations except ammonium hydroxide have been reduced to one-half of previous levels (2), resulting in the following reactant concentrations in the standard bath:

$$[CdCl_2] = 0.001\ M$$
$$[NH_4Cl] = 0.0025\ M$$
$$[NH_4OH] = \sim 1.4\ M$$
$$[(NH_2)_2CS] = 0.01\ M$$

The QE curves of 3 devices, for which the CdS was deposited for different times, are shown in Figure 26. The relative thickness of the CdS can be determined from the QE at 400 nm, assuming there is no change in collection. These thicknesses are shown in Figure 27 as a function of deposition time.

Experiments were done using reactant baths composed of Nanopure® analytical grade processed water with 18MΩ-cm resistivity. Figure 28 presents a comparison of CdS film growth on 7059 glass in baths with and without Nanopure water. Without the Nanopure water, standard de-ionized water is used and the resistivity is typically ~10MΩ-cm. Nanopure-based reactant baths resulted in approximately a 40% increase in growth rate as well as a slower rate of homogeneous precipitation in the bath during film growth. Initial experiments have resulted in improved device parameters for CdS/CdTe cells when the Nanopure water is used for the CdS film growth. However, results for $CuInSe_2$/CdS cells were inconclusive.

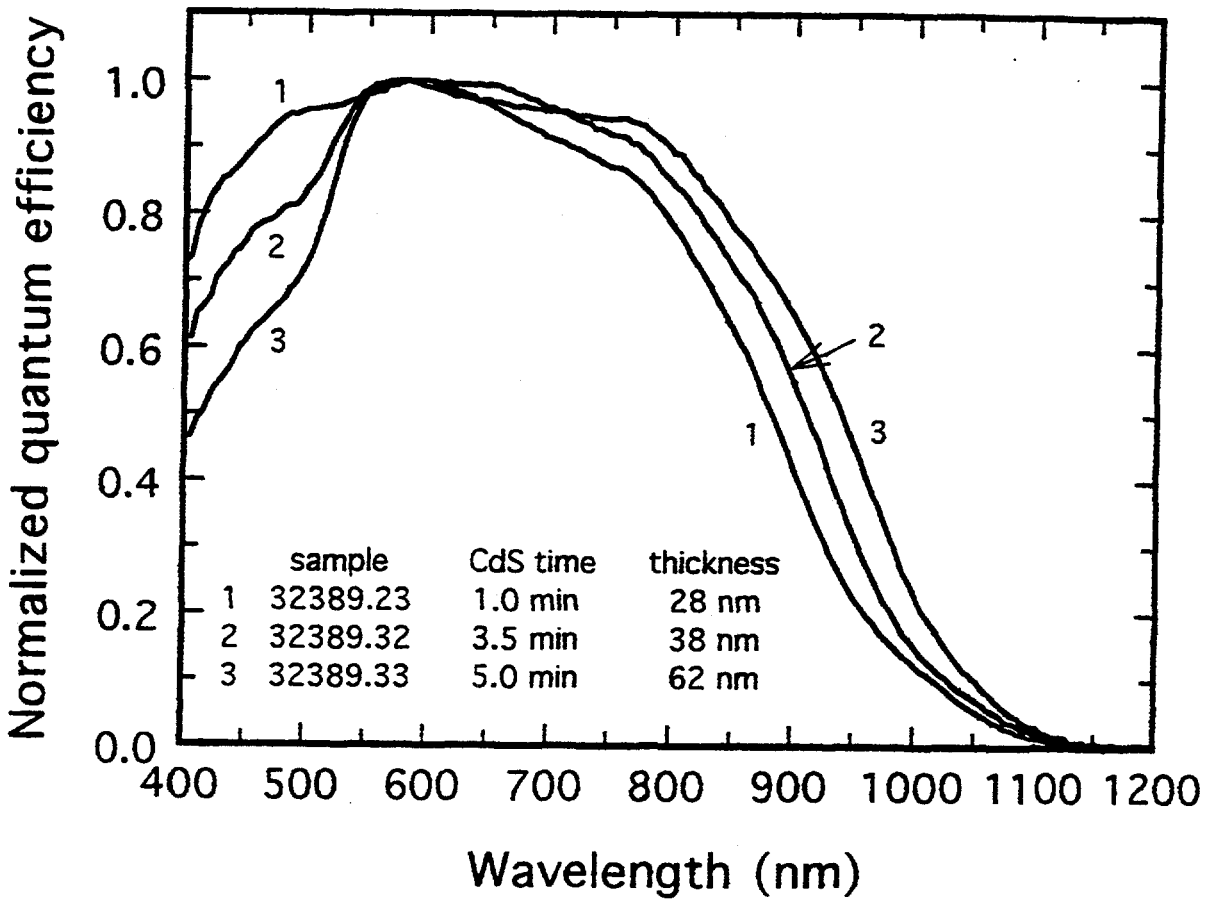

Figure 26. Quantum efficiency of 3 Cu(InGa)Se_2/CdS devices with increasing deposition time of the CdS.

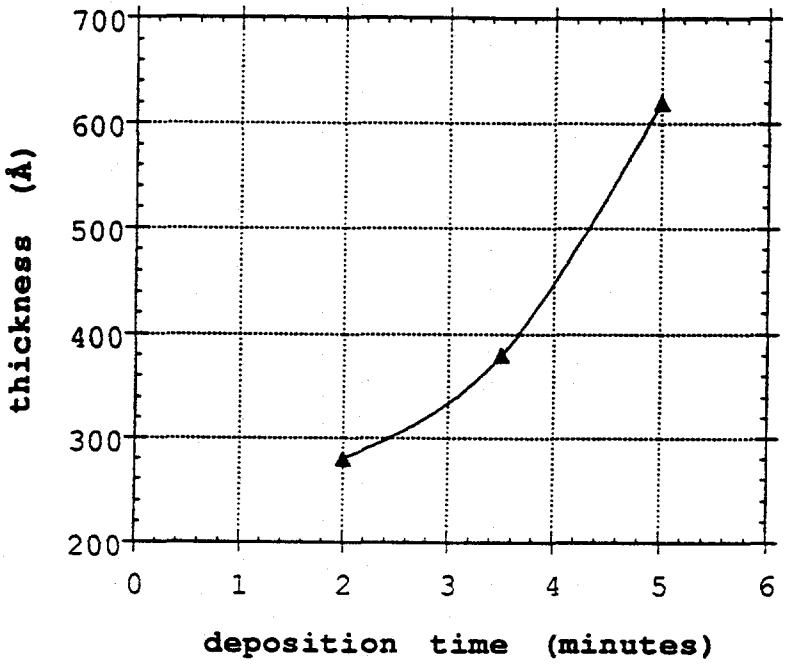

Figure 27. Film thickness versus deposition time of CdS by chemical bath deposition determined from quantum efficiencies of Cu(InGa)Se_2/CdS devices.

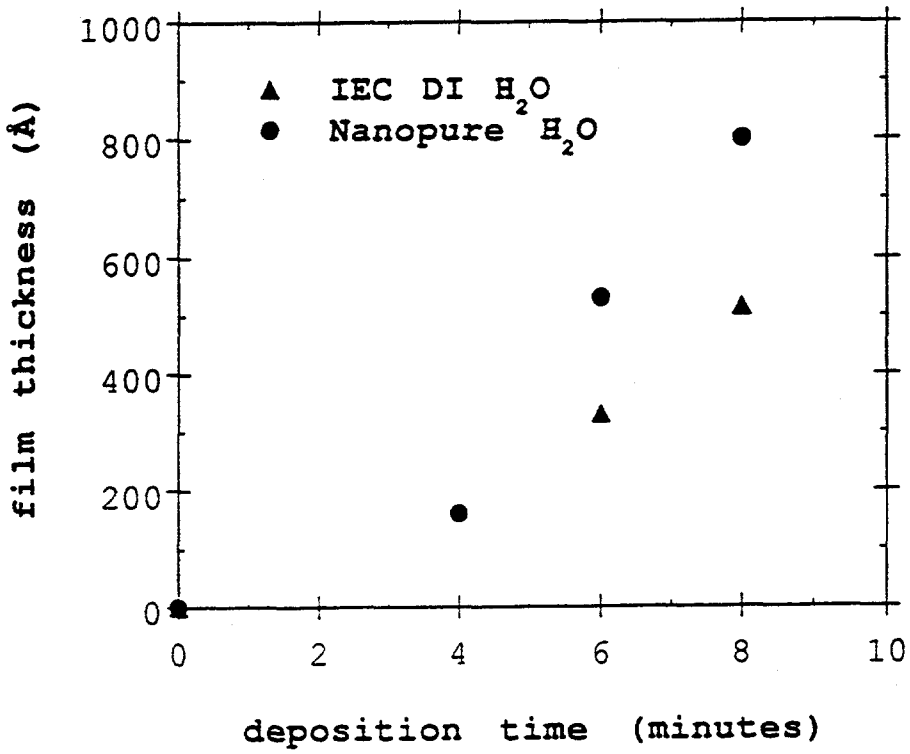

Figure 28. Comparison of growth rate of CdS on 7059 glass with and without Nanopure water in chemical bath.

CdS films were grown using various cadmium salts and the effect on $Cu(InGa)Se_2$ device performance was investigated. Non-buffered baths containing cadmium acetate, chloride, and sulfate were used for CdS deposition on $Cu(InGa)Se_2$. Results from completed devices are presented in Table 11. Comparable results were attained with the chloride and sulfate-based baths while the acetate-based bath resulted in poorer cell performance. Our standard chloride-based bath continues to be used for all general device processing.

Table 11. Solar cell parameters for $Cu(InGa)Se_2$ cells with CdS deposited from different Cd salts (n.b.=no buffer).

Cell #	CdS bath	V_{oc} (V)	J_{sc} (mA/cm^2)	FF (%)	Eff. (%)
32372.23	chloride	0.56	28	69	10.9
32372.22	chloride, n.b.	0.55	28	65	9.8
32372.33	sulfate, n.b.	0.57	27	72	11.2
32373.23	chloride	0.59	28	70	11.6
32373.22	acetate, n.b.	0.50	26	56	7.2
32373.33	sulfate, n.b.	0.58	25	71	10.5

Indium Sulfide Chemical Bath Deposition

A method for the chemical bath deposition of In_2S_3 developed by R. Noufi was reproduced at IEC. Nanopure water was used for reactant stock solutions and some of the experimental baths. The bath conditions were as follows:

In ion source	0.005 M $InCl_3$
S ion source	0.05 M thioacetamide (CH_3CSNH_2)
buffer	0.005 M NH_4Cl
temperature	~80-85°C
pH	1.4-1.8

Thin yellow films were grown in about 20 minutes which had poor adherence to glass but fairly good adherence to SnO_2. The deposition progressed as expected at the bath volume specified, but there was no indication that the reaction had even started after 60 minutes when the bath volume was scaled up in order to accommodate more substrates.

EDS analysis indicated the presence of indium and sulfur, but XRD analysis of the film on SnO_2 was not conclusive, since the film was so thin in comparison to the SnO_2. Optical measurements revealed an estimated bandgap in the range of 2.3-2.5 for the film on SnO_2. A $CuInSe_2/In_2S_3/ZnO$ device was processed using

evaporated $CuInSe_2$ (32310.22), yielding V_{oc} = 0.22 V, J_{sc} = 9.1 mA/cm^2, FF = 34%, and EFF = 0.7 %.

ZnO Deposition

ZnO:Al films have been deposited by rf magnetron sputtering from a pressed ZnO/Al_2O_3(2%) target with different compositions of the O_2/Ar sputtering atmosphere and electrical and optical properties have been characterized. Results from Boeing (8) and the University of Stuttgart (9) have indicated an increase in V_{oc} of $Cu(InGa)Se_2/CdS$ cells by optimizing the properties of a thin high resistivity ZnO layer deposited between the CBD CdS and the low resistivity ZnO. The resistivity can be increased with a single ZnO target by increasing the O_2 in the sputter atmosphere, thereby reducing the number of oxygen vacancies in the film. Films were deposited with 0.1-2.0% O_2 in the sputter gas and the results are listed in Table 12. The resistivity increased from $1x10^{-3}$ to 40 Ω-cm as shown in Figure 29. An increase in the O_2 in the sputtering atmosphere also decreases the optical absorption of the ZnO:Al. The normalized transmission is shown in Figure 30 for the three most conductive ZnO films in Figure 29, deposited with 0.1-0.3% O_2. The ZnO films have increasing losses for wavelengths above ~1000nm due to free carrier absorption. The transmission is also shown for a sputtered ITO film with comparable sheet resistance, ~20Ω/□ and slightly better than the ZnO films.

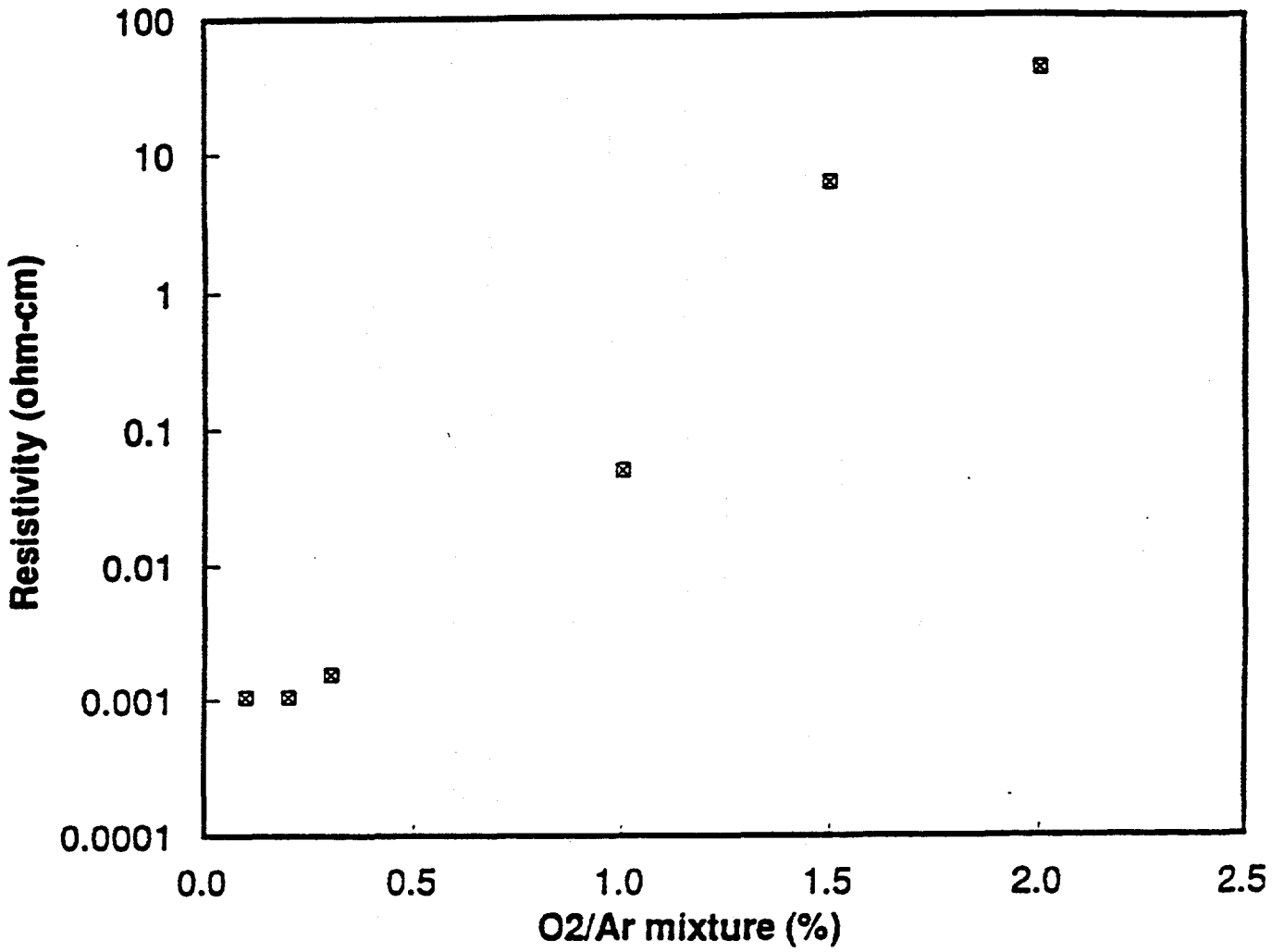

Figure 29. Resistivity increase of ZnO:Al films with increasing oxygen partial pressure in the sputter atmosphere.

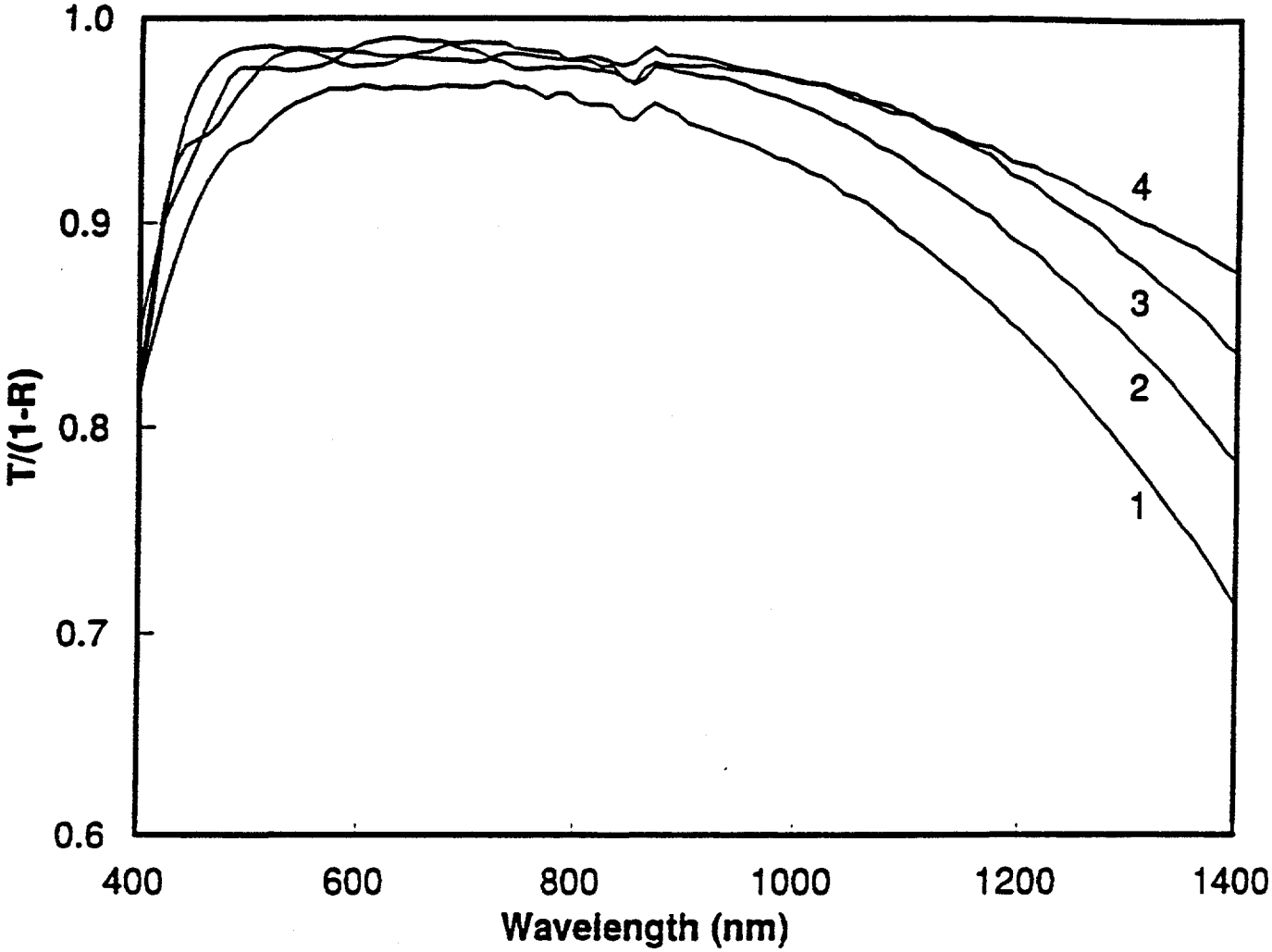

Figure 30. Normalized transmission of three 500nm thick ZnO:Al films deposited with different oxygen partial pressures: 1) 0.1%, 2) 0.2%, and 3) 0.3%, and 4) a 200nm thick ITO film.

Table 12. Resistivity of ZnO:Al films deposited with increasing O_2 partial pressure in the sputter atmosphere and an rf magnetron sputtered ITO film for comparison.

	run #	O_2/Ar (%)	d (nm)	R_s (Ω/□)	Resistivity (Ω-cm)
ZnO:Al	91468 A	0.1	500	20	1.0E-03
ZnO:Al	91470 B	0.2	500	21	1.1E-03
ZnO:Al	91471 B	0.3	500	31	1.5E-03
ZnO:Al	91468 B	1.0	100	5E+03	3E-01
ZnO:Al	91470 A	1.5	100	6E+05	6E+00
ZnO:Al	91471 A	2.0	100	4E+06	4E+01
ITO	91449	-	200	21	4.2E-04

Based on these results and the device results in references 1 and 2, bi-layer ZnO films are being used in Cu(InGa)Se_2/CdS cells. The first layer, deposited with 2% O_2, has a thickness of ~100nm and $R_s \approx 10^6 \Omega/\square$. The second layer is deposited with 0.2% O_2 with thickness ~500nm and $R_s \approx 15 \Omega/\square$. The stability of the bi-layer film was evaluated by heat treating a monitor film deposited on glass at 200°C for 1 hour and R_s increased to only 25Ω/□ with no increase in absorption.

2.3 CdTe FILMS AND DEVICES

The relation between the microstructure and composition of CdTe/CdS thin films and the processing used to fabricate high efficiency devices has been investigated further. Material characterization of structures with ~0.5 μm CdS and 2-3 μm CdTe was used to construct an operational model of the device which defines the issues related to devices with thinner CdS and lends to refinements in the fabrication process and higher efficiency. Key components of the processing are CdS thickness, CdTe and CdS crystallinity, CdS-CdTe interdiffusion and doping in the CdTe layer.

In this report we show that devices with a diffused CdS-CdTe interface using evaporated layers have good junction properties, with V_{oc} over 800 mV and FF over 70%. Thick (>2000Å) CdS layers have good crystallinity which yields a low density of grain boundaries in the as-deposited CdTe layer. This layer deposits heteroepitaxially on the CdS so that the crystallinity of the CdS film influences that of the CdTe film and defines the initial condition of the structure. Treatment of the entire structure with $CdCl_2$ increases the CdTe grain size, thus reduces the grain boundary density. Diffusion doping with Cu from the back of the structure completes the device. Treatments of CdS prior to CdTe deposition are used to further improve the overall crystallinity in the structure. Interdiffusion is controlled by this pre-treatment of CdS and by further refinements in the CdTe treatment. These process refinements have resulted in devices with efficiencies over 12% using CdS less than 1500Å thick.

An alternative process in which CdTe films were heat treated in chlorine gas was investigated. Heat treatments in Cl_2/Ar at ~ 400°C promoted uniform grain growth by formation of $CdCl_2$ on the CdTe surface, as expected from the equilibrium chemistry.

2.3.1. Fabrication Process

The process used to fabricate CdTe/CdS solar cells is summarized in Figure 31. This process is analogous to others used to make high efficiency devices with a $CdCl_2$ treatment following the CdTe deposition to improve the physical and electronic properties of the CdTe layer. Thus, the interpretation of the effects of the $CdCl_2$ treatment presented here, on evaporated CdTe layers, can be extended to other CdTe solar cell fabrication processes. Each of the steps shown in Figure 31 is discussed below.

Transparent Conductive Oxide

Tin oxide films deposited by Solarex Corporation onto Corning 7059 glass were used as the superstrate for this work. The SnO_2 films are ~1 μm thick, have a sheet resistance of ~17 Ω/□ and are textured.

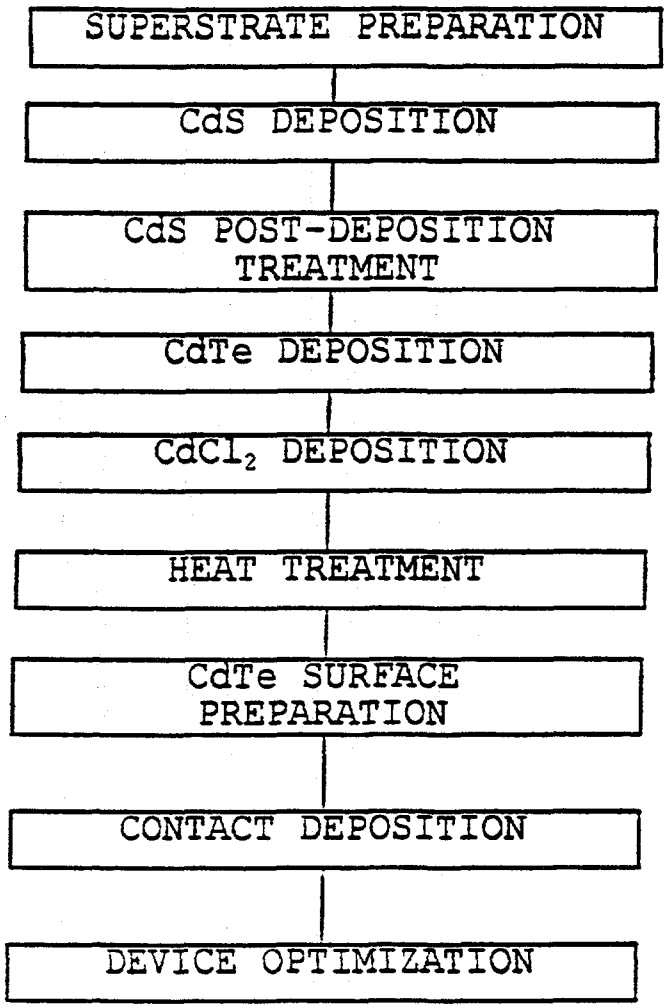

Figure 31. CdTe/CdS superstrate thin film solar cell process.

When planar superstrates were necessary for characterization indium-tin oxide (ITO) coated superstrates were used.

The optical transmission, normalized for front surface reflection, of representative 7059, 7059/SnO_2 and 7059/ITO samples used in the work are shown in Figure 32. The tin oxide layer is textured, which reduces the measured external transmission due to scattering and light trapping. In devices, however, a CdTe layer on textured CdS/SnO_2 utilizes more light as a result of these processes, yielding higher light generated current (10).

CdS Deposition

Undoped cadmium sulfide films were deposited by physical vapor deposition (PVD) and by chemical bath deposition (CBD). For PVD, high purity General Electric CdS powder was evaporated from a boron nitride effusion source at ~800°C. The substrate temperature was maintained at 130°C during the deposition, yielding a growth rate of 200 Å/min.

CdS thickness ranging from 1000 Å to 5000 Å were used for investigation of CdTe/CdS microstructural properties before and after various $CdCl_2$ treatments. For high efficiency devices, however, parasitic light absorption in the CdS layer limits the light generated current. Maximizing the light generated current in CdTe means minimizing this loss in the CdS layer and is achieved by reducing the CdS thickness. The maximum J_{sc} obtainable for devices with different CdS layer thicknesses, assuming no front surface reflection loss, is summarized in Table 13.

Table 13. Maximum J_{sc} values in CdTe/CdS obtainable for different CdS thicknesses assuming no reflection loss, 5% collection loss, and AM 1.5 global spectral illumination.

CdS Thk (Å)	J_{sc} (mA/cm^2)
5000	19.0
1500	20.5
800	22.5
0	25.8

Reducing the thickness of the CdS layer is complicated by discontinuities in the CdS (such as pinholes and out-diffused zones in finished devices) which result in $CdTe_{1-x}S_x$/TCO junctions and lower V_{oc}. Tellurium diffusion into the CdS is more pronounced with thinner CdS because of its poorer crystallinity. This produces a lower bandgap $CdS_{1-y}Te_y$ layer

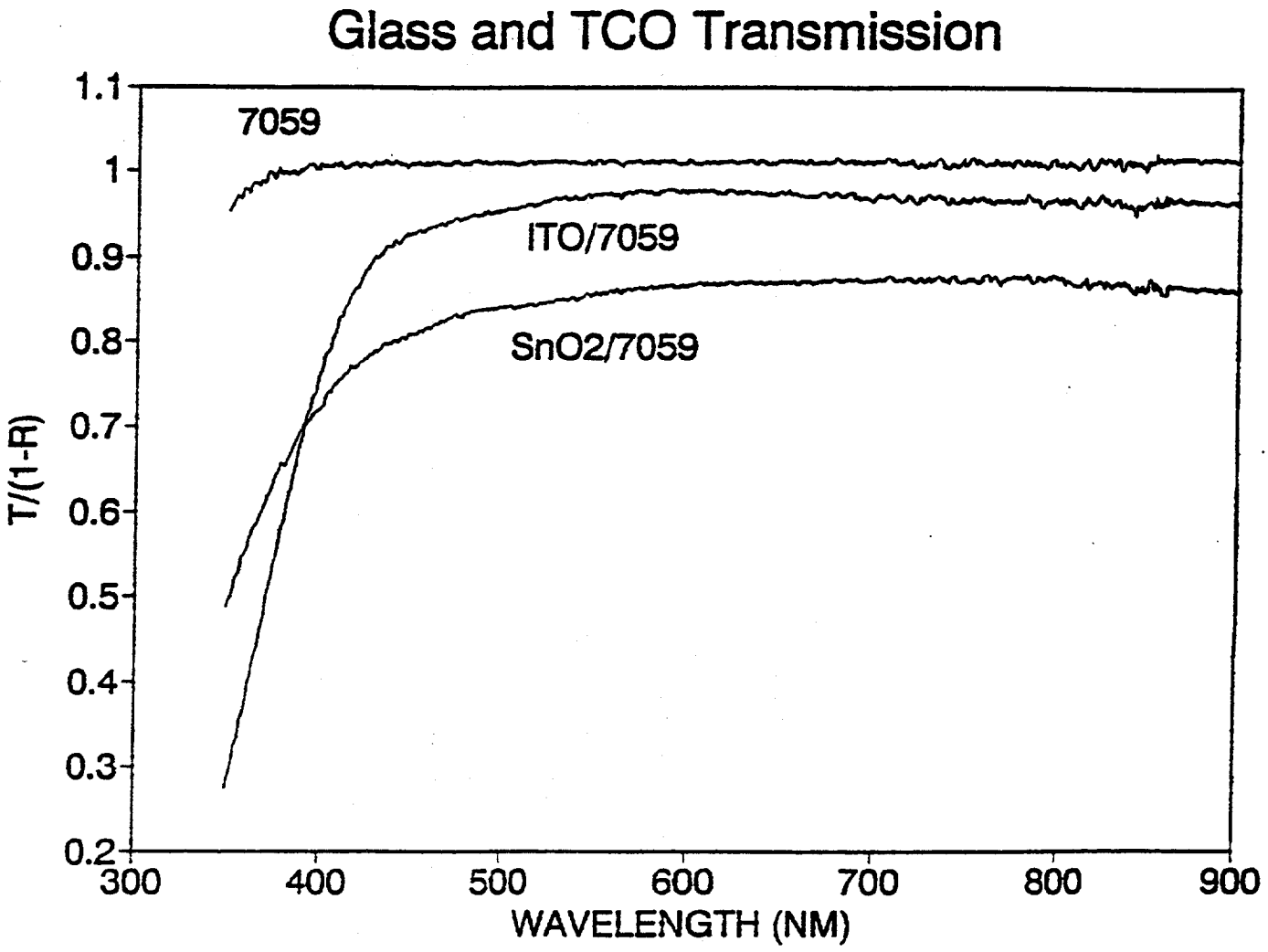

Figure 32. Optical transmission, normalized for front surface reflection, of 7059, 7059/SnO_2, and 7059/ITO.

having lower optical transmission, which results in lower J_{sc}. In previous work (10,11) we showed how the spectral response of CdTe/CdS devices is sensitive to the interdiffusion of the CdTe and the CdS.

The spectral response is shown in Figure 33A for devices with the different CdS thicknesses of Table 13. These are shown for ~5 collection loss and no reflection loss. The regions between each curve show the current density lost by window layer absorption, obtained by integration of the curves with the AM1.5 global spectrum. For the thinner CdS cases, additional current can be lost by poor response from 500 to 600 nm due to Te diffusion and formation of a $CdS_{1-y}Te_y$ layer as shown in Fig. 33b. The difficulty in controlling these effects during post-CdTe deposition processing is the driving force behind the microstructural analysis of this system and for investigation into techniques for "stabilizing" the CdS layer prior to CdTe deposition. CdS treatments are considered in Section 2.3.3.

CdTe Deposition

Undoped cadmium telluride films were deposited by PVD from an effusion source at 750°C using 100 mesh (120 μm particle size) CdTe powder made by grinding 99.999% pure CdTe ingots from Alfa/Johnson Matthey. The substrate temperature was 250°C, the growth rate was 250 Å/min, and the base pressure in the bell jar prior to evaporation was 1×10^{-5} torr. For microstructural analyses the CdTe thickness was varied from 0.5 μm to 4 μm, but for devices a thickness of 2.5 μm was employed.

Post-Deposition Processing

After CdTe film deposition the structures must be treated chemically and thermally to improve their properties for high performance devices. A $CdCl_2$ treatment in air increases grain size in both layers and promotes reaction of CdTe with oxygen. After contacting, a second heat treatment is used to diffusion-dope the CdTe with Cu (12). The steps taken for a device with 2000 Å thick CdS are summarized below. Investigations with thinner CdS led to variations in some of the steps but, not to the overall procedure.

$CdCl_2$ Deposition

1. Coat w/ 1% (wt) $CdCl_2$:CH_3OH @ 5 drops per sq in.
2. Dry @ 80-90°C.
3. Inspect for uniformity.

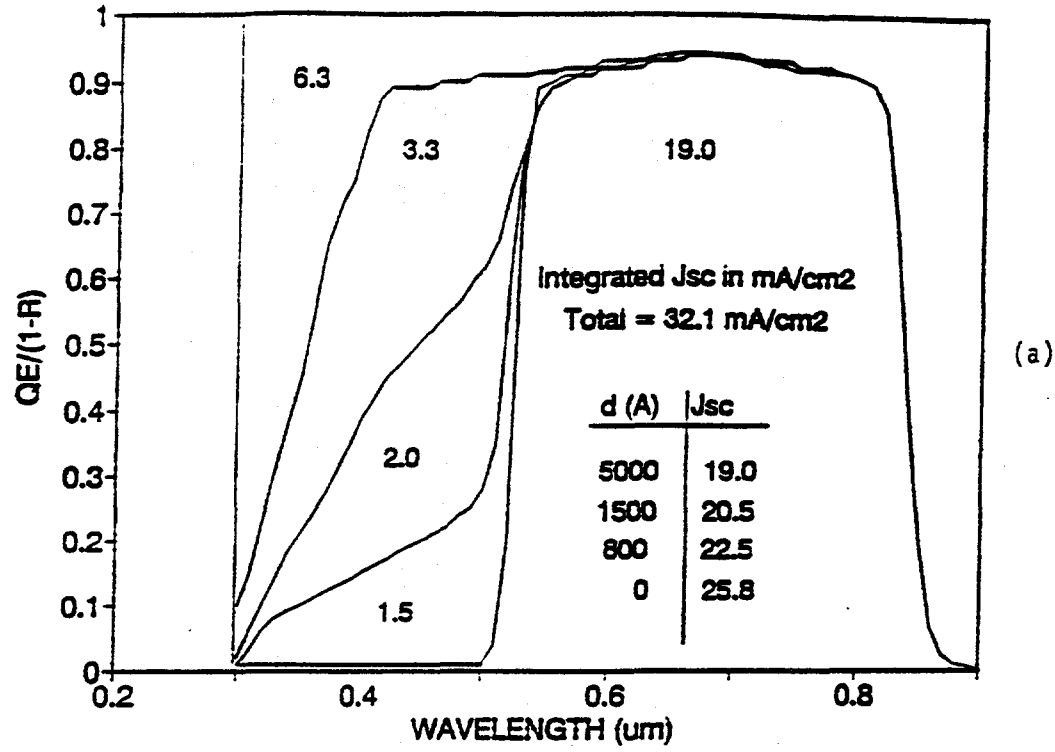

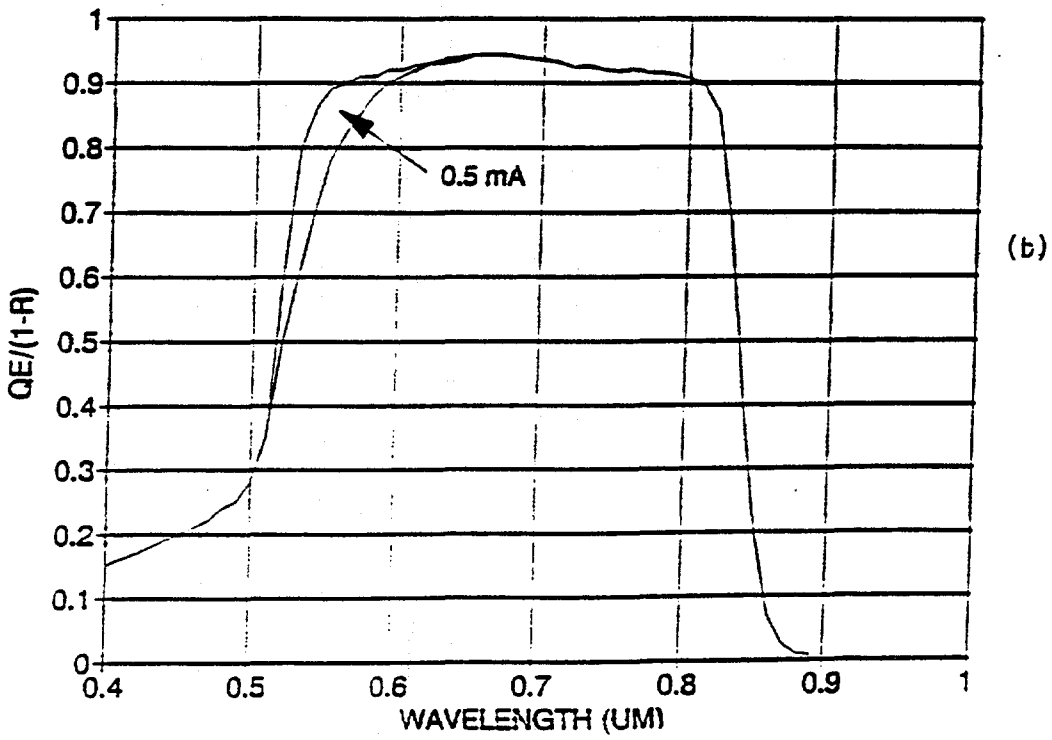

Figure 33. Spectral response of CdTe/CdS for different CdS conditions: a) different CdS thickness and b) with ~1200Å thick CdS and Te diffusion into CdS layer.

Heat Treatment

1. Purge sample in Ar/O_2 for 30 min.
2. Transfer to hot zone: 410°C, 30 min.
3. Transfer to cool zone, remove after 30 sec.

CdTe Surface Preparation

1. Rinse in DI-H_2O for 30 sec.
2. Rinse in CH_3OH for 10 sec.
3. Dry on hot plate @ 100°C.

Contact Deposition

1. Dry in box oven @ 100°C for 15-30 min.
2. Load "warm" into evaporator.
3. Perform N_2 pump/purge.
4. Flash evaporate Ti.
5. Deposit Cu/Au layers.

Device Optimization

1. Heat in Ar @ 160°C for 30 min increments.
2. Immerse in 0.01% Br_2:CH_3OH for 5 sec.

2.3.2. Characterization of $CdCl_2$ Processing

Although treatment of CdTe/CdS with $CdCl_2$ is now widely performed as part of device fabrication processes, the effects of such treatment on the microstructure and composition are not understood. We have sought to characterize the CdTe/CdS microstructure as it is changed by the heat treatment with $CdCl_2$. In addition, we have begun to characterize the dynamics of the changes. In this section we present the results of materials analyses of CdTe/CdS film surfaces and cross-sections. These include an assessment of the relative rates of changes within the structure along with determinations of diffusion constants. Finally, we present alternative methods for achieving the desired structure that are amenable to low-cost large area manufacture.

$CdCl_2$ Deposition

To obtain a uniform action of $CdCl_2$ on the CdTe/CdS structure during heat treatment at atmospheric pressure in Ar, it is necessary to provide a uniform coating of $CdCl_2$. The $CdCl_2$ deposition occurs by precipitation from a saturated solution of $CdCl_2$ in methanol that is thinly applied over the entire CdTe surface. As the methanol evaporates, the solution becomes super-saturated and precipitation commences. The procedure is sensitive to ambient temperature, humidity, and turbulence in the air flow above the $CdCl_2$ solution.

Temperature determines the rate at which the methanol evaporates and thus affects the type and size of precipitates obtained. Excessive temperature (>100°C) causes rapid evaporation, especially at the edges and corners, and produces a non-uniform precipitate as shown in Figure 34. The sample is coated with a uniform, but thin, base layer of $CdCl_2$ and a non-uniform over-coating. The uniform undercoating is visible as minute particulates in the 300X micrograph. A lower temperature reduces the methanol evaporation rate and produces uniform coatings. Too low, however, and the precipitate is dendritic, with many needles protruding from a single nucleation point. As Figure 35 shows, such a sample appears to have a uniform coating to the eye or at low, stereoscopic magnifications, but higher magnification reveals the dendritic nature of the $CdCl_2$ coating.

If the $CdCl_2$-methanol solution is exposed to significant humidity as the methanol dries, then water becomes part of the surfacial liquid and produces clumping of the $CdCl_2$.

A sample coated at 90% relative humidity and dried in air exhibits extensive clumping with regions between clumps that have no $CdCl_2$ at all as seen in Figure 36.

Turbulence in the drying environment causes non-uniform evaporation which results in spatially non-uniform morphology and thickness. Conditions which produce uniform $CdCl_2$ films include use of a covered dish to reduce air flow turbulence, an argon ambient to reduce moisture, and a temperature of ~90°C. If, during device processing, a particular $CdCl_2$ coating is non-uniform, it is rinsed off with methanol. The sample is dried and the coating procedure is repeated. As we have demonstrated previously (13), there is a direct correlation between the thickness of $CdCl_2$ and the J_{sc} which can be obtained for a given CdS thickness. Thus, non-uniformities during the $CdCl_2$ application step will translate into non-uniformities in device performance and will reduce the maximum efficiency that can be achieved over a large area.

Table 14 shows the estimated $CdCl_2$ thicknesses obtained for different quantities of solutions and different solution dilutions, assuming uniform and dense coverage.

Microstructural Characterization

Continuing the analysis cited in the previous Annual Report (14) has led to more detailed measurements of the CdTe/CdS grain structure and composition. This provides an improved understanding of the variables associated with the heat treatment and of the dynamics of the changes in structure and composition with time.

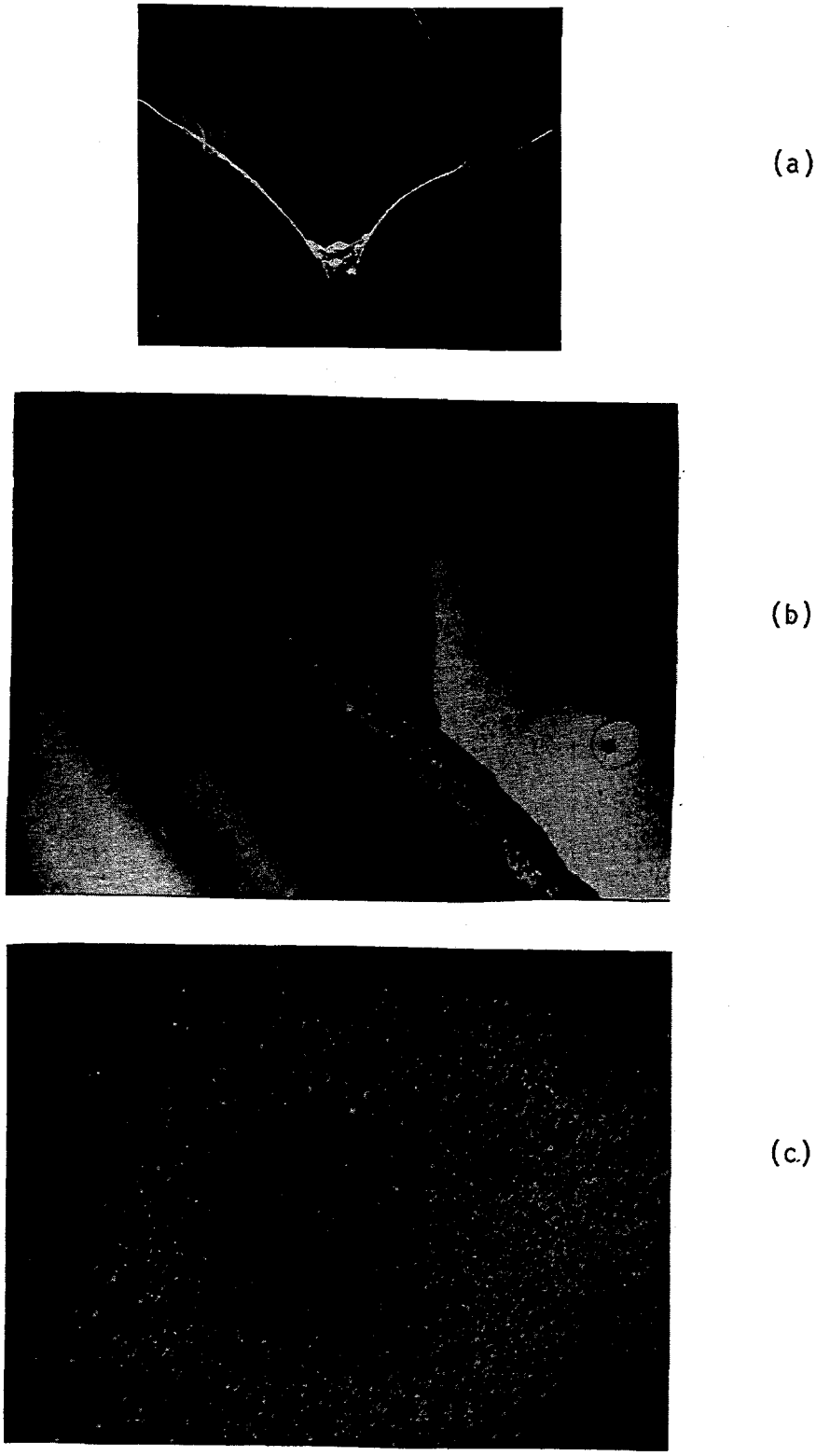

Figure 34. Micrographs of $CdCl_2$-coated CdTe/CdS for a sample dried at 120°C in dry ambient: a) 2X; b) 38X; c)300X.

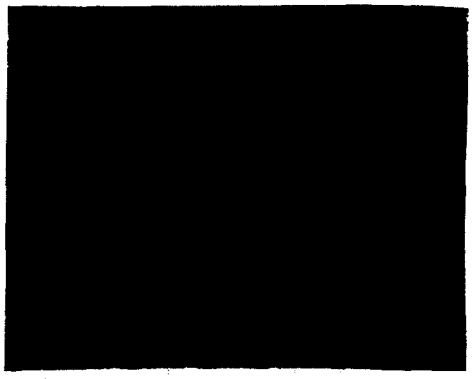

(a)

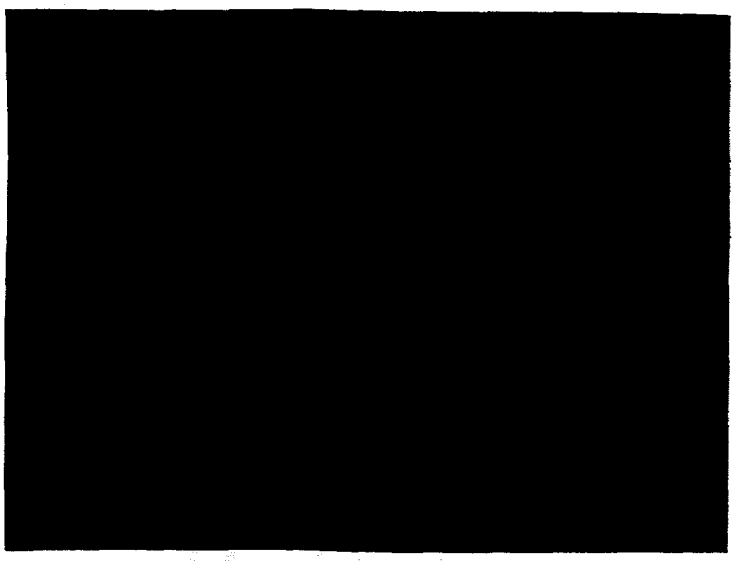

(b)

(c)

Figure 35. Micrographs of $CdCl_2$-coated CdTe/CdS for a sample dried at 80°C in dry ambient: a) 2X; b) 38X; c) 300X.

(a)

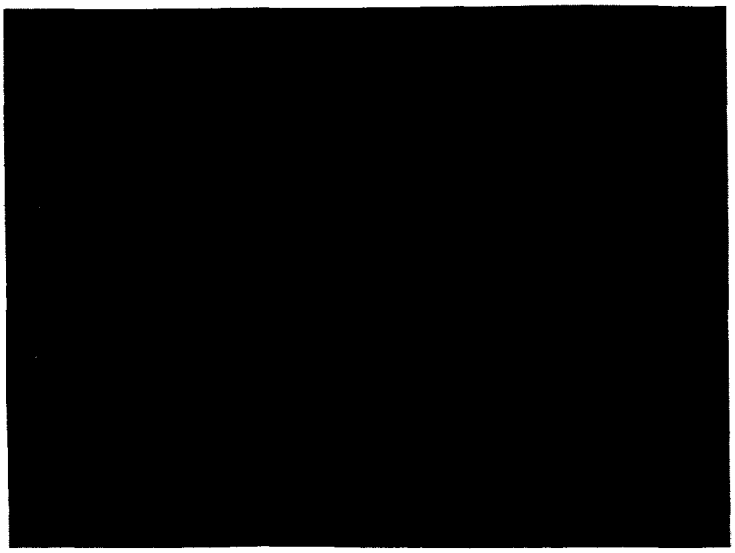

(b)

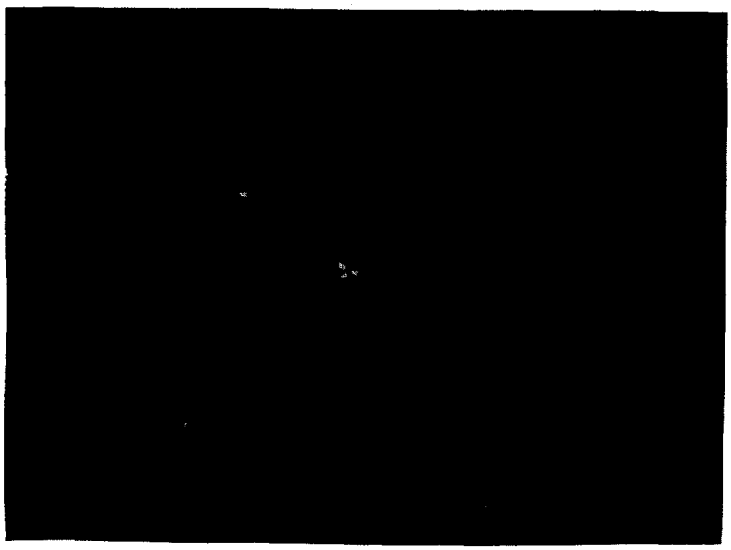

(c)

Figure 36. Micrographs of $CdCl_2$-coated CdTe/CdS for a sample dried at 100°C in humid ambient: a) 2X; b) 38X; c) 300X.

Table 14. Estimated $CdCl_2$ thickness obtained for different quantities of $CdCl_2$:CH_3OH of different strengths.

Solution Strength (wt% $CdCl_2$:CH_3OH)	Quantity (drops/sq in)	$CdCl_2$ Thk (μm)
1	14	2
1	7	1
0.1	14	0.2
0.1	7	0.1
0.01	14	0.02
0.01		0.01

Below we list the measurements that have been made on structures with 0.2-0.5 μm thick CdS and 2.5 μm thick CdTe:

1. OM - Optical Microscopy of surfaces and cross-sections of CdTe/CdS/ITO/glass. Samples on ITO were chosen for planarity.

2. SEM - Scanning Electron Microscopy of surfaces and cross-sections of CdTe/CdS/ITO/glass before and after heat treatment.

3. STM - Scanning Tunneling Microscopy of surfaces before and after heat treatment, performed at NREL by F. Abou-Elfotouh.

4. TEM - Transmission Electron Microscopy of CdTe/CdS/ITO/Si cross-sections before and after heat treatment, performed at NREL by M. Al-Jassim. Samples were prepared at IEC on polished Si wafers with semi-transparent Cu/Au dot contacts to allow backwall J-V testing. Companion cells on CdTe/CdS/ITO/glass were measured in the same configuration to verify that devices on Si were of comparable performance to the standard devices made on glass.

5. AES - Auger Electron Spectroscopy of CdTe/CdS/ITO/glass (depth profiles), performed at NREL by A. Nelson.

6. SIMS - Secondary Ion Mass Spectroscopy of CdTe/CdS/ITO/glass (depth profiles), performed at NREL by S. Asher.

7. EDS - Energy Dispersive X-ray Spectroscopy of CdTe/CdS/ITO/Si cross-sections, performed at NREL by M. Al-Jassim, on the same pieces as used for TEM.

8. XPS - X-ray Photoemission Spectroscopy of CdTe surface.

9. XRD - X-Ray Diffraction of CdTe/CdS/ITO/glass structures using Cu K_α radiation at 35 kV. The penetration depth for CdTe is ~10 μm, so the entire CdTe/CdS structure (~3 μm thick) is sampled during measurement in the standard two-theta angular range of 10 to 90 degrees. X-ray diffraction peak profiles provide

information on lattice spacing variations, therefore compositional variations. Full widths at half maximum (FWHM) of single peaks provide dimensions of average scattering sites which is related to the lateral grain dimension via Scherrer's Equation.

10. T,R - Optical Transmission and Reflection of CdTe/CdS/ITO/glass structures.

Significant results from this characterization of the effects of the $CdCl_2$ heat treatment are listed below:

1. Prior to heat treatment, CdTe grains are columnar and are heteroepitaxially located on CdS grains. The maximum CdTe lateral grain dimension is 2500 Å and typical dimensions are 1000-2000 Å. After heat treatment with $CdCl_2$ the grains coalesce to micron dimension throughout their thickness. The lattice mismatch between (001) CdS and (111) CdTe is ~12% and is expected to induce stress in the CdTe layer. After heat treatment with $CdCl_2$ the CdTeS grains are full of defects such as twin planes and stacking faults. Thermal sublimation terraces are visible on many grains. After heat treatment the lateral grain dimension in each layer is comparable to the layer thickness, i.e., the aspect ratio of the grains tends toward 1. [OM, SEM, STM, TEM, XRD]

2. Before heat treatment the chemical interface between CdTe and CdS is sharp. No S is detected within the CdTe and no Te is detected within the CdS. After heat treatment there is a distinct, planar interface, but it is between CdTeS and CdSTe. The S content in the CdTeS varies parallel and perpendicular to the CdTeS/CdSTe interface and extends to the CdTe surface. The S content is also higher in regions of defects such as grain boundaries, twin planes, and stacking faults.
[AES, EDS, SIMS, XPS, XRD, T, R]

3. Significant oxygen diffusion into CdTe occurs during heat treatment. [SIMS]

4. Significant chlorine residue remains in the top 1000 Å of the CdTe layer after heat treatment and rinse. [AES, EDS, SIMS, XPS]

Scanning electron micrographs of the surface of CdTe films with 0.5 μm, 1.0 μm, and 2.0 μm thickness before and after 10 and 30 minute treatments are shown in Figure 37. In each case the CdS thickness was 0.5 μm. The initial grain dimension is ~0.25 μm, regardless of the CdTe film thickness, which reflects the size of the underlying CdS grains. After 10 minutes of treatment the average CdTe grain size has reached an aspect ratio of 1 with its thickness. Subsequent treatment, up to 20 additional minutes, results in limited additional growth, particularly among clusters of small grains which seem to coalesce.

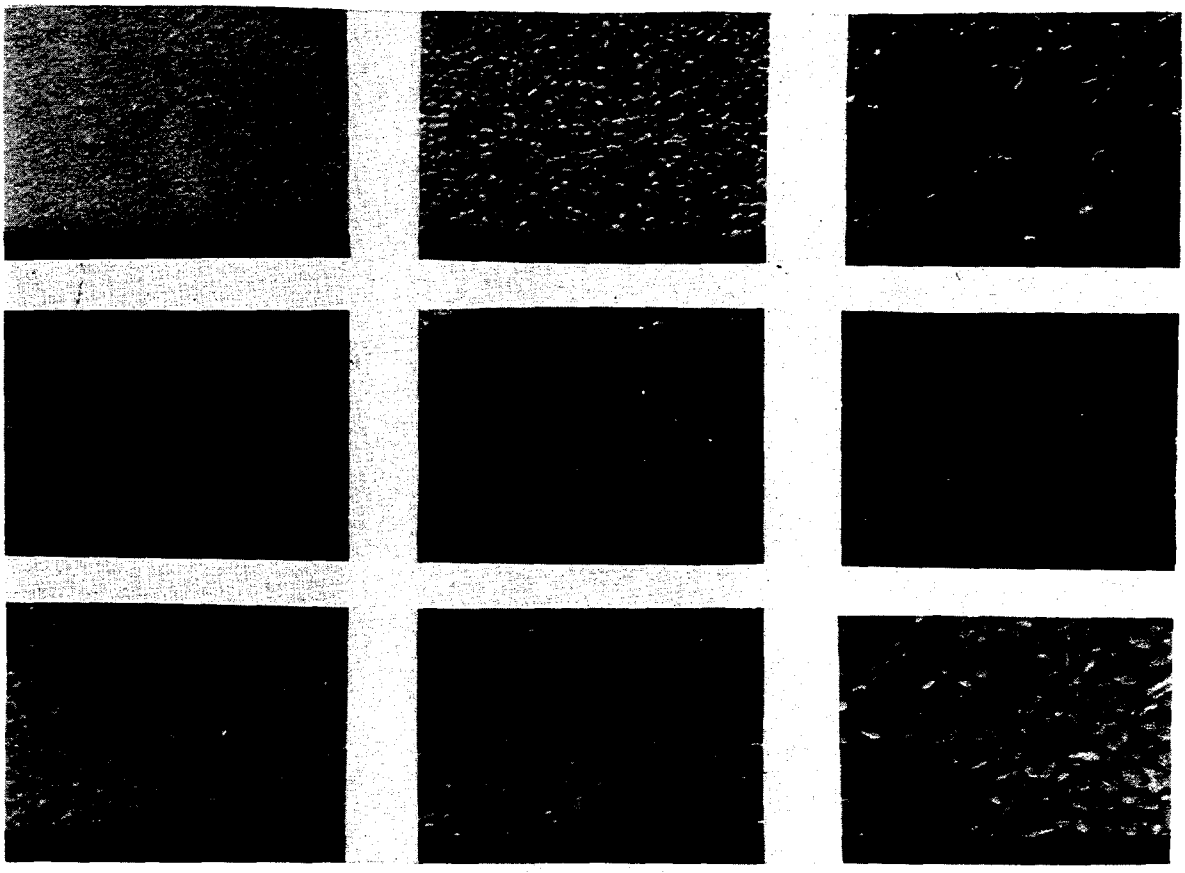

Figure 37. SEM of CdTe surface before treatment (L), after 10 minutes at 410°C (M), and after 30 minutes at 410°C (R). Top: 0.5 μm CdTe; Mid: 1.0 μm CdTe; Bot: 2.0 μm CdTe.

Scanning tunneling micrographs for 4 μm CdTe films before and after 30 minutes of treatment also show the grain growth (Figure 38), independent of the underlying medium. In addition the high magnification views show terraces associated with thermal etching or sublimation from the surface of on some grains.

Transmission electron micrographs of polished cross-sections on Si reveal a great deal of detail. The samples also were used for spot EDS measurements. Figure 39 shows a CdTe/CdS/ITO/Si structure in the as-deposited condition. The heteroepitaxial columnar growth of the CdTe grains on CdS is evident and corroborates XRD patterns which show as-deposited films to consist of CdTe (111) orientation and CdS (001) orientation. Normally, there is a small deviation in the XRD lattice spacing of the CdTe (111) films on CdS compared to the powder standard. This offset is attributed to stress in the CdTe film arising from the CdTe-CdS lattice mismatch. EDS of this sample shows the interface to be chemically sharp.

Heat treatment with $CdCl_2$ at 410°C for 30 minutes changes the grain structure and size in both films as shown in Figure 40. The grain growth visible in the SEM images extends through the depth of the CdTeS film. In each layer of the structure, the CdTeS and the CdSTe, the lateral grain size after heat treatment approaches or exceeds the film thickness with the maximum grain dimension observed to be nearly twice the film thickness.

XRD patterns show randomization of the CdTe film orientation and reduction of the CdTe lattice parameter. Taken with AES, SIMS, EDS, and optical measurements, it is clear that the CdTe and CdS layers have interdiffused during the heat treatment with $CdCl_2$. Spot EDS analysis of this and other samples shows non-uniform distribution of S within the CdTe layer, with the greatest concentrations occurring at grain boundaries and within other crystallographic defects such as twin planes and stacking faults.

Diffusion Profile Model

The challenge for fabrication of high current devices is in quantifying the rates of recrystallization and diffusion and controlling them. Information on time dependent changes is obtained from high resolution XRD scans of films of different thickness heat treated with $CdCl_2$ for different times. An XRD peak of a given orientation centered on a specific angle is interpreted as originating from a region in the film possessing that orientation and associated lattice parameter. The diffractogram does not tell whether this lattice parameter (or set of lattice parameters) arises from a set of grains within the film or from a specific layer. Thus, the diffraction pattern is used in conjunction with the other materials data to construct a model of the film as it changes during heat treatments.

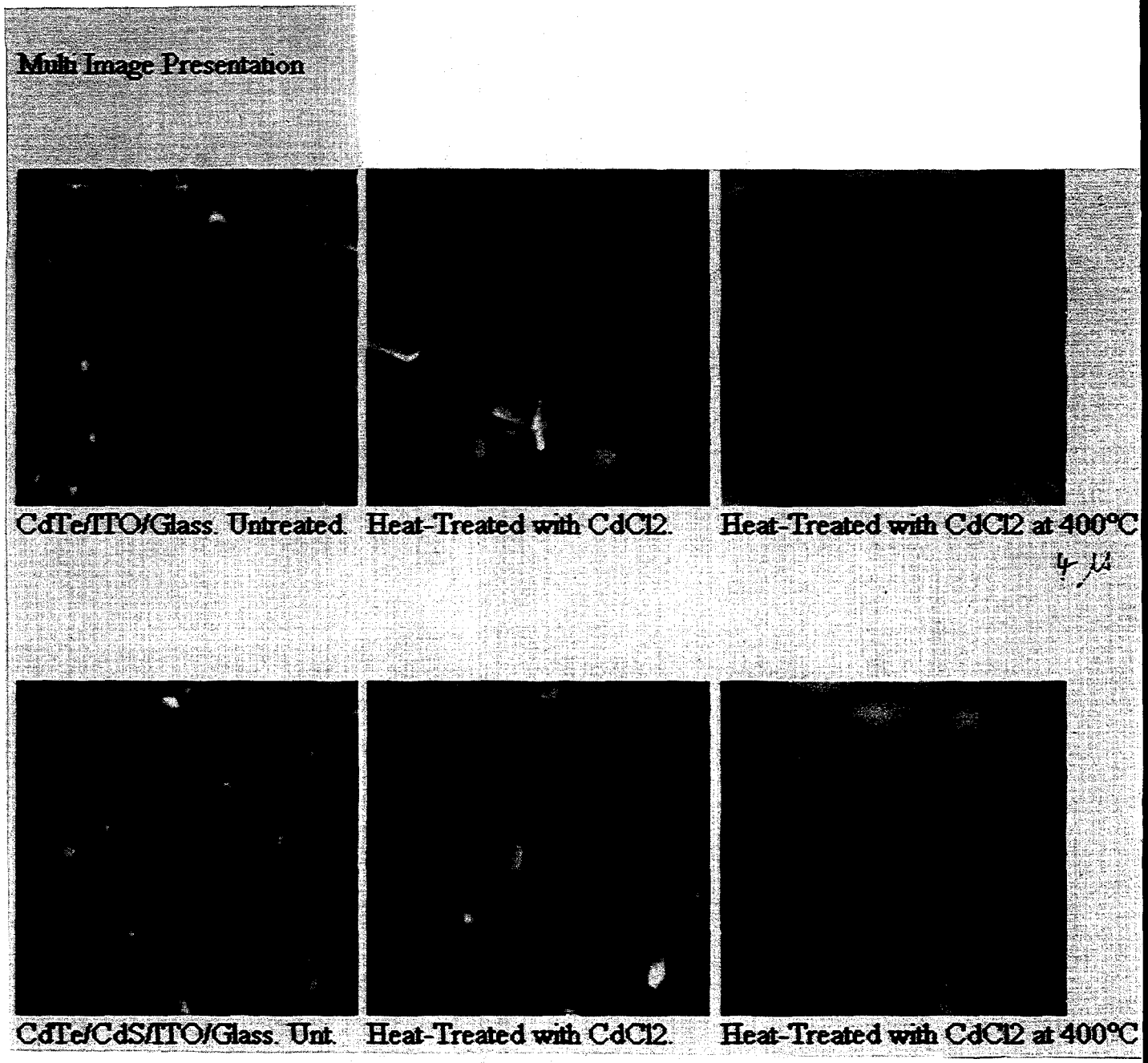

Figure 38. STM of surface of 4 μm thick CdTe before (L) and after treatment for 30 minutes at 410°C. Top: CdTe on ITO/glass; Bottom: CdTe on CdS/ITO/glass.

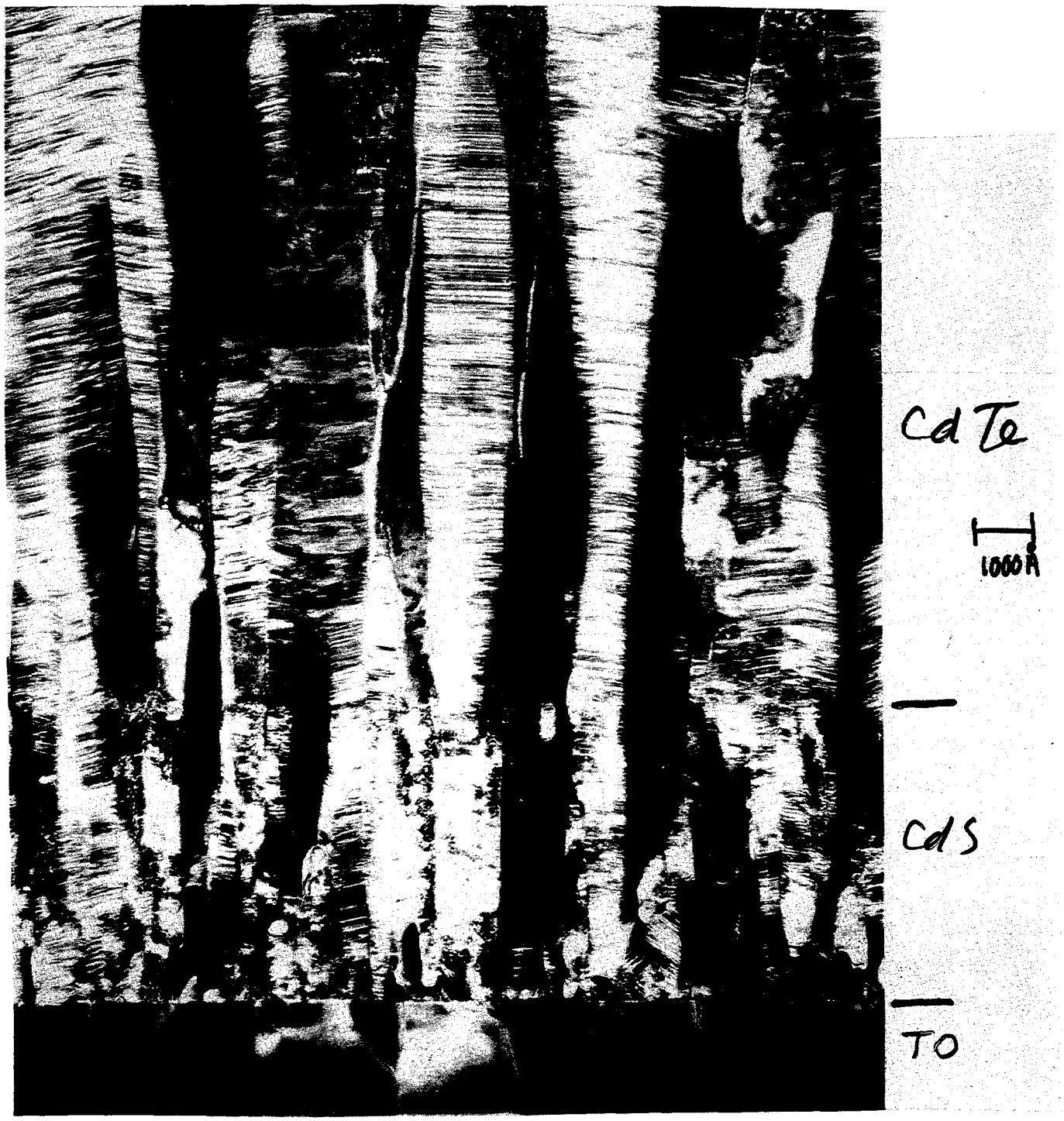

Figure 39. TEM of CdTe/CdS/ITO/Si cross-section before treatment. The CdS thickness is 0.5 μm.

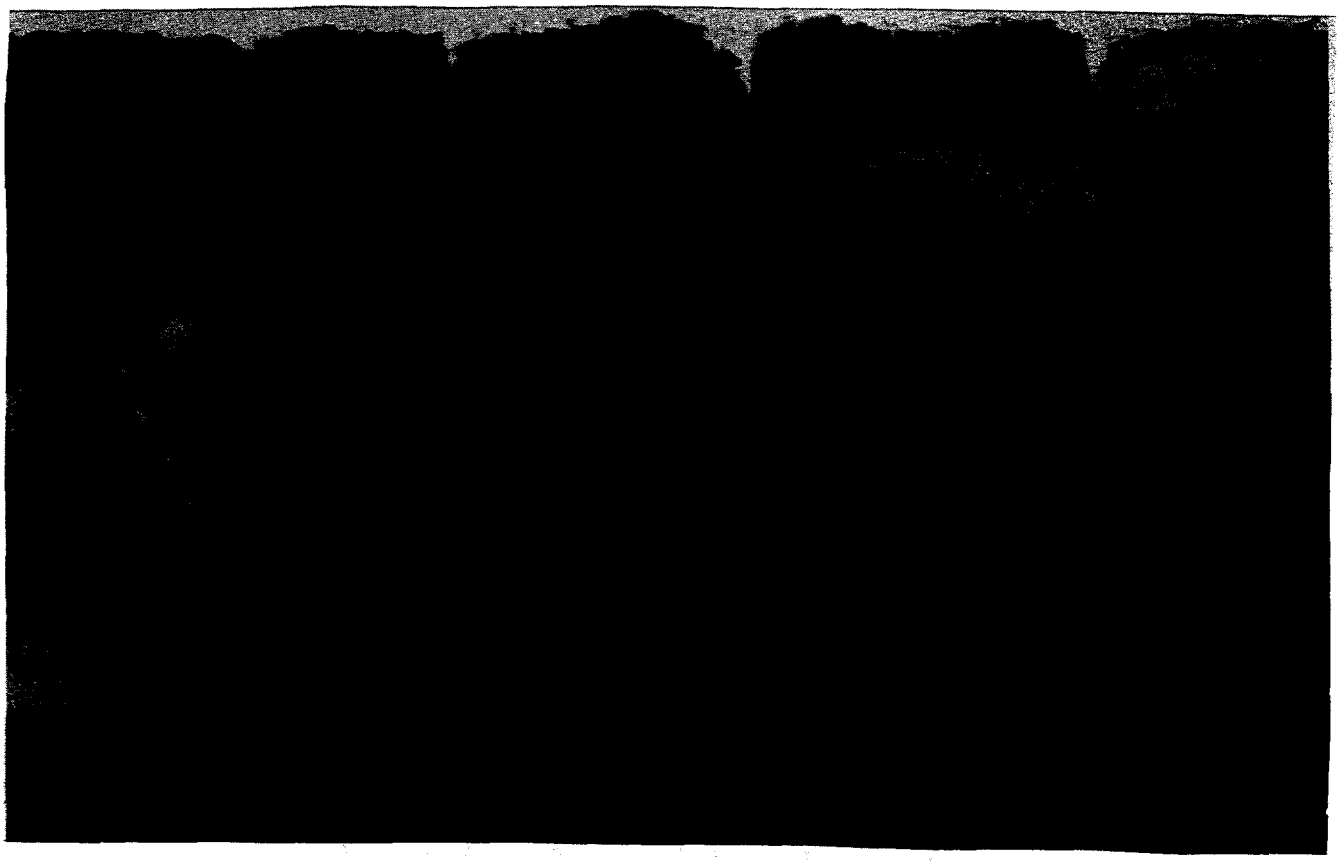

Figure 40. TEM of CdTe/CdS/ITO/Si cross-section after treatment at 410°C for 30 minutes.

As-deposited films are dominated by (111) orientation, reflecting the heteroepitaxial growth with CdS. It is reasonable to conclude that in the as-deposited case most of the grains are therefore (111) oriented with the {111} planes parallel to the superstrate surface. After heat treatment the pattern randomizes and the (111) peak intensity drops. Also, the peaks become strongly asymmetric and split into multiple peaks with additional treatment (Figure 41). The diffraction peak profiles obtained for a 2 μm thick CdTe film after treatment are different than obtained for a 1 μm thick film treated for the same time. However, if the thickness of the treated 2 μm film is reduced to 1 μm by etching the same peak profile is obtained as for the treated 1 μm film (Figure 42).

In these scans the high angle (right-most) components of the peak profiles correspond to regions of S-enriched CdTeS, presumably regions around grain boundaries and other crystallographic faults, while the low angle components are CdTeS with less S, corresponding to the crystallites themselves. Since the diffusion profile is the same for a 1 μm film as for the bottom half of a 2 μm film, the compositional profile for S in CdTeS near the interface must be the same for all films over a range of CdTe thickness. Experiments with samples treated progressively, but in smaller time increments, were performed to allow observation of the dynamics of the changes incurred during heat treatment. Some of the observable quantities measured on these samples are listed in Table 15 for incremental treatments from 2 to 20 minutes.

Table 15. Observable quantities in CdTe/CdS structures with progressive heat treatment time with $CdCl_2$ at 410°C. Values are entered below the time at which the observed quantities were measured.

OBSERVED QUANTITY	TIME (min) 0	2	4	6	8	10	12	14	16	18	20
Max. grain Size (μm)	0.2	------->1.0									>2.0
(111) FWHM	0.13	0.10									>0.1
Orientation	(111)	------>Random									>
(512) a/a_o	1.0020				>0.9982						>0.9970
x in $CdTe_{1-x}S_x$	0				>0.018						>0.030
E_g (eV)	1.52				>1.49						>1.47
x in $CdTe_{1-x}S_x$	0				>0.030						>0.055

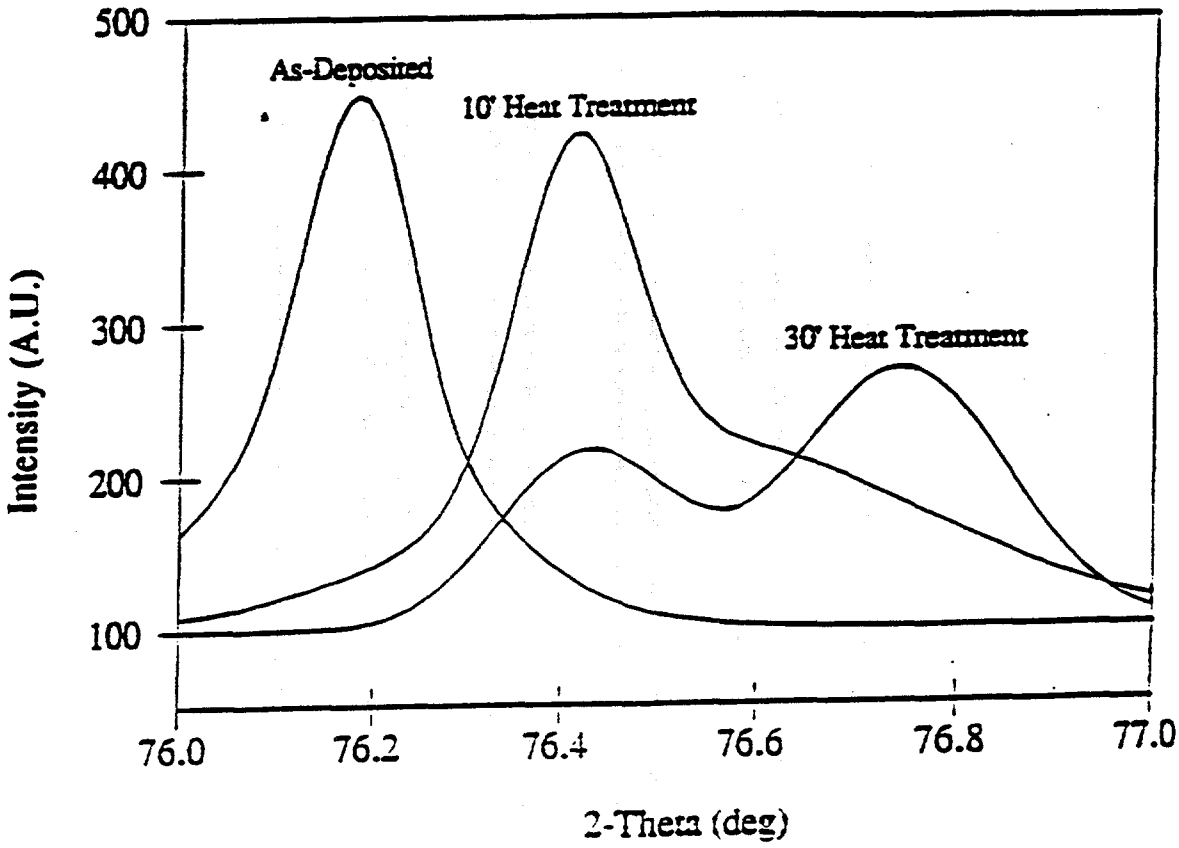

Figure 41. Diffractogram of CdTe (511) for 0.2 μm CdS/1 μm CdTe showing peak asymmetry and splitting associated with progressive heat treatments. Alpha-2 components have been removed for clarity.

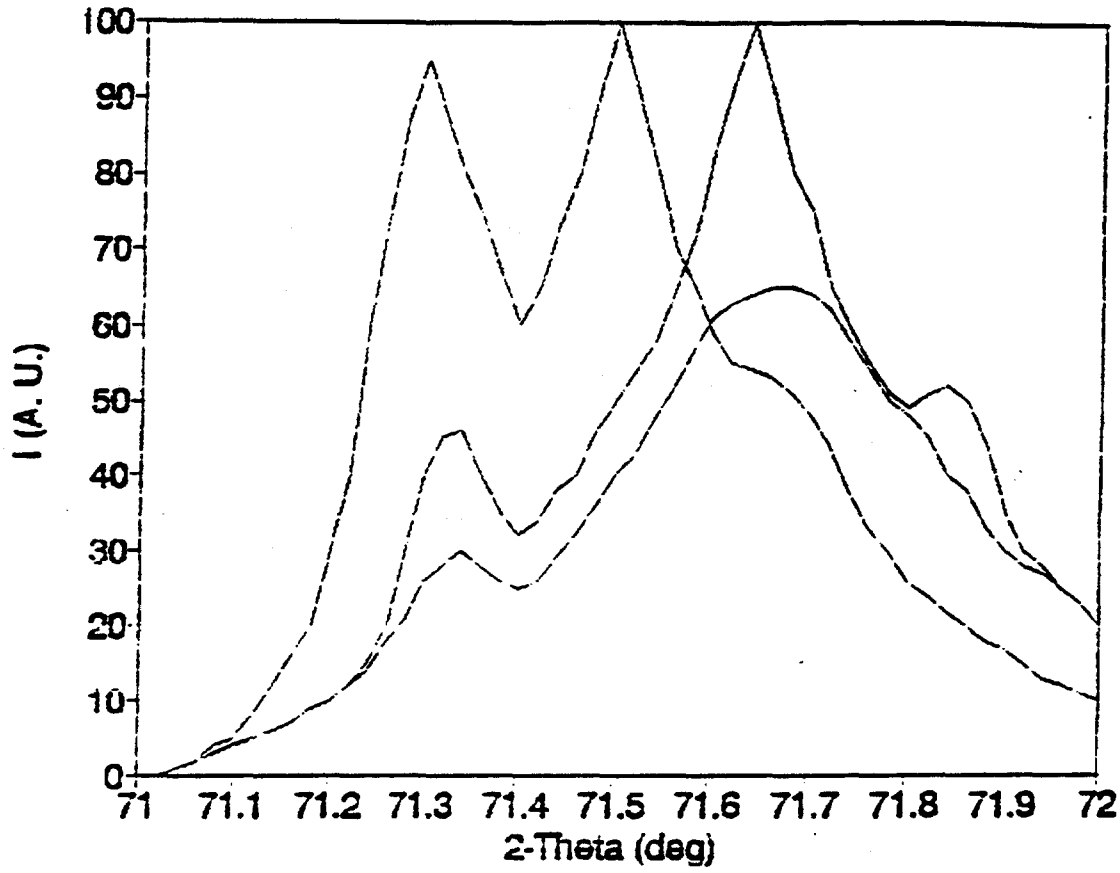

Figure 42. Diffractogram of CdTe (422) comparing treated 0.2 μm CdS/1 μm CdTe with 0.2 μm CdS/2 μm CdTe before and after etching 1 μm away.

This data shows that the recrystallization of the CdTe layer occurs rapidly, within the first 2-5 minutes of heat treatment. Diffusion, on the other hand, appears to proceed slowly but constantly. The diffusion of S into CdTe can be represented as proceeding along grain boundaries and thence into the crystallites. This physical situation is shown in Figure 43. A simple geometrical model based on this situation was used to estimate diffusion coefficients for S along grain boundaries and into CdTe by assuming cylindrical grain structure.

Samples of different CdTe thickness were heat treated for various times to provide data from which diffusion coefficients were estimated. It was found that diffusion of S along grain boundaries was 7 orders of magnitude greater than bulk diffusion of S into CdTe crystallites. This information is useful from a device processing perspective since it indicates one way to control CdS consumption during heat treatment without compromising the required grain growth.

Alternative Treatment Methods

Table 16 lists some thermodynamic data for CdTe, CdS and $CdCl_2$. At the processing temperature of ~410°C, these substances exist as solids in equilibrium with their vapors. In the case of $CdCl_2$, the equilibrium vapor pressure is ~ 20 mtorr at this temperature and solid-vapor phase reactions between CdTe and $CdCl_2$ may be expected. In previous work (14) we showed that a vapor stream of $CdCl_2$ could be used to promote the recrystallization of CdTe layers. This technique was further explored and extended to reactions of CdTe with chlorine gas.

Table 16. Selected thermodynamic properties of CdTe, CdS, and $CdCl_2$. (ΔH_f is the heat of formation, M.P. is the melting point, B.P. is the boiling point, and P is the equilibrium vapor pressure)

Material	ΔH_f (25°C) (kcal/mol)	M.P. (C)	B.P. (C)	P(410°C) (mtorr)
CdTe	-23.8	1041	1091	1
CdS	-38.0	1750	-	0.1
$CdCl_2$	-93.7	568	960	20

The reactor used for the $CdCl_2$ vapor experiments consisted of an evacuated/purged quartz tube in a tube furnace. Within the reactor was an ampoule containing $CdCl_2$ powder, a CdTe film specimen, and quartz wool. Argon flow was established at reduced pressure to produce a sufficient gradient of $CdCl_2$ vapor and a flow of $CdCl_2$ vapor over the specimen. This experimental arrangement is depicted in Figure 44.

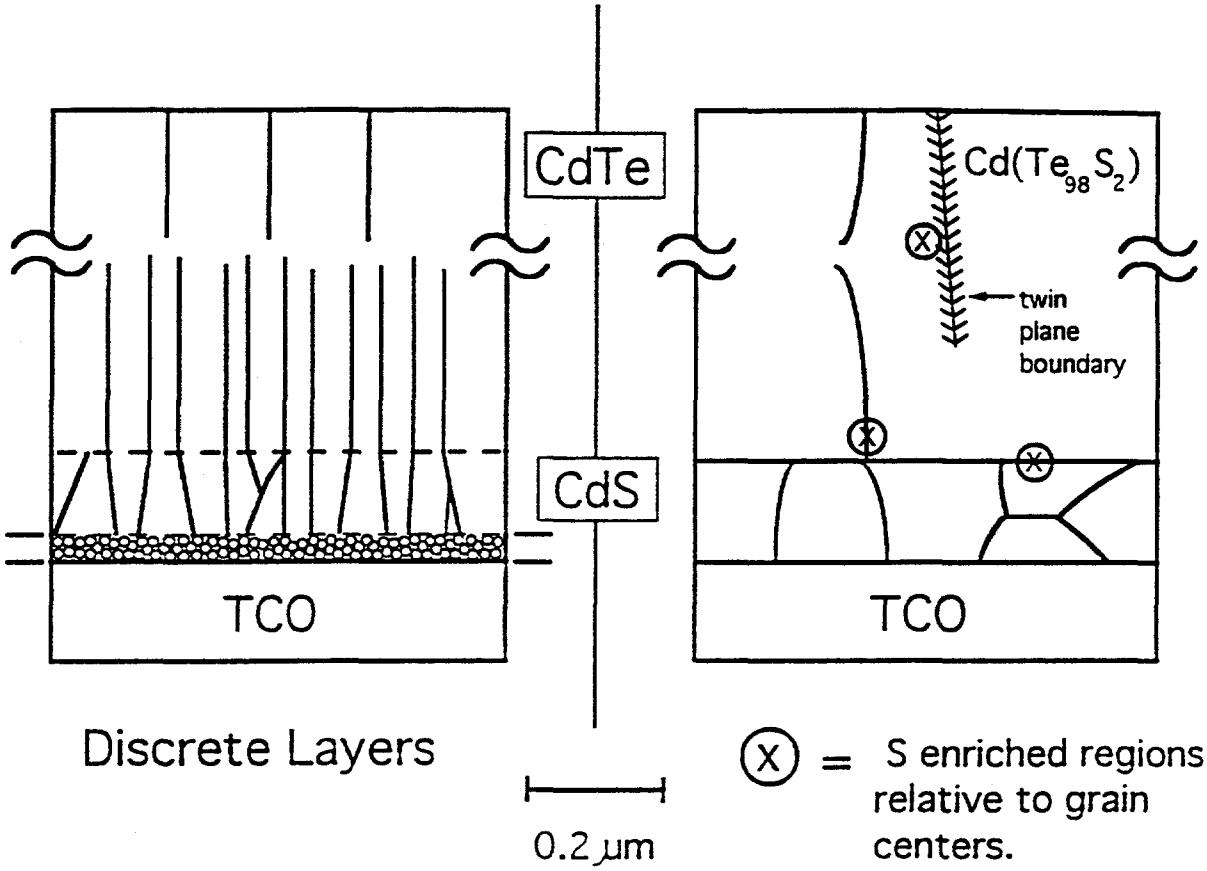

Figure 43. Schematic of the physical situation in CdTe/CdS before and after heat treatment.

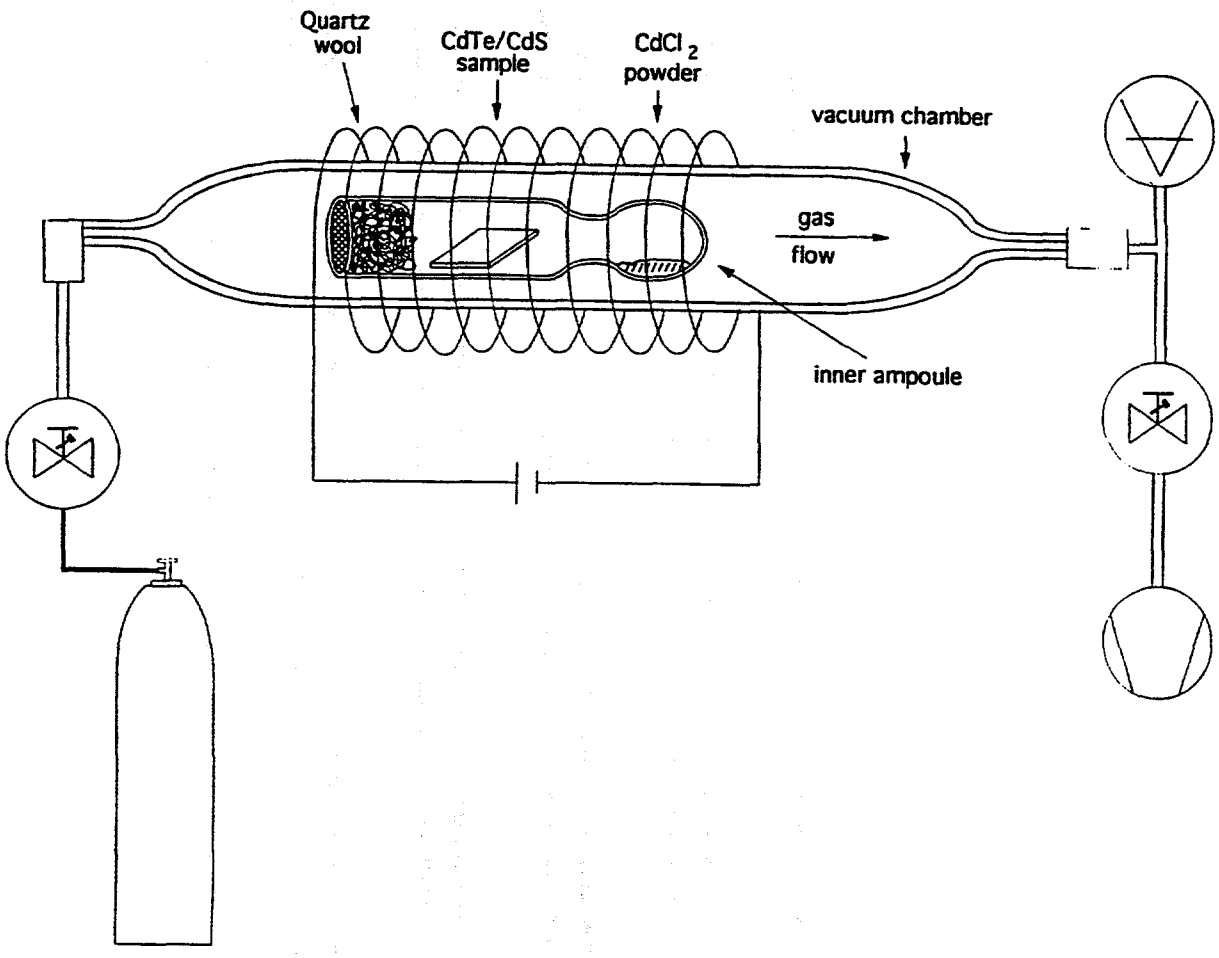

Figure 44. Schematic of system used to perform $CdCl_2$ vapor phase reactions with CdTe/CdS structures.

The procedure for treatments of CdTe/CdS samples in $CdCl_2$ vapor was as follows:

1. Evacuate reactor, set Ar or Ar/O_2 mixture and pressure.
2. Move reactor into hot zone of furnace to initiate reaction.
3. After prescribed time, quench reaction with Ar and remove reactor from hot zone.

The temperature was varied from 410°C to 480°C and the reaction time from 6 to 20 minutes. The CdTe and $CdCl_2$ were at thermal equilibrium and the temperature determined the partial pressure of the $CdCl_2$ vapor, which varied from 20 to 150 mtorr. The total pressure was varied from 0.2 to ~40 torr and consisted of either pure argon or argon/oxygen with 30% oxygen.

The CdTe grains coalesced and the CdTe (111) XRD peak sharpened in all cases. The maximum grain size achieved was 8 μm, on a sample treated at ~480°C. CdTe-CdS interdiffusion was observed, and no residual surface chlorides were detected by EDS measurements.

Devices were fabricated on selected samples and had high yield. Devices with greater than 10% efficiency were obtained for samples treated at 450°C for 6 to 20 minutes at 10-40 torr total pressure with 30% oxygen. At lower total pressures, the efficiencies were less than 9% due to low V_{oc}. At total pressure exceeding 100 torr, no $CdCl_2$ transport was observed and no recrystallization occurred.

This investigation shows that the vapor treatment produces similar effects as the surface $CdCl_2$ treatment generally employed to make high efficiency devices. From a device perspective, the balance between $CdCl_2$ partial pressure and Ar/O_2 total pressure appears to be a significant control parameter.

Recognizing the significance of the halide component of the $CdCl_2$ treatments, an investigation was made into reactions of CdTe with pure chlorine gas. In these experiments, the concentration of reactant was controlled in bath reactions by partial pressure in argon ambient.

The equilibrium reaction for the CdTe-Cl_2 system is:

$$CdTe + Cl_2 \text{ ----> } CdCl_2 + Te.$$

The reactor used for these experiments is depicted in Figure 45. A transparent gold furnace was used to heat the quartz reaction chamber with a heating time of ~10 minutes to 415°C. The base

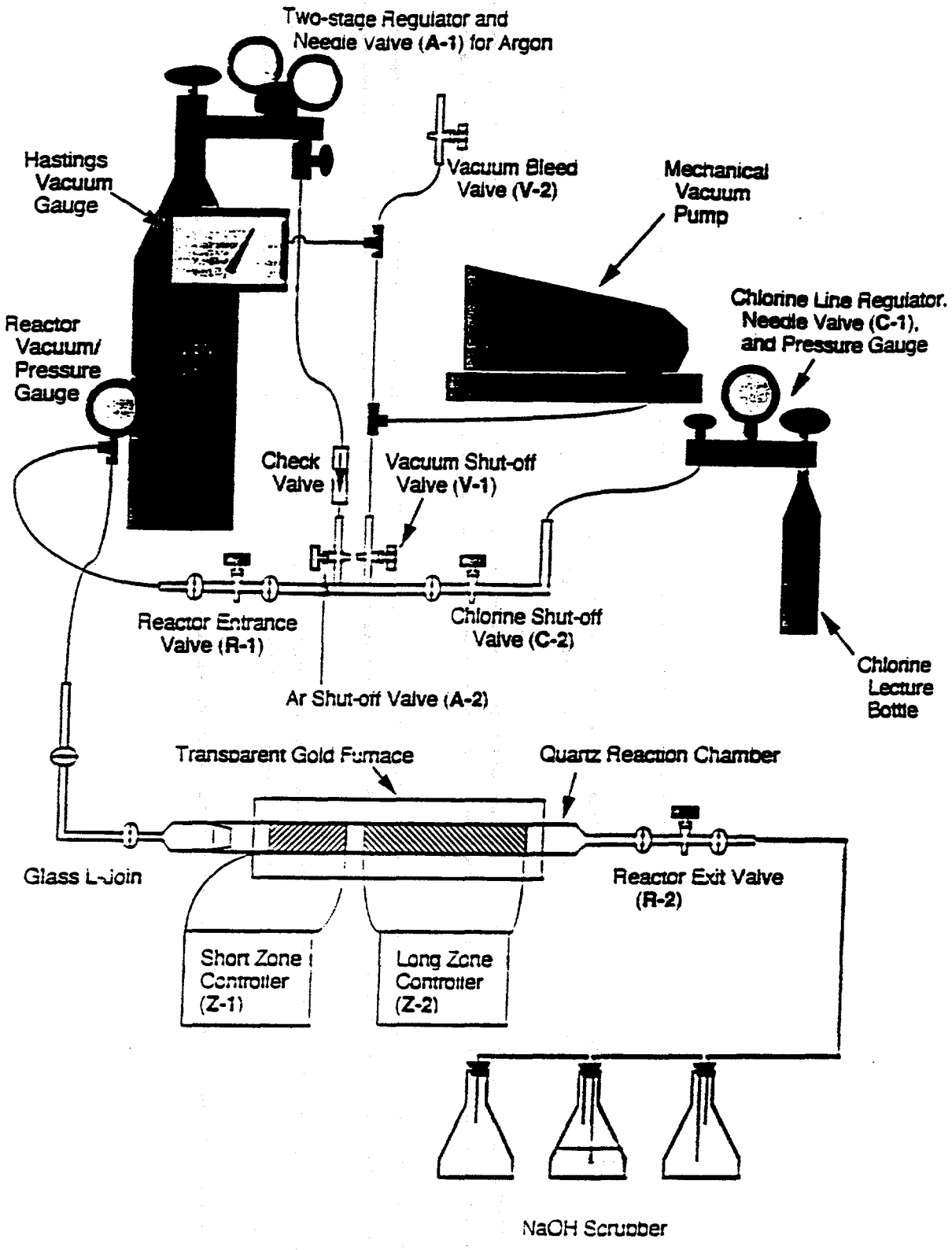

Figure 45. Schematic of system used to perform Cl_2 reactions with CdTe/CdS structures.

pressure was <50 mtorr, the chlorine partial pressure range examined was 50 mtorr to 40 torr, and the reaction time was varied from 10 to 30 minutes.

The procedure for performing a batch reaction was as follows:

1. Evacuate reactor containing specimen.
2. Backfill to desired partial pressure of Cl_2.
3. Backfill with Ar to desired total pressure.
4. Heat reaction chamber to desired temperature.
5. Quench reaction with Ar purge and reduce temperature.

In all cases, XRD and EDS showed that a portion of the CdTe layer converted to $CdCl_2$ and Te. The extent of this reaction depended on Cl_2 concentration and time. At the high Cl_2 partial pressures, the CdTe film completely converted to $CdCl_2$ and Te after 30 minutes; at low Cl_2 partial pressure only a surface layer was produced and the underlying CdTe grains coalesced to micron-size. The $CdCl_2$ layer was rinsed off in deionized water, leaving CdTe and Te. In all cases, strong grain-boundary reaction was observed, so no devices were fabricated on these samples.

Reaction with lower Cl_2 concentrations may bring this process under control. Such experiments were not performed with this system since dilute Cl_2 mixtures are required. These are generally provided as high pressure mixtures with inert gases and exceed the operating capabilities of the system as built.

2.3.3 Process Optimization for Devices

From a device perspective the microstructural characterization of the $CdCl_2$ treatment indicates that treatment time can be used to balance grain growth against diffusion. Also, compositional analyses of $CdCl_2$-treated CdTe films show that the exposed surface of CdTe is rich in chlorine, which may operate as an n-type or compensating dopant in CdTe. This implies that subsequent processing and optimization steps must overcome residual $CdCl_2$ an n-type dopant. This means that the p-type dopants, copper and oxygen, which are part of the fabrication process are even more critical.

Influence of Processing on Devices

Addressing the Cu dopant as a critical process component, the quantity used in the contact was varied. Previously, we found

that a very thin layer (<100Å) produces a non-ohmic contact while a very thick (> 1000 Å) layer produced shorted devices. This general result was also found for galvanically deposited ZnTe contacts containing Cu (15). If the Cu concentration in the deposition bath was too low, poor contact and FF were obtained, while too much produced Cu_xTe preferentially along grain boundaries which shorted devices. As Table 17 shows for devices with 0.2 μm CdS, an improvement in Voc is observed by increasing the Cu film thickness from the usual 100 Å to 200 Å. At 400 Å, the V_{oc} and FF are reduced by shunting.

Table 17. Device results (AM 1.5 at 25°C) for the best cell on 0.2 μm CdS/2.5 μm CdTe with different Cu thicknesses in the Cu/Au contact.

Sample	Cu Thk (A)	V_{oc} (mV)	J_{sc} (mA/cm^2)	FF (%)	Eff (%)
723.11	100	790	20	69	10.9
793.32	200	810	19	73	11.2
793.23	200	830	18	73	10.9
793.22	200	820	19	75	12.0
793.31	400	740	19	60	8.6

For thinner CdS, 0.12 μm, the entire $CdCl_2$ treatment process was reoptimized to determine conditions for best device performance. The $CdCl_2$ quantity, O_2 content in the Ar/O_2 heat treatment atmosphere, and treatment time were varied. Cells were completed with the 200 Å Cu/200Å Au contact. The device results for the best cell on each piece are summarized in Table 18. The best cells were obtained after treatment for 12 minutes at 415°C in an atmosphere containing 50% O_2 and 5 drops/sq in of $CdCl_2$-methanol solution. The sensitivity to the O_2, which is a p-type dopant, requires further study, with emphasis on doping during CdTe film deposition. Note that the piece 802.11 used CdS which was treated with $CdCl_2$ prior to the CdTe deposition which yielded higher J_{sc}. The slightly lower V_{oc} and yield, however, was due to shunts attributed to pinholes in the CdTe layer.

Table 18. Device results (AM 1.5 at 25°C) for the best cell on 0.12 μm CdS/2.5 μm CdTe and different $CdCl_2$ processing conditions.

Sample	$CdCl_2$ (dr/in^2)	Oxy (%)	Time (min)	V_{oc} (mV)	J_{sc} (mA/cm^2)	FF (%)	Eff (%)
801.11	0.7	30	12	677	16	54	6
801.12	**1.4**	30	12	645	12	36	3
801.13	5.0	**30**	12	660	19	60	8
801.32	5.0	**50**	12	796	18	72	10
802.11*	5.0	**50**	12	746	21	64	10
801.31	5.0	**70**	12	715	19	57	8
801.23	**10.0**	30	12	660	19	60	8

*-this sample with $CdCl_2$-treated CdS. The run suffered from pinholes in the CdTe layers.

As stated, one device in Table 18 was processed with pre-treated CdS to limit Te diffusion into the CdS layer. This resulted in higher response in the 500 to 600 nm range and a higher J_{sc}. This experiment was continued using 0.13 μm thick CdS, the optimal O_2 level of 50% shown in Table 18, and the optimal Cu thickness of 200 Å. The CdS used in the devices shown in Table 19 was either not pre-treated, air heat treated at 415°C for 20 minutes, or air heat treated with $CdCl_2$ at 415°C for 20 minutes. The best results were obtained for a piece with CdS treated with 10 drops/sq in of 0.1% $CdCl_2$:CH_3OH, yielding an AM 1.5 efficiency of 12%. The optimal CdS treatment found in this experiment corresponds to that found for 0.24 μm thick CdS in 1991 (10).

Table 19. Device results (AM 1.5 at 25°C) for the best cell on 0.13 CdS/2.5 μm CdTe for different CdS pre-treatments. The $CdCl_2$ treatment is expressed as a percentage of saturated solution (10 $drps/in^2$).

Device	Pre-$CdCl_2$ Treat	(%)	V_{oc} (mV)	J_{sc} (mA/cm^2)	FF (%)	Eff (%)
40803.11	N	0	691	19.2	65	8.6
40803.32-7	Y	0	656	20.6	63	8.5
40803.31-8	Y	1	724	19.7	66	9.4
40803.23-6	Y	5	777	21.0	71	11.6
40803.22-8	Y	10	782	22.4	71	12.4

The current-voltage trace and spectral response of Sample 40803.22-8, which used treated CdS, are shown in Figure 46 and 47 respectively.

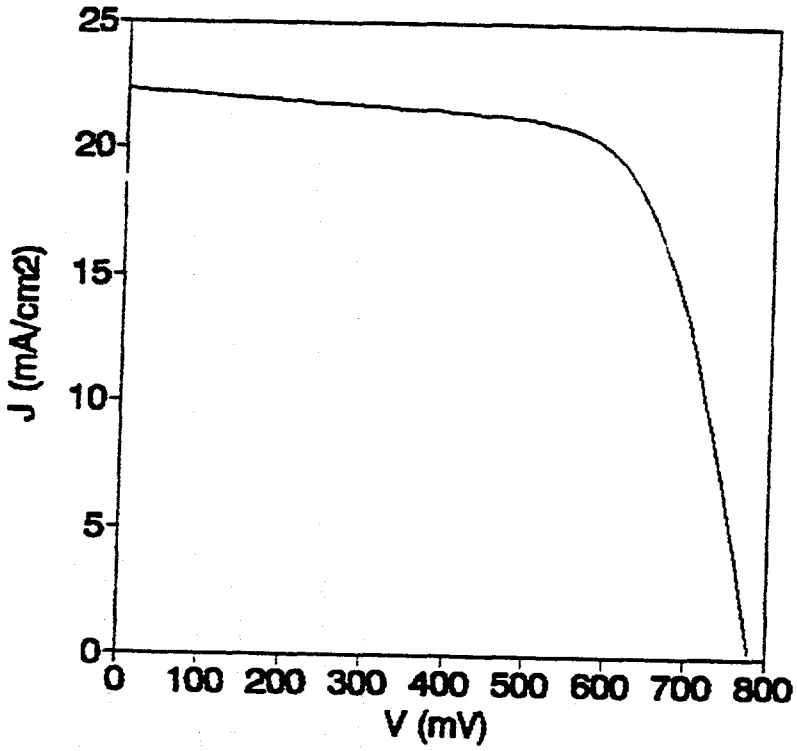

Figure 46. Current-voltage trace of cell 8 on piece 40803.22, having V_{oc}=782 mV; J_{sc}=22.4 mA/cm^2 and FF=71%.

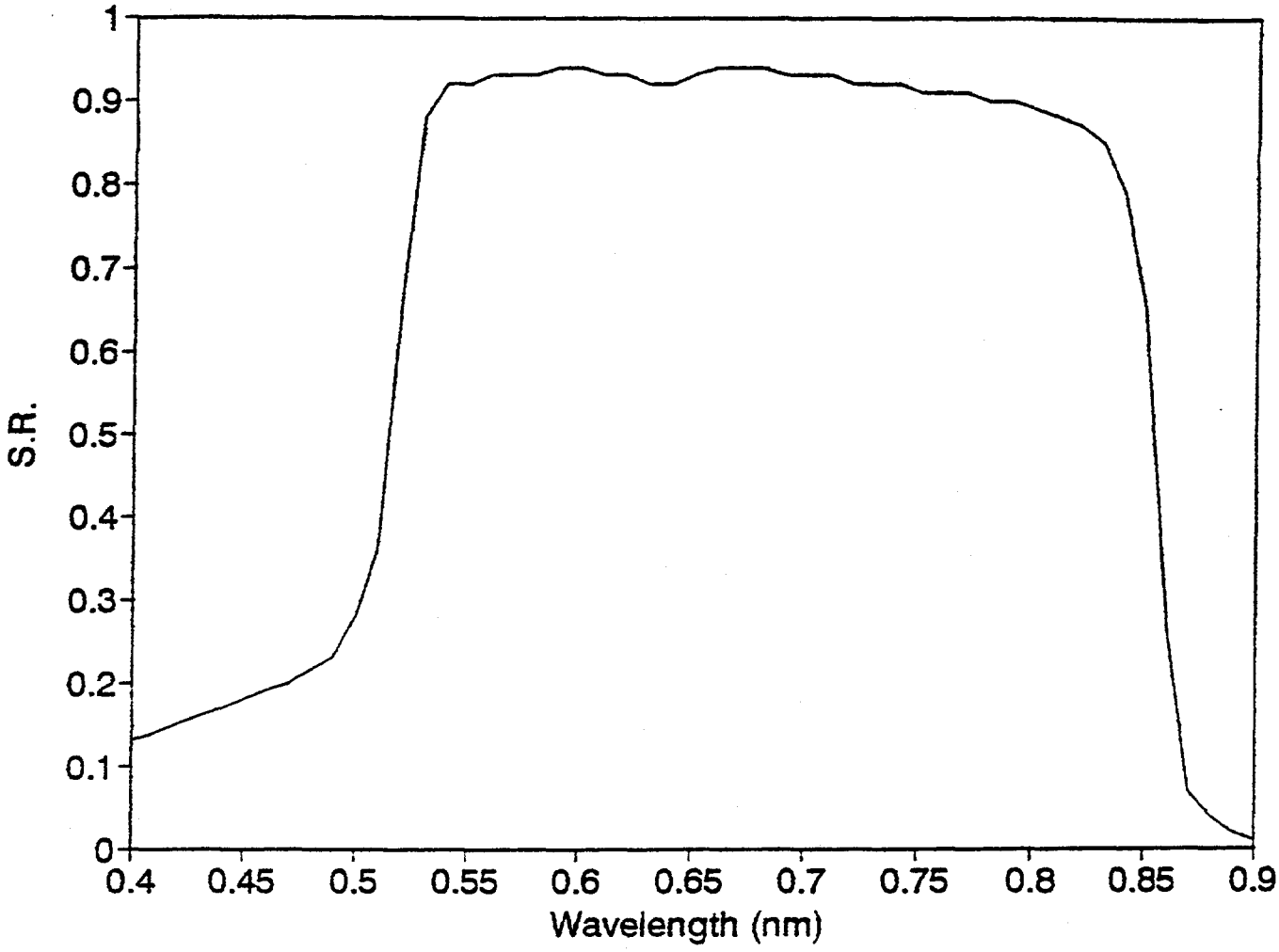

Figure 47. Spectral response of cell 8 on piece 40803.22.

2.4 a-Si DEPOSITION AND PROCESS RESEARCH

The goal during this year was to identify deposition conditions leading to reproducible fabrication of a-Si:H single junction devices with 9% initial efficiency using our PECVD reactor. These devices would be used for studies in support of our role as device maker for the NREL a-Si Research Teams. Cells with an efficiency of 9% are adequate for the device-related studies which were identified by the Device Design and Interface Team, and are comparable to the standard devices routinely made by industrial research groups. To support the team objectives, we would be investigating methods of improving cell performance through higher performance TCO materials and reduced interface losses. Deposition of both superstrate and substrate cells are needed to support industry. In addition, we planned to continue fabrication and analysis of stability and grading in a-SiGe devices.

These plans were predicated on the assumption that the design of the PECVD reactor was adequate for reproducible deposition of 9% cells. Our PECVD reactor had produced cells with 8% efficiency two years ago but had since been used exclusively for materials studies. There had been no effort to determine reliability of the reactor and no effort to reproduce a device run since the initial 8% result.

Following the 4 month shut-down for safety-related modifications to the laboratory facilities and reactor as described in Final Report XG-1-10063-4, the photo-CVD reactor was run to check the integrity of the process gases in the system with which we had the most experience. Cell performance improved from 6% to 9% in just five runs by adjusting p and i-layer thicknesses and gas flows. Minor adjustments to our standard device recipe were required since we had new gases and a new UV lamp installed as a result of the accident. This verified the quality of the gases, the gas delivery system and the post-deposition cell fabrication processing, which are common for the photo-CVD and PECVD devices.

Subsequently, the effort for the rest of the year remained focussed on improving the performance and reproducibility of devices in the PECVD system. Although both single layers and devices were made, emphasis was placed primarily on device production. Eighty device runs were made in seven months. The fabrication of PECVD devices with FF=70-72% and V_{oc}=0.86-0.88 V indicated that the doped layers and i-layer were certainly of device quality. Two chronic problems which limited our progress were lack of reproducibility due to variations in FF and low J_{sc} due to poor blue response. There was no evidence of cross contamination based on routine monitoring of the reactor performance - leak-up rates, ultimate pressure, or RGA scans, or based on deposition and characterization of individual films. However, based on device results, several features in the PECVD reactor design were discovered which severely impacted on the reproducible of devices.

We relied primarily on device results to guide changes in the operation and modifications to the reactor. Contamination of the i-layer with boron and phosphorous were separately identified using device measurements. These effects were reduced somewhat by changing deposition temperatures, pump/purge conditions and the internal configuration of the reactor. An optical analysis of the QE was developed as tool to diagnose the low J_{sc}. Excessively thick p-layers were found to be responsible for the poor blue response. Despite these problems, we fabricated several substrates with cells over 8% efficiency.

In this section, we describe the basic film properties of the p, i, and n-layers, and diagnosis of contamination using QE which was used to motivate the many changes to the deposition conditions and the reactor. The optical analysis of the QE to identify the source of the low J_{sc} is presented in Section 3.2 and our collaborations are described in Section 4.

2.4.1 PECVD Reactor Design and Configurations

Reactor Design

The plasma-assisted CVD reactor is a three chambered load-locked design (figure 48). The center chamber houses the deposition "can". The two outer chambers are the load-lock chambers.

High vacuum pumping is achieved through the first chamber using a 170 l/s Balzers turbomolecular pumping unit. Process pumping is through a 13 l/S Leybold D408CS corrosive series rotary vane pump. Gases are delivered via mass flow controllers through a manifold into the bottom of the center chamber. Pressure is controlled by an MKS throttle valve controller and capacitance manometer. The substrates are heated with quartz resistance heaters, while the deposition can is heated with a single coiled resistance heating element. Temperature is controlled by Eurotherm temperature controllers. RF power is delivered by an ENI 300W power supply and matching network. The anode is a 5 in. diameter Mo disc with small holes. The electrogap spacing is 0.625 in.

Reactor Configurations

Modifications have been made to the deposition can in order to improve device performance. These modifications can be included under three configurations. Configuration A is the design of the system and is shown in Figure 49. In this configuration, the gas inlet is connected to the bottom of the can with a VCR flexible bellows line. A showerhead is located above this for gas dispersal. The powered electrode is attached 1.5" above the showerhead on ceramic standoffs. The RF power lead passes through the showerhead and is insulated with a quartz tube. This unit is enclosed by a 2.75" high ring. The substrate holder assembly fits tightly on top of the ring. A series of eight 1/8" holes in the

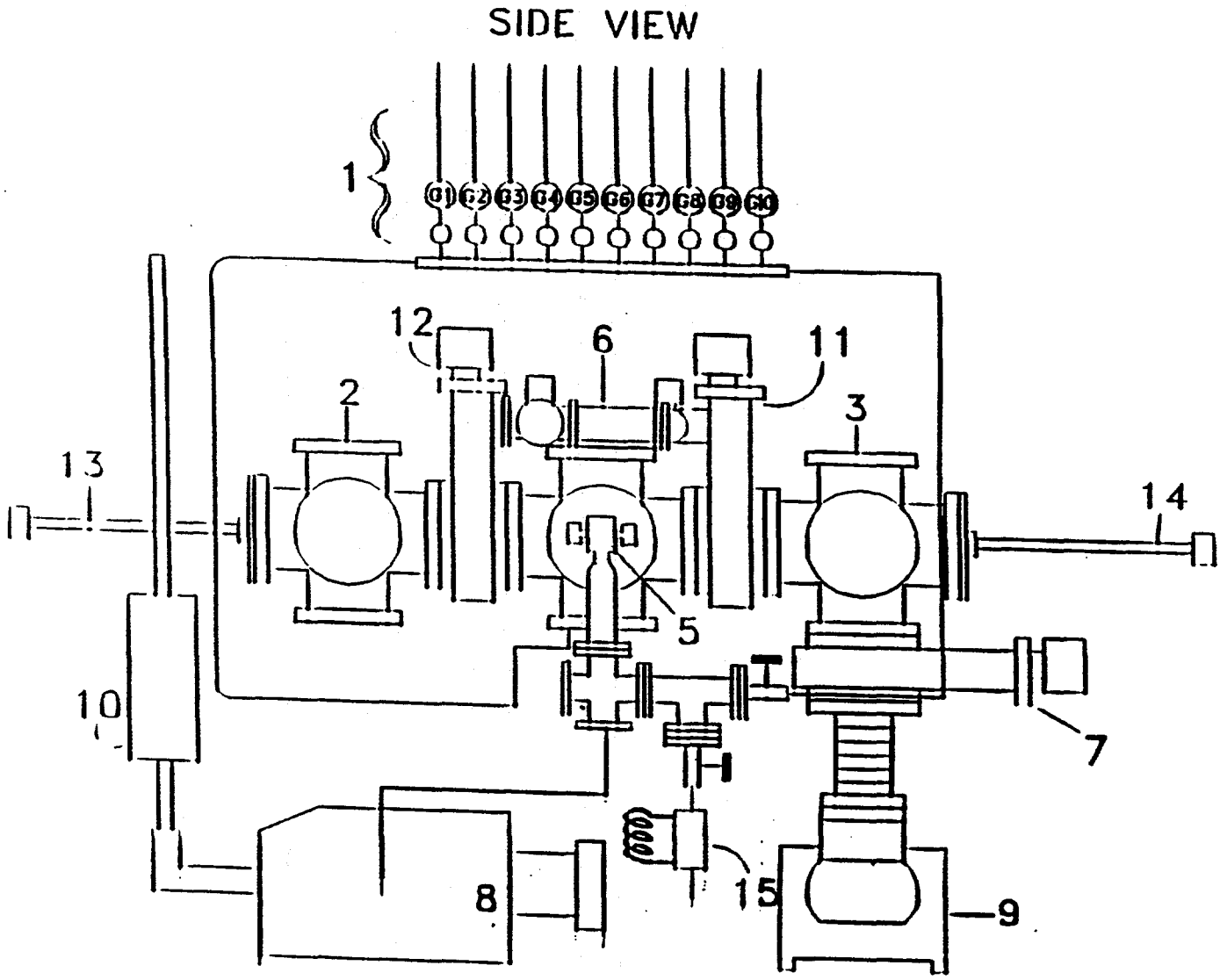

Figure 48. Schematic of Plasma-CVD Reactor

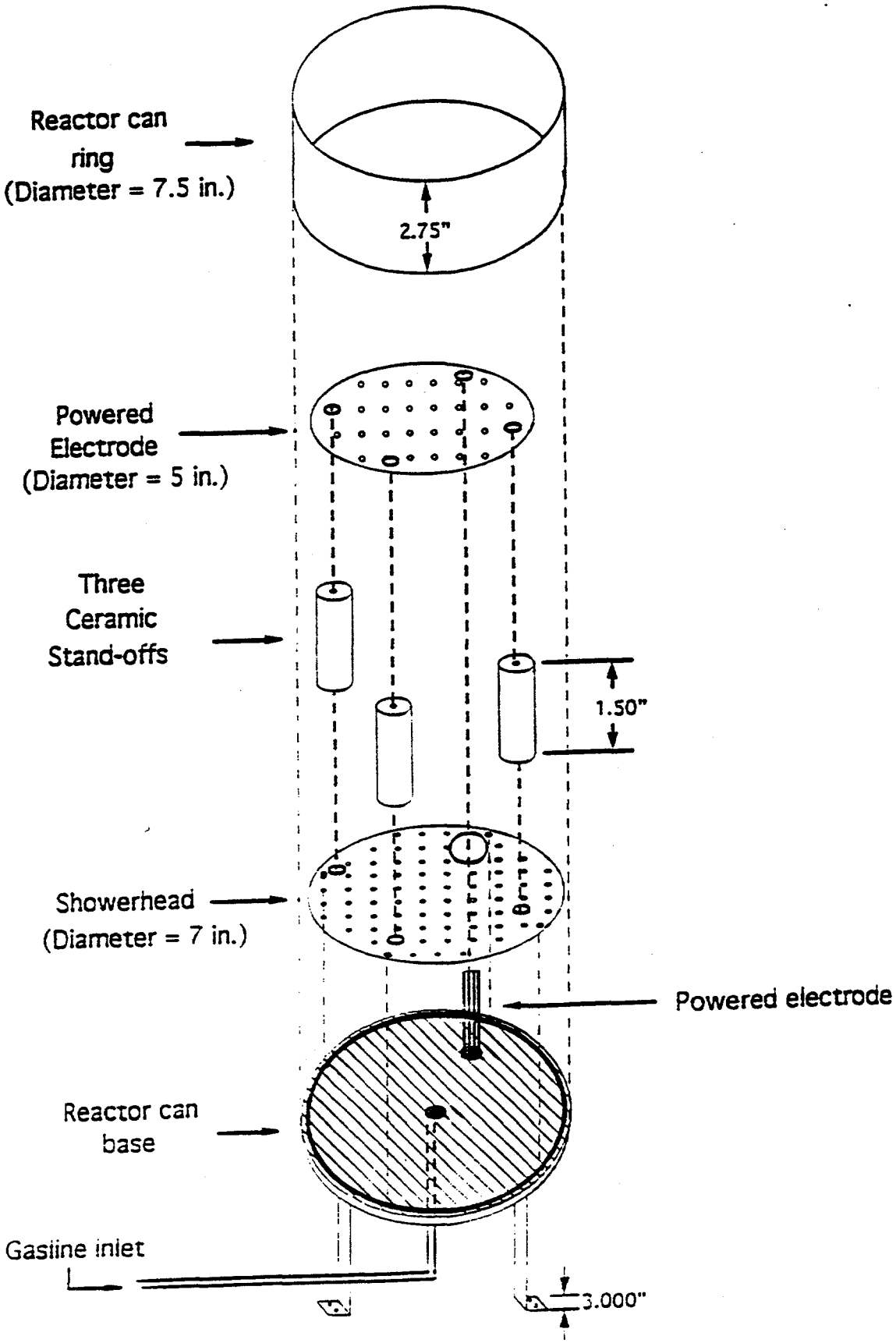

Figure 49. Deposition can - Configuration A

substrate holder assembly (not shown) provide exhaust ports for the gases to the outer chamber. Several features of this design were flawed and resulted in: 1) high gas velocities, of the order of 10^4-10^5 cc/min., exiting the can; 2) unusual flow patterns within the can and mostly likely 'dead spaces' where the process gases were stagnate; and 3) RF discharge below the powered electrode resulting in unwanted film growth in the can.

In configuration B, shown in Figure 50, the exhaust ports in the substrate holder assembly are enlarged 2 to 3 times their original size. Eight 3/8" holes are added symmetrically around the top of the ring to improve conductance and minimize any pressure drop between the can and the chamber. The gas line is disconnected at the VCR fitting at the base of the can so the gases are delivered into the chamber instead of the can.

Configuration C (Figure 51) maintains the exhaust improvements of configuration B. The showerhead and ceramic standoffs are removed and the gas line is connected. A variation of this configuration has the gas line disconnected.

Configuration D is the same as C with the gas line connected. The can ring is inverted with the 3/8" exhaust holes at the bottom.

Reactor Calibration and Integrity

Reactor calibration is performed on a routine basis. This includes mass flow controller calibration, temperature calibrations, leak-up rates, and RGA scans. The reactor is "helium-leak-checked" on a monthly basis and whenever a fitting or connection is broken. The base pressure in the reactor with an overnight bake-out is $6x10^{-8}$ torr. SIMS analysis of devices and layers show no significant levels of impurities in these films. Table 20 shows that the level of impurities are comparable to those found in the photo-CVD reactor. This same reactor has recently produced devices with efficiencies of 9%. These low impurity levels and reactor integrity are also confirmed in the RGA scans and leak checking results.

Safety

The safety modifications to the laboratory and reactors as described in the 91-93 final report (Subcontract No. XG-1-10063-4) have performed without flaw. The formal safe operating procedures have been in effect and are strictly enforced. Further improvements have been made as necessary and an ongoing effort is being made to improve safety at all times.

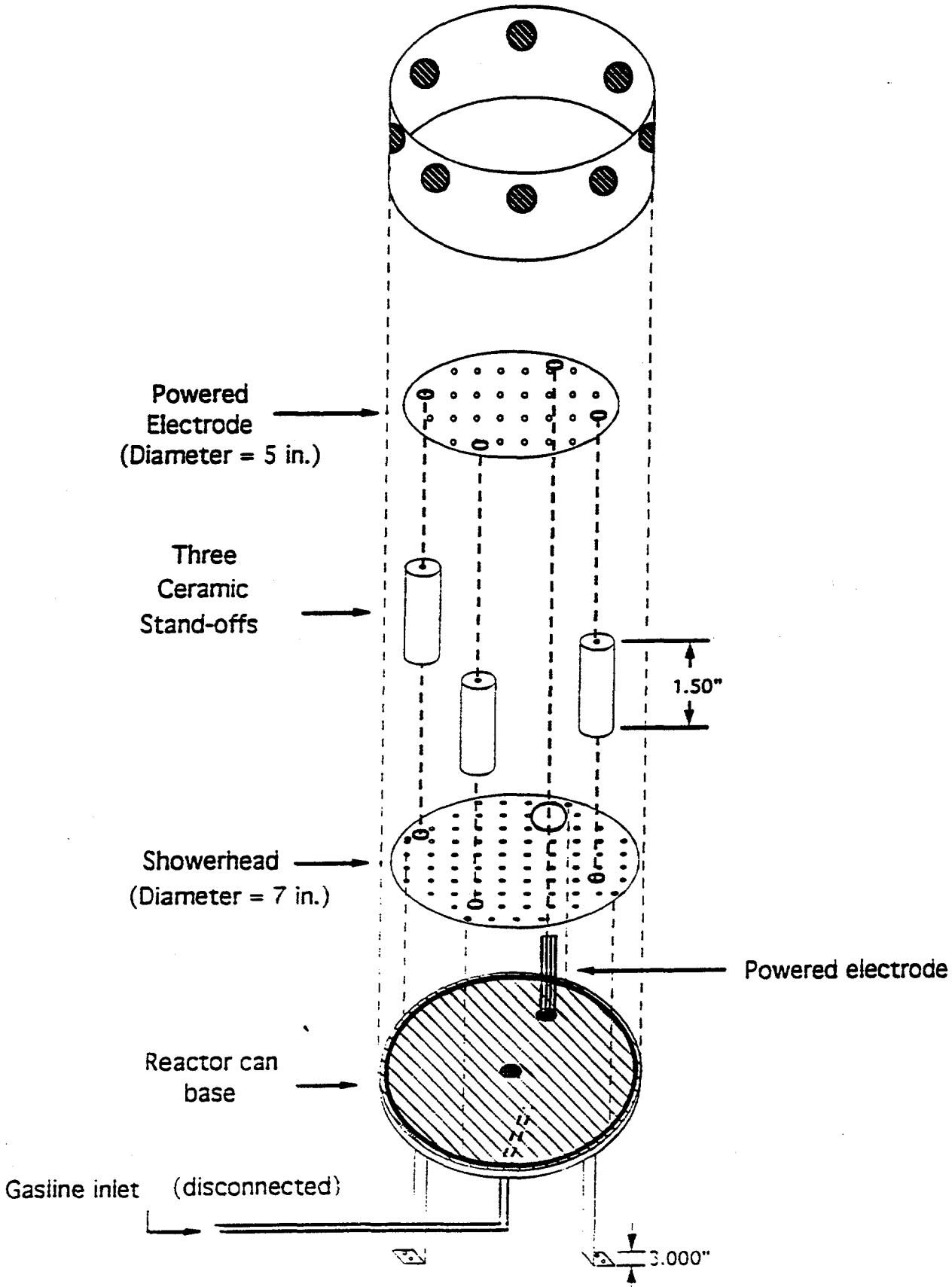

Figure 50. Deposition can - configuration B.

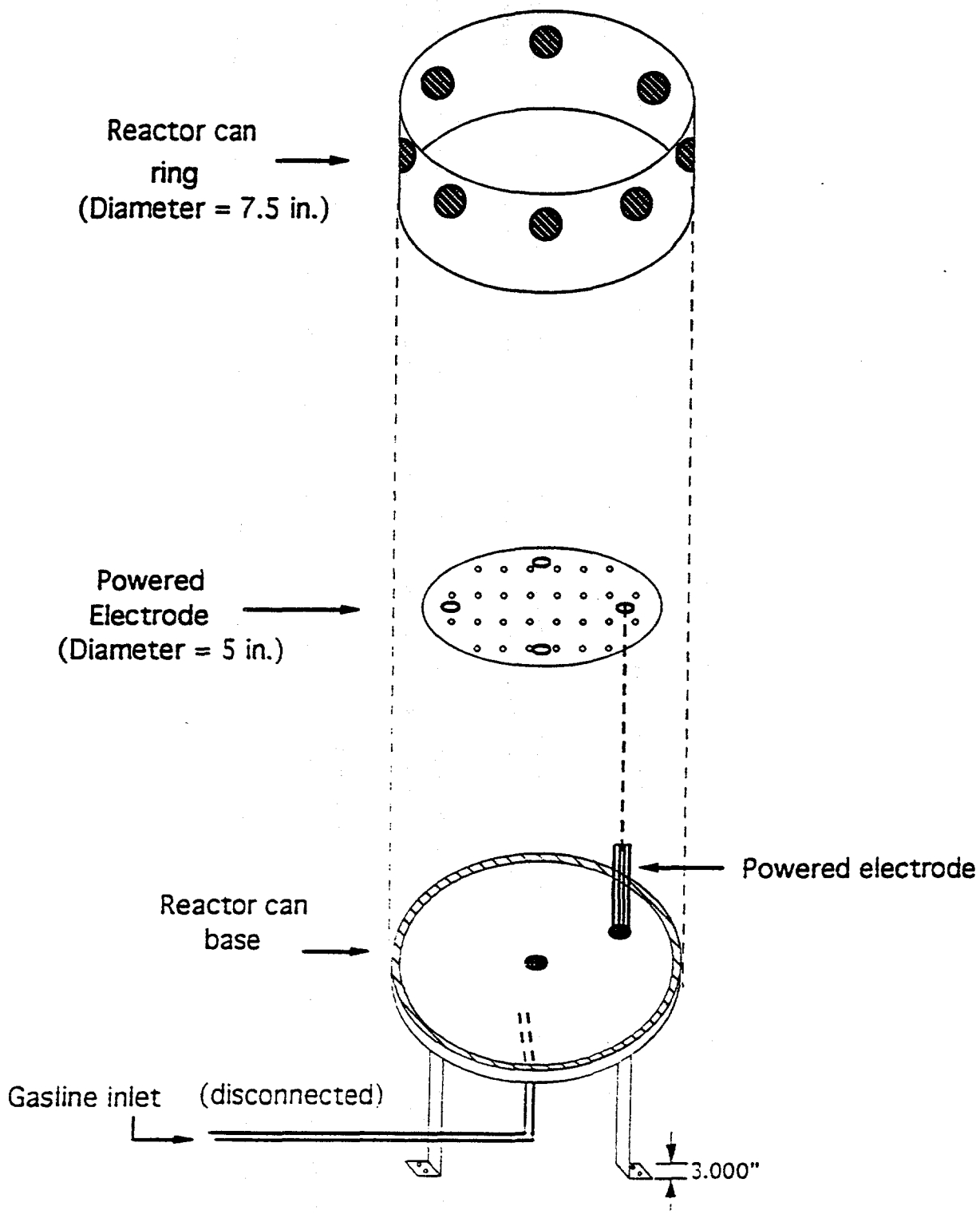

Figure 51. Deposition can - configuration C.

Table 20. Comparison of SIMS Analysis of Photo-CVD and Plasma-CVD Films

Sample	Run Date	SIMS Date	Reactor	C (x 10^{21} cm^{-3})	O	N
3494	4/91	Chas. Evans 7/91	photo	0.005	0.02	not meas.
4005	1/91	NREL	plasma	0.002	0.05	0.00005
4116	5/93	7/93	plasma	0.003	0.03	0.00008
4118	5/93	NREL	plasma	0.006	0.03	0.0003
4221	11/93	12/93	plasma	0.003	0.02	0.0003
4223	11/93		plasma	0.003	0.025	0.0003
4225	12/93		plasma	0.004	0.03	0.0002

2.4.2 a-Si Film Characterization

Single layer p, i, and n films were initially characterized to identify deposition conditions needed for films with appropriate properties for devices. These conditions were then used as a starting point to deposit devices. The deposition conditions were then varied based on cell properties to optimize the deposition conditions.

p-layers-

A-SiC p-layers were deposited under a variety of conditions to determine deposition conditions required for high conductivities (small E_a) while having band gap energies ≥ 2.0 eV. Table 21 shows deposition conditions and p-layer properties. Figure 52 plots σs_{photo} versus E_g. The well documented (17,18) trend of decreasing σs_{photo} with increasing E_g, and C, is observed. While the data in the plots include layers prepared under a wide range of conditions, the lack of any strong deviations from the general trend suggests that for a given band gap, deposition parameters have only a minor effect on the film conductivities. For the devices we chose p-layer conditions similar to those for layers 4097 and 4201, not only because of the relatively large conductivities, but also for: 1) the low chamber pressures (0.2 Torr) and B_2H_6 flows (1 sccm) used to minimize potential incorporation of boron in the i-layer by plasma sputtering or thermal CVD and 2) the lower growth rates allows better control of p-layer thicknesses in the devices.

n-layers -

A range of deposition parameter space was evaluated for the n-layer to identify conditions which gave high conductivities and high doping efficiencies and also to minimize PH_3 contamination. High rf powers and hydrogen dilution of the plasmas were used to produce microcrystalline material (19).

Table 22 lists data for n-layers prepared using different rf powers, hydrogen, PH_3 and SiH_4 flows, and pressure. The combination of hydrogen dilution with high rf power gave high conductivities with reduced PH_3 flow. Thus, higher doping efficiencies were likely obtained. The lower deposition rate for 4085 will allow better control of n-layer thicknesses in the device. The high σ_{photo} and σ_{dark} values for run 4094 suggest that this film was microcrystalline. However, 400-600Å films prepared under nominally identical conditions as those for 4094 (a 6200Å film) had significantly lower conductivities and E_a ≈0.3-0.4 eV, suggesting the film was amorphous which is consistent with films reported by others (20). The conditions for run 4085 were selected for initial device runs.

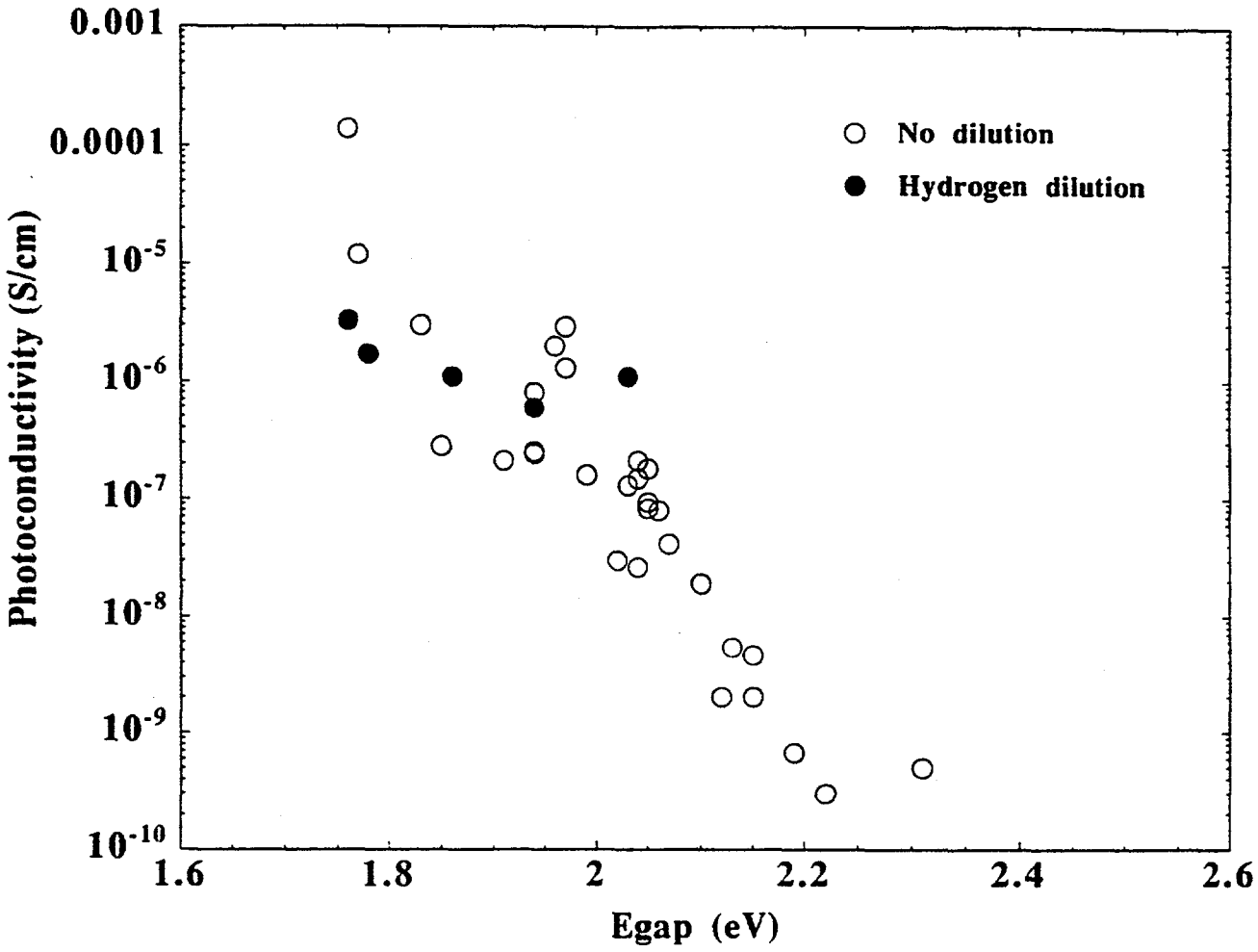

Figure 52. Photoconductives for p-layers plotted against bandgap energy.

Table 21. p-layer Deposition Parameters and Properties

Sample	Power (W)	T_s (°C)	Pressure (T)	B_2H_6 (sccm)	CH_4 (sccm)	CH_4/SiH_4	H_2 (sccm)	Dep.Rate (Å/s)	E_{gap} (eV)	Photo (S/cm)	Dark (S/cm)	E_{act} (eV)
4078	20.0	250	0.50	3.0	8.4	1.50	0	2.1	2.47			
4079	20.0	250	0.50	5.0	8.4	1.50	0	2.0	2.31	5.0e-10	6.0e-13	0.69
4080	20.0	250	0.50	9.0	8.4	1.50	0	2.1	2.12	2.0e-09	2.0e-11	0.74
4081	20.0	250	0.50	18.0	8.4	1.50	0	2.1	1.96	2.0e-06	1.0e-06	0.40
4086	20.0	250	0.50	3.0	7	1.00	0	7.4	2.15	2.0e-09	4.4e-10	0.58
4087	15.0	250	0.50	3.0	7	1.00	0	8.5	2.04	2.6e-08	1.6e-08	0.49
4088	15.0	250	0.50	3.0	7	1.00	0	8.2	2.02	3.0e-08	3.0e-08	0.48
4089	17.5	250	0.50	3.0	7	1.00	0	7.9	2.10	1.9e-08	1.2e-08	0.50
4090	10.0	250	0.50	3.0	7	1.00	0	8.9	1.91	2.1e-07	1.4e-07	0.43
4091	5.0	250	0.50	3.0	7	1.00	0	8.7	1.83	3.0e-06	2.5e-06	0.38
4092	2.5	250	0.10	3.0	7	1.00	0	2.7	1.65			
4093	5.0	250	0.10	3.0	7	1.00	0	2.8	1.76	1.4e-04	1.4e-04	0.30
4096	20.0	250	0.50	18.0	8.4	1.50	0	5.5	1.85	2.8e-07	2.3e-07	0.40
4097	10.0	250	0.20	1.0	4	1.00	0	2.2	1.97	2.9e-06	2.0e-06	0.40
4103	20.0	250	0.50	3.0	8.4	1.50	0	5.7	2.22	3.0e-10	2.0e-13	0.85
4104	20.0	250	0.50	3.0	5.6	1.00	0	5.7	2.13	5.4e-09	1.6e-09	0.53
4105	15.0	250	0.50	3.0	8.4	1.50	0	6.3	2.19	6.7e-10	3.6e-13	0.84
4106	15.0	250	0.50	3.0	5.6	1.00	0	6.3	2.10	1.9e-08	9.4e-09	0.49
4107	15.0	250	0.35	3.0	5.6	1.00	0	5.0	2.04	2.1e-07	1.3e-07	0.44
4108	15.0	250	0.35	3.0	8.4	1.50	0	5.3	2.15	4.6e-09	1.4e-09	0.55
4113	15.0	250	0.35	3.0	5.6	1.00	0	4.7	2.06	7.9e-08	5.3e-08	0.46
4115	15.0	250	0.35	3.0	5.6	1.00	0	4.2	2.05	1.8e-07	1.6e-07	0.43
4117	15.0	250	0.35	3.0	5.6	1.00	0	5.2	2.05	8.3e-08	6.6e-08	0.45
4119	15.0	250	0.35	3.0	5.6	1.00	0	4.8	2.05	9.3e-08	6.1e-08	0.46
4121	15.0	225	0.35	3.0	5.6	1.00	0	5.2	2.04	1.5e-07	1.1e-07	0.44
4122	15.0	250	0.35	1.5	2.8	1.00	140					
4123	15.0	225	0.27	1.5	2.8	1.00	0					
4124	15.0	225	0.35	1.5	2.8	1.00	140	0.9	1.78	1.7e-06	3.1e-07	0.47
4125	15.0	275	0.35	1.5	2.8	1.00	0	4.2	1.94	2.4e-07	1.9e-07	0.42
4126	15.0	250	0.35	1.5	2.8	1.00	140	0.9	1.76	3.3e-06	3.1e-06	0.40
4127	15.0	225	0.35	1.5	5.9	2.12	140	0.9	1.86	1.1e-06	7.0e-07	0.42
4128	15.0	200	0.35	1.5	5.9	2.12	140	0.8	1.94	5.9e-07	3.2e-07	0.45
4130	15.0	200	0.35	1.5	11.3	4.00	140	0.8	2.03	1.1e-06	2.5e-08	0.49
4145	10.0	200	0.20	1.0	4	1.00	0	2.9	1.94	8.0e-07	2.1e-07	0.43
4164	14.0	230	0.50	1.0	2	0.25	0	8.1	1.77	1.2e-05	9.1e-06	0.38
4174	14.0	200	0.50	1.0	4	0.50	0	9.0	1.94	2.5e-07	1.9e-07	0.46
4201	14.0	150	0.20	1.0	4	0.50	0	3.0	1.97	1.3e-06	5.0e-07	0.45
4202	14.0	150	0.20	1.0	8	1.00	0	3.1	2.07	4.1e-08	1.0e-08	0.55
4203	14.0	200	0.20	1.0	8	1.00	0	3.0	2.03	1.3e-07	5.7e-08	0.49
4205	7.0	150	0.20	1.0	8	1.00	0	3.4	1.99	1.6e-07	9.2e-08	0.48

Table 22
n-layer deposition parameters and properties

Sample	T_s (°C)	Chamber Pressure (Torr)	Applied Power (W)	SiH_4 Flow (sccm)	PH_3 Flow (sccm)	H_2 Flow (sccm)	Film Thickness (Å)	Dep. Rate (Å/s)	E_g (eV)	σ_{photo} (S/cm)	σ_{dark} (S/cm)	E_a (eV)
4083	250	0.5	10	10	5.0	0	7000	3.9	1.72	$2x10^{-2}$	$8.6x10^{-3}$	0.19
4085	250	0.5	55	2.0	1.6	85	6600	1.2	1.75	$3.2x10^{-2}$	$2.4x10^{-2}$	0.22
4094	250	0.27	65	1.3	1.0	95	6200	1.1	1.99	1.4	1.4	0.04
4095	250	0.27	65	1.3	1.0	95	400	1		$1.3x10^{-4}$	$3.5x10^{-5}$	0.35
4161	250	0.5	6	8.0	8.0	0	10600	5.9	1.72	$7.4x10^{-3}$	$5.4x10^{-3}$	0.20

i-layers -

Table 23 lists i-layer properties. Some of the films peeled off the smooth glass substrates, suggestive of high compressive stresses in the films (21), so no measurements could be performed. Of the films we were able to measure, all had s_{photo} ~10^{-4}-10^{-5} S/cm, s_{photo}/s_{dark} ~10^5-10^6 and E_g ~1.7-1.8 eV, values usually associated with "device quality" material (22). Also Urbach energies of 42-45 meV were obtained from the long wavelength edge of the spectral response for devices with i-layers deposited at 150-230°C, suggestive of relatively sharp band edges. Low concentrations of C and O were found by SIMS as reported in the last section. We therefore concluded that our i-layers have reasonably good properties. All further optimization was based on device performance.

Of interest are the changes in growth rate with variation in deposition parameters. No change in the deposition rate was observed when the pressure was decreased from 0.5 to 0.25 Torr, consistent with a lack of gas depletion. However, the decrease in growth rate with decreasing SiH_4 flow suggests the contrary. This discrepancy is most likely related to the gas flows in the canister. (All single layers were deposited using the original can configuration.)

2.4.3 a-Si p-i-n device characterization

The reactor geometry, deposition parameters, and device structure were varied to improve device performance. We will emphasize how the boron and phosphorous contamination was limited through changes in deposition parameters and the effect of the contaminants (B,P) on device performance. Full descriptions of the device deposition conditions are not given in the text but are listed in Table 24. The reported properties are averages of 8-12 cells from each deposition run. Cells were deposited on textured SnO_2 on 7059 obtained from Solarex Thin Film Division. The i-layers were typically 0.4 to 0.5 μm thick. Unless otherwise specified, the cells were 0.071 cm^2 in area with 25 Å Ti/ 5000Å Ag contacts. They were heat treated at 170°C for 30 minutes after contact deposition and prior to cell testing. This heat treatment significantly improved FF.

Different Canister Configurations

Based on the assumption that the PECVD was appropriately designed and reproducible, deposition conditions and operating procedures were varied to optimize device performance. This effort was not successful since the device deposited using identical deposition conditions could not be reproduced. This lead to a re-evaluation of the system design and modification to the design to improve

Table 23
i-layer deposition parameters and properties

Sample	T_S (°C)	Chamber Pressure (Torr)	Applied Power (W)	SiH_4 Flow (sccm)	Film Thickness (Å)	Dep. Rate (Å/s)	E_g (eV)	σ_{photo} (S/cm)	σ_{dark} (S/cm)	E_a (eV)
4100	250	0.5	10	20	20000	11	1.71	2.1×10^{-5}	1.5×10^{-11}	0.79
4102	250	0.5	5	20	8000	6.5	1.71	1.7×10^{-4}	7.7×10^{-10}	0.75
4138	250	0.25	5	20	12400	6.9	-	films	peeled	-
4140	250	0.5	5	5.0	8000	4.4	-	8.7×10^{-5}	4.0×10^{-10}	0.74
4142	230	0.5	5	2.0	4600	2.6	1.74	3.9×10^{-5}	1.5×10^{-10}	0.76
4149	230	0.5	5	2.0	4400	2.4	1.75	- films	peeled	-

Table 24a. Deposition Conditions for p-i-n Device Runs

Layer	Dep. Param.	4155	4159	4168	4177	4178	4184	4185	4189
p-layer	T_s (°C)	230	230	150	150	150	150	150	150
	P (Torr)	0.5	0.5	0.5	0.5	0.5	0.5	0.5	0.5
	SiH_4 (sccm)	8.0	8.0	8.0	8.0	8.0	8.0	8.0	8.0
	CH_4 (sccm)	2.0	2.0	2.0	4.0	4.0	4.0	4.0	4.0
	B_2H_6 (sccm)	1.0	1.0	1.0	1.0	1.0	1.0	1.0	1.0
	H_2 (sccm)	0	0	0	0	0	0	0	0
	Power (W)	14	14	14	14	14	14	14	14
	Dep time (s)	20	20	20	20	20	20	20	20
Flush Conditions		a)	a)	a)	b)	b)	b)*	b)	b)**
i-layer	T_s (°C)	230	230	150	150	150	150	150	150
	P (Torr)	0.5	0.5	0.5	0.5	0.5	0.5	0.5	0.5
	SiH_4 (sccm)	8	8	8	8	8	8	8	8
	H_2 (sccm)	0	0	0	0	0	0	0	0
	Power (W)	7	7	7	7	7	7	7	7
	Dep time (m)	15	15	15	15	15	15	15	15
n-layer	T_s (°C)	230	230	150	150	150	150	150	150
	P (Torr)	0.5	0.5	0.5	0.5	0.5	0.5	0.5	0.5
	SiH_4 (sccm)	8.0	8.0	8.0	8.0	8.0	8.0	8.0	8.0
	PH_3 (sccm)	8.0	8.0	8.0	8.0	8.0	8.0	8.0	8.0
	H_2 (sccm)	0	0	0	0	0	0	0	0
	Power (W)	6	6	6	6	6	6	6	6
	Dep time (m)	4	4	4	1	1	1	1	1

a) One cycle of 5 min., 20 sccm SiH_4 flush and quick purge after p-layer
b) One cycle of 5 min., 20 sccm SiH_4 flush and two hour purge after p-layer
* First run with holes on side of canister
** Made in the afternoon after morning a-SiC:H layer

Table 24b. Deposition Conditions for p-i-n Device Runs (cont'd)

Layer	Dep. Param.	4194	4195	4196	4197	4198	4208	4212
p-layer	T_s (°C)	150	150	150	150	150	150	150
	P (Torr)	0.5	0.5	0.5	0.5	0.5	0.5	0.5
	SiH_4 (sccm)	8.0	8.0	8.0	8.0	8.0	8.0	8.0
	CH_4 (sccm)	4.0	4.0	4.0	4.0	4.0	4.0	4.0
	B_2H_6 (sccm)	1.0	1.0	1.0	1.0	1.0	1.0	1.0
	H_2 (sccm)	0	0	0	0	0	0	0
	Power (W)	14	14	14	14	14	14	14
	Dep time (s)	15	15	15	15	15	15	15
buffer layer	T_s (°C)					150	150	150
	P (Torr)					0.5	0.5	0.5
	SiH_4 (sccm)					8.0	8.0	8.0
	CH_4 (sccm)	none	none	none	none	2.0	2.0	2.0
	Power (W)					14	14	14
	Dep time (s)					15	20	15
Flush Conditions		c)	c)	c)	c)	c)	c)***	c)
i-layer	T_s (°C)	200	200	200	200	200	200	200
	P (Torr)	0.5	0.5	0.5	0.5	0.5	0.5	0.5
	SiH_4 (sccm)	8	8	8	8	8	8	8
	H_2 (sccm)	0	0	0	0	0	0	0
	Power (W)	7	7	7	7	7	7	7
	Dep time (m)	10	10	10	10	10	10	10
n-layer	T_s (°C)	200	200	200	200	200	200	200
	P (Torr)	0.5	0.5	0.5	0.5	0.5	0.5	0.5
	SiH_4 (sccm)	2.0	2.0	2.0	2.0	2.0	2.0	2.0
	PH_3 (sccm)	1.6	1.6	1.6	1.6	1.6	1.6	1.6
	H_2 (sccm)	85	85	85	85	85	85	85
	Power (W)	55	55	55	55	55	55	55
	Dep time (m)	4	4	4	4	4	4	4

c) One cycle of 5 min., 20 sccm SiH_4 flush and one hour purge before i-layer
*** canister heated at 200°C

Table 24c. Deposition Conditions for p-i-n Device Runs (cont'd)

Layer	Dep. Param.	4216	4217	4218	4224	4235
p-layer	T_s (°C)	150	150	150	150	150
	P (Torr)	0.5	0.2	0.2	0.2	0.2
	SiH_4 (sccm)	8.0	8.0	8.0	8.0	8.0
	CH_4 (sccm)	4.0	4.0	4.0	4.0	4.0
	B_2H_6 (sccm)	1.0	1.0	1.0	1.0	1.0
	H_2 (sccm)	0	0	0	0	0
	Power (W)	14	14	14	14	14
	Dep time (s)	15	45	45	22	20
buffer layer	T_s (°C)	150	150	150	150	150
	P (Torr)	0.5	0.2	0.2	0.2	0.2
	SiH_4 (sccm)	8.0	8.0	8.0	8.0	8.0
	CH_4 (sccm)	2.0	2.0	2.0	2.0	2.0
	Power (W)	14	14	14	14	14
	Dep time (s)	15	45	45	22	20
Flush Conditions		c)****	c)	c)	c)	c)
i-layer	T_s (°C)	200	200	200	200	200
	P (Torr)	0.5	0.2	0.2	0.2	0.2
	SiH_4 (sccm)	8	8	8	8	8
	H_2 (sccm)	0	0	0	0	0
	Power (W)	7	7	7	7	7
	Dep time (m)	10	30	30	15	20
n-layer	T_s (°C)	200	200	200	200	200
	P (Torr)	0.5	0.5	0.5	0.5	0.5
	SiH_4 (sccm)	2.0	2.0	2.0	2.0	2.0
	PH_3 (sccm)	1.6	1.6	1.6	1.6	1.6
	H_2 (sccm)	85	85	85	85	85
	Power (W)	55	55	55	55	55
	Dep time (m)	4	4	4	4	4

**** Made in the afternoon after morning i-layer

reproducibility of the system. Most of the changes were of limited success and only acted as 'band-aids' for a poor design. A new design of the internals of the system is currently being developed. Below are examples of the changes made.

As an example, the results for devices prepared between runs 4170 and 4183 suggested that the flow out of the canister was too restricted and the gas velocities into the canister too large. A key run was 4179 in which two substrates were removed from the holder and replaced with steel screen. This greatly increased the conductance of the can. Significant powder formation resulted around the screen openings but devices had the best efficiencies to date. Therefore after run 4183, six 3/8" diameter holes were drilled into the side of the canister.

There were two reasons for this change. Opening the conductance of the internal chamber insured that there was no pressure build-up in the can when gases were flowing (i.e., decreased the potential pressure drop). The second reason was to allow better pumping of the internal can in order to reduce lingering dopant gases. The gas line was also disconnected for device 4184 in order to diminish the gas velocities in the canister. Properties for device 4184 are compared with those for previous devices prepared under nominally the same conditions in Table 25. Within experimental error, there are no discernible differences in these properties.

Later, the gas line was reconnected to reestablish the large gas velocities with the canister now more open due to the six side holes. As can be seen from the data in the second part of Table 25, a small increase in V_{oc} was noted when the gas line was re-connected, however, because of a slightly lower FF, the efficiency for this cell (4224) was comparable with those prepared with the gas line disconnected.

While none of these changes resulted in significantly improved efficiencies, we still may alter the canister configuration and/or the gas flow pattern further, possibly to allow for a more uniform gas flow across the electrode surfaces.

The devices whose properties are described in the next five sections were obtained, for the most part, in a chronological order.

Boron Contamination

Our early devices were limited by J_{sc} below 10 mA/cm^2. An extremely low blue response was attributed both to poor generation and poor collection based on bias dependent QE measurements. The large bias dependence of the blue spectral response shown in Figure 53 suggests poor electron collection. For a-Si:H devices, poor electron collection is commonly attributed to boron contamination of the i-layer (23). Various conditions of pumping and flushing

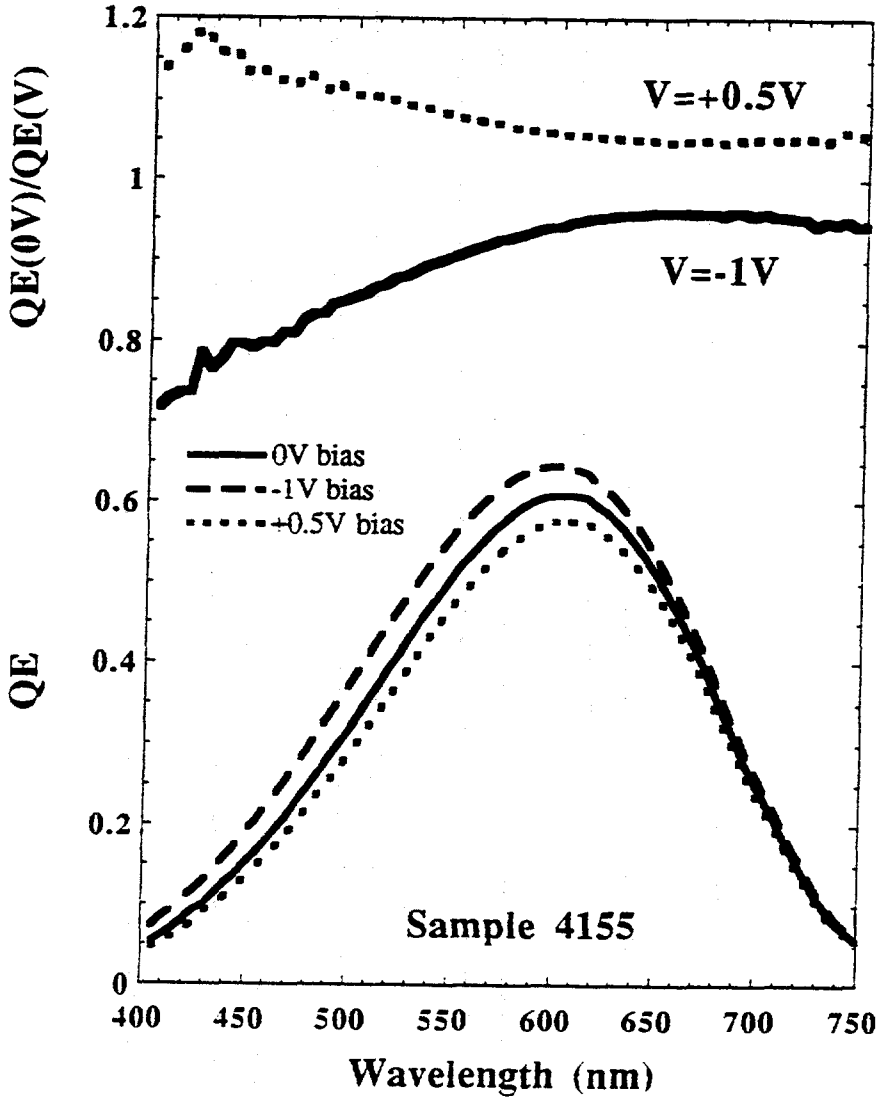

Figure 53. Bias dependence of quantum efficiencies for device 4155

Table 25
Devices prepared using different cannister configurations

Device	Holes on the Side of the Cannister ?	Gas Line	V_{oc} (V)	FF (%)	J_{sc} (mA/cm^2)	η (%)
4177	No	connected	0.87	51	11.1	5.0
4178	No	connected	0.89	55	11.0	5.4
4184	Yes	disconnected	0.87	56	11.2	5.2
4217	Yes	disconnected	0.85	70	11.7	6.9
4218	Yes	disconnected	0.86	70	11.7	7.1
4224	Yes	connected	0.88	67	11.8	7.0
4235	Yes	disconnected	0.85	68	12.3	7.2

after the p-layer, ranging from minutes to hours and from one to six cycles, were tried to no avail. This suggested that residual B_2H_6 was not the source of the boron. We speculated that the boron contamination was related to boron diffusion from the p to the i-layer or to plasma sputtering of B-doped material grown by thermal CVD on the internal reactor surfaces. We lowered the substrate temperature during all three layer depositions from 230°C to 150°C to minimize both effects.

Figure 54 compares the ratios of the quantum efficiencies measured with no applied electrical bias to those obtained with electrical biases of -1V and +0.5 V for devices prepared at 230 and 150°C. The ratios for wavelengths less than 550 nm are clearly closer to 1 for the device prepared at T_s = 150°C. Reduced bias dependence in the blue region is associated with improved electron collection. Accompanying this smaller bias dependence are larger V_{oc} values and J_{sc} values greater than 11 mA/cm^2, as is displayed in Table 26.

Table 26

Devices prepared at different substrate temperatures

Device	T_s all layers (°C)	V_{oc} (V)	FF (%)	J_{sc} (mA/cm^2)	η (%)
4155	230	0.79	68	8.3	4.4
4159	230	0.77	68	9.2	4.8
4168	150	0.86	67	11.3	6.6

The larger V_{oc} is, at least in part, due to a larger E_g for the i-layer because of the known larger hydrogen content for a-Si:H films prepared at lower substrate temperatures (24). The larger currents are probably related to the improved carrier collection and perhaps a larger p-layer band gap resulting from the lower temperatures (see Table 21).

Devices sent for SIMS analysis did not show any B contamination, but this is not surprising since B is very difficult to detect. Our strongest evidence that the poor blue response was indeed due to B contamination was that devices deposited after one or more thick p-layers had significantly lower J_{sc} and blue response than devices deposited just before the p-layers. This occurred even after baking and pumping out the reactor for three days after the thick p-layer runs. This would confirm our assumption that it is not residual B_2H_6 but B-doped film in the reactor which is the source of the B contamination in devices.

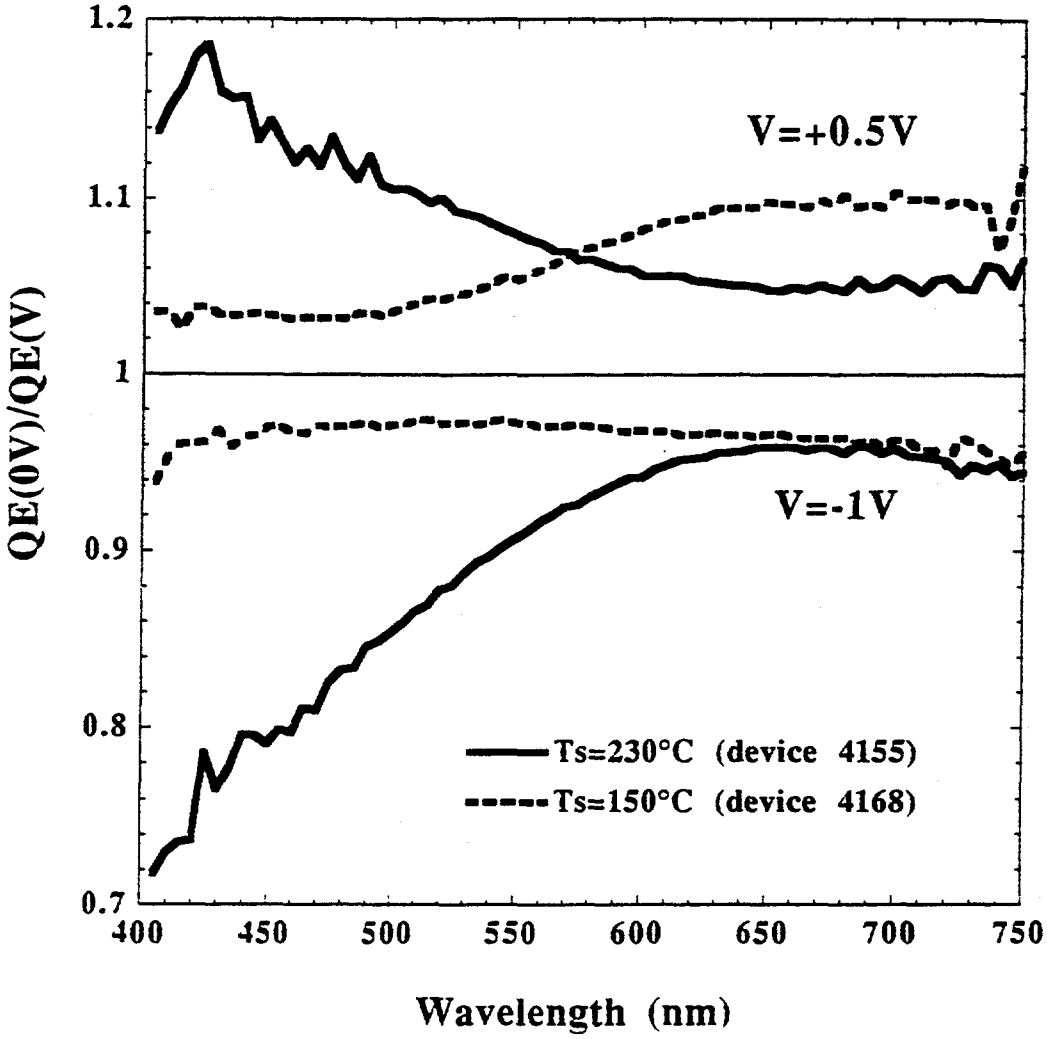

Figure 54. Ratios of quantum efficiencies measured using no electrical bias to those obtained using 0.5 and -1V biases for devices prepared at substrate temperatures of 150°C and 230°C.

Phosphorus Contamination

Although lowering the deposition temperatures for all layers from 230°C to 150°C led to improved electron collection, it created a problem, as is displayed in Figure 55. With three successive runs at T_s = 150°C after the canister was cleaned (runs 4168-4170), the bias dependence of the red response increased, implying a deterioration of hole collection in the cells.

The poorer hole collection led to smaller FF as is also shown in the figure. When the reactor was cleaned, the subsequent device (4171), again prepared at 150°C, showed little bias dependence of the red response and FF≈67-69%. The second run at 150°C after cleaning (4172) had a large bias dependence to the red response and low FF (58-59%). Thus cleaning the canister restored the good hole collection but only for one run.

Phosphorus contamination of the i-layer was suspected, caused by trapping of PH_3 in a porous film deposited on the canister wall and its release during the next device deposition. The use of low substrate temperatures often leads to columnar/porous film formation (25,26) and others have reported similar P contamination problems at low substrate temperatures (27).

In an attempt to produce a denser film on the walls of the canister, devices were prepared with the p-layer deposition temperature set at 150°C and the i and n-layer deposition at 200°C. This temperature was a compromise between 150°C which caused P contamination and 230°C which caused B contamination. Figure 56 shows that with these higher temperatures, we were able to do successive runs (4195, 4196) with no change in the bias dependence in the red region or the FF, as can be seen from Table 27. However the 200°C temperature did lead to lower V_{oc}, likely a result of the lower i-layer band gap.

Table 27
Devices prepared at different i and n-layer substrate temperatures

Device	T_s for i and n-layers (°C)	T_s for p-layer (°C)	V_{oc} (V)	FF (%)	J_{sc} (mA/cm^2)	η (%)
4168	150	150	0.86	67	11.3	6.5
4194	200	150	0.84	68	10.9	6.2
4195	200	150	0.83	68	10.7	6.1
4196	200	150	0.84	67	11.4	6.4

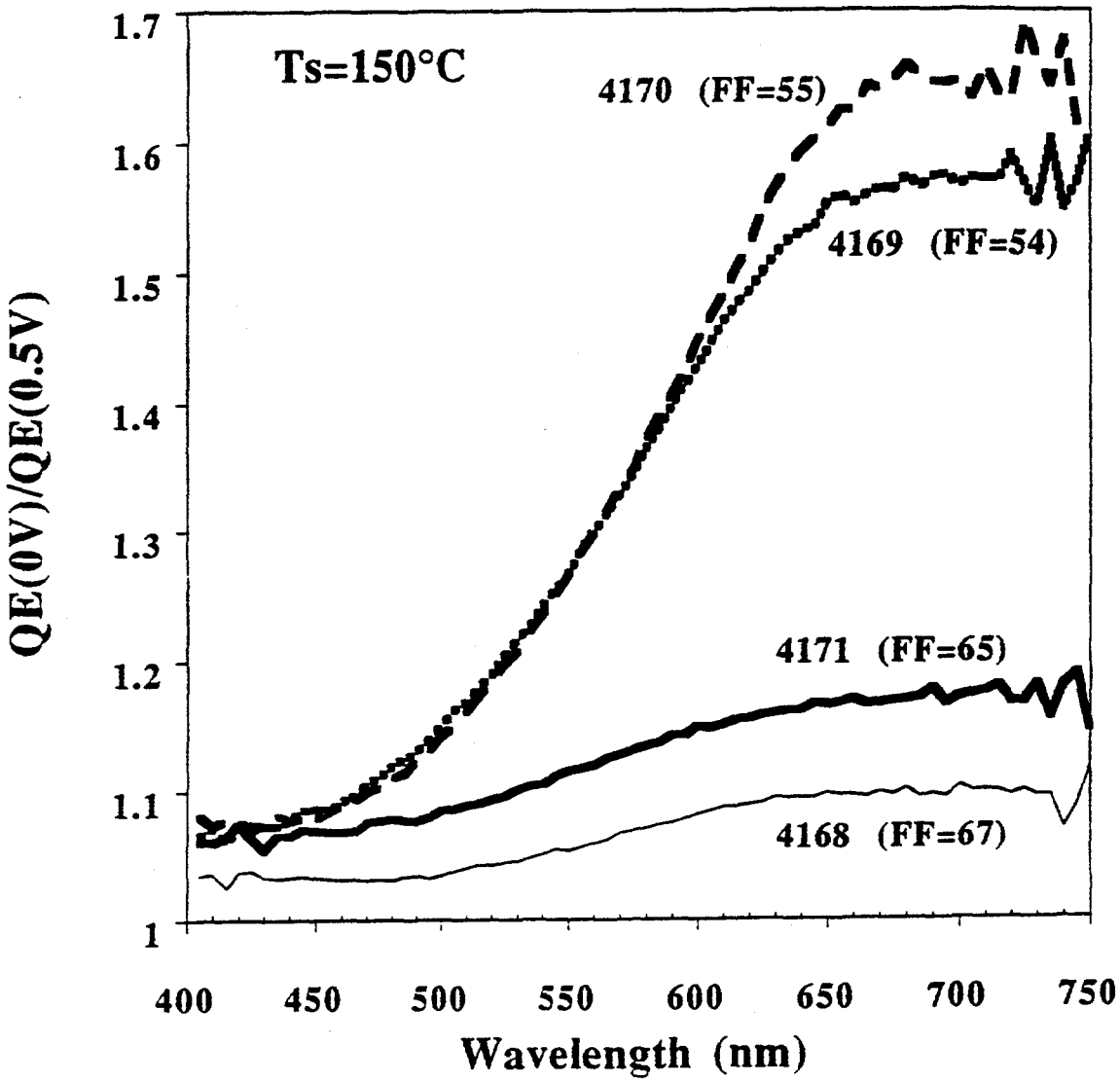

Figure 55. Ratios of quantum efficiencies obtained using electrical biases of 0 and 0.5V for devices prepared at 150°C on successive days.

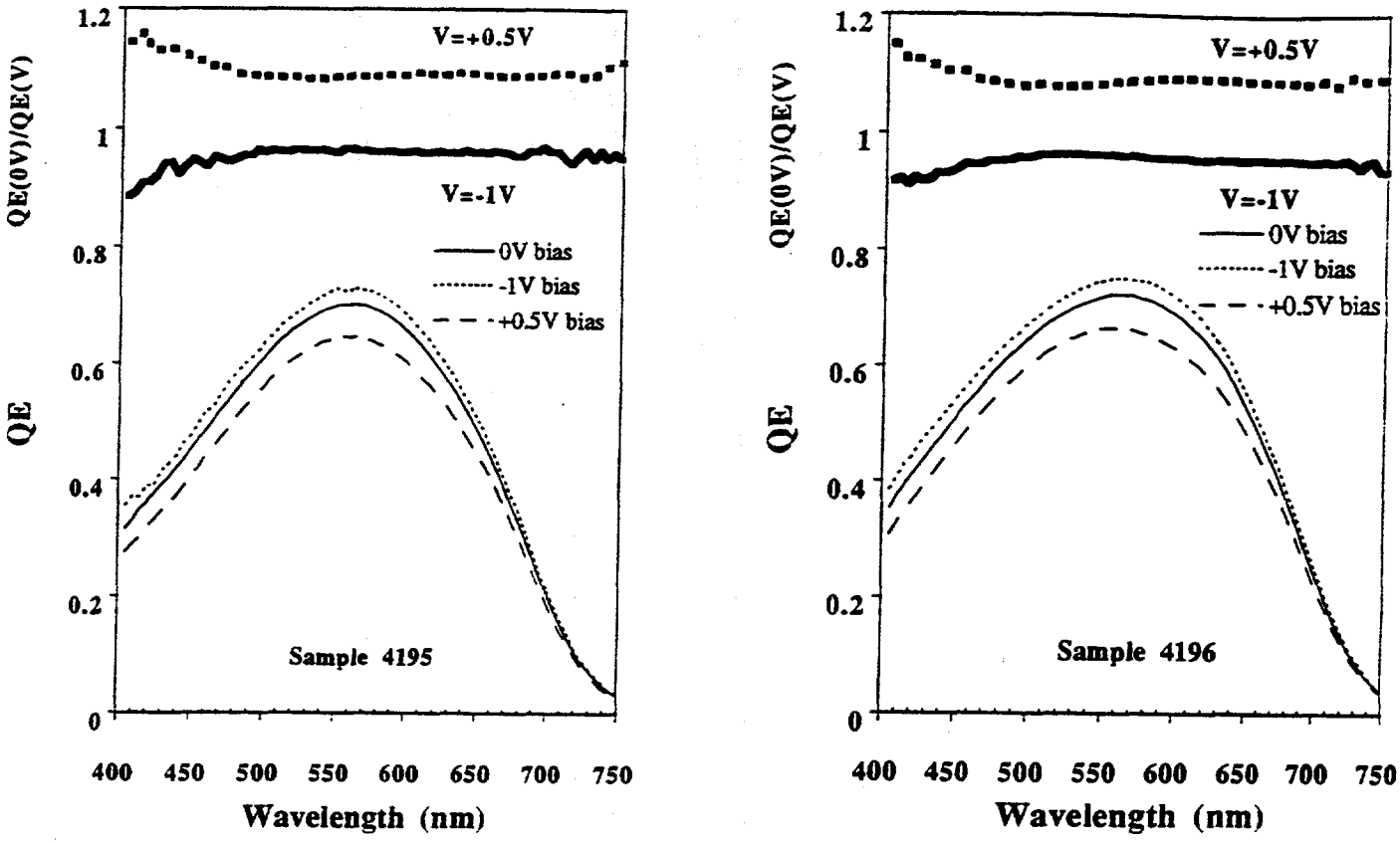

Figure 56. Quantum efficiencies measured using electrical biases of ϕV, 0.5V and -1V for devices prepared on successive days with i and n-layer substrate temperatures of 200°C

Use of a Buffer Layer

Comparing the bias dependence of the blue response in Figure 52 to that of Figure 55 shows that the 200°C i-layer/n-layer substrate temperature led to electron collection losses which were less than those for 230°C i-layers but greater than those found for devices with 150°C. This problem was solved by using an ungraded a-SiC:H buffer layer deposited between the p and i-layers. The buffer layer was produced under the same conditions as the p-layer except no B_2H_6 was used and the CH_4 flow was cut in half. It has been suggested that this type of buffer layer can limit B diffusion into the i-layer and minimize stress, and thus defects which act as recombination sites at the p/i interface (23). We have previously reported the positive influence of the buffer layer on blue response and V_{oc} in photo-CVD devices (28,29).

Figure 57 displays the decreased bias dependence in the blue with the addition of the buffer layer. Tables 28 and 29 show improvements in V_{oc}, FF and blue response (QE at 400 nm) with the addition of the buffer layer. Table 28 lists devices with Ti/Ag contacts while Table 29 includes devices with more reflective ITO/Ag contacts. Even larger improvements are expected with a graded buffer layer (23). We plan to incorporate a graded buffer layer into our devices after solving other problems.

Heating of the Reactor Walls

In an attempt to densify the film deposited onto the canister wall without having to resort to substrate temperatures ≥ 200°C during i- and n-layer depositions, the canister was heated to 200°C during run 4208. This was one of the best devices, having V_{oc} = 0.83 V , J_{sc} = 13.1 mA/cm^2, FF = 71%, EFF = 7.8% , and very little bias dependence of the spectral response in the red or blue. With ITO/Ag contacts, the properties were V_{oc} = 0.83 V , J_{sc} = 15.4 mA/cm^2 , FF = 64 % and EFF = 8.4 %. Attempts to repeat this run failed. Significant powder formed on the substrates during the next two depositions where the can temperature was also heated at 200°C but no film adhered. Only after reducing the can temperature down to 120°C during run 4211 was an adherent film obtained.

It was surprising that we could not reproduce the results from run 4208 since other PECVD reactors reportedly produce good devices with 200°C can temperatures. The cause for this limitation in our system is not known, however using a can temperature close to or equal to the p-layer deposition temperature (150°C) has yet to be tried and may prove to be beneficial.

Use of Lower Pressures

To increase throughput, it is necessary to produce two devices a day, one in the morning and one in the afternoon. However when using a chamber pressure of 0.5 Torr throughout device production,

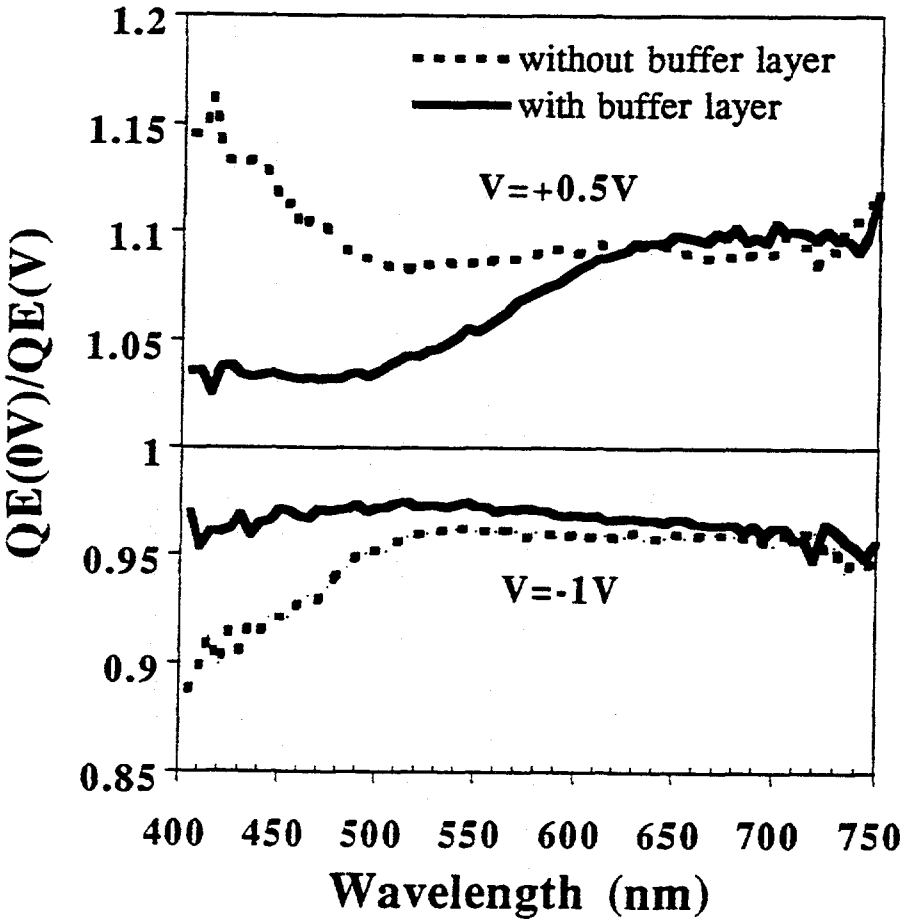

Figure 57. Ratios of quantum efficiencies measured using no electrical bias to those obtained using 0.5 and -1V bias for devices prepared with and without buffer layers.

Table 28. Devices prepared with and without buffer layers and Ti/Ag contacts

Device	Buffer layer	V_{oc} (V)	FF (%)	J_{sc} (mA/cm^2)	η (%)
4194	No	0.84	68	10.9	6.2
4195	No	0.83	68	10.7	6.1
4196	No	0.84	67	11.4	6.4
4198	Yes	0.86	69	11.2	6.6

Table 29. Devices prepared with and without buffer layers and ITO/Ag contacts

Device	Buffer layer	V_{oc} (V)	FF (%)	J_{sc} (mA/cm^2)	η (%)
4194	No	0.83	64	13.9	7.4
4195	No	0.82	63	13.7	7.0
4198	Yes	0.86	67	14.0	8.0

the device quality in the afternoon is always poorer than the one made in the morning. Figure 58 and Table 30 show bias dependencies of the red response and smaller FF noted for the afternoon devices, suggestive of poor hole collection due to P contamination.

Reducing the pressure to 0.2 Torr produced morning and afternoon devices which were identical. Very little bias dependence of the red response is seen in the spectra displayed in Figure 59 for either the morning and afternoon runs produced at the lower pressure, and both had similar cell properties, as shown in Table 30. We suspect that the lack of reproducibility at 0.5 Torr pressure is related to lingering PH_3.

<u>i-layer deposition prior to device preparation</u>

Another technique known to improve reproducibility is to deposit an i-layer between device depositions. This procedure is standard in other systems including our photo-CVD reactor. The i-layer deposition coats the canister and reactor walls, reducing the possibility for dopant contamination related to previous runs. Our first attempt to coat the reactor used an a-SiC:H layer (4188). The following device (4189) had an extremely low FF (32%) and J_{sc} (8 mA/cm^2). A second attempt, this time with an a-Si:H i-layer (4215), led again to a device (4216) with a low J_{sc} (8 mA/cm^2) but a reasonable FF (68%). In both cases, the small J_{sc} was associated with low blue response. The cause for these poor cell results is not obvious.

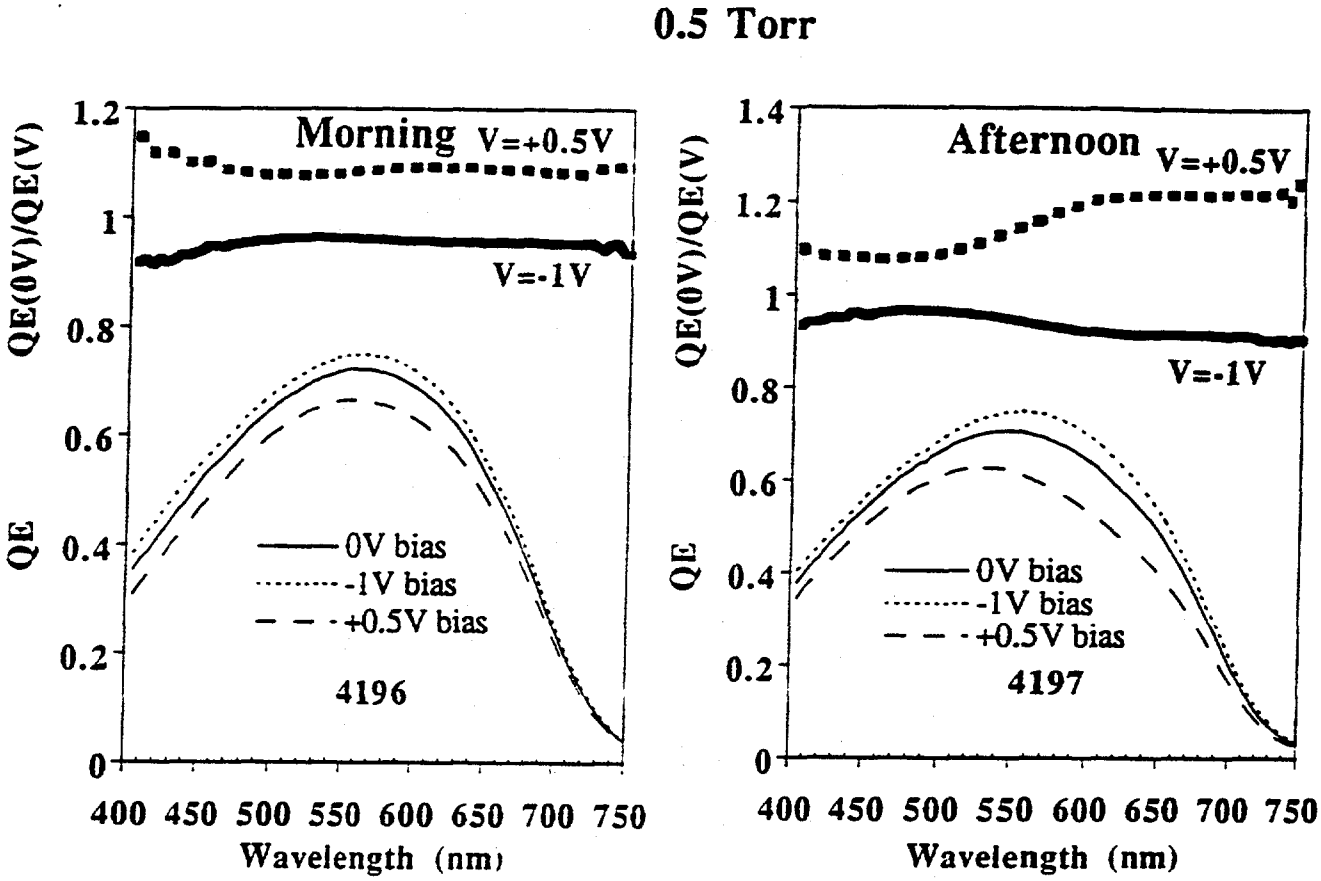

Figure 58. Quantum efficiencies measured using electrical biases of ϕV, 0.5V and -1V for devices prepared in the morning and afternoon of the same day with a chamber pressure of 0.5 Torr.

0.2 Torr

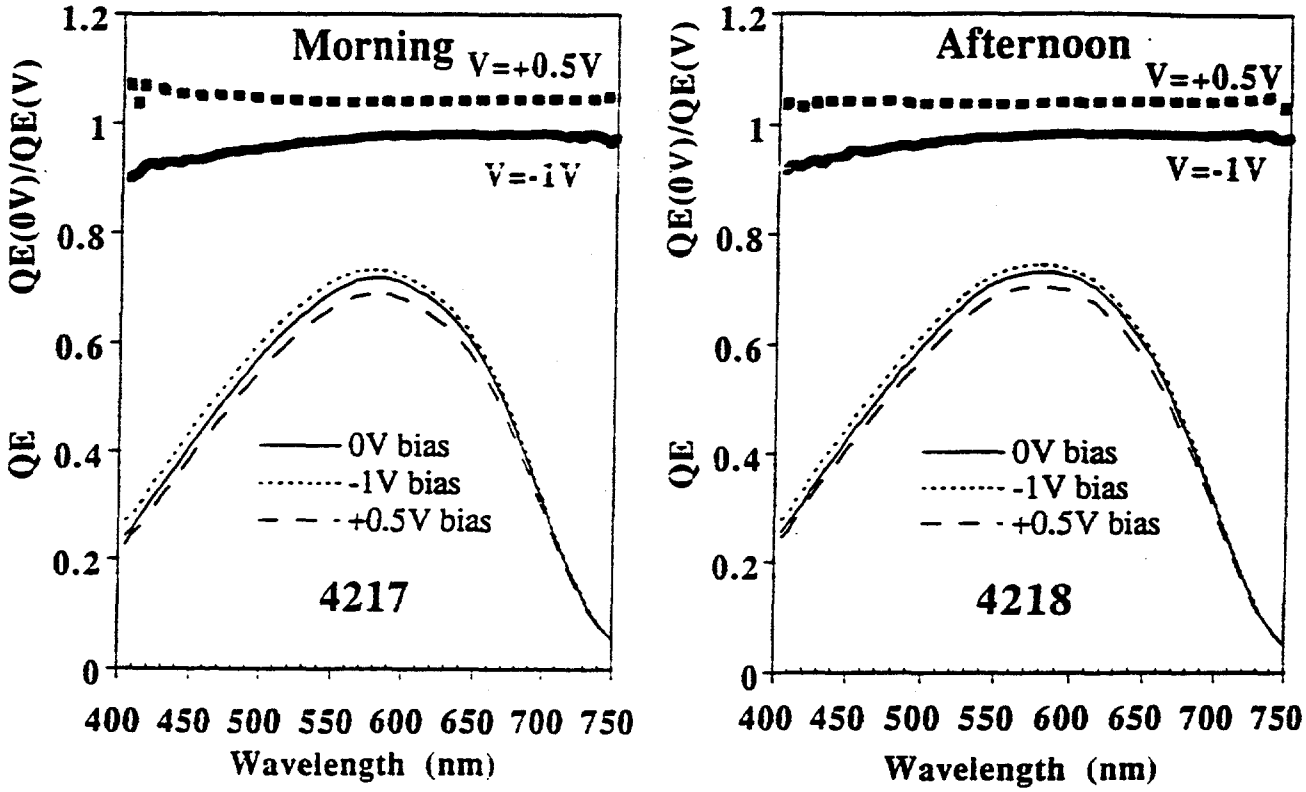

Figure 59. Quantum efficiencies measured using electrical biases of ϕV, 0.5V, and -1V for devices prepared in the morning and afternoon of the same day with a chamber pressure of 0.2 Torr.

Table 30

Devices prepared using different chamber pressures

Device	Buffer layer ?	Chamber Pressure (Torr)	Date of Deposition	Time of Day	V_{oc} (V)	FF (%)	J_{sc} (mA/cm^2)	η (%)
4194	No	0.5	10/22	Morning	0.84	68	10.9	6.2
4195	No	0.5	10/25	Morning	0.83	68	10.7	6.1
4196	No	0.5	10/26	Morning	0.84	67	11.4	6.4
4197	No	0.5	10/26	Afternoon	0.84	63	10.9	5.7
4217	Yes	0.2	11/18	Morning	0.85	70	11.7	6.9
4218	Yes	0.2	11/18	Afternoon	0.86	70	11.7	7.1

J_{sc} Improvements

Table 30 showed that we were able to deposit two devices in the same day, back-to-back, having good V_{oc} and FF. However, the J_{sc} values are 20% lower than expected for that back contact and i-layer thickness. QE measurements indicated that we should focus on improving the blue response by reducing the p-layer absorption loss.

We developed a method of extracting the p-layer thickness and bandgap from the measured QE. This tool proved very valuable in guiding device depositions. The technique and its application are described in detail in Section 3.2. The key result was that the effective p-layer thickness was 4-5 times greater than we had expected based on characterization of thick p-layers, suggesting that the growth rate of the initial stages of thin p-layers on TCO is 4-5 times greater than the growth rate of thick films on glass, on the order of 10-17 Å/s. This is not reported by others. Thus, even an 11 second p-layer was 190 Å thick. This observation lead us to reduce growth rates with H dilution. We found it necessary to increase both the CH_4 and B_2H_6 flows. This resulted in cells with the highest J_{sc} yet for Ti/Ag contacts, 14 to 15 mA/cm^2. Analysis of the QE showed that the p-layer growth rate was reduced significantly to 1.5 Å/s. The QE at 400 nm had increased to 65%. However, V_{oc} and FF were lower. Improving the TCO/p-layer interface with H diluted p-layers will be investigated in the future.

Summary of Device Results

By incorporating the various techniques to reduce B and P contamination, we were able to reproducibly prepare devices with $V_{oc}\approx 0.84\text{-}0.88V$, $J_{sc}\approx 12$ mA/cm^2 and $FF\approx 68\text{-}70\%$ leading to $EFF\approx 7\%$. Figure 60 shows the trend of average efficiency from each run versus run number for this year. Note the general trend of increasing efficiency, indicating progress, and reduced scatter, indicating improved reproducibility. We deposited several devices having efficiencies greater than 8% with Ti/Ag or ITO/Ag contacts. To reach 9% efficiencies, our immediate plans are to attempt to improve J_{sc} through variations in the p and buffer layer thicknesses and the use of a hydrogen diluted plasma during p-layer growth.

We also plan to start grading the buffer layer to possibly increase V_{oc} and FF further.

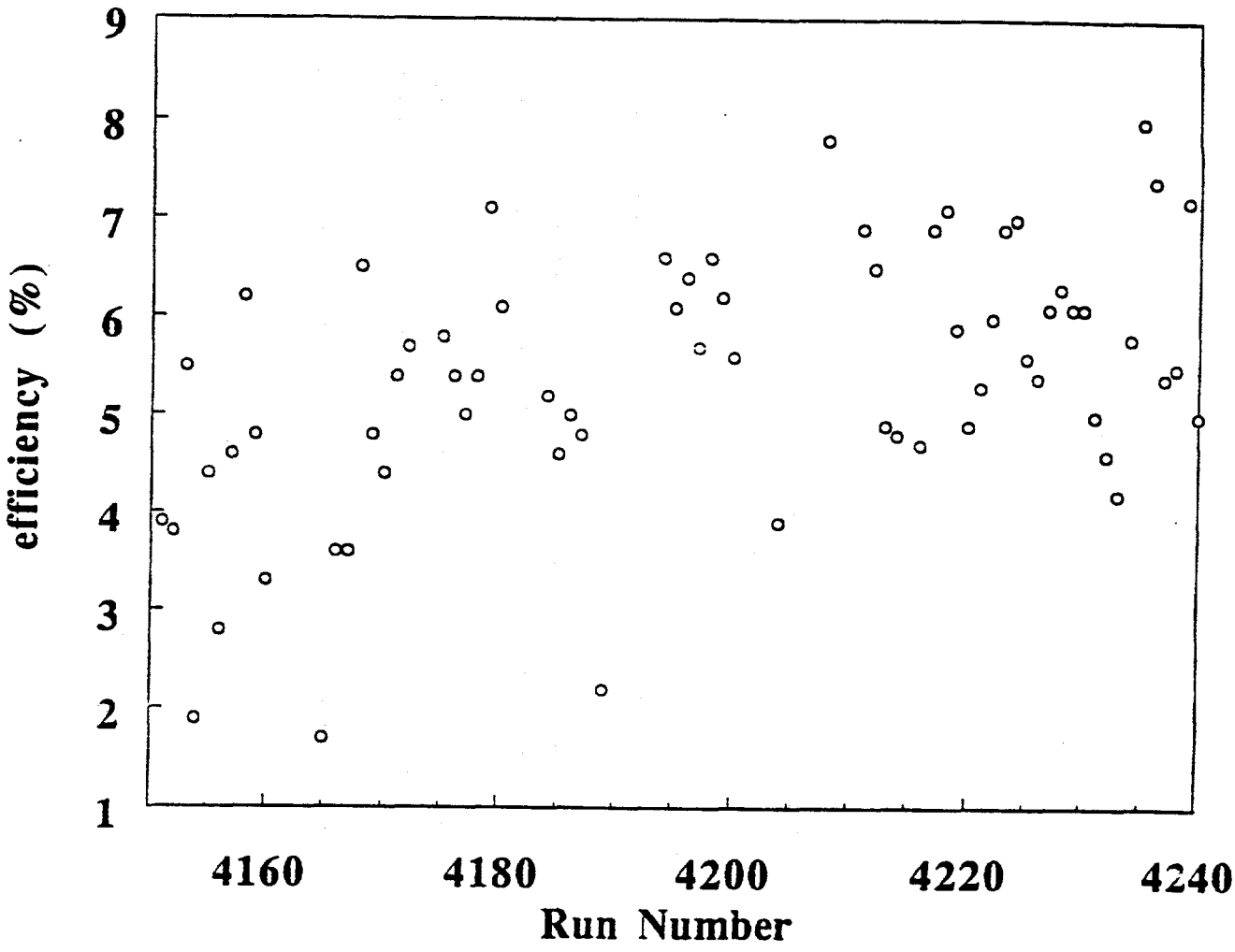

Figure 60. Progression in cell efficiencies during FY1993.

3.0 SOLAR CELL MEASUREMENTS AND ANALYSIS

3.1 POLYCRYSTALLINE SOLAR CELL MEASUREMENTS AND ANALYSIS

The current voltage characteristics of a number of $CuInSe_2$/CdS and $Cu(InGa)Se_2$/CdS solar cells made by various conditions and laboratories have been measured under a wide range of temperatures and illumination conditions and then been analyzed and compared. The results of the analysis are also compared with a device model that assumes the forward current of these devices is controlled by recombination within the $CuInSe_2$ or $Cu(InGa)Se_2$ absorber layer through a continuous exponential distribution of localized states within the bandgap. Preliminary current voltage measurements on CdTe/CdS solar cells are also analyzed and compared.

3.1.1 $Cu(InGa)Se_2$ Device Measurements

Current-voltage characteristics of eleven different $CuInSe_2$/CdS and $Cu(InGa)Se_2$/CdS devices are analyzed in this report. Nine of these cells had complete current-voltage curves taken over a temperature range from 218K to 373K at four different light intensities (dark, ~5mW/cm^2, ~20mW/cm^2, and ~80mW/cm^2). The remaining two $Cu(InGa)Se_2$/CdS cells from NREL only had V_{oc} and J_{sc} measured in this temperature range, but an additional light intensity (~1mW/cm^2) was used. A listing of the devices as well as their origin and processing is shown in Table 31. The table also references other publications wherein measurements on these devices were reported.

Table 32 gives the basic solar cell parameters when these devices were tested under AM1.5 illumination at 298K.

Analysis of the J-V data of $CuInSe_2$ -based solar cells has consisted of examining the V_{oc} at different temperatures and light intensities (30-33). In these cases it was assumed that V_{oc} was linear with respect to both temperature and $\log(J_{sc})$. The results of fitting V_{oc} in this way are shown in Table 33.

Here the T=OK intercept of V_{oc} is V_o and the slopes of the fitted lines, if one assumes a constant diode quality factor (A) would range between 1.3 and 1.8, with qV_o approximately equal to the bandgap of the absorber layer. Previously, this behavior was ascribed to recombination by a set of discrete midgap states in the absorber (discrete state Shockley-Read-Hall recombination). However, this model does not quantitatively explain the range of values obtained for the diode quality factors. Below we suggest an alternative method for analyzing the data using an exponential distribution of localized states within the bandgap of the absorber material as a first attempt to quantitatively explain these results.

Table 31 Origin, identification and method of manufacture of the $CuInSe_2$-based cells discussed in this analysis.

(Origin) Device I.D. #	Absorber Fabrication	(ref. no.)
(Institute of Energy Conversion)		
IEC-32187-22-12	evaporated $CuInSe_2$	30, 31, 32 & 33
IEC-32220-22-5	evaporated $CuInSe_2$	30 and 31
IEC-89095-2-9	$CuInSe_2$ selenized with H_2Se	31 and 32
IEC-61079-23-5	$CuInSe_2$ selenized with Se	31 and 32
IEC-32356-33-5	evaporated $Cu(In,Ga)Se_2$	33
IEC-32361-33-3	evaporated $Cu(In,Ga)Se_2$	33
(Siemens Solar Industries)		
SSI-16543-4-3	proprietary	31 and 32
(Institute for Physical Electronics, University of Stuttgart)		
STU-M243-4	evaporated $CuInSe_2$	32
(Energy Photovoltaics Inc.)		
EPV-11133-21-5	$CuInSe_2$ selenized with Se	32
(National Renewable Energy Laboratory)		
NREL-S478-14-5	evaporated $Cu(In,Ga)Se_2$	
NREL-S416-23-3	evaporated $Cu(In,Ga)Se_2$	

Table 32 J-V parameters of the $CuInSe_2$-based solar cells at 25°C under AM1.5 global illumination

Device I.D. #	Absorber Fabrication	V_{oc} (V)	J_{sc} (mA/cm^2)	FF (%)	Eff. (%)
IEC-32187-22-12	evaporated $CuInSe_2$	0.44	34	68	10.1
IEC-32220-22-5	evaporated $CuInSe_2$	0.42	34	67	9.3
IEC-89095-2-9	$CuInSe_2$ selenized with H_2Se	0.45	35	65	10.2
IEC-61079-23-5	$CuInSe_2$ selenized with Se	0.43	33	65	9.5
IEC-32356-33-5	evaporated $Cu(In,Ga)Se_2$	0.57	27	65	10.0
IEC-32361-33-3	evaporated $Cu(In,Ga)Se_2$	0.59	24	69	9.9
SSI-16543-4-3	proprietary**	0.45	37	62	10.2
STU-M243-4	evaporated $CuInSe_2$	0.44	38	68	11.2
EPV-11133-21-5	$CuInSe_2$ selenized with Se	0.43	35	63	9.7
NREL-S478-14-5	evaporated $Cu(In,Ga)Se_2$	0.60	29	72	12.5
NREL-S416-23-3	evaporated $Cu(In,Ga)Se_2$	0.65	29*	73	13.8*

* with antireflection coating

**contains a small unspecified Ga content.

3.1.2 $Cu(InGa)Se_2$ J-V Analysis

As an example, the current voltage measurements made on an IEC $CuInSe_2/CdS$ device prepared by elemental evaporation (#32220-22-5) is discussed. Graphs of the J-V curves are shown in Figure 61. The contact resistance-like non linear behavior that seems to be characteristic of almost all $CuInSe_2/CdS$ and $Cu(InGa)Se_2/CdS$ solar cells is evident in the forward current (J>0) J-V curves below 298K. Figure 62 shows the slope of the J-V curve (dV/dJ from numerical differentiation) plotted as a function of the inverse total current $[1/(J+J_{sc})]$. In this case the contact resistance-like behavior at lower temperatures is quite evident at higher total currents. If these plots are linear, as they are at higher temperatures,a diode quality factor (A) and a constant series (R_s) can be extracted from the slope and intercept respectively. Since then:

$$dV/dJ = R_s + (AkT/q)/(J+J_{sc}).$$

An example is shown in Figure 63. After R_s has been determined, another form of the J-V data $[\ln(J+J_{sc})$ vs. $(V-R_sJ)]$ is shown in Figure 64. In this case, linear behavior implies that the reverse saturation current (J_o) and the diode quality factor (A) can be extracted. Since:

$$\ln(J+J_{sc}) = \ln(J_o) + (q/AkT)(V-R_sJ)$$

The same example shown in Figure 63 is replotted in Figure 65 to demonstrate this.

From about room temperature and above (T>=300K), the plots of dV/dJ vs. $1/(J+J_{sc})$ and $\ln(J+J_{sc})$ vs. $(V-R_sJ)$ are quite linear over a wide range of voltage for almost all $CuInSe_2/CdS$ and $Cu(InGa)Se_2/CdS$ devices measured. The only exceptions were the dark J-V measurements of the device from the University of Stuttgart (#STU-M243-4), which were unstable apparently due to highly photoconductive CdS appeared to play a role.

The linear behavior in Figures 64 and 65 imply that all of the devices at or above room temperature follow a simple thermally activated diode behavior of the form:

$$J = J_o\exp[(q/AkT)(V-R_sJ)] - J_{sc}$$

$$\text{with: } J_o = J_{oo}[\exp(-E_a/kT)]$$

Table 33 Listing of the intercept (V_o) and slope (dV_{oc}/dT) parameters used to describe the V_{oc} vs. temperature data measured at 3 different light intensities as shown in Figures 66a-66k.

Device#	Average J_{sc} (mA/cm^2)	Vo±0.05 (V)	dV_{oc}/dT±0.1 (-mV/°C)
EPV-11133-21-5	30.0	1.00	2.0
	8.44	1.00	2.2
	1.89	0.95	2.2
IEC-32187-22-12	23.3	0.99	1.9
	5.84	0.99	2.0
	1.65	0.97	2.1
IEC-32220-22-5	22.8	0.91	1.7
	5.80	0.92	1.9
	1.64	0.90	2.0
IEC-32356-33-5	21.2	1.19	2.1
	5.82	1.18	2.3
	1.29	1.14	2.4
IEC-32361-33-3	18.1	1.10	1.8
	5.03	1.06	1.9
	1.13	1.02	2.1
IEC-61079-23-5	25.6	1.00	1.9
	7.40	1.00	2.1
	1.80	1.01	2.2
IEC-89095-2-9	25.9	1.00	1.9
	7.60	0.97	2.0
	1.82	0.92	2.1
NREL-S416-23-5	23.4	1.24	2.0
	6.49	1.24	2.2
	1.47	1.22	2.3
	.361	1.23	2.6
NREL-S478-14-5	24.8	1.17	2.0
	6.99	1.16	2.1
	1.54	1.14	2.2
	.380	1.11	2.3
SSI-16543-4-3	29.0	1.03	2.0
	8.27	1.04	2.2
	1.98	1.03	2.3
STU-M243-4	29.1	0.98	1.9
	8.20	1.00	2.1
	2.02	0.98	2.2

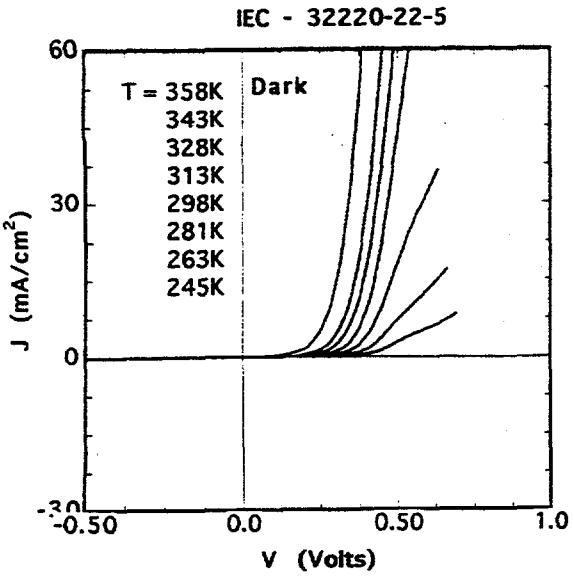

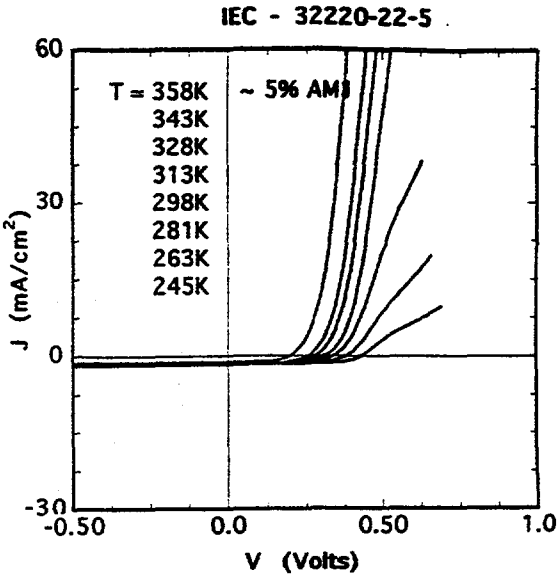

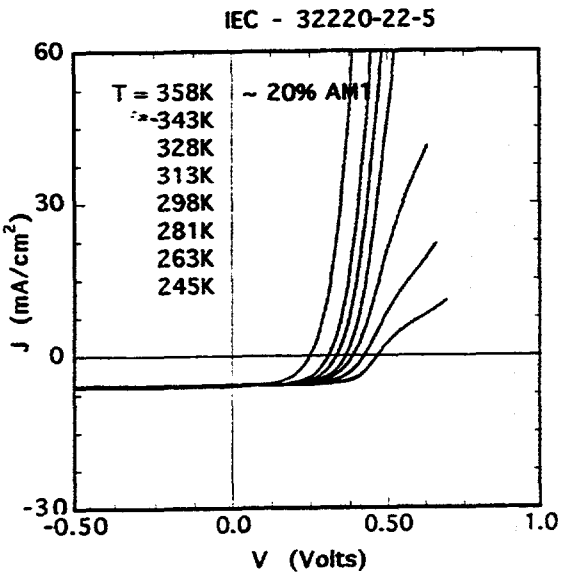

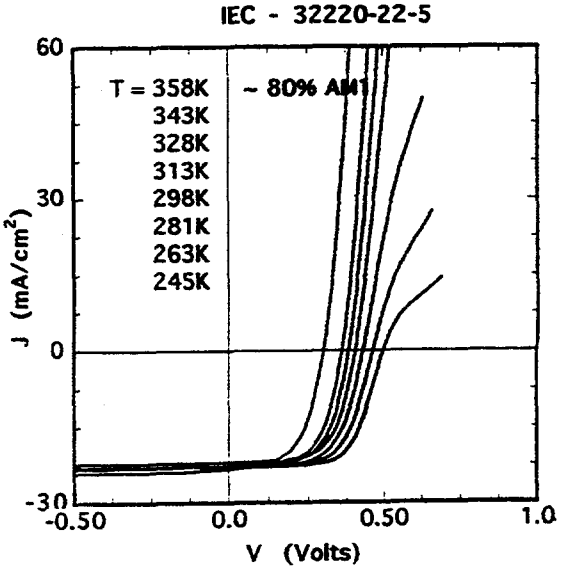

Figure 61. J-V curves as a function of light intensity and temperature for the $CuInSe_2$ device discussed. In each plot the temperature decreases from left to right over the range indicated.

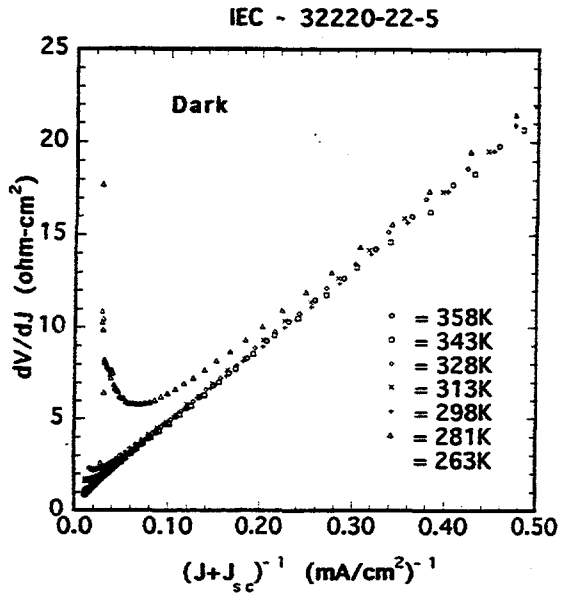

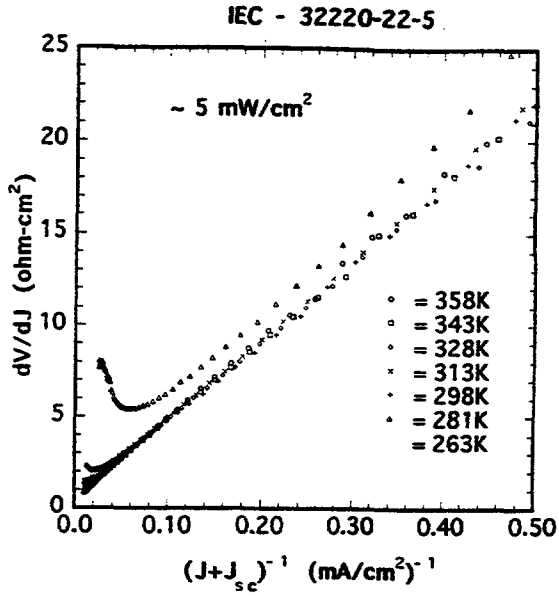

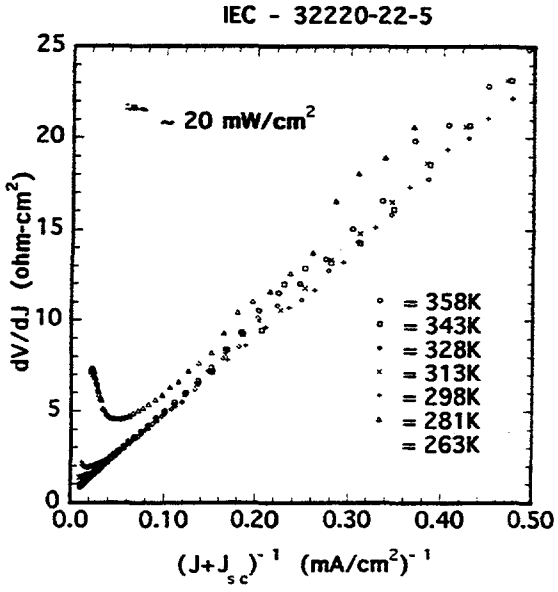

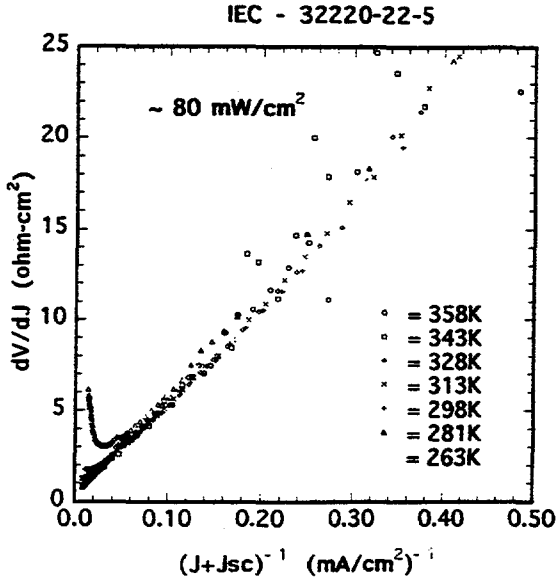

Figure 62. Slope (dV/dJ) of the J-V curve vs. 1(J+J_{sc}) as a function of light intensity and temperature for the $CuInSe_2$ device discussed.

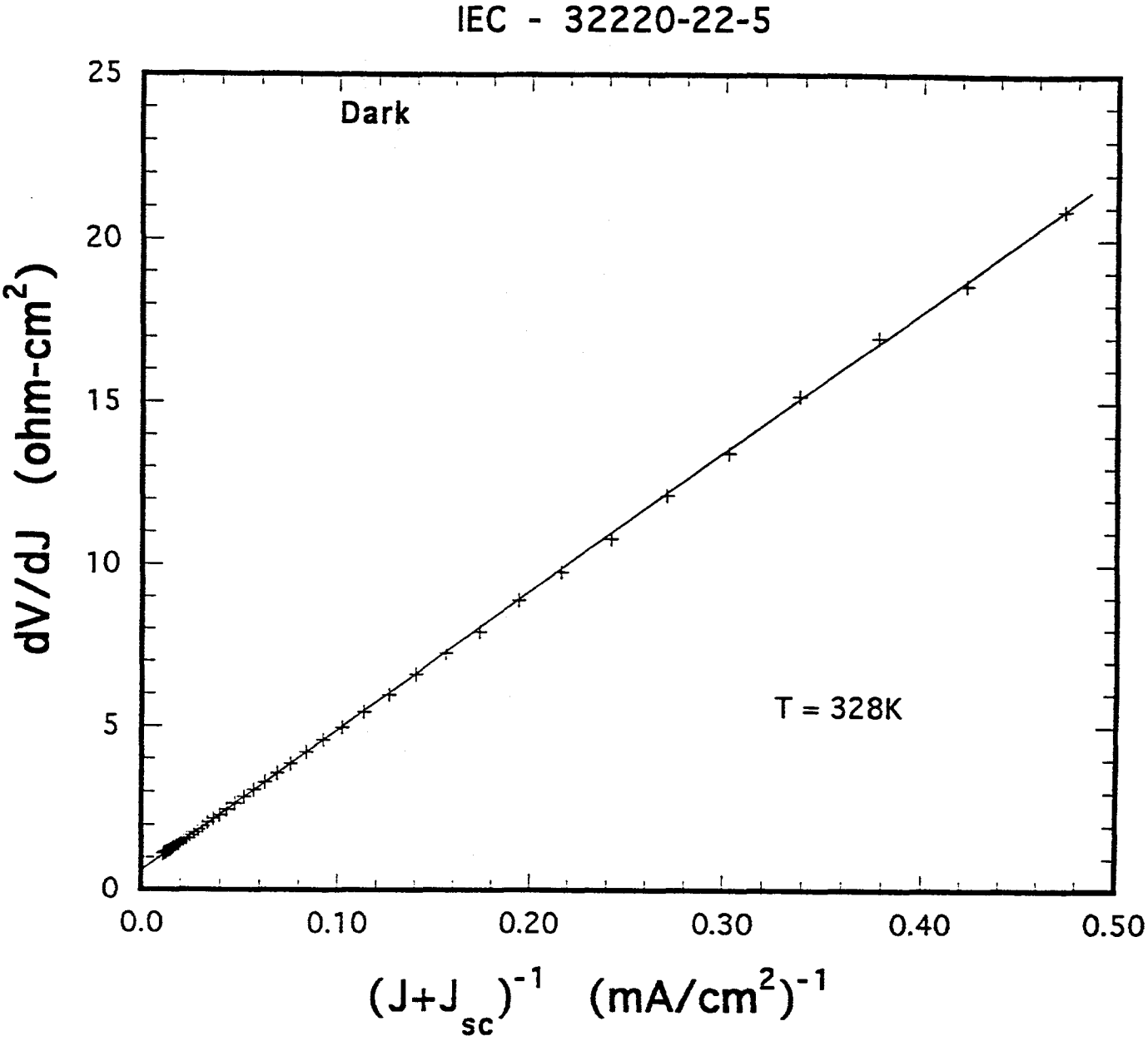

Figure 63. Slope (dV/dJ) of the J-V curve vs. $1(J+J_{sc})$ in the dark at 328K. The line is a fit to a diode A-factor of 1.5 and a series resistance of 0.6 (ohm-cm^2).

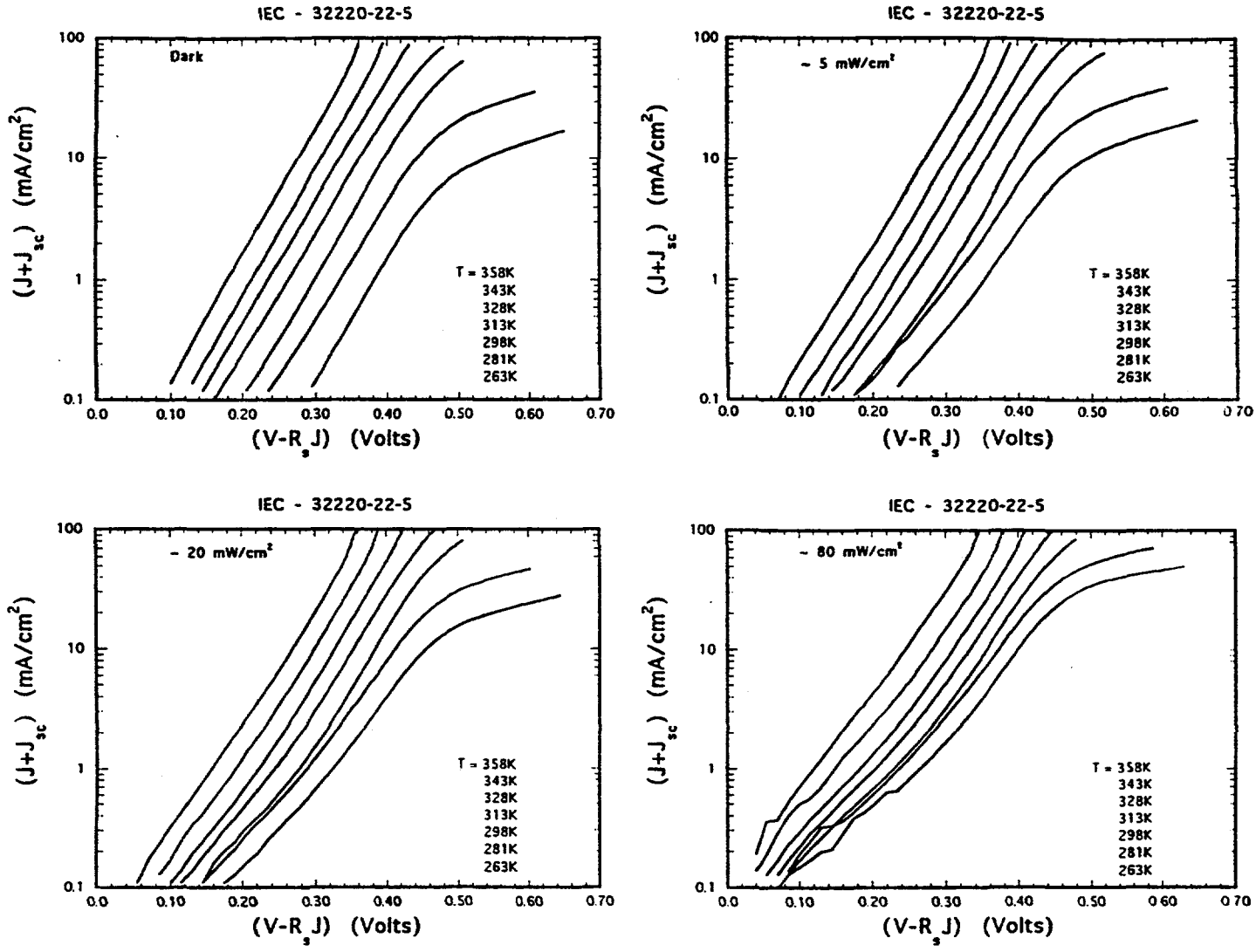

Figure 64. Log $(J+J_{sc})$ vs. $(V-R_sJ)$ as a function of light intensity and temperature for $CuInSe_2$ device discussed. The value of R_s is 0.6 (ohm-cm^2) for all the plots. In each plot the temperature decreases from left to right over the range indicated.

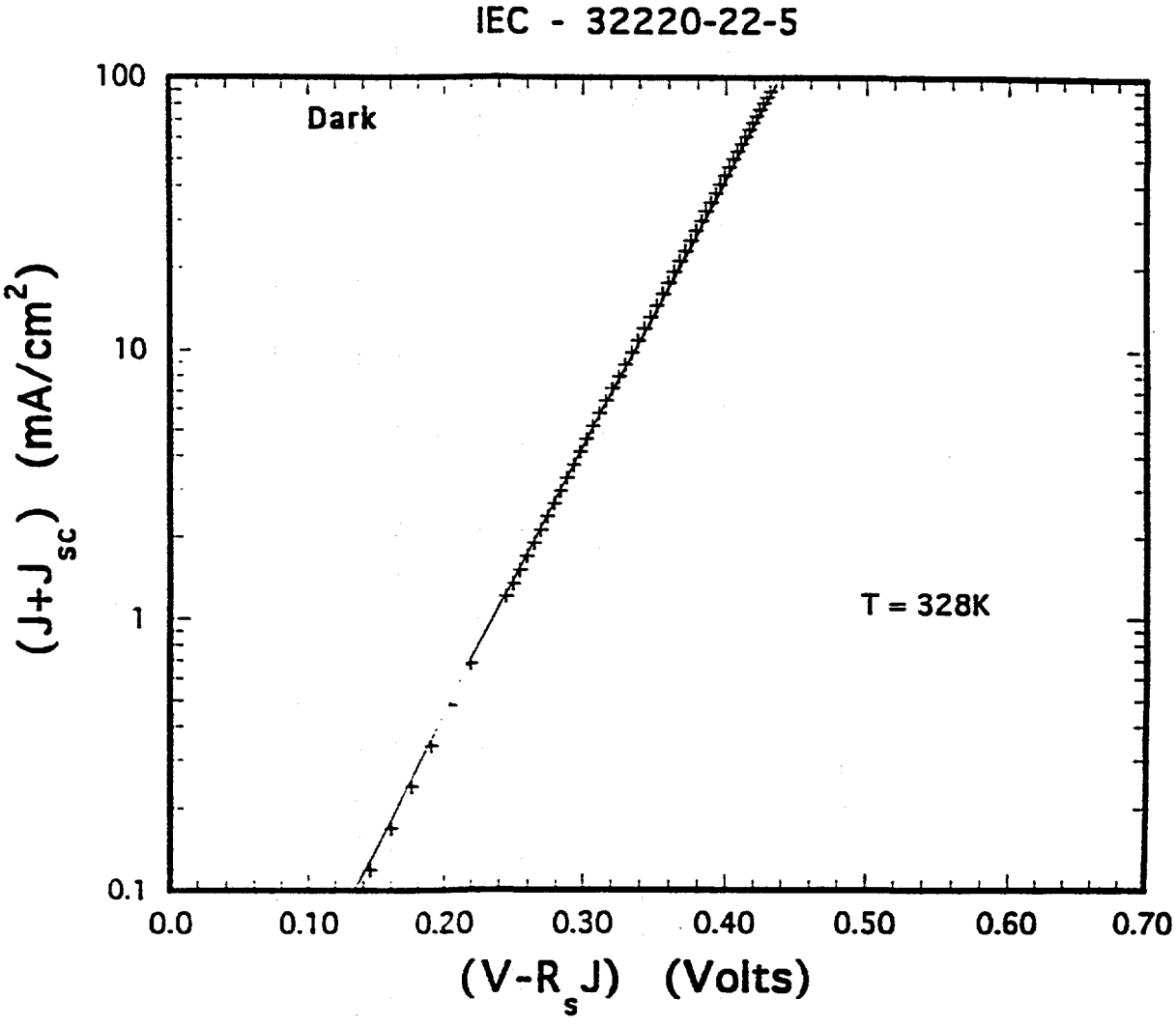

Figure 65. Log $(J+J_{sc})$ of the J-V curve vs. $(V-R_sJ)$ in the dark at 328K. The line is a fit to a diode A-factor of 1.5 and a J_o of 3.9E-03 (mA/cm^2). Note: the value of R_s is 0.6 ($ohm-cm^2$).

Because of the limited temperature range, it is difficult to accurately determine the value of E_a. For the same reason, small temperature dependencies of the diode quality factor (A) and series resistance (R_s) cannot be deduced from the data. However, all of the diode quality factors determined from these J-V measurements lie in a range between 1.3 and 2.0 with activation energies between about 0.5 and 0.9 eV for the $CuInSe_2$/CdS devices.

Previously, because the diode quality factors measured were close to two and the measured activation energies were about equal to half the bandgap of the $CuInSe_2$ or $Cu(InGa)Se_2$ absorber, it was suggested that the mechanism controlling the forward current in these devices was electron - hole recombination in the absorber layer through a discrete set of defect or impurity states within the bandgap (34,35). This mechanism, known as Shockley - Read - Hall recombination, would explain an exponential J-V characteristic with a diode quality factor of two and an activation energy of half the bandgap of the absorber. However, the range of diode quality factors and activation energies discussed here cannot be explained quite that easily.

Recently (36,37), it has been suggested that an exponential distribution of localized states within the bandgap of the $CuInSe_2$ or $Cu(InGa)Se_2$ absorber, as used in early photoconductive devices or amorphous silicon solar cells (38,39), could be used to describe the J-V measurements. The distribution of recombination centers were represented by:

$$N_r(E) \sim \exp[-(E_c-E)/kT^*] \text{ or } \sim [\exp-(E-E_v)/kT^*],$$

where T* is a parameter that describes the distribution.

In this case, in the junction or space charge region of the absorber, the recombination current can be expressed as, for $T < T^*$:

$$J_r = J_o[\exp(qV/AkT)]$$

with: $A = 2T^*/(T+T^*)$ and $1 <= A <= 2$

and: $J_o = J_{oo}[\exp(-E_g/(2kT))]$

In this case:

$$V-R_sJ = (AkT/q)\ln(J+J_{sc}) - (AkT/q)\ln(J_o)$$

or:

$$V-R_sJ = (AkT/q)\ln(J+J_{sc}) - A[(kT/q)\ln(J_{oo}) + E_g/2]$$

and then: $E_a = E_g/2$.

Because of the limited temperature range, it is difficult to accurately determine the value of E_a and the small temperature dependence of the diode quality factor (A) predicted by this model. However, this model, unlike the previous one, does explain the diode quality factors that are not equal to two and activation energies not equal to half the bandgap of the absorber.

To extend the temperature range over which these parameters can be determined requires that the non-ohmic "contact-like", series resistance be eliminated. This can accomplished by examining V_{oc} (J=0) as a function of temperature and light intensity. Graphs of V_{oc} vs. temperature at the various light intensities are shown in Figures 66a to 66k. The dashed lines fit the equation are a fit to the equation :

$$V_{oc} = A[E_g/2q - (kT/q)\ln(J_{oo}/J_{sc})]$$

with: $A = 2T^*/(T+T^*)$

This is the J=0 case of the equation predicted by the model discussed above. In this case, the adjustable parameters are E_g, T^*, and J_{oo}. The values of these parameters are shown in Table 34.

Considering the wide range of devices measured, the behavior predicted by a simple exponential distribution of recombination states fits the V_{oc} vs. temperature and illumination (J_{sc}) data well. However, the values derived for the bandgaps as can be seen from Table 34 are usually larger than that of the actual $CuInSe_2$ or $Cu(InGa)Se_2$ absorber. Also, in one case (device # IEC-32361-33-3), the best fit to the data requires a distribution of recombination centers which increases exponentially towards the middle of the bandgap. Whether these anomalies are due to an oversimplification in the model, insufficient data at lower temperatures, or other difficulties needs to be determined.

Recently (40), measurements of free carrier lifetime and mobility have been made on evaporated polycrystalline thin films of $CuInSe_2$ prepared in the same way as films used for solar cells.

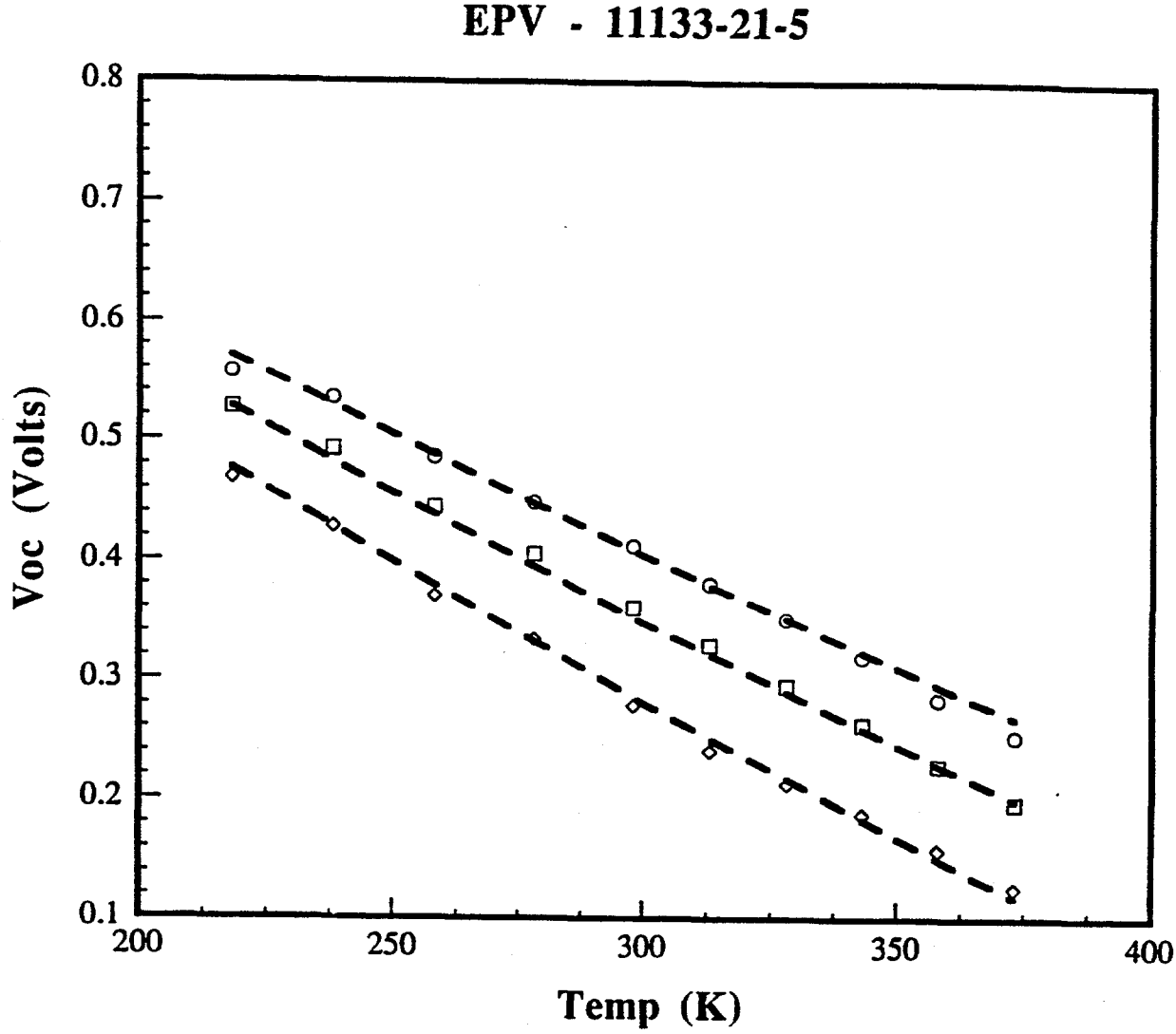

Figure 66a-k. V_{oc} as a function of temperature for the various light intensities for all the devices measured. The dashed lines are the values predicted from the model parameters shown in Table 34.

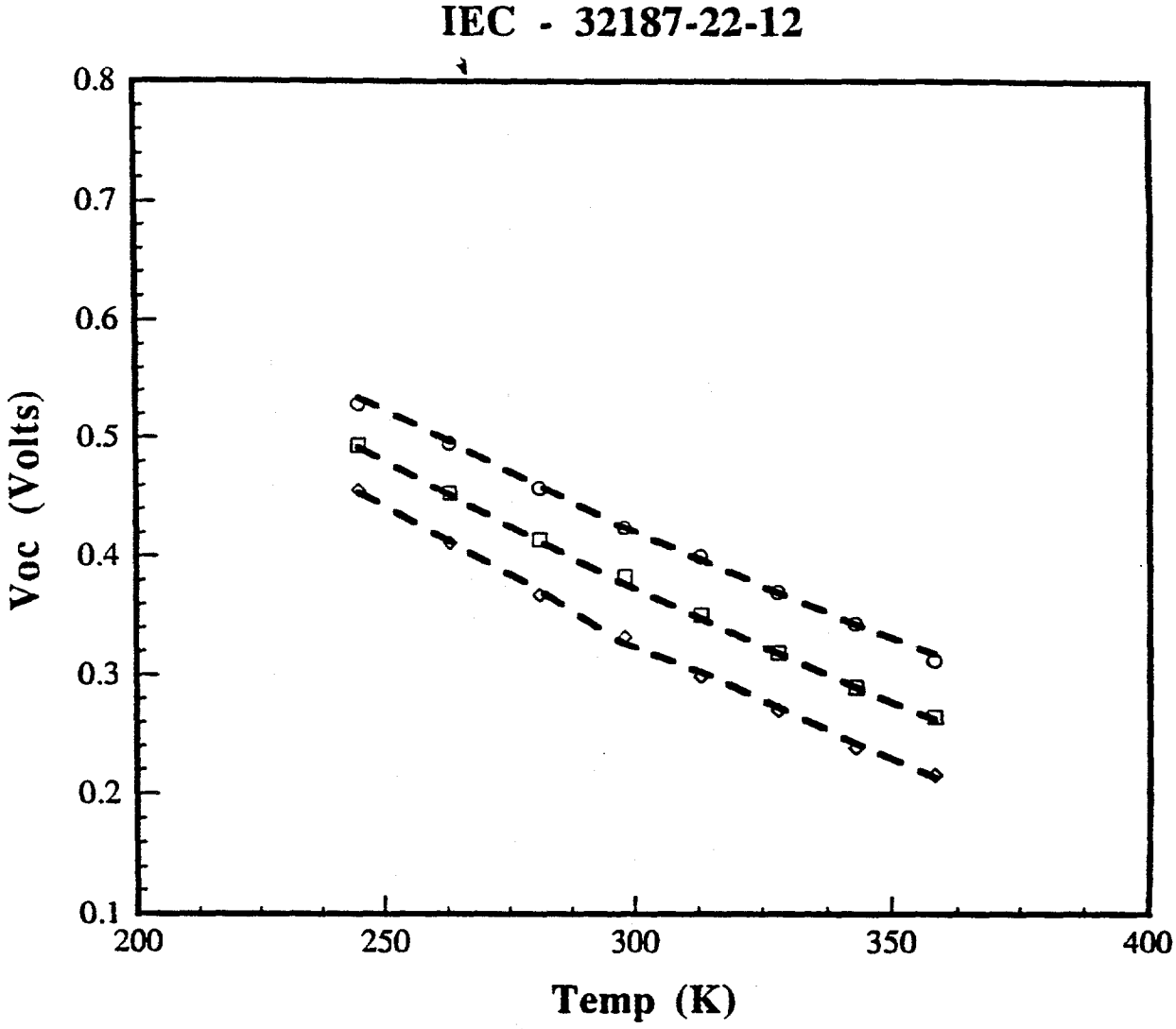
IEC - 32187-22-12
0.8
0.7
0.6
0.5
0.4
0.3
0.2
0.1
Voc (Volts)
200
250
300
350
400
Temp (K)

IEC - 32220-22-5

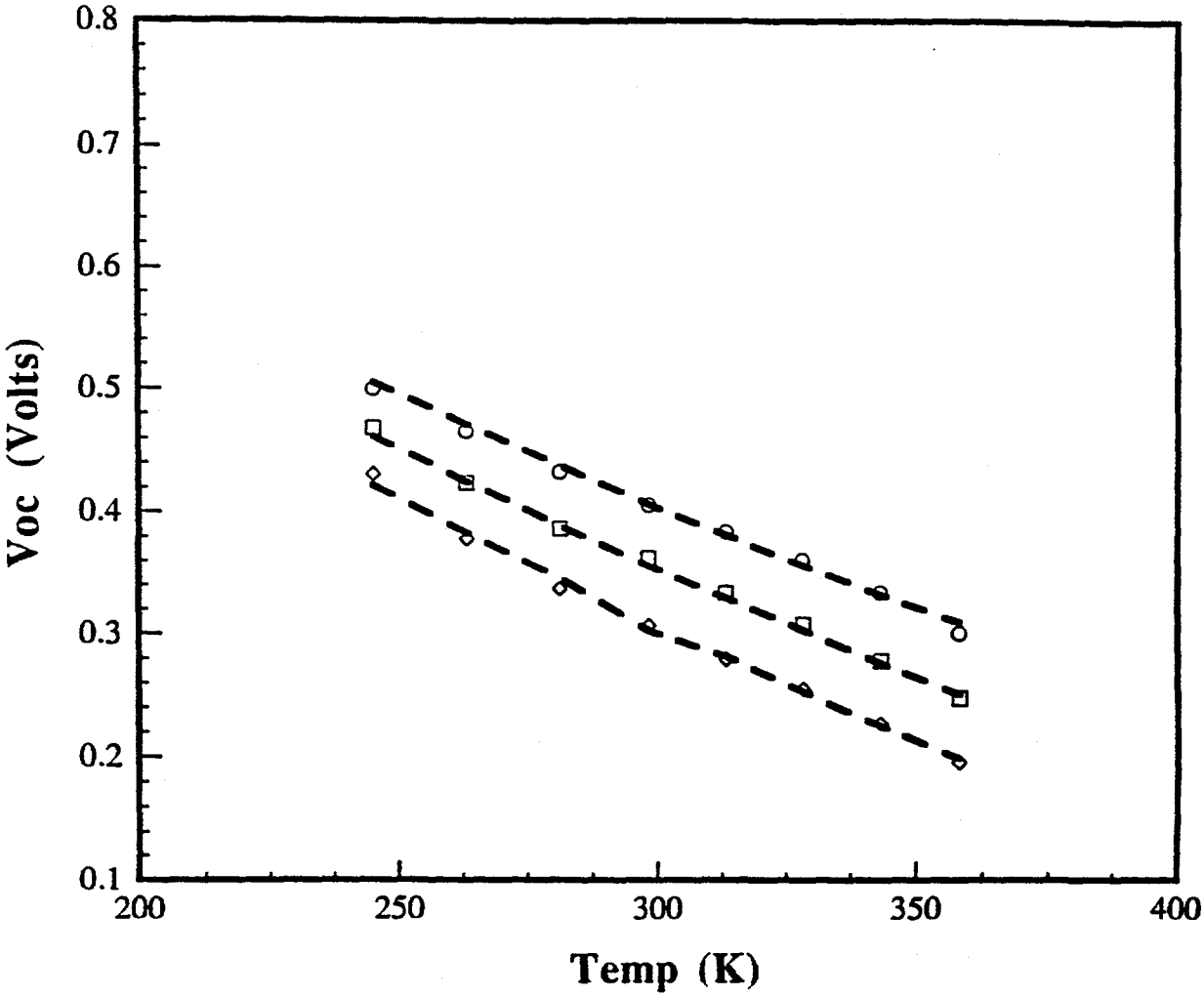

IEC - 32356-33-5

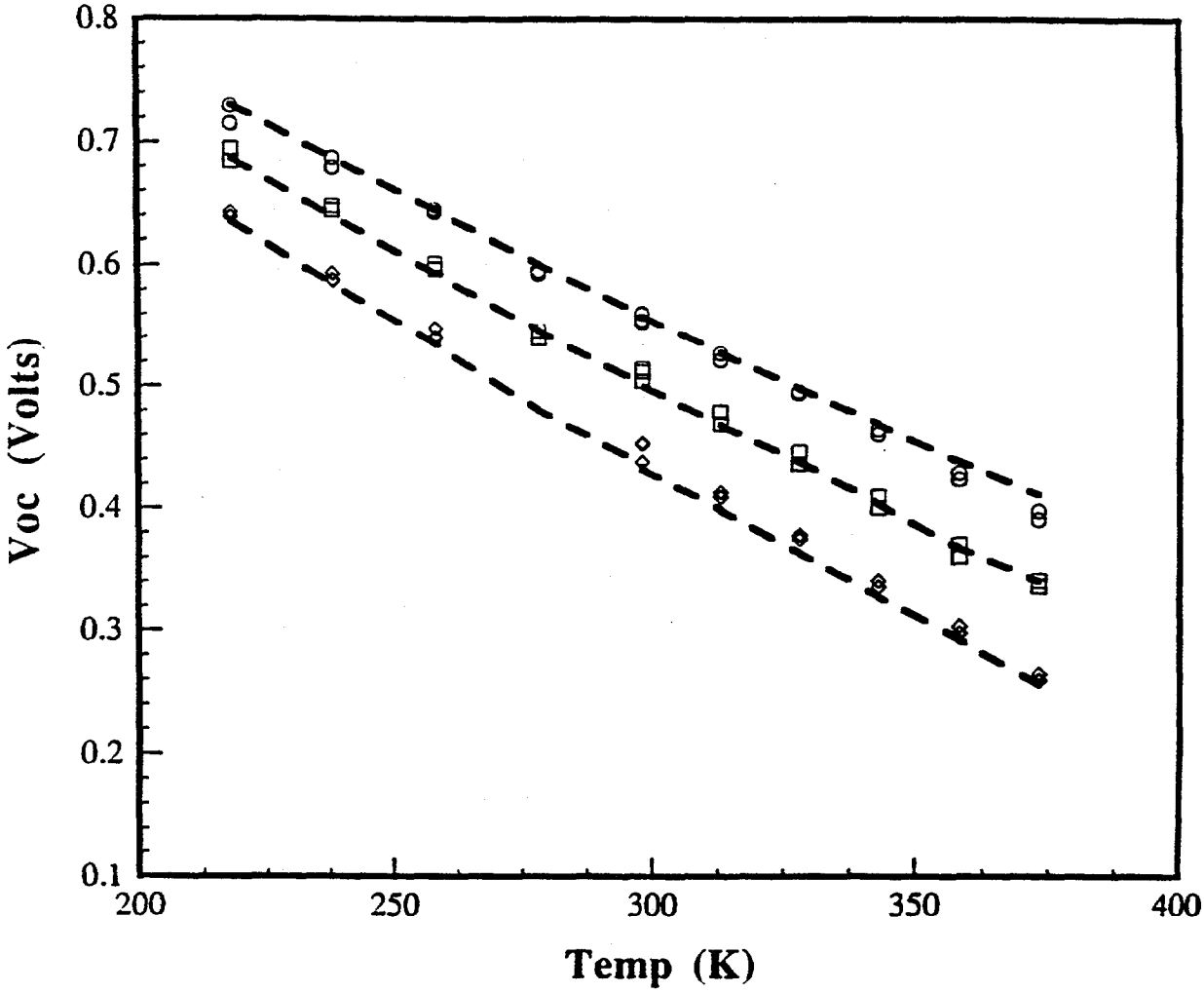

IEC - 32361-33-3

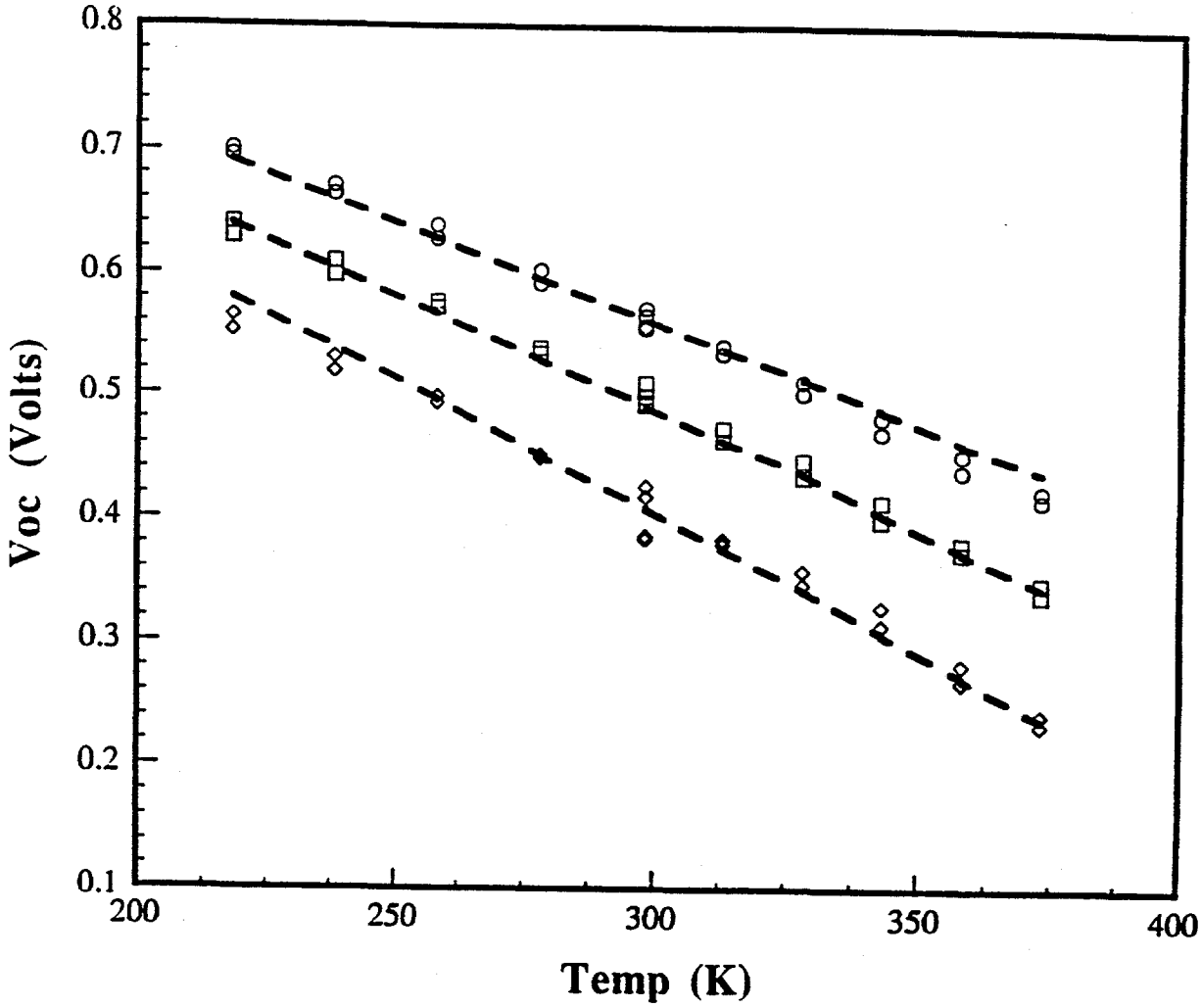

IEC - 61079-23-5

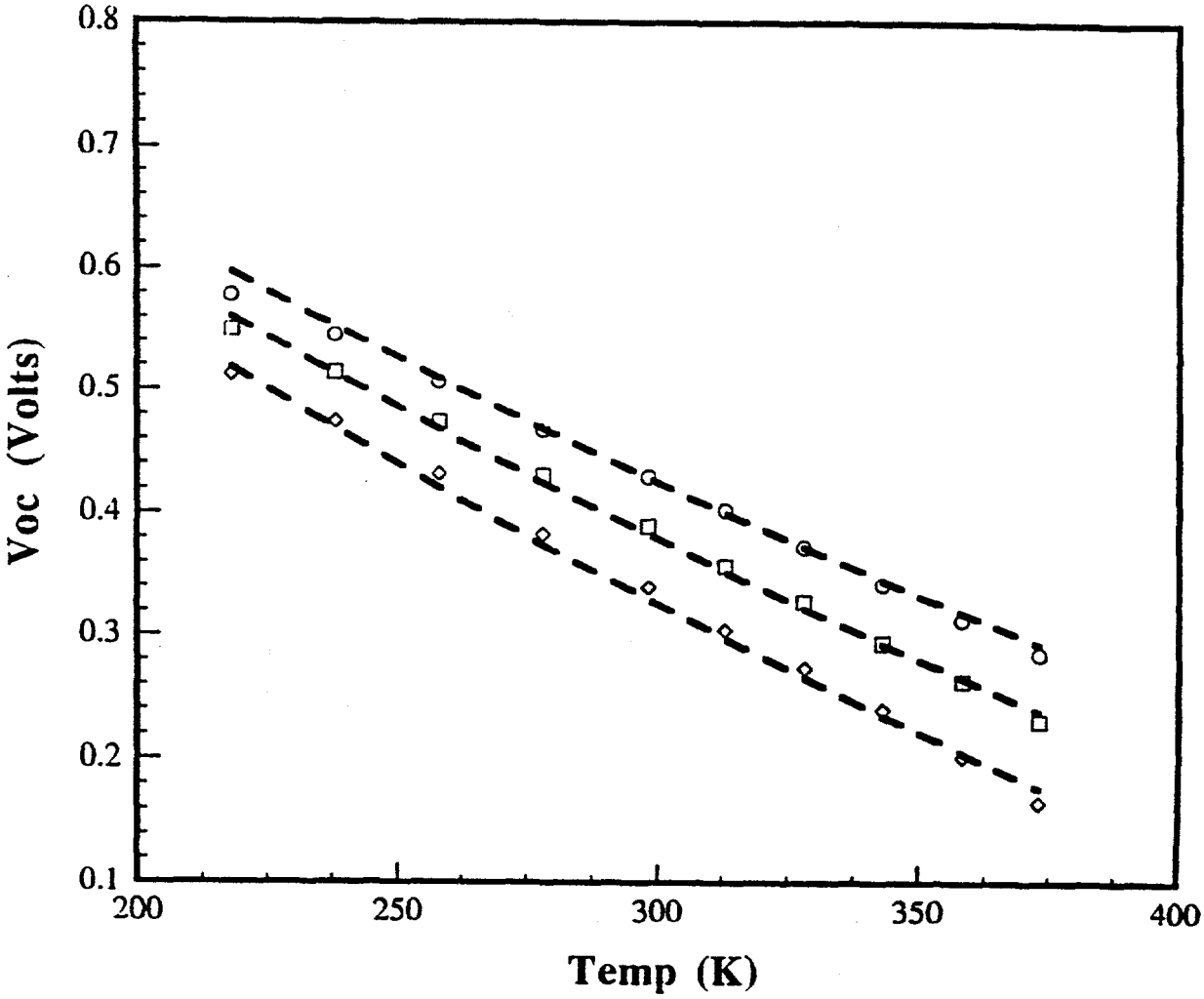

IEC - 89095-2-9

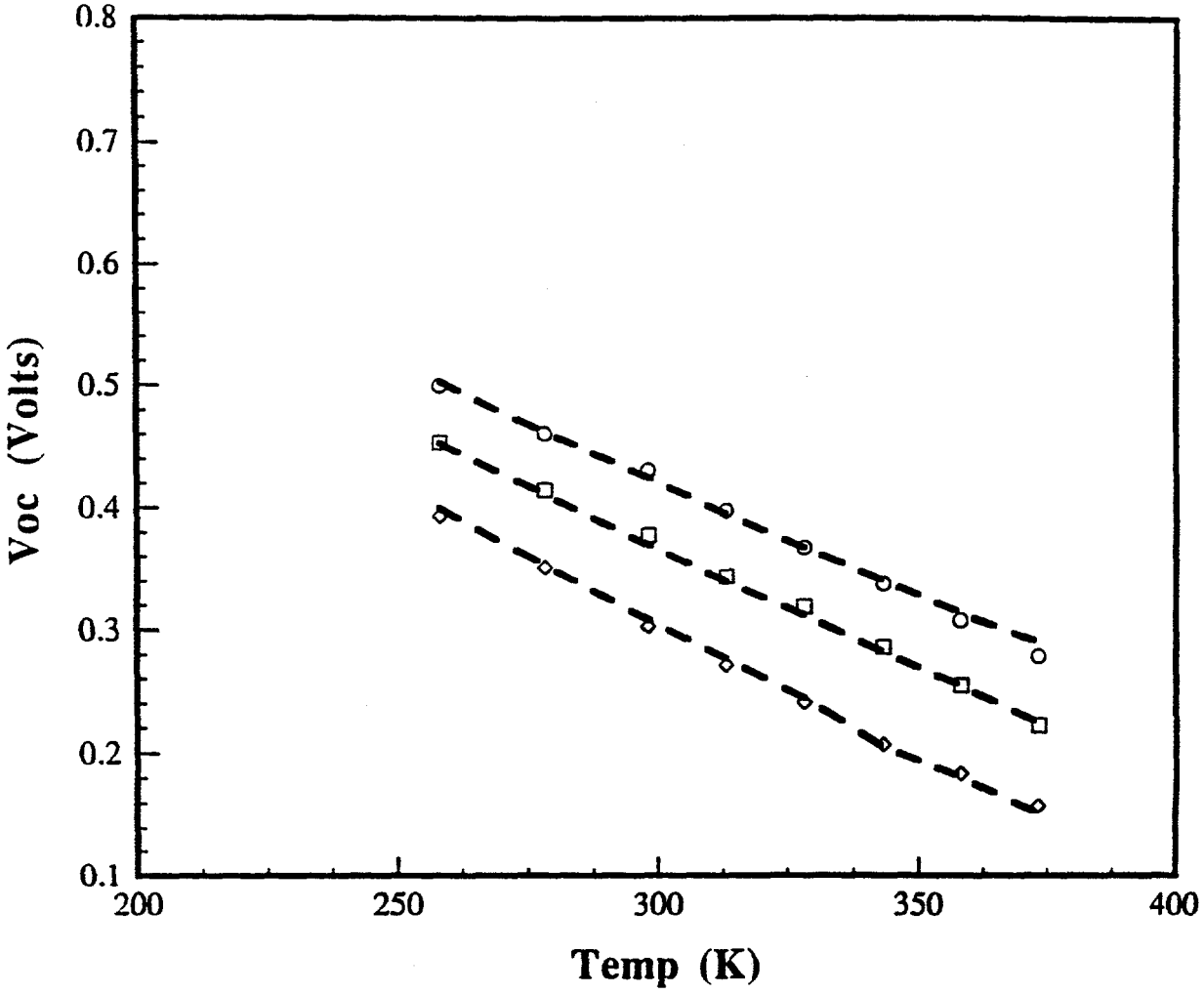

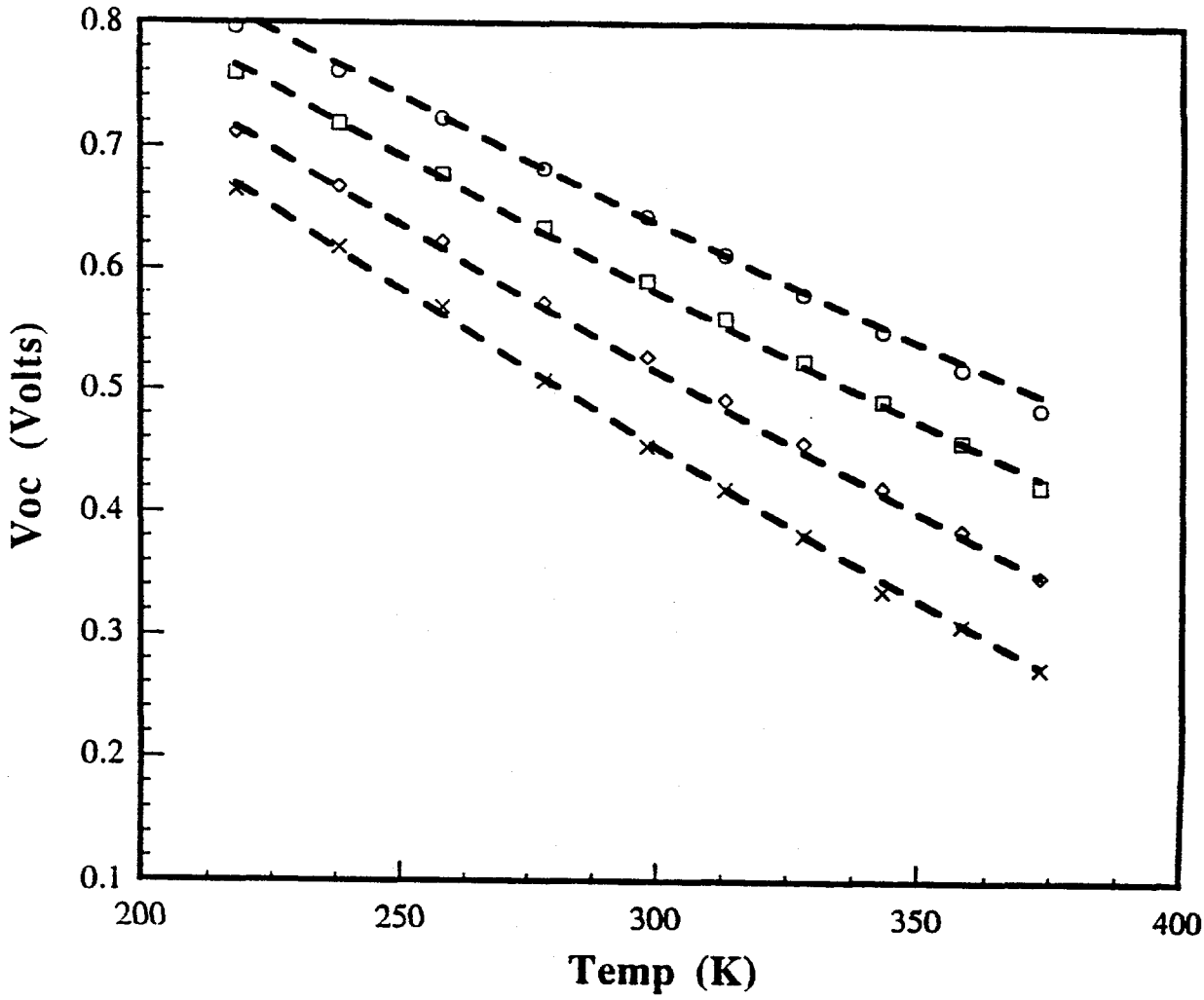
NREL - S416-23-5
Voc (Volts)
0.8
0.7
0.6
0.5
0.4
0.3
0.2
0.1
200
250
300
350
400
Temp (K)

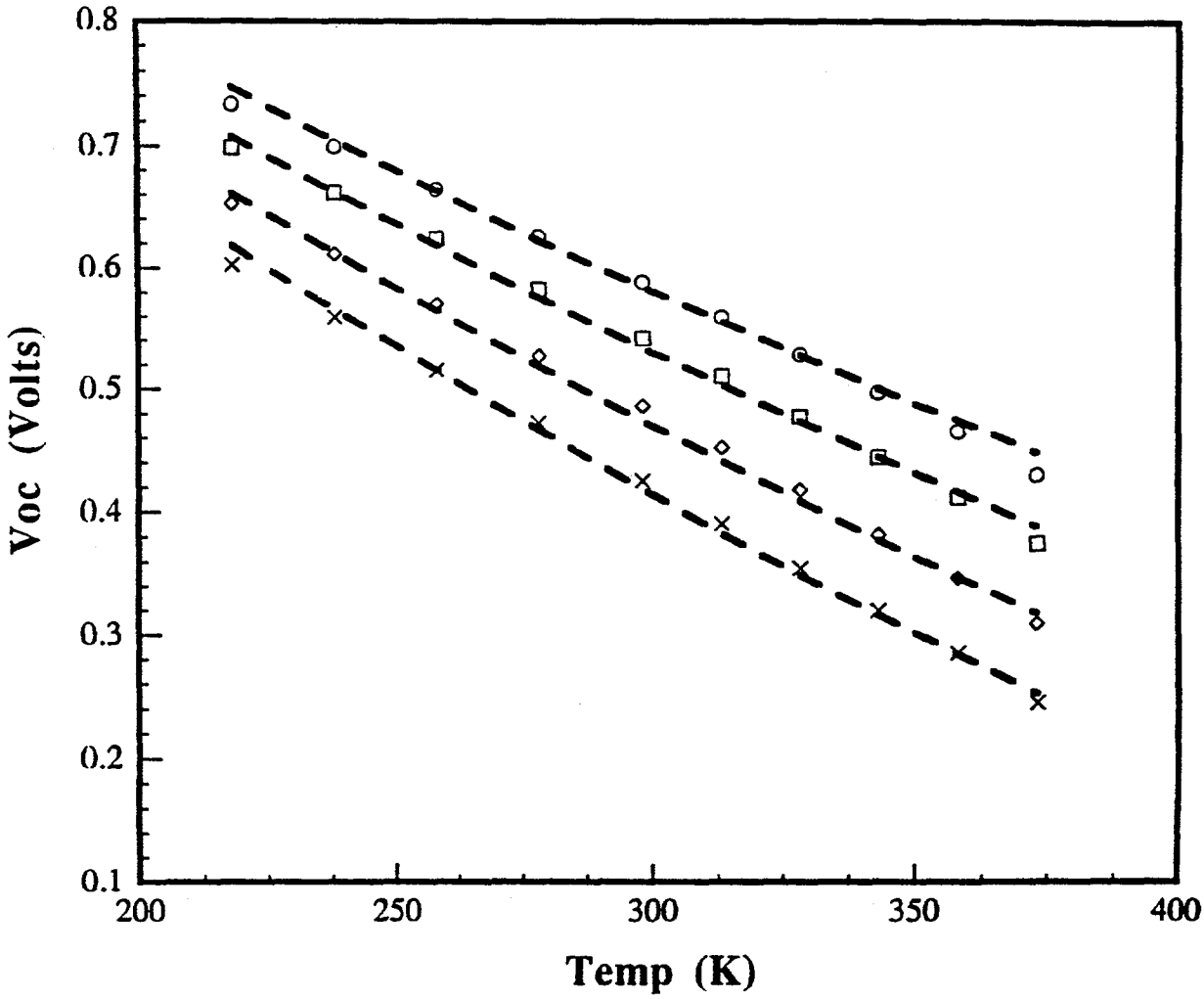
NREL - S478-14-5
Voc (Volts)
0.8
0.7
0.6
0.5
0.4
0.3
0.2
0.1
200
250
300
350
400
Temp (K)

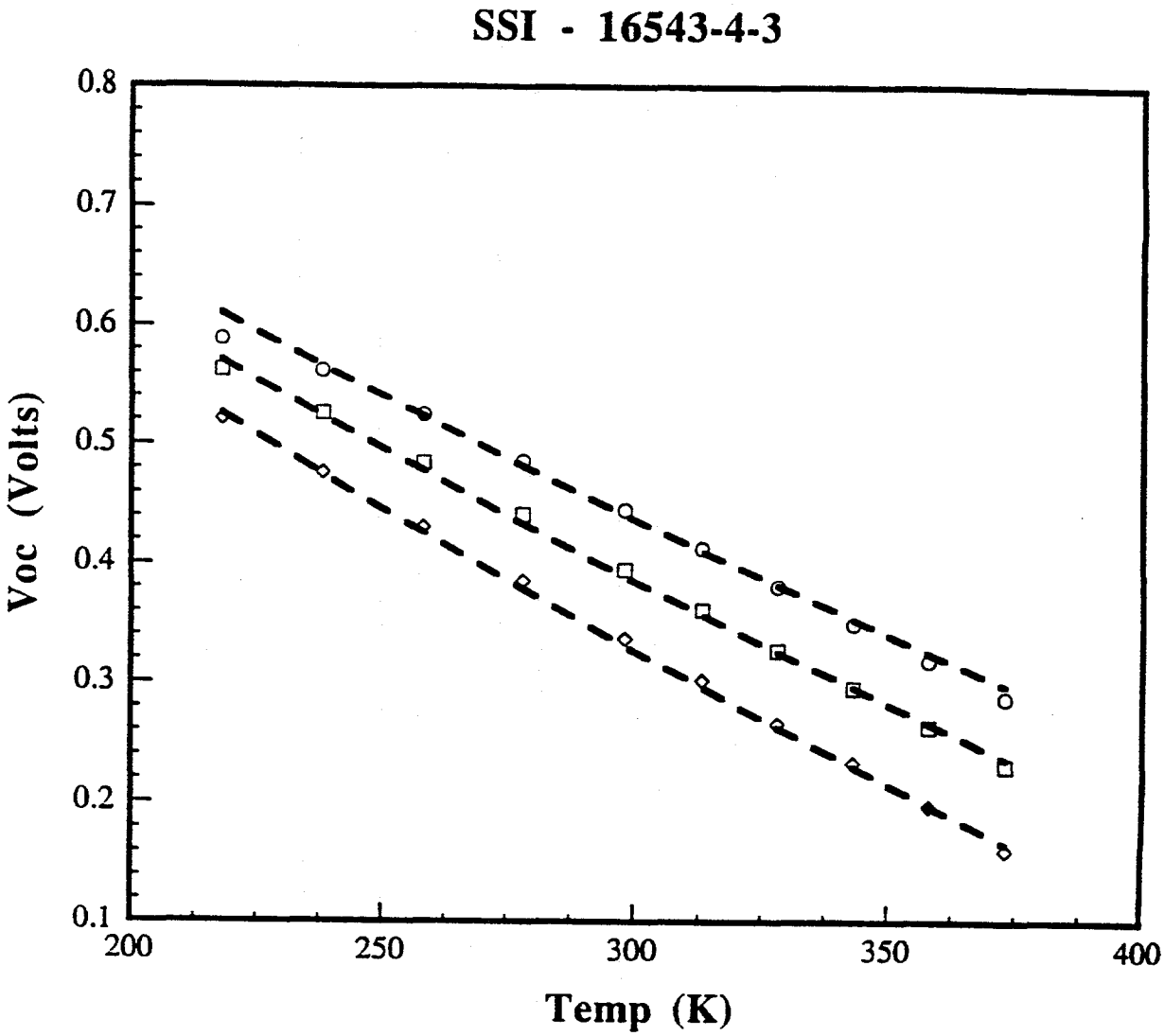
SSI - 16543-4-3
0.8
0.7
0.6
0.5
0.4
0.3
0.2
0.1
Voc (Volts)
200
250
300
350
400
Temp (K)

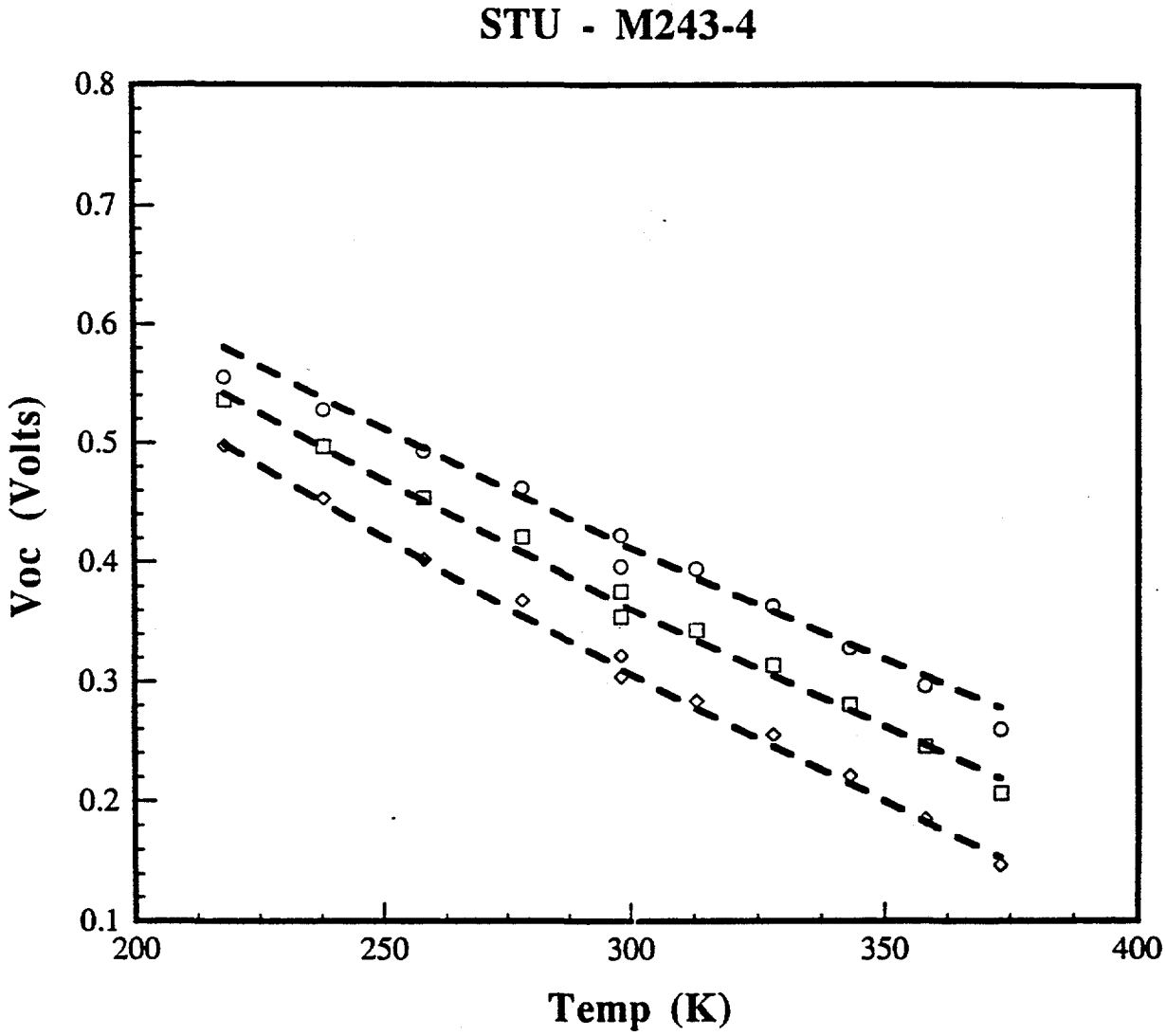
STU - M243-4
0.8
0.7
0.6
0.5
0.4
0.3
0.2
0.1
Voc (Volts)
200
250
300
350
400
Temp (K)

Table 34. Listing of the model parameters used to describe the V_{oc} vs. temperature data shown in Figures 66a-66k. Here E*=kT*.

Device#	E_g* (eV)	T* (K)	E* (meV)	J_{oo}* (mA/cm^2)
EPV-11133-21-5	1.08	1964	169	4.0E+06
IEC-32187-22-12	1.27	632	54	6.4E+06
IEC-32220-22-5	1.13	756	65	1.4E+06
IEC-32356-33-5	1.27	2013	173	4.2E+06
IEC-32361-33-3	1.01	-3751	-323	2.7E+05
IEC-61079-23-5	1.22	799	69	5.7E+06
IEC-89095-2-9	1.08	1644	142	2.0E+06
NREL-S416-23-5	1.34	1775	153	2.3E+06
NREL-S478-14-5	1.32	1004	86	1.5E+06
SSI-16543-4-3	1.19	1176	101	7.6E+06
STU-M243-4	1.17	990	85	5.8E+06

These measurements, made as a function of temperature, can also be explained if these transport properties are controlled by a continuous distribution of localized states within the bandgap of the $CuInSe_2$.

Current-voltage characteristics of CdTe/CdS solar cells measured as a function of temperature and light intensity are also being analyzed. Preliminary analysis indicate these devices behave similarly to the $CuInSe_2$/CdS solar cells. As an example, partial analysis of an IEC evaporated CdTe/CdS solar cell (device #40803-22-8) is shown. This device had an active area (0.071 cm^2) efficiency of about 12% (V_{oc}=0.76V, J_{sc}=22.4 mA/cm^2, FF=0.71%) under AM1.5 global illumination at 25°C. Figures 67 and 68 show plots of the slope of the J-V curve vs $1/(J+J_{sc})$. Figures 69 and 70 are plots of $\ln(J+J_{sc})$ vs. $(V-R_sJ)$ which are similar to $CuInSe_2$ based devices.

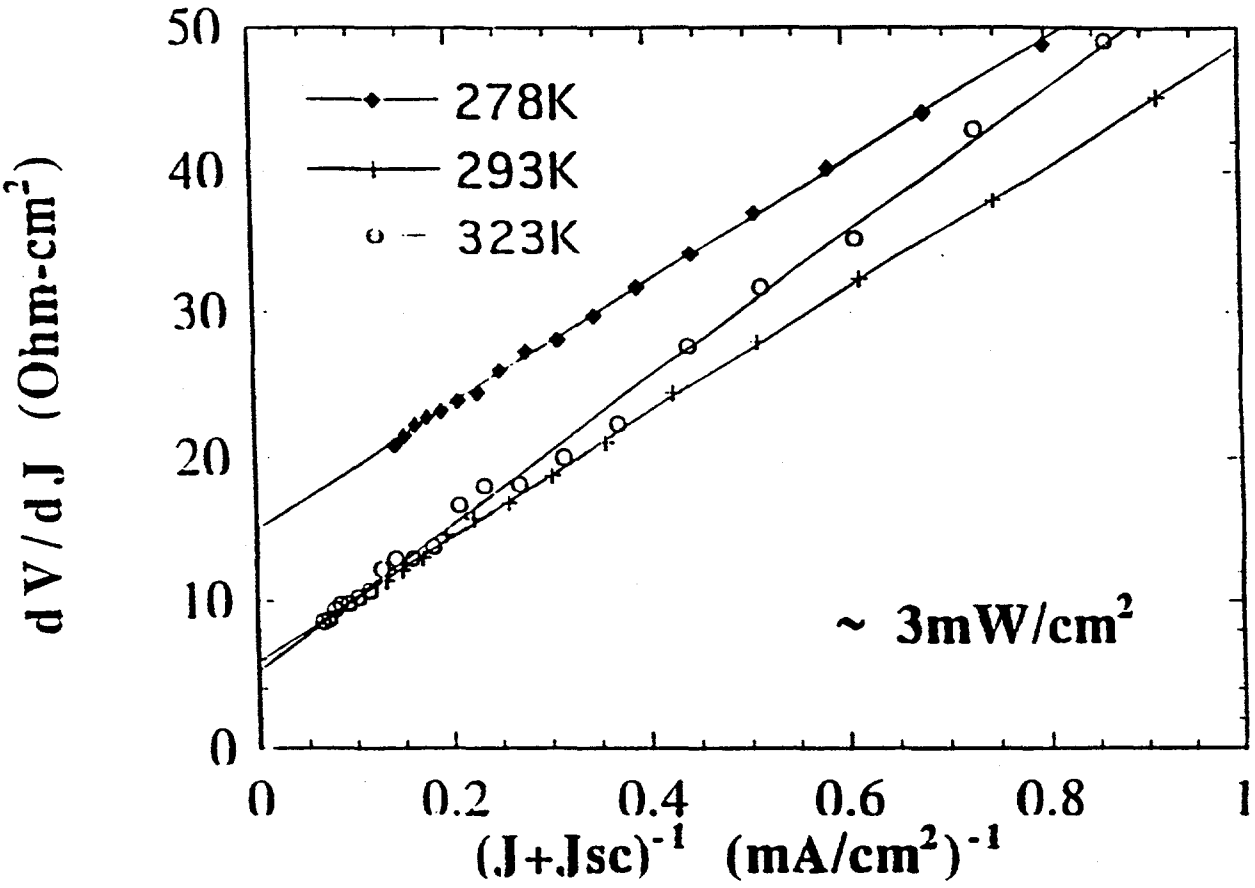

Figure 67. Slope (dV/dJ) of the J-V curves vs. $1/(J+J_{sc})$ as a function of temperature for the CdTe device discussed.

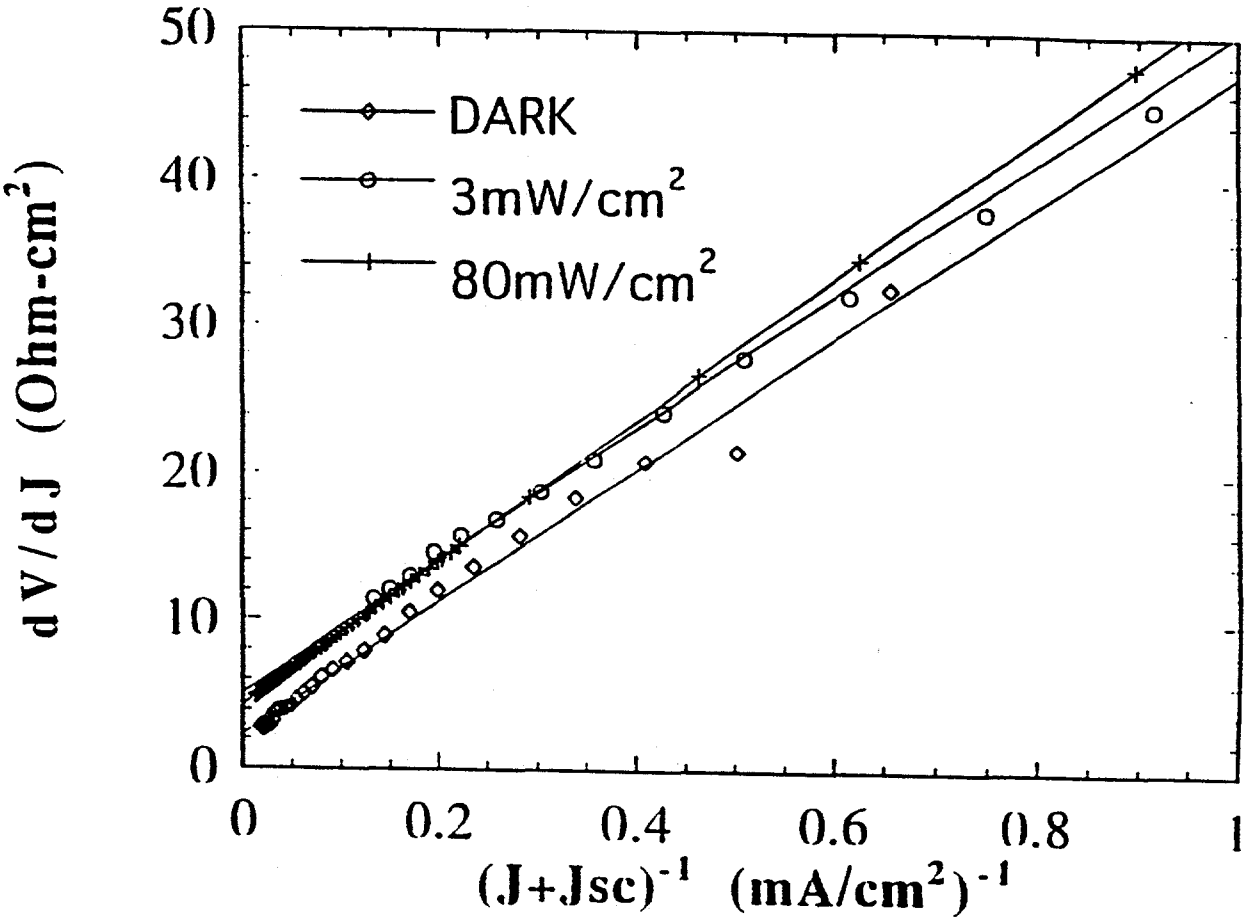

Figure 68. Slope (dV/dJ) of the J-V curves vs. $1/(J+J_{sc})$ as a function of light intensity at 293K for the CdTe device discussed.

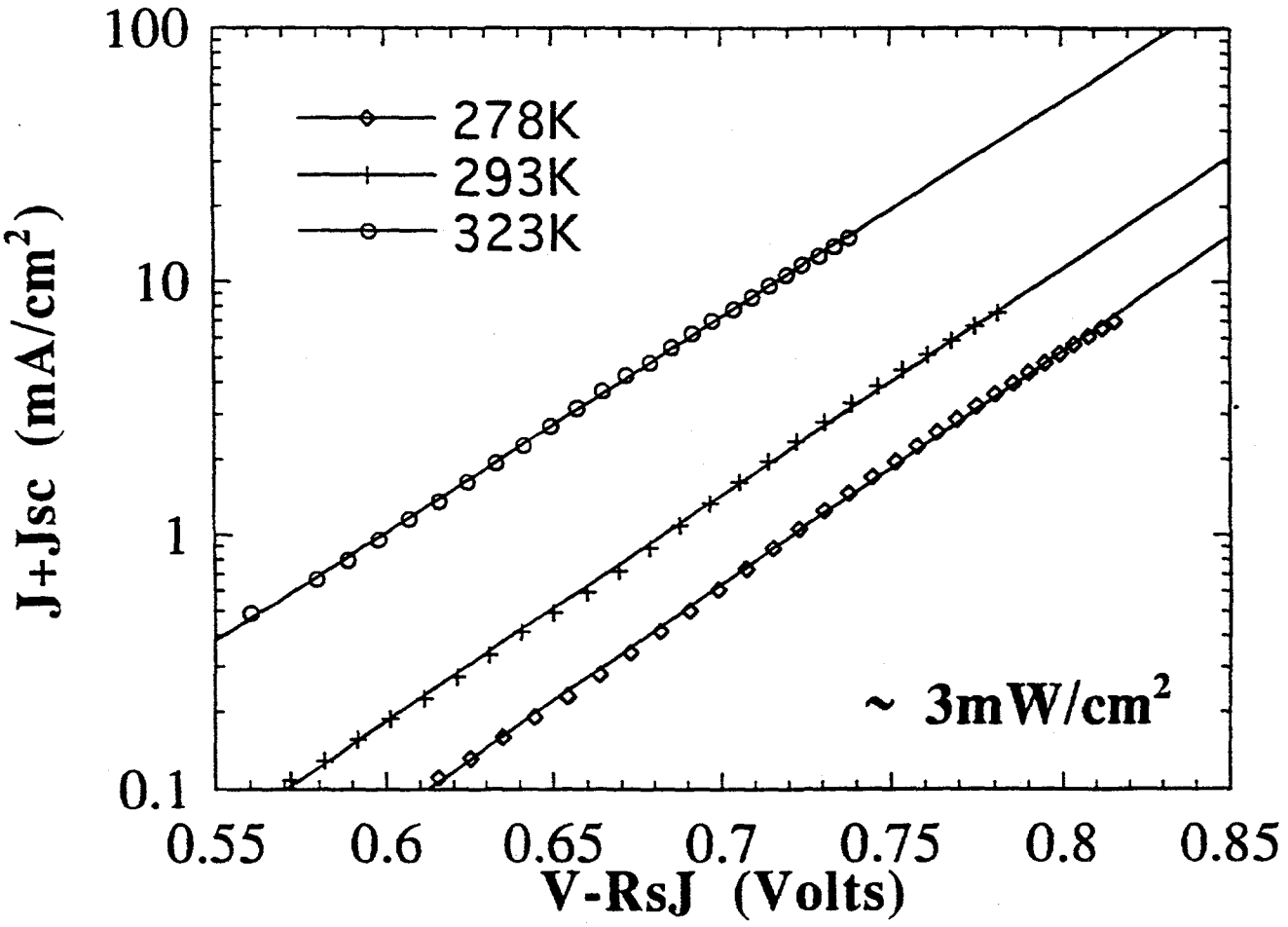

Figure 69. Log ($J+J_{sc}$) vs. ($V-R_sJ$) as a function of temperature for the CdTe device discussed.

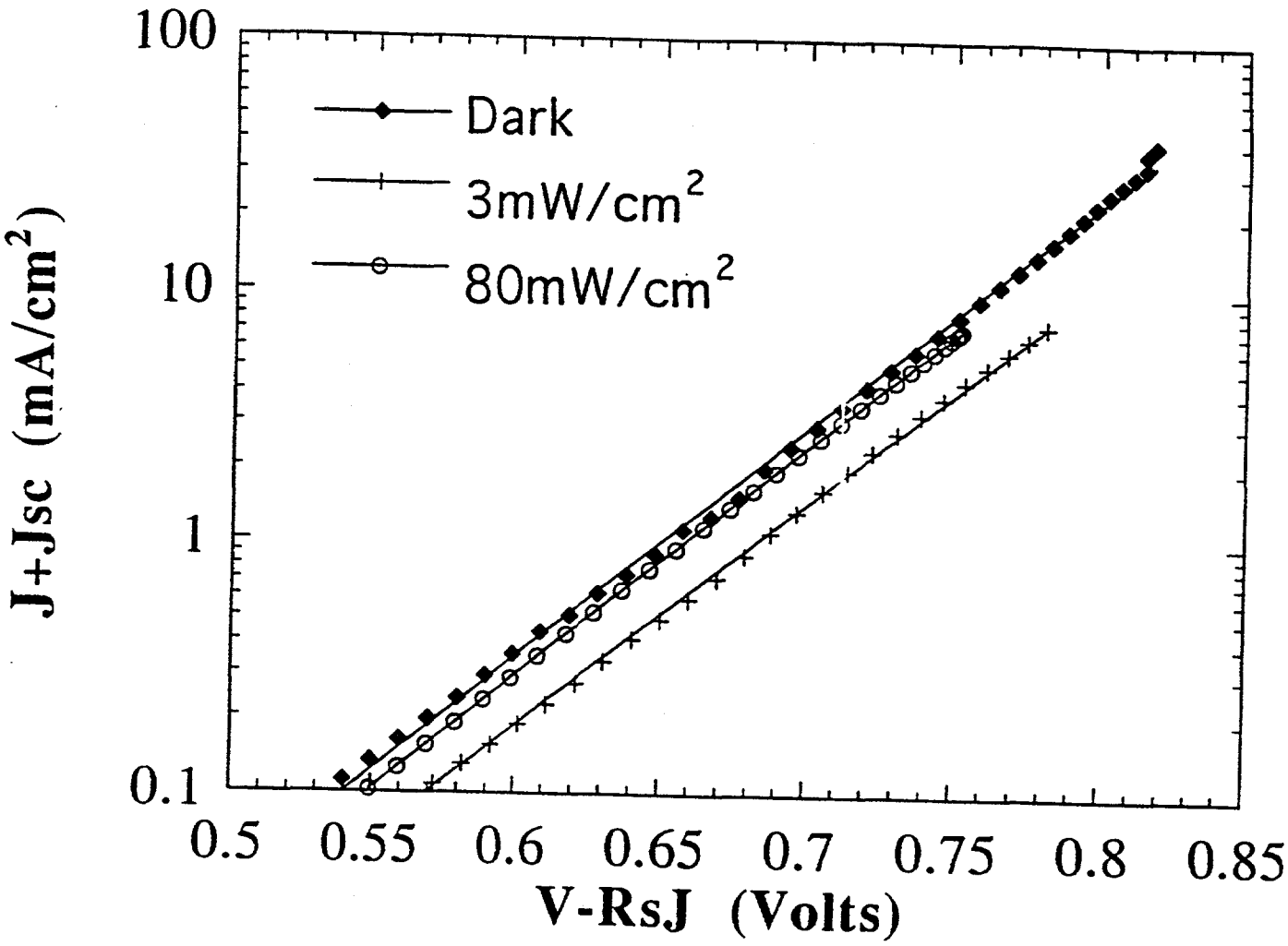

Figure 70. Log ($J+J_{sc}$) vs. ($V-R_sJ$) as a function of light intensity at 293K for the CdTe device discussed.

Tables 35 and 36 show the values derived from the linear fits of the previous graphs. The limited values of J_o as a function of temperature are consistent with an activation energy of approximately $E_g/2$. This preliminary analysis is so far consistent with the forward current being controlled by electron - hole recombination within the CdTe absorber layer as has been previously suggested (41). However, a wider range of both measurements and samples will be needed before it can be determined if the CdTe devices have the type of diode quality factor and activation energy values and distribution that would suggest a continuous distribution of recombination centers as in the case of $CuInSe_2$/CdS and $Cu(InGa)Se_2$/CdS devices.

Although the case is not yet as strong for CdTe/CdS devices as it is for both $CuInSe_2$/CdS and $Cu(InGa)Se_2$/CdS devices, for all of these polycrystalline thin film devices the forward J-V current behavior appears to be dominated by the same mechanism, which is, electron - hole or Shockley-Read-Hall recombination in the absorber layer. There are indications, at least in the case of the $CuInSe_2$ based materials, that this recombination is through a continuous exponential - like distribution of recombination centers within the bandgap of the light absorbing material. The $CuInSe_2$-based devices all show the same basic diode behavior with differences which can be explained by different distribution of mid-gap recombination centers. Although not as pronounced, this behavior is quite similar to that of photovoltaic devices made from amorphous semiconductors. Possibly this is because the crystalline order in these polycrystalline thin films, with grain sizes on the order of about a micron in diameter, is part way between that of crystalline and amorphous material although future measurements as a function of crystallite size might be able to prove or disprove this conjecture.

Table 35 Parameters derived from the J-V measurements of CdTe/CdS device #4-803-22-8 for an illumination intensity of about $3mW/cm^2$

T (K)	Diode Quality (A) Factor	Jo (mA/cm^2)
323	1.8	8E-06
293	1.9	8E-07
278	2.0	3E-07

Table 36 Parameters derived from the J-V measurements of CdTe/CdS device #4-803-22-8 for a temperature of 293K

Illum. (mW/cm^2)	Diode Quality (A) Factor	Jo (mA/cm^2)
Dark	1.8	9E-07
~3	1.9	8E-07
~80	1.9	1E-06

3.2 a-Si DEVICE ANALYSIS

A. Optical Analysis of a-Si Devices

Devices from the PECVD system had a low blue response which limits J_{sc}. Typical values of the QE at 400 nm were 0.25-0.40, with occasional values of 0.50. We typically obtained QE(400) values of 0.6-0.65 from devices from the photo-CVD system using the same SnO_2. The low values of QE(400) from the PECVD system resulted in J_{sc} values of 11-12 mA/cm^2 with our standard back contact of TiAg and 13-15 mA/cm^2 with a more reflective ITO/Ag contact. Although the QE increased 10-20% with reverse bias as described in Section 2.4, it still remained relatively low suggesting the losses were related to optical generation. Therefore, analysis of the QE was necessary to diagnose the optical losses.

A model of the QE was developed which accounted for glass reflection (R_f), TCO absorption (A_{tco}), p-layer absorption [$\exp(-\alpha_p D_p)$], generation in the i-layer, multiple passes (m) due to light trapping and back reflection (R_B). Measured values of R_f (7%) and literature values of A_{tco} and R_B were used. The SnO_2 absorption accounted for a 15% loss at 400 nm, and decreases to 7% at 550 nm. Thus the maximum possible QE(400nm) is 78% without any p-layer absorption. It was found necessary to include an exponential (Urbach) absorption tail for the i-layer in order to accurately model the red response. Both p and i-layer absorption were described with a Taucs expression. The resulting QE is given by

$$QE=(1-R_F)(1-A_{TCO})\exp(-\alpha_p D_p)[A_i(1+R_B(1-A_i))],$$

with the i-layer absorption (A_i) given by

$$A_i=[1-\exp(-\alpha_i m D_i)],$$

where α_i is the i-layer absorption coefficient (sum of Taucs and Urbach terms) and D_i is the i-layer thickness. Values of R_f=0.07, m=3, D_i=0.4 μm and R_b=.9 were used as defaults for studying the effect of p-layer absorption. The parameters A_i, m, D_i, and R_B primarily influence the red response. The p-layer thickness was varied from 100 to 300 Å and the p-layer bandgap from 1.8 to 2.0 eV.

Figure 71 shows the QE for devices having p-layer bandgaps of 1.8, 1.9, and 2.0 eV with D_p=100 Å. Also shown is the measured QE at -1V from the cell with highest efficiency to date (8%) using our standard TiAg back contacts. Higher currents were obtained on cells from this same run using ITO/Ag as discussed in

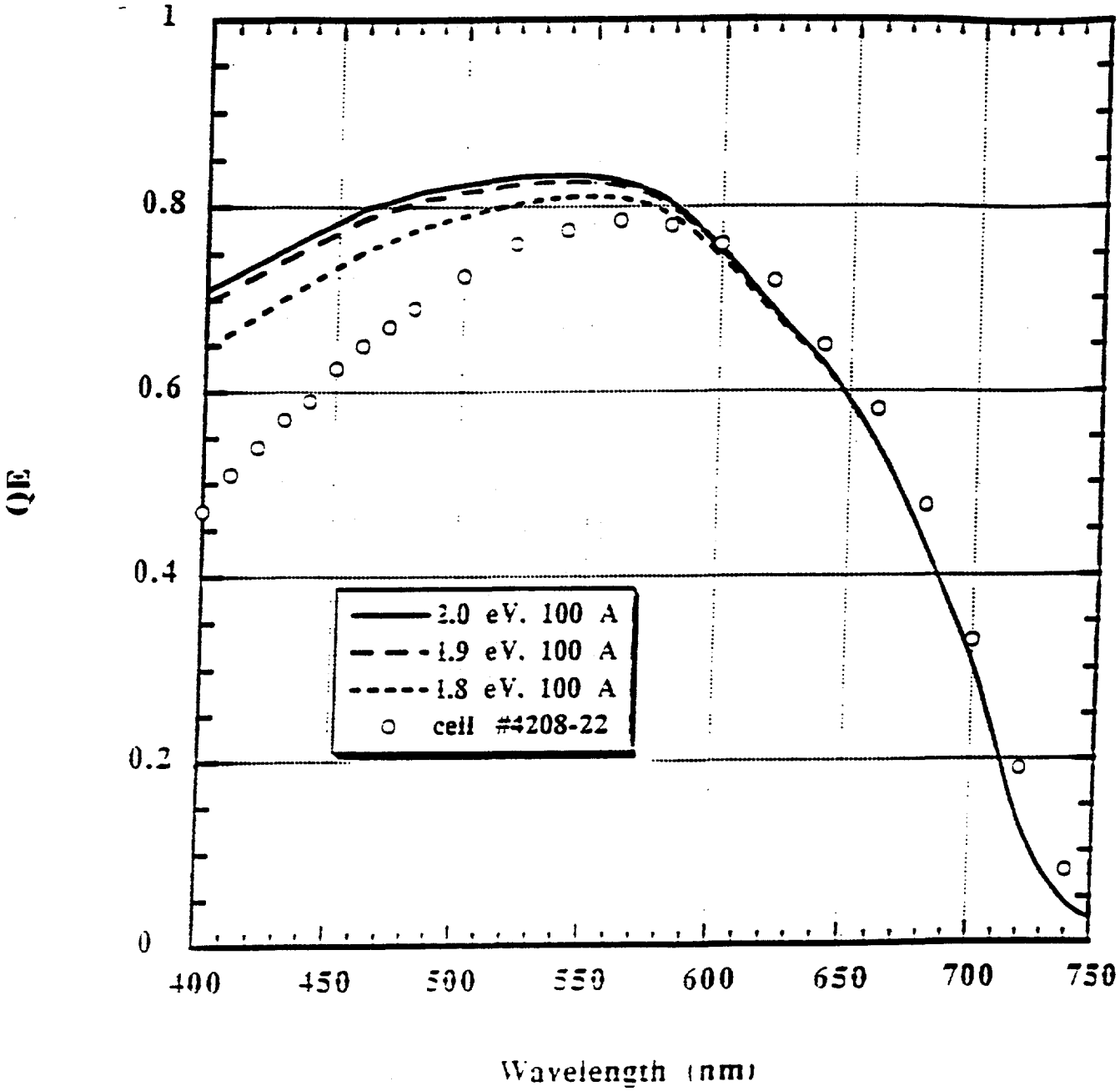

Figure 71. QE from model calculations with p-layer bandgap of 2.0, 1.9, 1.8 eV for p-layer thickness of 100Å. Measured QE for cell #4208-22 shown.

section IV. From characterization of thick p-layers, we estimate that p-layers in devices should be 100-140 Å thick with a bandgap of 1.9-1.95 eV. Figure 71 suggests that a bandgap of much less than 1.8 eV would be necessary to account for our optical losses. This is not consistent with the high V_{oc}. Figure 72 shows the calculated QE for p-layer thicknesses of 100, 200, and 300 Å with E_{gp}=1.9 eV. The measured QE is consistent with a thickness approximately 400 Å. This would imply a growth rate in excess of 20 Å/s, considerably higher than the 3-8 Å/s obtained from thick p-layers under a wide range of conditions as discussed in Section 2.4 (see Table 21).

Neither an extremely low bandgap nor extremely high growth rate could be easily justified based on thick p-layer properties. It appeared that the p-layer or buffer layer in devices behaved quite differently than expected. It was also possible that the excess absorption losses were not occurring in the p-layer at all but in the TCO, the buffer, or at one of the p-layer interfaces. Thus, it became necessary to develop an analysis to extract p-layer properties of devices directly from the QE measurement on devices in order to identify the source of the low blue response.

Under conditions of a few volts reverse bias such that all carriers are collected, the QE at short wavelengths is limited only by optical generation, i.e. A_i is unity. This can be verified by comparing QE data at -1, -2V etc. The only losses are those which prevent photons from reaching the i-layer. Back reflection and scattering are negligible for such strongly absorbed light. The QE at short wavelengths under reverse bias is given by the product of three optical losses: light lost due to front surface reflection, light lost due to absorption in the glass/TCO, and light lost due to p-layer absorption, or

$$QE(<550nm)=(1-R_f)(1-A_{tco})\exp(-\alpha_p D_p) \quad .$$

Reflection losses ($1-R_f$) are easily quantified on devices on glass/TCO using a spectrophotometer. The textured TCO eliminates any fringing. The absorption losses of the textured TCO ($1-A_{tco}$) are more difficult to measure due to scattering and lightpiping. Therefore, we have relied on published data from Solarex (42). The p-layer absorption characteristic is given by a Taucs relation

$$\mathrm{sqrt}(\alpha E)=B(E_{gp}-E)$$

where B is the Taucs coefficient (slope of the plot) and E is the photon energy. Typically, we find that B is around 7.0 $(\mu m\text{-}eV)^{-0.5}$ on both p and i-layers, ranging from 6.5 to 7.5. However, only the product $\alpha_p D_p$ is available from the measured QE, since

$$\alpha_p D_p = \ln\{(1-R_f)(1-A_{tco})/QE\}.$$

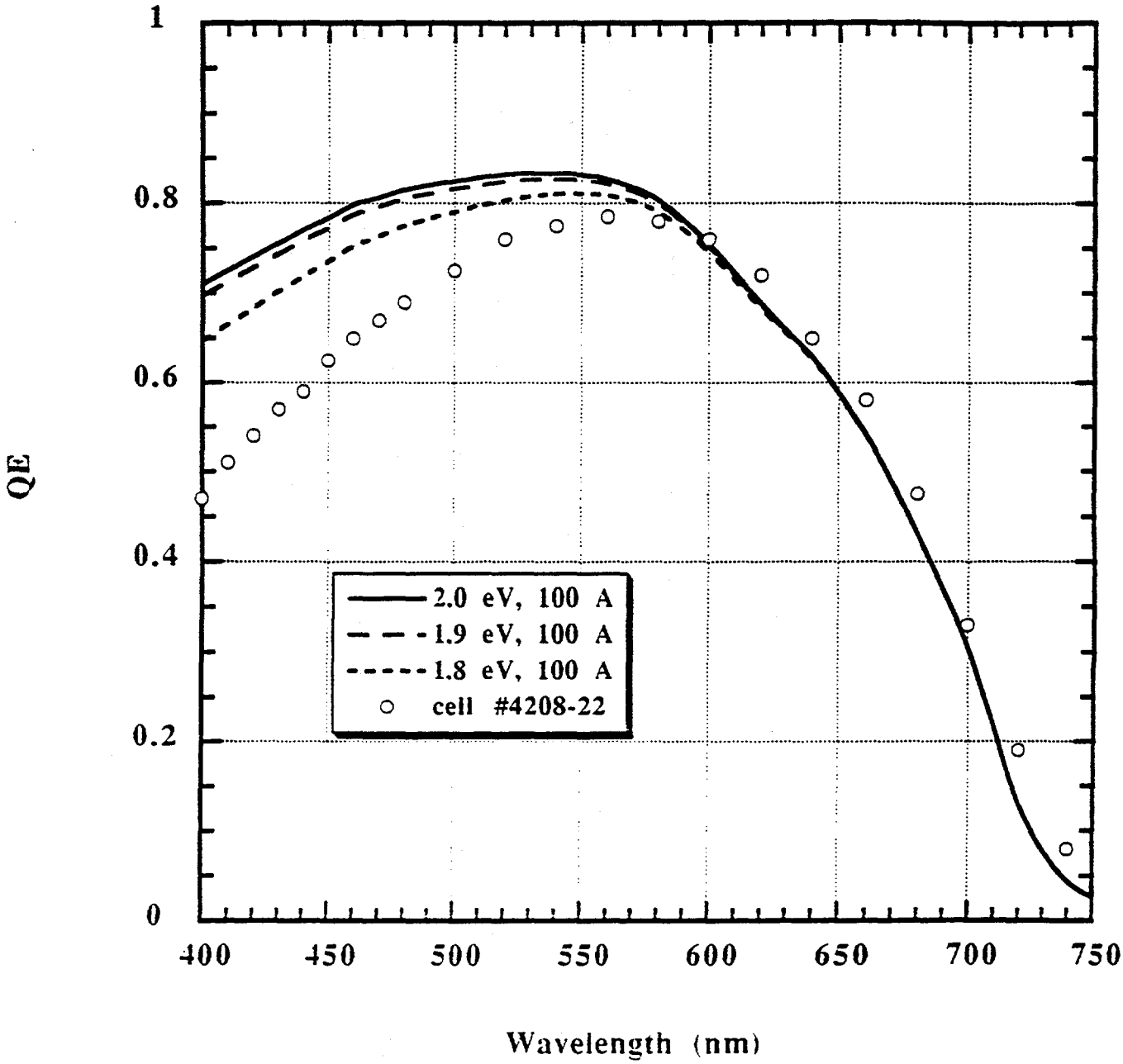

Figure 72. QE calculated for p-layer thickness of 100,200,300A for p-layer bandgap of 1.9 eV. Measured QE for cell #4208-22 shown for comparison.

Thus, a pseudo Taucs plot of sqrt($\alpha_p D_p E$) vs. E gives E_{gp} directly from the intercept as in a standard Taucs plot, but has a slope of $B*(D_p)^{.5}$. We can obtain the thickness from the slope if we assume that a thin p-layer on TCO has the same value B as a thicker film characterized on glass. A key feature of this analysis is that it allows both the p-layer thickness and bandgap to be obtained separately in a device. Previously, we have only been able to look at the blue response as a lumped parameter influenced by D_p and E_{gp} together. Also, it should be pointed out that the product ($\alpha_p D_p$) is really the absorption of whatever layer(s) are limiting the QE, which may not be just the p-layer (i.e. could be the buffer as well). If ($\alpha D_p E$) is linear in a Taucs plot, this suggests that the losses are due to amorphous semiconductor layers, not semi-metallic or direct gap (TCO) layers.

The QE of all devices since run #4218 were analyzed to determine D_p and E_{gp}. All i-layers were deposited at 200°C, 0.2 Torr and 7W. All p-layers were deposited at 150°C and 0.2 Torr. The p- and buffer layer thickness and bandgap have been varied by changing the deposition time, rf power, and CH_4 flow. The last 4 runs have H-diluted p-layers. The p and buffer layers were almost always changed together (i.e., if the p-layer was changed from 22 to 11 sec or from 14 to 7 W, so was the buffer). Thus analysis of the blue QE is relevant since only deposition parameters which directly affect the p and buffer layer were changed. The reactor was in both configurations (gas line connected or disconnected). This changed growth rates. Thus not all devices have had the same i-layer thickness. Most i-layers were 0.38-0.44 μm but a few that were 0.6-0.7 μm are included. They will be separately identified when relevant (i.e. when considering J_{sc}).

Figure 73 shows the p-layer Taucs plots obtained with different bias (light or dark, -1 or -2V) on the same device (4220-22-5) and at -2V on another cell from a different piece from the same run (4220- 12-5). The bandgap and thickness resulting from the linear fit to the data are also shown. The agreement between different bias on the same cell is excellent, within 10% for thickness and 5% for E_{gp}. Based on these results, QE measurements taken at -2V without light bias were typically used for analysis and comparison of devices.

Figure 74 shows the Taucs plot for three devices with p-layer depositions of 11, 22, and 44 seconds. The bandgaps from the intercepts are essentially the same (1.92-1.95 eV) for all three devices. This is in agreement with the value expected based on Taucs plots of thick p-layers deposited under identical conditions. The thickness determined from the slope scales with deposition time leading to a nearly constant growth rate of 16-17Å/s. These growth rates are 4-5 times greater than expected. The thickness of the layer(s) responsible for the blue absorption

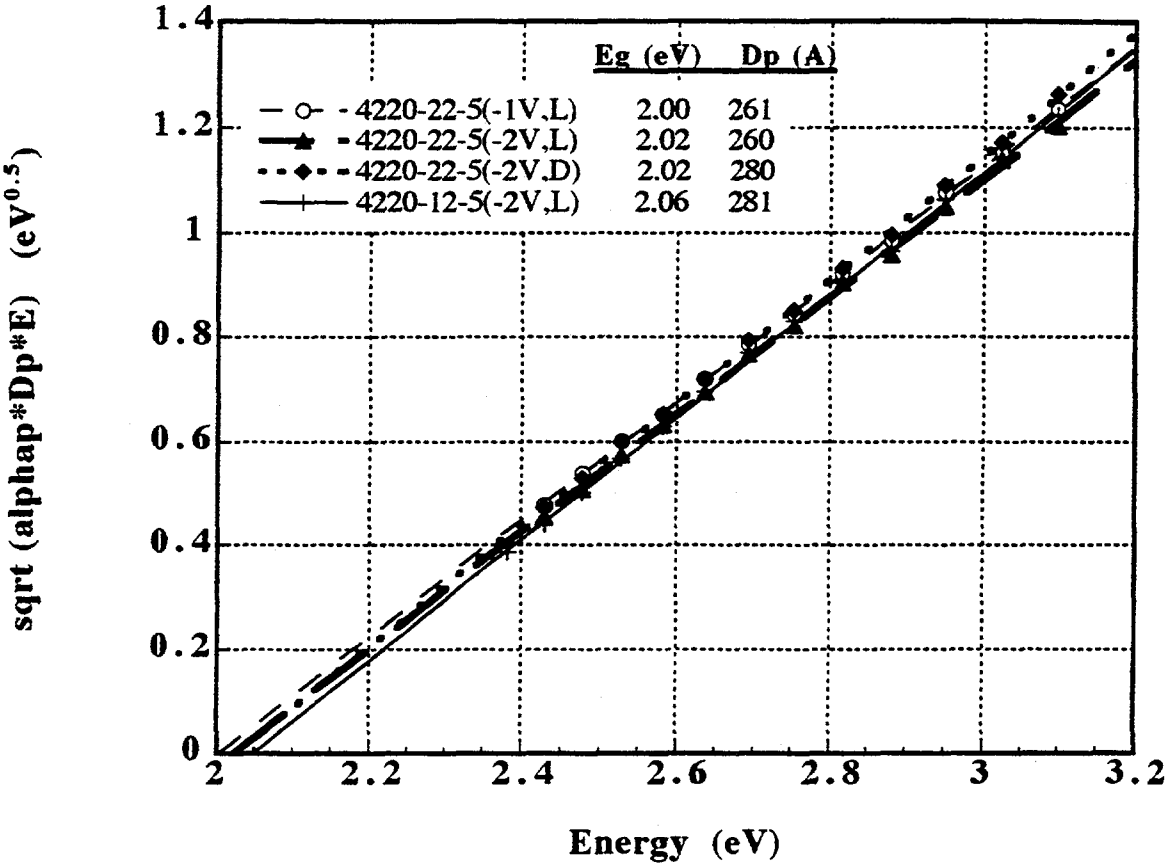

Figure 73. Taucs plot from QE analysis of 2 devices from same run under different bias conditions yielding p-layer thickness and bandgap as shown.

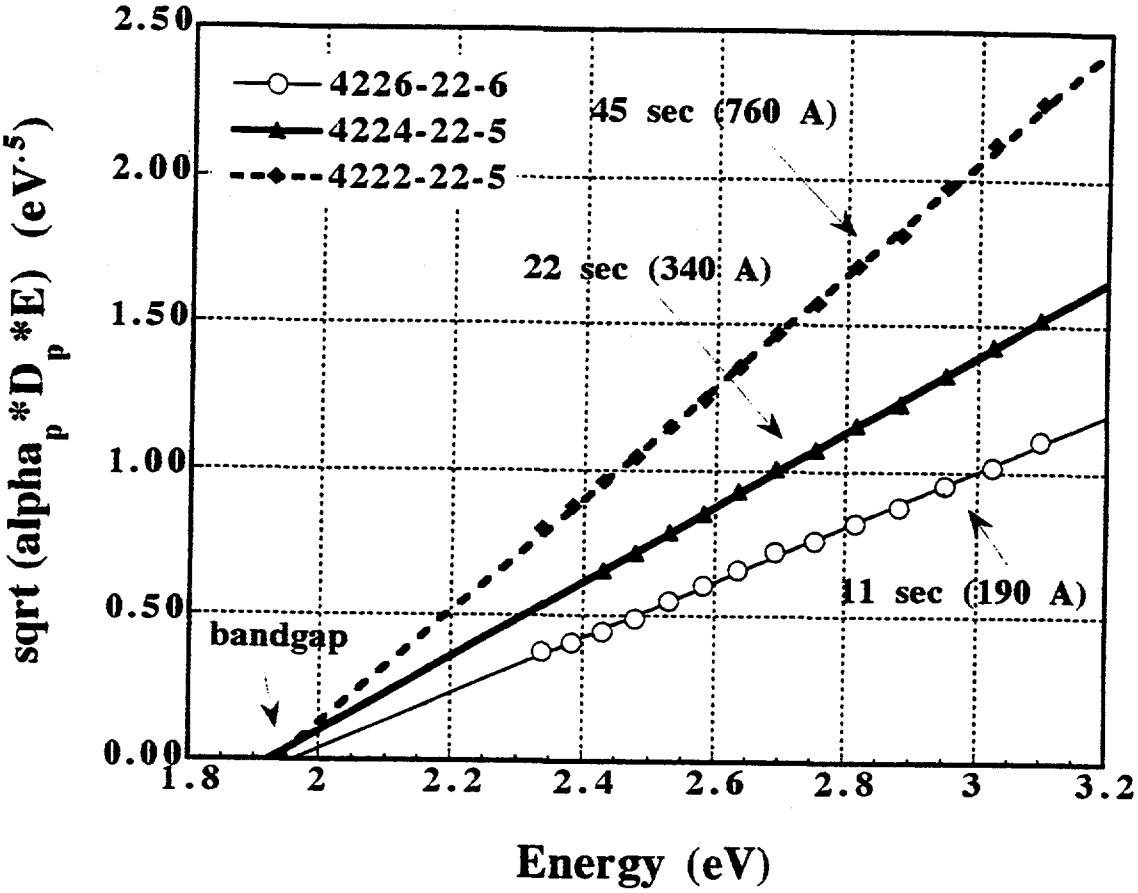

Figure 74. Taucs plot from three devices having p-layer deposition times of 11,22, and 45 sec.

losses scale with p and buffer deposition time, and have a Tauc-like absorption. We conclude that the optical losses are due to p or buffer absorption. There is no evidence for energy-independent interface layer absorption (e.g., a thin metallic tin layer at the SnO_2/p interface leading to a neutral density effect.)

Table 37 shows the p-layer conditions (which are described in Table 21), reactor configuration (as shown in Figures 48-50), and the thickness, growth rate, and bandgap obtained from the analysis of the QE. The most startling result is that the thicknesses are all 4-5 times larger than expected based on growth rates of thicker p-layer films on glass. Thus, the optically absorbing layer is 4-5 times thicker than expected. Figures 75 and 76 show that the QE(400) is closely correlated with the p-layer thickness but not the optical bandgap in the range of bandgaps studied. This is in agreement with the modelling results of Figures 71 and 72.

Our standard p-layer conditions were 14 W, and flow rates of 8 and 4 sccm respectively, with SiH_4 and CH_4 flow rates of 8 and 4 sccm respectively, but we also made devices with lower power and higher CH_4 flow rates in both configurations (4218 and 4219 with the gas line disconnected, and 4224 and 4225 with it connected). With the line disconnected, lowering the power and raising the CH_4 flow rates increased E_{gp} by 0.13 eV, but had no effect on growth rate (hence thickness). With the line connected, E_{gp} stayed the same but thickness doubled.

Since we could not lower GR with lower power or higher CH_4 flow rate, and we were at the limit of lower pressure for our system, we decided to lower the p-layer growth rate by dilution in H. The growth rate of the four H-diluted runs (4231-34) is much lower (1.5 Å/s). This is only slightly higher than expected based on the thicker H-diluted films. The H-dilution apparently suppresses whatever is responsible for the growth of the excessively absorbing layer in non-H diluted films. However, the bandgap is much lower for the same CH_4 flow, as we had observed in thick film properties as well. By increasing the CH_4 flow rate from 4 to 10 sccm and using H-dilution, the QE(400) rose to over 60% for the first time on runs 4233 and 4234 due to the combination of thinner p-layer and higher bandgap. These H-diluted devices (4233-34) have had excellent J_{sc} values, 14-15 mA/cm^2, indicating that it is possible to obtain high J_{sc} with our present system. These are expected to increase by at least 1.5 mA/cm^2 with a more reflective ITO/Ag back contact. Figure 77 shows a general trend of increasing J_{sc} with increasing blue response. Inspection of the QE plots shows that the peak QE, which occurs near 550 nm, has a weak inverse relation with the QE at 400 nm. Thus, gains in current due to increases in the blue response are somewhat offset by losses in the green. The source of this behavior is unknown.

Table 37. Device p-layer deposition conditions, thickness and bandgap from Taucs analysis of QE.

Run	RF Power (W)	CH_4 (sccm)	H dilution (sccm)	gas line	time (sec)	thickness D_p (Å)	E_g (eV)	growth rate (Å/sec)
4218	14	4	0	disconnect	45	443	1.95	9.8
4219	7	8	0	"	45	472	2.08	10.5
4220	14	4	0	"	45	282	2.02	6.3
4222	14	4	0	connect	45	762	1.93	16.9
4223	14	4	0	"	22	440	1.93	20
4224	14	4	0	"	22	341	1.92	15.5
4225	7	8	0	"	22	180	1.91	8.2
4226	14	4	0	"	11	186	1.95	16.9
4227	14	4	0	disconnect	45	450	1.89	10
4228	14	4	0	"	45	665	2.02	14.8
4229	14	4	0	"	30	497	1.9	16.5
4230	14	4	0	"	20	370	1.94	18.5
4231	14	4	65	"	90	162	1.81	1.8
4232	14	4	65	"	90	136	1.71	1.5
4233	14	10	86	"	90	174	2.16	1.9
4234	14	10	86	"	90	354	2.34	3.9

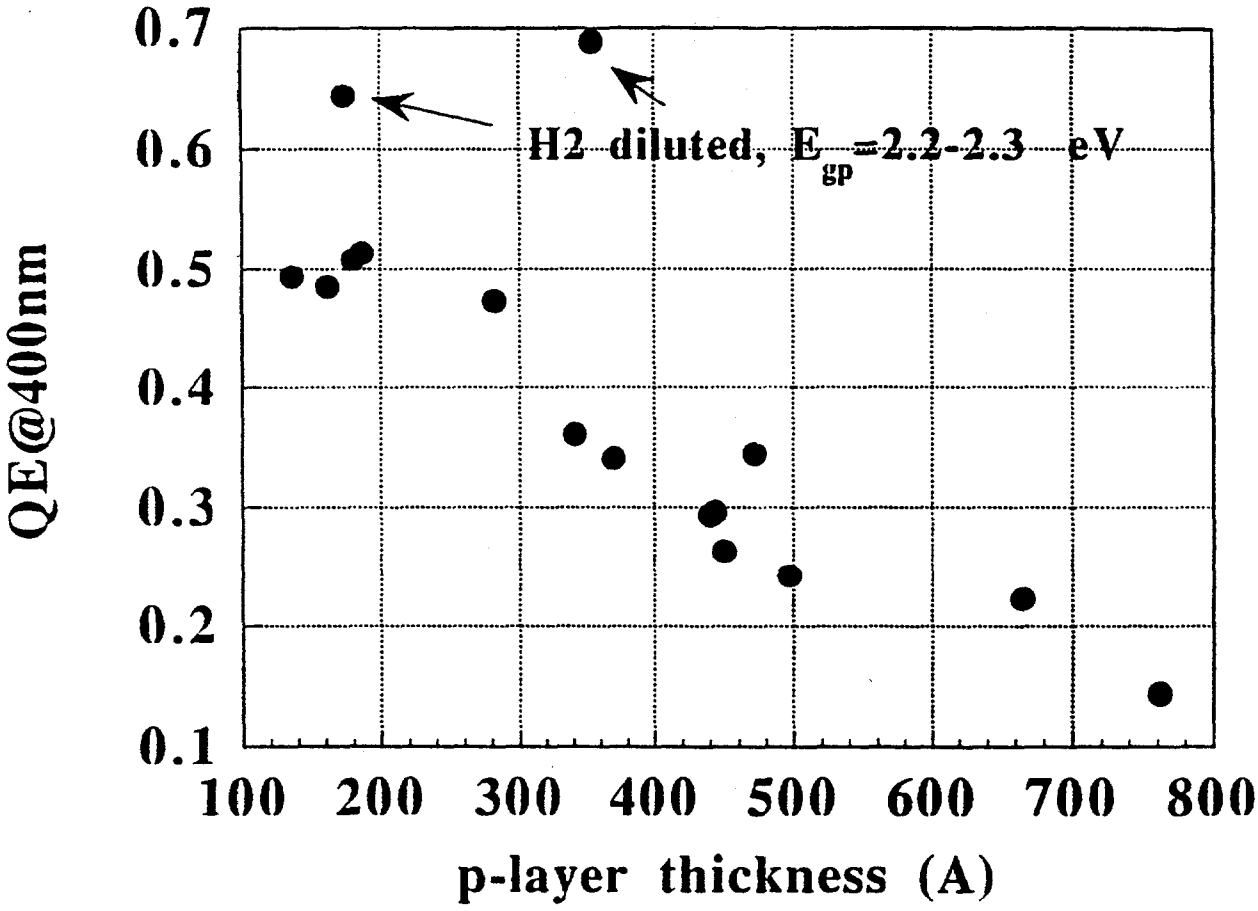

Figure 75. Dependence of QE @ 400 nm on p-layer thickness from Taucs analysis.

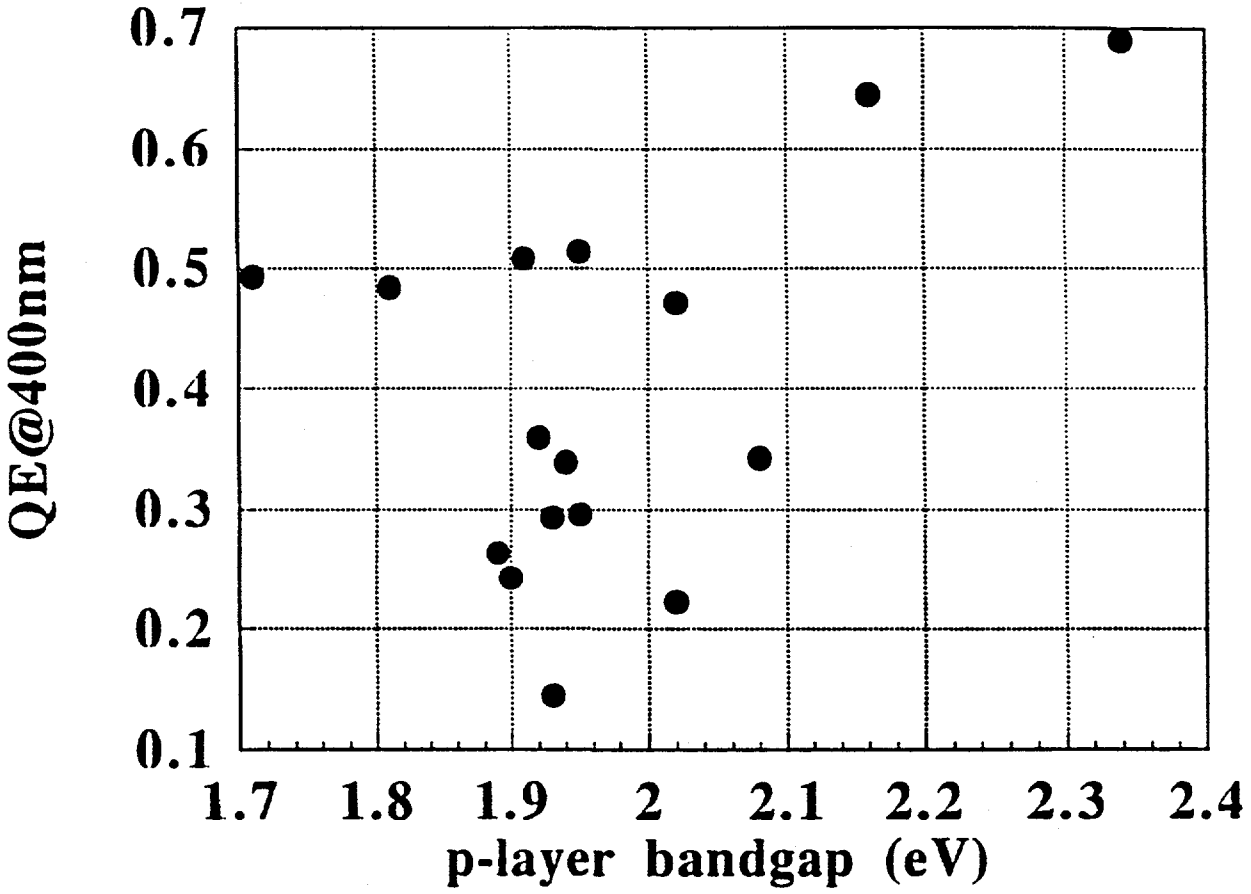

Figure 76. Dependence of QE @ 400 nm on p-layer bandgap from Taucs analysis.

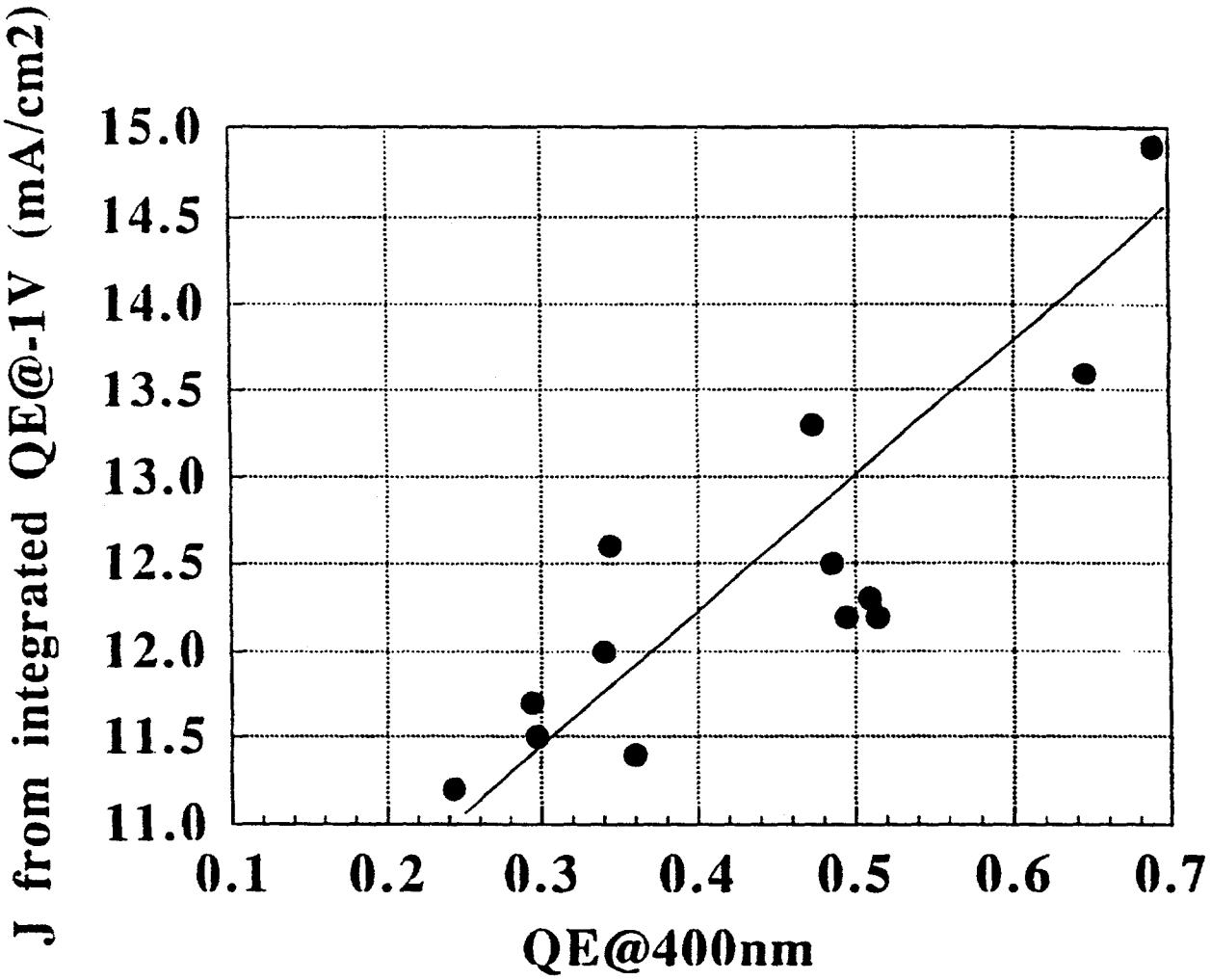

Figure 77. Correlation between light generated current (from integration of QE) and blue response QE @ 400 nm.

Figures 78 and 79 show the dependence of V_{oc} on p-layer thickness and bandgap. V_{oc} is independent of D_p, as expected for p-layers which are this thick. D_p will limit V_{oc} if D_p<100Å. Figure 79 shows that V_{oc} does not increase with E_{gp}, suggesting that V_{oc} is limited by bulk i-layer recombination, not low built-in voltage.

B. JV Analysis of a-SiGe p-i-n devices

The stability and performance of devices with graded and ungraded a-SiGe i-layers has been previously discussed (43). These studies confirmed the superiority of a front loaded type of device design which has compositionally inhomogeneous i-layers with 500 Å a-SiGe/500 Å a-Si. There are reports that V_{oc} decreases proportionally to the bandgap in ungraded devices. However, the dependence of V_{oc} on bandgap of graded devices is not known. We analyzed the J_{sc}-V_{oc} behavior of existing a-SiGe devices since no new a-SiGe devices were deposited this year in either the photo-CVD or PECVD systems.

V_{oc} and J_{sc} were measured at room temperature on three front loaded devices. The i-layers were all 500 Å a-SiGe/500 Å a-Si, with the a-SiGe bandgaps of 1.3, 1.4 and 1.5 eV. A standard a-Si cell was also included. The intensity and spectral content of the light was varied. The results are shown in Figure 80. The diode A-factor and prefactor J_o were determined by fitting the data to $V_{oc}=AkT/q*\{\ln(J_{sc})-\ln(J_o)\}$. Results in Table 38 show that the A factor of the a-SiGe devices is 1.9-2.1. Figure 81 shows that $\ln(J_o)$ is inversely proportional to bandgap with a slope of $(-1.9kT)^{-1}$. This suggests J_o is proportional to n_i not n_i^2 where ni is the intrinsic carrier density in the a-SiGe. Together with an A factor of ~2, this is constant with a V_{oc} which is determined by space charge recombination in the low bandgap a-SiGe region of the i-layer. However, since we have observed that V_{oc} is also dependent on the interface grading, it is likely that V_{oc} is determined by both space charge and interface recombination terms.

Table 38. Diode parameters obtained from analysis of J_{sc}-V_{oc} for three front loaded a-SiGe devices and a-Si device.

Device	Eg(eV)	V_{oc}(V)	A	Jo(mA/cm^2)
std a-Si	1.73	0.85	1.6	2.9E-8
FL3528	1.5	0.67	1.9	1.5E-5
FL3520	1.4	0.63	1.9	4.7E-5
FL3527	1.3	0.57	2.1	3.3E-4

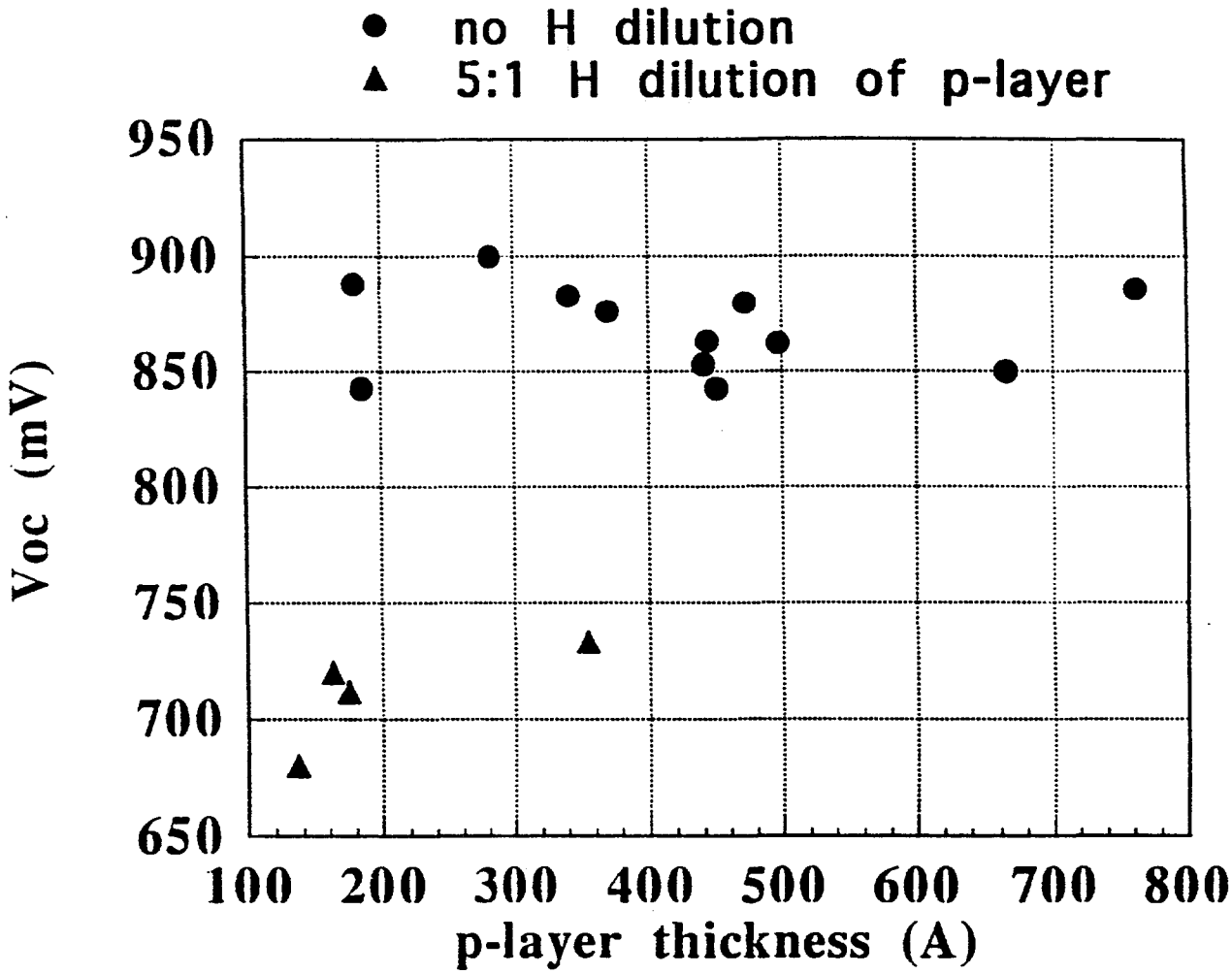

Figure 78. Dependence of V_{oc} on p-layer thickness, showing effect of H-dilution.

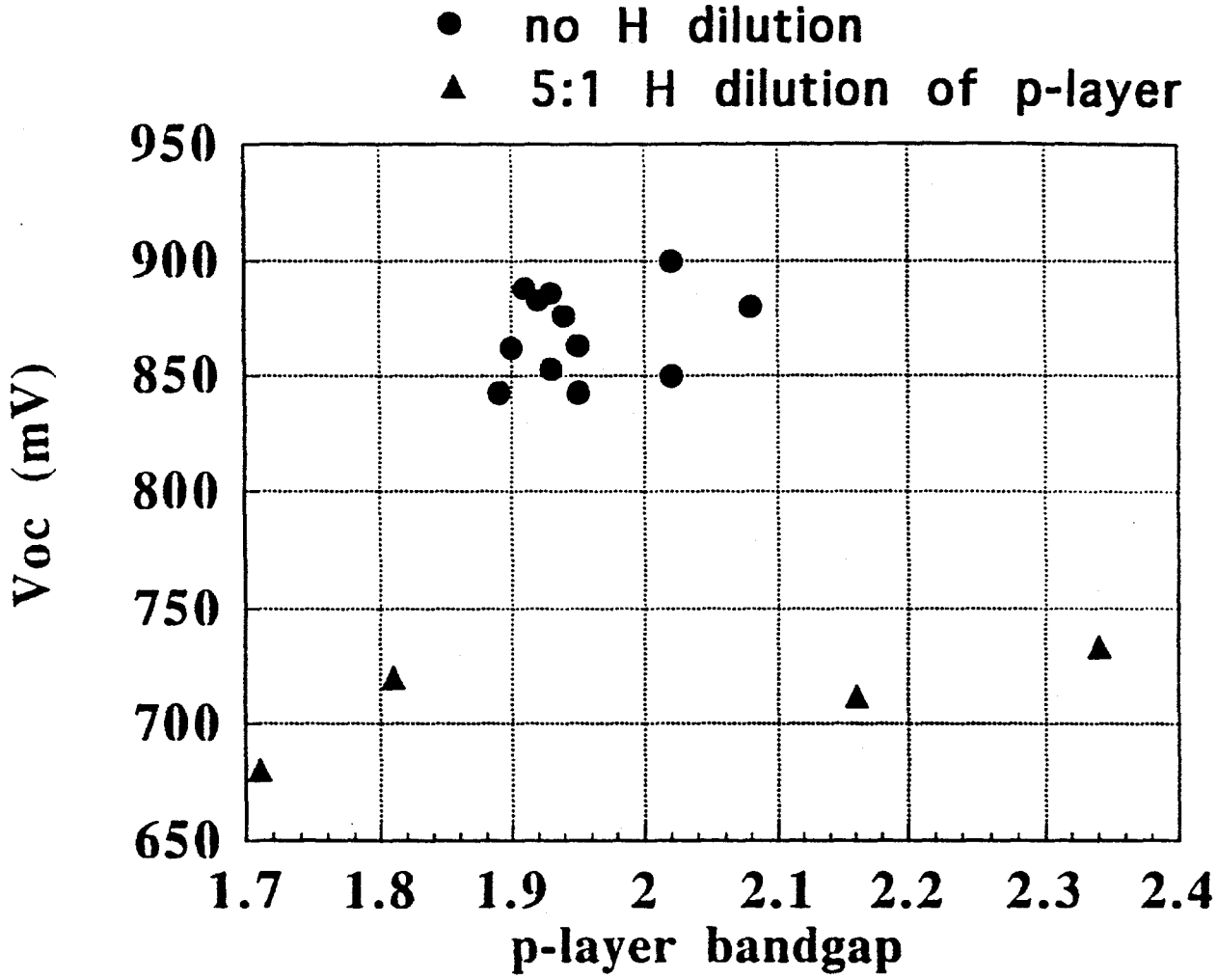

Figure 79. Dependence of V_{oc} on p-layer bandgap, showing effect of H-dilution of p-layer.

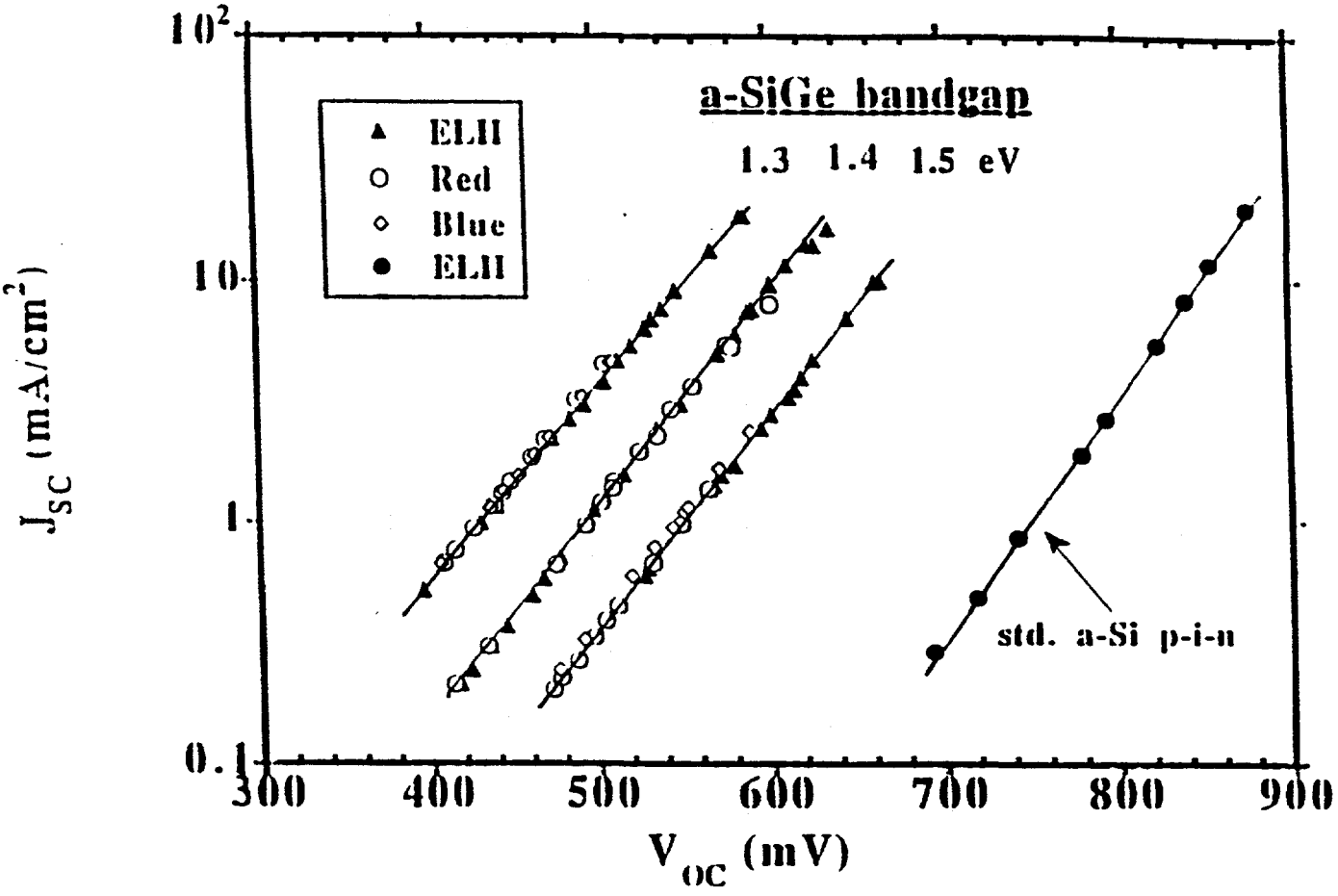

Figure 80. Log J_{sc} vs. V_{oc} for three graded bandgap a-SiGe devices and one a-Si device, measured with light of different spectral content.

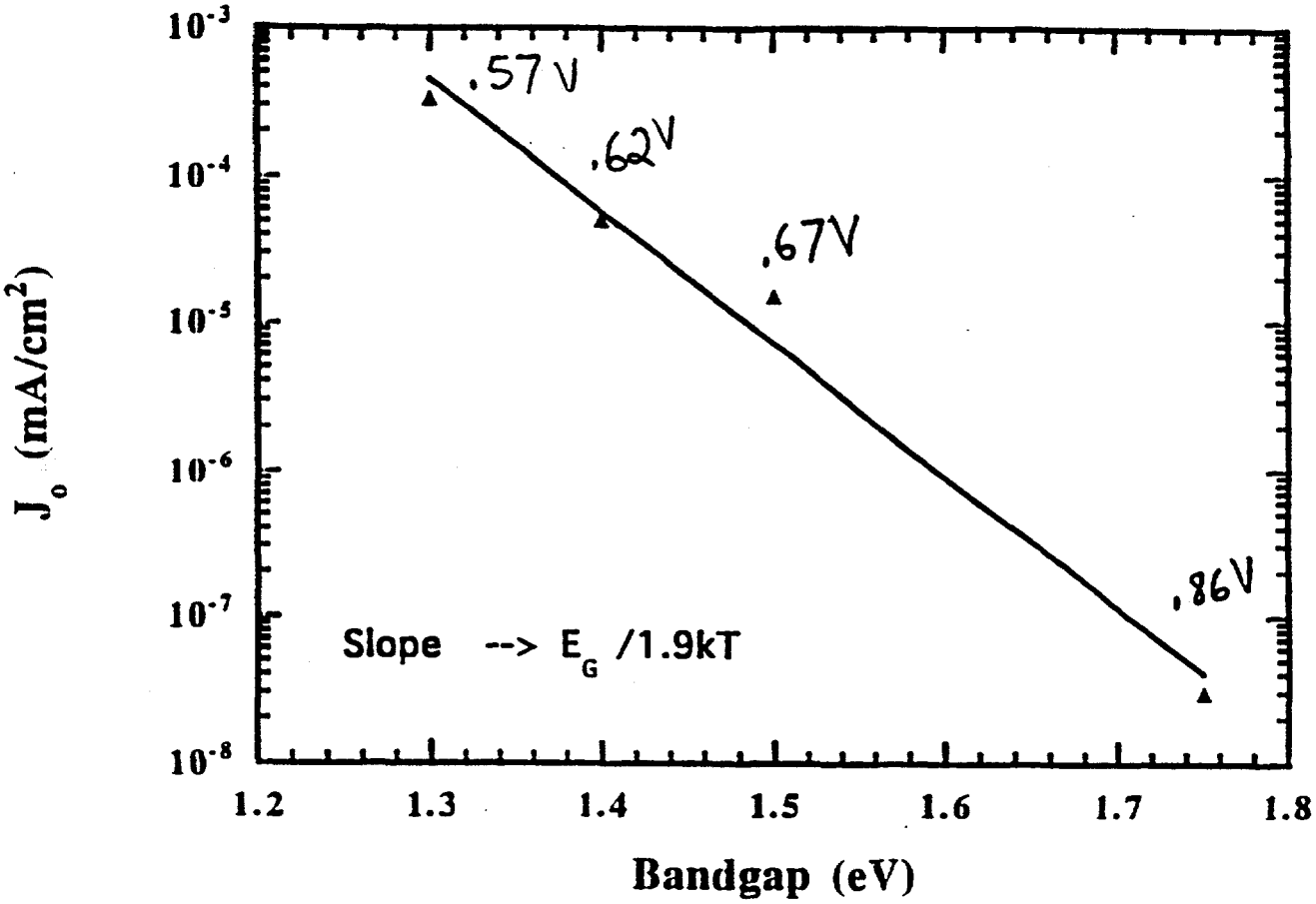

Figure 81. Log J_o vs. bandgap of i-layer, showing slope of nearly Eg/2kT. V_{oc} values are shown.

4.0 RESEARCH AND DEVELOPMENT COLLABORATION

IEC has continued its ongoing collaboration with industry, national laboratories and other research organizations to assure that IEC's capabilities are efficiently utilized by the photovoltaic community and that the focus of its research is relevant to the advancement of PV technology. Collaborations deal with all aspects of thin film solar cell research including sharing of information regarding process, material, and device characterization and the supplying and sharing of films, devices, measurements and analyses.

IEC is the team leader of the Device Design and Interface (DDI) Team, for which we are the primary device makers. We are also on the Low Bandgap Team because of our strong interest in design and characterization of a-SiGe devices. Specific collaborations have included work with APS on tunnel junctions, ECD on sputtered TCO, and Harvard University on device deposition on their textured ZnO. This represents our first collaborations with each of these groups, and was motivated by our commitment to meeting Team goals.

A description of the collaborative activities is listed below for the polycrystalline materials, $CuInSe_2$ and CdTe, and for a-Si under the NREL Teams.

Polycrystalline Device Measurement Data Base

A data base of the current-voltage data measured on a wide variety of polycrystalline solar cells has been established. This data set includes cells fabricated at IEC as well as several other manufacturers and laboratories which are listed in Section 3.1. This data base has been made available to the solar cell community via the Internet. In particular, the results have been supplied to groups doing analysis and modeling at Colorado State University, Purdue, and Penn State University.

Solarex

IEC has supplied $CuInSe_2$, CdS and ZnO films and fabricated devices to assist Solarex in the development of its process. Also, assistance was provided on deposition of $CuInSe_2$ by thermal evaporation, ZnO deposition, and other process development for $CuInSe_2$ module fabrication.

International Solar Electric Technology (ISET)

Glass/Mo substrates deposited by ISET for $CuInSe_2$ devices were characterized by X-ray diffraction measurements to characterize their structure.

University of Illinois

IEC has continued to assist the University of Illinois in evaluating the $CuInSe_2$ deposited by their hybrid sputtering process by doing material measurements and device fabrication and characterization. IEC has also supplied $CuInSe_2$ and $Cu(InGa)Se_2$ samples to the U. of Illinois for detailed materials measurements.

Institute of Physical Electronics (IPE), University of Stuttgart

Samples were exchanged to evaluate CdS and ZnO layers used as window/heterojunction layers in $CuInSe_2$ devices. Detailed device measurements of a $CuInSe_2$ device from IPE were done at IEC as discussed in Section 3.1.

An electrical engineering graduate student from the University of Stuttgart, Axel Hartmann, spent 6 months during 1993 at IEC. He worked on depositing Mo, Cu, and In layers by sputtering and characterizing the film properties and deposition system. These layers have been successfully used for selenization to produce $CuInSe_2$ cells as discussed in Section 2.1.

Solar Cells Inc.

Structural characterization and cell fabrication were completed on CdS/CdTe samples from SCI. X-ray diffraction measurements showed that the CdTe films have a different orientation than the evaporated CdTe films from IEC, both as-deposited and after heat treatment. Solar cells were completed to evaluate the role and optimum thickness of the Cu in evaporated Cu/Ni and Cu/Au contacts. In all cases the inclusion of Cu in the contact resulted in a significant increase in V_{oc}.

National Renewable Energy Laboratory (NREL)

IEC collaborated with NREL to complete detailed microstructural characterization of CdTe solar cells investigating the effects of the $CdCl_2$ heat treatment. This work is detailed in Section 2.3.

IEC performed current-voltage measurements on NREL $Cu(InGa)Se_2$ cells as discussed in Section 3.1.

Martin Marietta

IEC has collaborated with Martin Marietta on their development of $CuInSe_2$ solar cells and modules deposited on flexible substrates. This work was performed under a separate contract. This included the evaluation of different substrate materials, deposition of the $CuInSe_2$ by selenization, assistance with the deposition of CdS and ZnO layers and the evaluation of all these layers primarily by the fabrication and characterization of complete devices.

Mobil Solar Energy Corporation

IEC, under a separate contract with Mobil Solar, fabricated and evaluated solar cells with a deposited a-Si emitter layer on EFG Si wafers. Preliminary results lead to a solar cell with greater than 10% efficiency using a process done completely at low temperatures.

AstroPower

IEC is collaborating with AstroPower under a separate contract to investigate the loss analysis of thin film Si solar cells. This contract includes the support and supervision of two graduate students.

Advanced Photovoltaic Systems (APS)

IEC has collaborated with APS to characterize n^+/p^+ recombination junctions, also known as tunnel junctions (TJ), which interconnect individual cells in a multijunction stack. They are required to support very high recombination rates under reverse bias with negligible voltage drop. They must also be transparent to red light. It has been reported that a p/n junction, formed using a conventional process for a-Si p and n-layers, produces a recombination junction, which is non-ohmic and has too high a resistance. Two techniques for improving the junction properties are to insert a thin layer of a defective or highly doped material, or to make one or both of the layers microcrystalline. Improving recombination junctions was a specific goal of the DDI team. Results of tunnel junctions made at IEC were presented at a team meeting. Afterwards, APS expressed an interest in collaborating with us to improve their tunnel junctions. They had reported that the TJ was limiting their tandem cell performance and suspected that the TJ was unstable under lightsoaking.

Tunnel junctions were deposited by photo-CVD with and without a 25Å recombination interlayer (3530 and 3529, respectively). The a-SiC p-layer and a-Si n-layer were approximately 1000Å thick. The 25Å recombination layer was a heavily boron doped a-Si p-layer (no carbon). This p^+ layer would supply holes needed to recombine with electrons in the n layer since the standard wide bandgap a-SiC p-layer has a very low conductivity and carrier density. These junctions were characterized using JV, QE. and CV measurements. They were then light soaked under a Xe lamp and current soaked at high forward bias to determine if they degraded, and therefore would contribute to the degradation of tandem cells as reported by APS.

Measurements confirmed that the thin p^+ improved the recombination significantly without increasing absorption.

The conductance of 3530 with the p^+ layer was twice that of device 3529 without the p^+ layer. Figure 82 shows the QE of the two devices. The QE of 3530 is much less than that of 3529, consistent with a major increase in recombination. Plots of $1/C^2$ vs. V were linear for both devices, suggesting space charge densities of $1\text{-}2x10^{+17}/cm^3$ for both. This is probably the space charge in the a-SiC p-layer since it has 2-3 orders of magnitude lower conductivity than the n-layer. Light soaking increased the conductance of both junctions by about 50%. This is consistent with the idea that light soaking creates defects, and more defects result in more recombination, which means a higher current can flow at a given injection level (bias voltage). Neither cell changed under current soaking at high forward bias.

Based on these results, APS fabricated a pair of devices with similar structure. Sample 233 had the extra a-Si p^+ recombination enhancing layer between the p and n layers ($n/p^+/p$) while sample 234 had a simple n/p junction structure. The doped p and n-layers were 100-200 Å, the same thickness as found in cells.

Figure 83 shows that the conductance was independent of voltage from -.2 to +.2 V on these cells, indicating they have ohmic not p/n junction-type JV characteristics. The p^+ layer increases conductance by a factor of two. Figure 84 shows that the QE for 233 was much lower than for 234 in agreement with results from IEC devices (Figure 82). Apparently, the p^+ layer is very effective in increasing recombination of photogenerated carriers across the junction. The capacitance was only a very weak function of voltage, probably due to the extreme thinness of the layers. This is unlike results on IEC devices which were thicker and presumably could support a greater space charge width than the APS samples. Light soaking the two APS samples for 100 hours equivalent or annealing had no significant effect on either of the two samples, as shown in Table 39.

Table 39. Conductance (J/V at V=0.1 V) of APS recombination junctions. #233 had the thin p^+ layer.

	Conductance (mS/cm^2)	
	233-1	234-2
initial	122	62
100 hrs LS	135	77
annealed	129	69

Thus, results from IEC and APS tunnel junctions with and without the p^+ layer are in agreement. The p^+ layer reduces the voltage drop without increasing absorption. The QE strongly suggests that the p^+ layer increases the recombination. TJ performance improves with light soaking. Therefore, the p^+ recombination

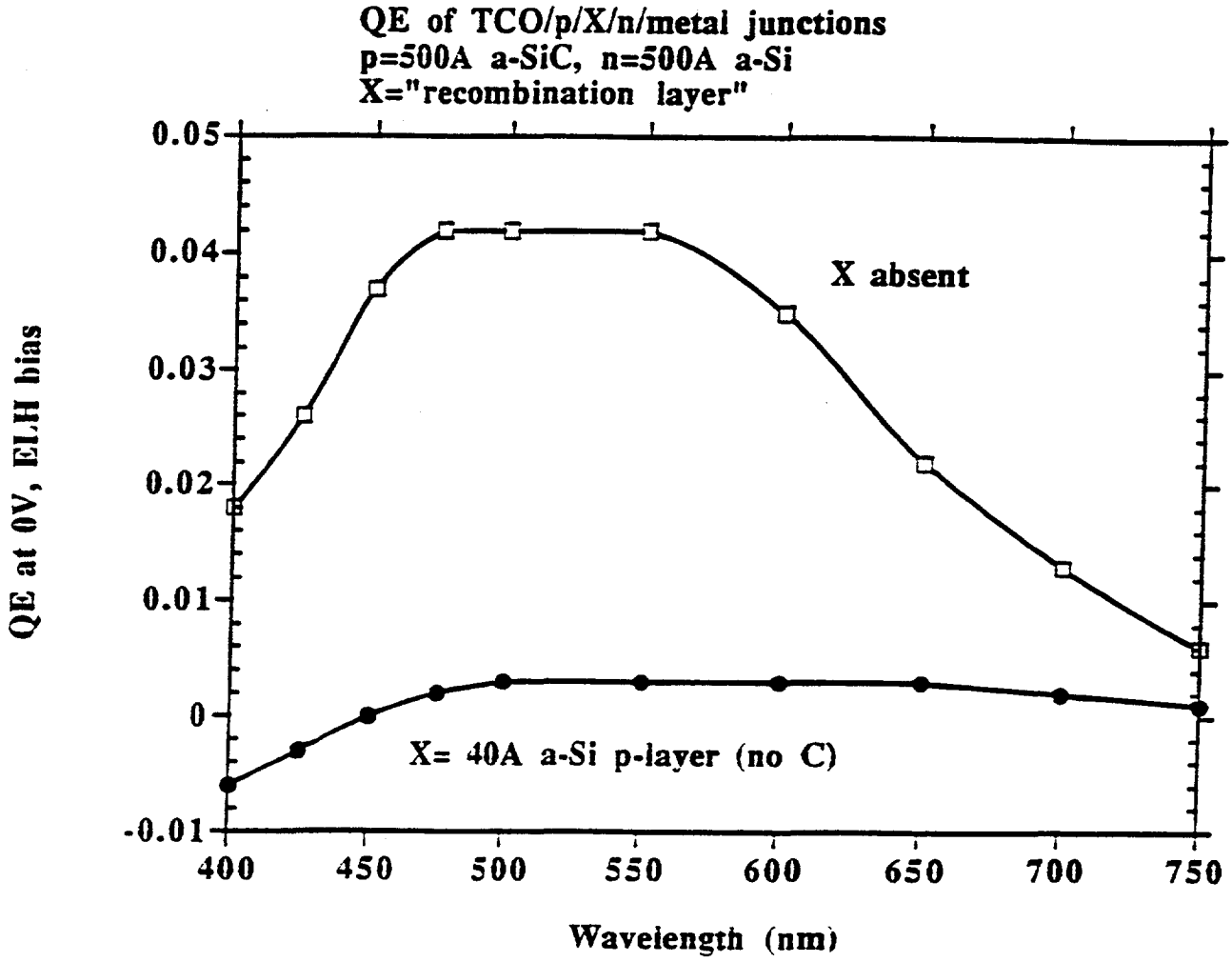

Figure 82. QE of IEC tunnel junctions with and without a-Si p+ recombination layer.

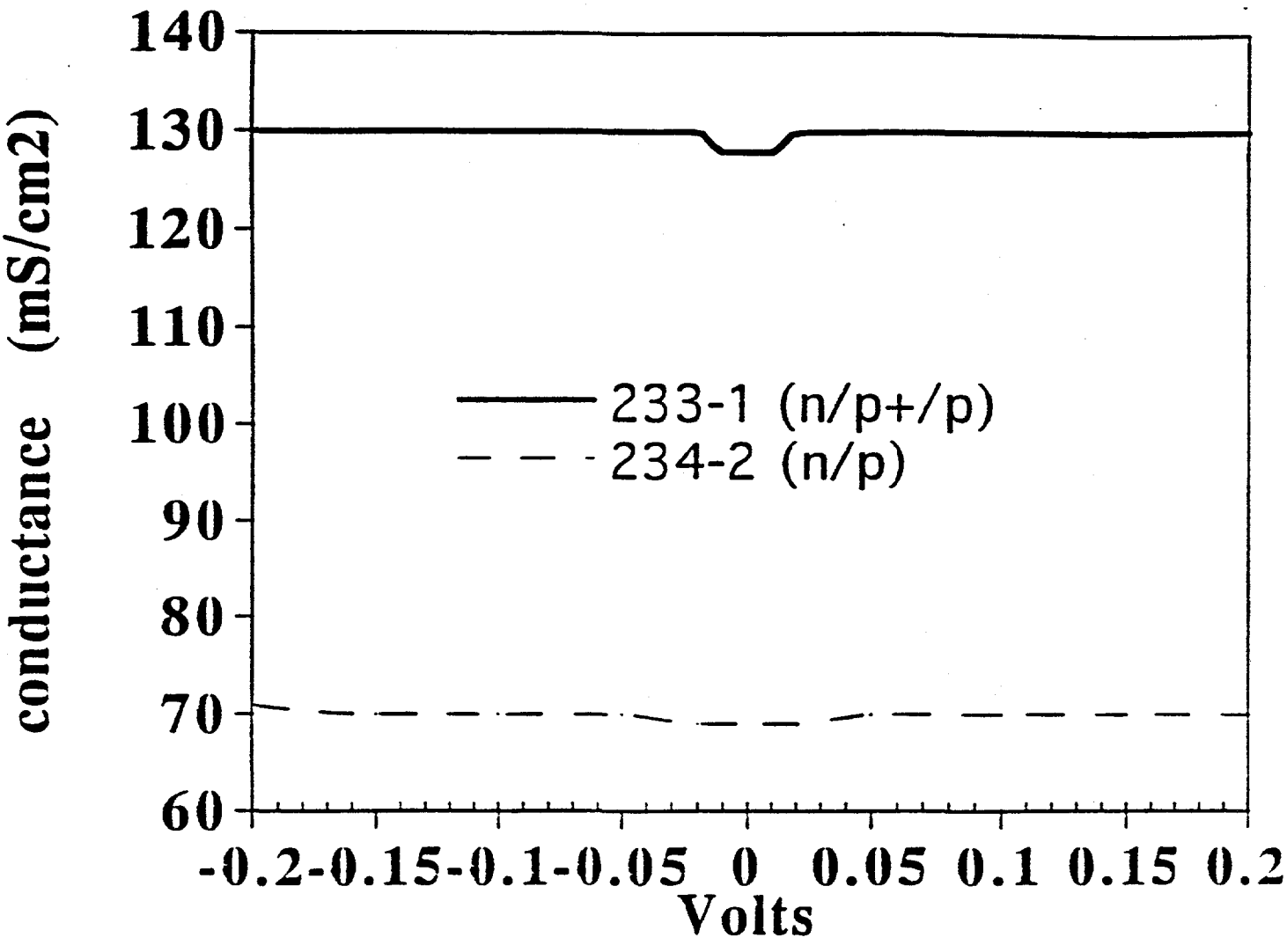

Figure 83. Conductance of APS tunnel junctions with and without thin p+ layer after light soaking.

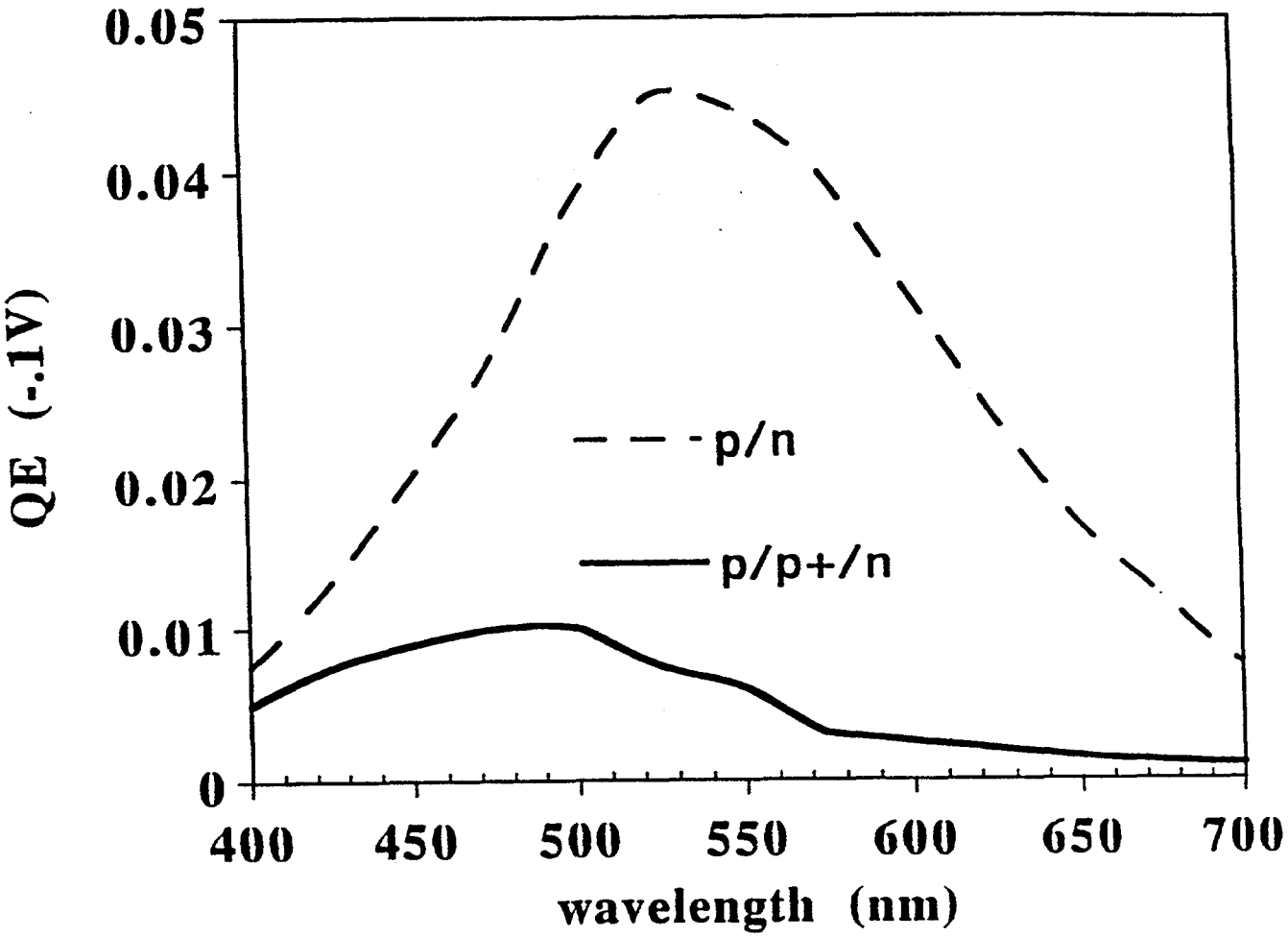

Figure 84. QE at -0.1V of APS tunnel junctions with and without thin p+ recombination layer.

layer improves the performance of the TJ without increasing instability. Future work will involve characterization of TJ from APS having microcrystalline doped layers with the thin p^+ layer.

Energy Conversion Devices (ECD)

IEC deposited TCO's on 8 substrate p-i-n cells from ECD in three ZnO and one ITO runs. This enables ECD to compare IEC's sputtered ZnO to their own. The ZnO was deposited by sputtering in 0.1% O_2 for 40 or 105 seconds, leading to sheet resistances of 160 and 90 Ω/□ respectively. The single ITO layer was sputtered in Ar/O_2 for 40 seconds leading to sheet resistance of 50 Ω/□. Cells with Ni bus bars were defined with standard photolithography processing at IEC. Optical properties of the devices and the witness slide were characterized, and the sheet resistance of the Ni/TCO/Ni contact was measured.

There was no correlation between cell performance and ZnO thickness, but a strong correlation with position in the sputtering system. This is not seen in IEC $CuInSe_2/CdS/ZnO$ devices. Comparable results were obtained for the 40 sec. ITO or ZnO layers. The best cell for each type of TCO had V_{oc}=0.89 V, J_{sc}=14.0-14.5 mA/cm^2, FF=58-60%, and eff.~7.5%. The V_{oc_2} and FF are similar to those obtained at ECD but J_{sc} is 2 mA/cm^2 lower than expected. FF ranged from 25 to 60% due to a double diode effect, not shunting. The low J_{sc} was due to low QE at all wavelengths, presumably due to excess absorption in the TCO. The appearance of the ZnO changed during the processing, indicating that there may have been chemical interaction between the TCO/p-layer during the photolithography processing. A follow-up exchange is planned with alternative processing.

Harvard University

Investigating higher performance TCOs is a key to achieving goals of the DDI team. For superstrate device structures, strategies include using textured ZnO and bilayers of ZnO coated with a thin layer of SnO_2 and vice versa.

Devices were deposited on textured ZnO on 7059 glass received from Harvard. The fluorine doped ZnO was deposited by APCVD in R. Gordon's group. The ZnO layers had different texture as determined by their haze. Sheet resistances ranged 10-15 Ω/□. IEC a-Si run #4208 had two pieces of standard Solarex SnO_2 and one piece each of the ZnO coated glass with different texture. The a-Si was deposited at 0.5 torr with a buffer; the i-layer thickness was 0.40 μm. One of the pieces on SnO_2 received Ti/Ag back contact, while the other three received ITO/Ag. Cell results are given in Table 40.

Table 40. Device results after heat treatment for the best cell on each piece from run #4208. Purpose was to compare Solarex SnO_2 with Harvard ZnO and to compare ITO/Ag with Ti/Ag contacts.

Piece	TCO	Front back contact	Voc (mv)	Jsc (mA/ cm2)	Rvoc (ohm/ cm2)	FF (%)	eff. (%)
4208-11	SnO2	ITO/Ag	832	15.6	6.9	66.2	8.6
4208-12	ZnO#262	ITO/Ag	823	13.9	15.0	58.3	6.7
4208-21	ZnO#275	ITO/Ag	823	13.4	13.1	61.2	6.8
4208-22	SnO2	Ti/Ag	835	13.3	4.9	72.4	8.0

Note that the -22 piece with Ti/Ag contacts had FF>72%, indicating the high quality of the devices. However, the ITO/Ag device (-11) had significantly poorer FF, presumably due to the contact resistance. Devices deposited on the ZnO were poor, having lower J_{sc} and FF. The poor FF is attributed to a contact resistance between the ZnO and the p-layer, not shunting.

The QE (Figure 85) shows fringing, suggesting that the film has insufficient texture. This is supported by reflectance measurements which showed fringing for the two ZnO-coated pieces, but not the SnO_2-coated piece. The lower blue response is surprising since ZnO should have less blue absorption.

In future collaboration with Gordon's group we intend to deposit devices on ZnO-coated glass with SnO_2 and on newly deposited ZnO having higher texture.

University of North Carolina

We provided several well-characterized p-i-n devices to Univ. of North Carolina for electroluminescence measurements. Their results on studying i-layer recombination and stability on these cells were published at the 1993 MRS and the 1993 ICAS.

Syracuse University

Several a-Si and a-SiGe devices were sent to Syracuse University for characterization of built-in potential using electroabsorption (EA). They found a value of ~.97 V, nearly identical to that which was found at IEC several years earlier on the same sample using J_{sc}-V_{oc}-T measurements. The EA technique was shown to be extremely sensitive to the a-SiC buffer layer. This work will be presented at the 1994 MRS conference.

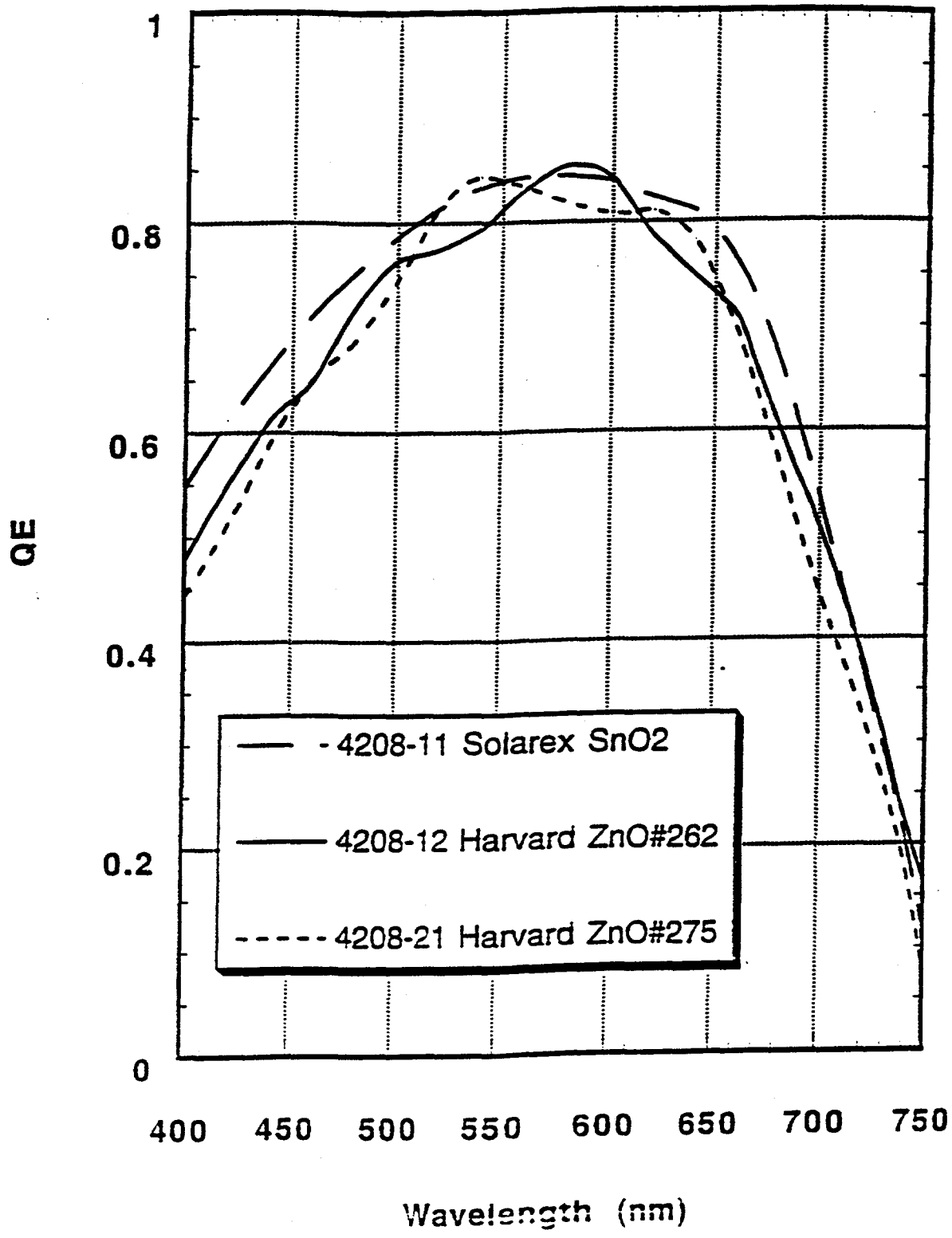

Figure 85. QE at -1V of three devices on different textured TCO.

5.0 REFERENCES

1. S. Verma, S. Yamanaka, R.W. Birkmire, B.E. McCandless and TWF Russell, 11th E.C. Photovoltaic Solar Energy Conf., Montreux, Switzerland, Oct. 12-16, 1992, 807 (1992).

2. Annual report from IEC to National Renewable Energy Laboratory for Subcontract #XN-0-10023-1, (1992).

3. R. Klenk, R. Menner, D. Cahen and H.W. Schock, Proc. 22nd IEEE Photovoltaic Spec. Conf, (1990).

4. P.R. Subramanian and D.E. Laughlin, Bulletin of Alloy Phase Diagrams **10**(5), 554 (1989).

5. W. E. Devaney, R. A. Mickelsen, and W. S. Chen, Proc. of the 18th IEEE PV Spec. Conf., Las Vegas, 1985. 1733 (1988).

6. J. Hedstrom, H. Ohlsen, M. Bodegard, A. Kylner, L. Stolt, D. Hariskas, M. Ruckh, and H. W. Schock, 23rd IEEE PV Spec. Conf., 364 (1993).

7. B. Dimmeler, H. Dittrich, R. Menner and H. W. Schock, 19th IEEE PV Spec. Conf., 1454 (1987).

8. W. E. Devaney, W. S. Chen, J. M. Stewart, and R. A. Mickelsen, IEEE Trans. on Electron Devices **37**(2), 428 (1990).

9. R.H. Mauch, et al., Proc. 22nd IEEE PVSC, 898 (1991).

10. B.E. McCandless and S.S. Hegedus, Proc. 22nd IEEE Photovoltaic Specialists Conf., Las Vegas, 969 (1991).

11. R.W. Birkmire, B.E. McCandless and S.S. Hegedus, Int'l J. Solar Energy **12**, 183 (1992).

12. B.E. McCandless and R.W. Birkmire, Solar Cells **31**, 527 (1991).

13. Annual report to NREL, subcontract no. XL-9-19032, 36 (1990).

14. Final report to NREL, subcontract no. XN-0-10023-1, 43 (1993).

15. Final report to NREL, subcontract no.XM-0-18110-2, 31 (1992).

16. unused

17. Y.-M. Li, A. Catalano and B.F. Fieselmann, Mat. Res. Soc. Symp. Proc. 258, 923 (1992).

18. M. Hirose, Semiconductors and Semimetals, Volume 21, Hydrogenated Amorphous Silicon, Part A, Preparation and Structure, Edited by J.I. Pankove, Academic Press, Inc., (New York, 1984) 35 (1984).

19. See for example S.C. Saha, A.K. Barua and S. Ray, J. Appl. Phys. 74, 5561 (1993).

20. See for example S.C. De, S. Ray and A.K. Barua, Thin Solid Films 167, 121 (1988).

21. J.P. Harbison, A.J. Williams and D.V. Lang, J. Appl. Phys. 55, 946 (1984).

22. See for example ref 5 p. 29.

23. R.R. Arya, A. Catalano and R.S. Oswald, Appl. Phys. Lett. 49,1089 (1986).

24. See for example ref 18.

25. J.C. Knights and R.A. Lujan, Appl. Phys. Lett. 35, 246 (1979).

26. S.J. Jones, Y. Chen and D.L. Williamson, AIP conference Proc.: Photovol. Adv. Res. & Dev. Proj. 268, 357 (1992).

27. Y.-M. Li, private communication.

28. R.E. Rocheleau, S.S. Hegedus, W.A. Buchanan, S.C.Jackson, Appl. Phys. Letters **51**, 133 (1987).

29. S.S. Hegedus et al, Proc. 20th IEEE PV Spec. Conf., 129 (1989).

30. W.N. Shafarman and J.E. Phillips, 22nd IEEE PV Spec. Conf., 934 (1991).

31. R.W. Birkmire et al., Final report under NREL subcontract XN-0-10023-1 for the period 1/16/90 to 1/15/93 (March 1993).

32. W.N. Shafarman and J.E. Phillips, 23rd IEEE PV Spec. Conf., 453 (1993).

33. T.W. Fraser Russell et al., 12th NREL PV Program Review Meeting, Oct. 13-15, 1993, Denver, CO (to be published).

34. M. Roy, S. Damaskinos, and J.E. Phillips, 20th IEEE PV Spec. Conf., 1618 (1988).

35. M. Roy, Ph.D. Thesis, University of Delaware (1988).

36. T. Walter and H. Schock, 12th NREL PV Program Review Meeting, Oct. 13-15, 1993, Denver, CO (to be published).

37. T. Walter, communication at Device Characterization and Modeling of $CuInSe_2$-based Photovoltaic Devices, Oct. 17-19, 1993, Estes Park, CO, sponsored by the Electric Power Research Group.

38. A. Rose, "Concepts in Photoconductivity and Allied Problems, Wiley, New York (1963).

39. C. van Berkel, M.J. Powell, A.R. Franklin, and I.D. French, J. Appl. Phys. 73(10), 5264, 15 May 1993.

40. Yi Tang, R. Braunstein and Bolko von Roedern, Appl. Phys. Lett. 63(17), 2393, 25 October 1993.

41. D.A. Fardig and J.E. Phillips, 22nd IEEE PV Spec. Conf., 1146 (1991).

42. S. Wiedeman et al., Proc. 21st IEEE PV Spec. Conf., 1529 (1990).

43. S. Hegedus, W. Buchanan, Proc. 23rd IEEE PV Spec. Conf., 991 (1993).

6.0 ABSTRACT

An integrated program of research on thin film deposition processes, materials, and devices based on a-Si:H, $CuInSe_2$ and CdTe is presented. $CuInSe_2$ films have been formed by the selenization of Cu/In bi-layers in both flowing H_2Se and an elemental selenium vapor with the reaction chemistry determined in each case and used to improve control and performance of devices. Bandgap modified $CuInSe_2$ has been evaluated with $Cu(InGa)Se_2$ deposited by thermal evaporation. As the Ga content increases, the compositional distribution in the film increases while the electrical performance of devices falls off. Microstructural characterization of CdTe/CdS devices explains the critical and inter-related roles of the $CdCl_2$ heat treatment, the CdS layer and the contact in controlling recrystallization, grain growth, and interdiffusion and fabricating high efficiency cells. Device measurements have been used to identify modifications needed in the plasma-CVD deposition of a-Si p-i-n devices leading to improved device performance and reproducibility. A model of the quantum efficiencies of a-Si devices was developed and used to identify losses in the p- and buffer layers. Current-voltage measurements of $CuInSe_2$ and $Cu(InGa)Se_2$ cells made by a variety of different processes and laboratories were analyzed showing that they all behave similarly, dominated by a distribution of states within the bandgap of the absorber layer. Finally, a number of collaborations with other laboratories and industries have dealt with all aspects of thin film solar cell research.

REPORT DOCUMENTATION PAGE

Form Approved
OMB NO. 0704-0188

1. AGENCY USE ONLY (Leave blank)	2. REPORT DATE	3. REPORT TYPE AND DATES COVERED
	September 1994	Annual Subcontract Report, 16 January 1993-15 January 1994

4. TITLE AND SUBTITLE

Processing and Modeling Issues for Thin-Film Solar Cell Devices

5. FUNDING NUMBERS

C: X-AV-13170-01

TA: PV431101

6. AUTHOR(S)

R.W. Birkmire, J.E. Phillips, W.A. Buchanan, S.S. Hegedus, B.E. McCandless, W.N. Shafarman, T.A. Yokimcus

7. PERFORMING ORGANIZATION NAME(S) AND ADDRESS(ES)

Institute of Energy Conversion
University of Delaware
Newark, Delaware 19716-3820

8. PERFORMING ORGANIZATION REPORT NUMBER

9. SPONSORING/MONITORING AGENCY NAME(S) AND ADDRESS(ES)

National Renewable Energy Laboratory
1617 Cole Blvd.
Golden, CO 80401-3393

10. SPONSORING/MONITORING AGENCY REPORT NUMBER

TP-451-7056

DE94011895

11. SUPPLEMENTARY NOTES

NREL Technical Monitor: B. vonRoedern

12a. DISTRIBUTION/AVAILABILITY STATEMENT

12b. DISTRIBUTION CODE

UC-1263

13. ABSTRACT *(Maximum 200 words)*

This report describes work performed during the first year of an integrated program of research on thin-film solar cells based on a-Si:H and its alloys, $CuInSe_2$ and its alloys, and CdTe. The overall objective of the research presented in this report is to advance the development and acceptance of thin-film photovoltaic (PV) modules by increasing the understanding of film growth and processing and its relationship to materials properties and solar cell performance. The specific means toward meeting this larger goal include (1) investigating scalable, cost-effective deposition processes; (2) preparing thin-film materials and device layers and completed cell stuctures; (3) performing detailed material and device analysis; and (4) participating in collaborative research activities that address the needs of PV manufacturers.

14. SUBJECT TERMS

processing ; modeling ; thin films ; devices ; photovoltaics ; solar cells

15. NUMBER OF PAGES
206

16. PRICE CODE

17. SECURITY CLASSIFICATION OF REPORT	18. SECURITY CLASSIFICATION OF THIS PAGE	19. SECURITY CLASSIFICATION OF ABSTRACT	20. LIMITATION OF ABSTRACT
Unclassified	Unclassified	Unclassified	UL